Effects of Density Control on the Internal Plasma Dynamics and Current Drive in HIT-SI

Brian Scott Victor

A dissertation
submitted in partial fulfillment of the
requirements for the degree of

Doctor of Philosophy

University of Washington

2012

Reading Committee:

Thomas R. Jarboe, Chair

Brian A. Nelson, Chair

Uri Shumlak

Program Authorized to Offer Degree:
Aeronautics and Astronautics

University of Washington

Abstract

Effects of Density Control on the Internal Plasma Dynamics and Current Drive in HIT-SI

Brian Scott Victor

Chair of the Supervisory Committee:
Professor Thomas R. Jarboe
Aeronautics and Astronautics

Professor Brian A. Nelson
Electrical Engineering

The Helicity Injected Torus with Steady Inductive Helicity Injection (HIT-SI) experiment investigates a method of current drive and spheromak formation through constant inductive helicity injection into a confinement volume of major radius 0.3 m. Using Steady Inductive Helicity Injection (SIHI) a DC plasma current is generated and formed in the confinement volume from the AC driven plasma injectors. Recent results have shown that helium plasmas can be used to condition the walls for deuterium plasmas. These deuterium plasmas have produced record toroidal currents (> 50 kA) and current amplifications ($\sim$3) on HIT-SI. In addition density measurements indicate that deuterium plasmas are the first plasmas on HIT-SI to achieve a ratio of current density to electron density, $j/n > 10^{-14}$ A·m, an important indication of plasma quality. Internal magnetic field measurements show these high performance plasmas have suppressed fields indicative of a region of low λ and that this region is built up and sustained during the injector drive. Currents in this low λ region that do not link the injectors—named separatrix currents—are sustained up to 40 kA. Finally a model that predicts the build up of toroidal current from the density and injector

current is developed. The implication of this model is that dynamo current drive can be entirely applied and does not need to result from instabilities in the plasma.

TABLE OF CONTENTS

LIST OF FIGURES

LIST OF TABLES

ACKNOWLEDGMENTS

I would like to thank my advisor Tom Jarboe for the opportunity to work on such an interesting project and for showing me his creativity and ability to always keep the project moving in a positive direction. I would also like to thank Brian Nelson for his ability to always be able to solve a problem, especially ones that I have created, and Roger Smith for always letting me bounce ideas off of him and for pointing me in the right direction with my work. I would like to thank John Rogers, Jon Hayward, and George Andexler for their technical support and knowledge. I would also like to acknowledge my fellow grad students for insights from discussing our work: Cihan Akcay, Aaron Hossack, Chris Hansen, and Kyle Morgan.

Finally, I would like to thank my wife and daughter for supporting me through my work here.

Chapter 1
INTRODUCTION

Fusion power has the potential as a nearly limitless energy source. Energy is released when two atoms of low atomic number fuse together to create a new atom and release energy. While the potential benefits of fusion power are large the implementation of a working fusion reactor has proven quite complex. Progress has been made in achieving reactor conditions, but a reactor that generates net positive energy has yet to have been developed. The complexity arises because of the high temperatures required for fusion to occur. At these temperatures matter is in a fully ionized plasma state. Material walls cannot withstand these temperatures to confine the plasma. Magnetic fields are used to keep the plasma away from the walls and are the leading method of plasma confinement. Because the matter is in an ionized state, particles follow the magnetic field lines. The success of magnetic confinement rests on the ability of the magnetic fields to keep particles confined at a high enough temperature and density for a sufficient length of time. The necessary parameters to achieve fusion in magnetic confinement devices are temperatures of $\sim$15 keV (174,000,000 K), pressures of $\sim$7 atm and energy confinement times of $\sim$1 s [1].

1.1 Magnetic confinement devices

Many novel approaches have been attempted to achieve fusion through magnetic confinement. Some of the configurations are tokamaks [2], stellarators [3], reversed field pinches [4], spheromaks [5], field reversed configurations [6], Z-pinches [7], θ-pinches [8] and mirror machines [9]. Each device attempts to confine particles by balancing a pressure gradient with the Lorentz force. Confinement is achieved in

steady state with $\nabla P = \vec{j} \times \vec{B}$. Where $\vec{j}$ is the current density and $\vec{B}$ is the magnetic field.

A disadvantage of magnetic confinement devices is the large cost associated with the coils necessary to create the magnetic field in the plasma. A measure of the efficiency of a magnetic confinement configuration is the ratio of the plasma pressure to the magnetic field energy density, referred to as β.

$$\beta = \frac{P}{B^2/2\mu_0} \tag{1.1}$$

The higher the plasma β the more effective a magnetic confinement configuration is at confining a plasma. However, high β is difficult to achieve because plasma instabilities develop as β is increased. The best configurations offer a compromise between stable confinement and high β.

Toroidal magnetic configurations (see Fig. 1.1) are used because field lines connect around the device so particles streaming along these field lines can orbit around the device. Simply speaking the toroidal field provides the stability for the configuration

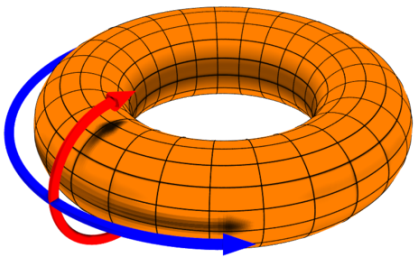

Figure 1.1: Torus. Toroidal direction is shown in blue. Poloidal direction is shown in red. Image is courtesy of Wikipedia Commons [10].

and the poloidal field provides the confinement. Stability is improved by using coils

that produce a DC toroidal field in the plasma. These fields are effective in providing stability to the plasma, but at a reduced β. Thus the stability is achieved through the, often significant, added cost of the coils.

In most magnetic confinement devices, internal plasma currents help to heat and confine the plasma. Toroidal current generates the poloidal fields which provide the pressure balance to confine the plasma. Plasmas Ohmically heat through current drive in a similar way to a light bulb heating when current is driven through the filament. One of the biggest challenges with toroidal devices is driving toroidal current. To achieve steady-state operations in tokamaks and spheromaks an economical method for driving the toroidal current for an indefinite period of time needs to be developed.

1.2 Tokamak

The most widely studied toroidal plasma configuration is the tokamak, Fig. 1.2. The tokamak uses three primary sets of magnetic coils: toroidal field coils, a central solenoid coil and poloidal field coils (located outside of the toroidal field coils in Fig. 1.2). Compared to other devices tokamaks have a large toroidal field. ITER [12] plans to use superconducting coils that generate 5.3 T fields. The central solenoid coil is a single pulsed coil that is used to create a loop voltage in the plasma to drive toroidal current. The central solenoid coil can be thought of as the primary coil of a transformer with the plasma the secondary coil. The poloidal field coils are used to shape the plasma.

Tokamaks have achieved the best physics performance with stable operation at near reactor relevant pressures, confinement times, and temperatures [1]. The Joint European Torus (JET) has achieved a Q factor, the ratio of power in to fusion power created, of near 1 [13]. It is likely that tokamaks will be able to produce net energy out, but the question is whether they can do it economically.

The large toroidal field on the tokamak is good for plasma stability, but lowers β. In addition the toroidal field coils need to link the plasma, adding cost and

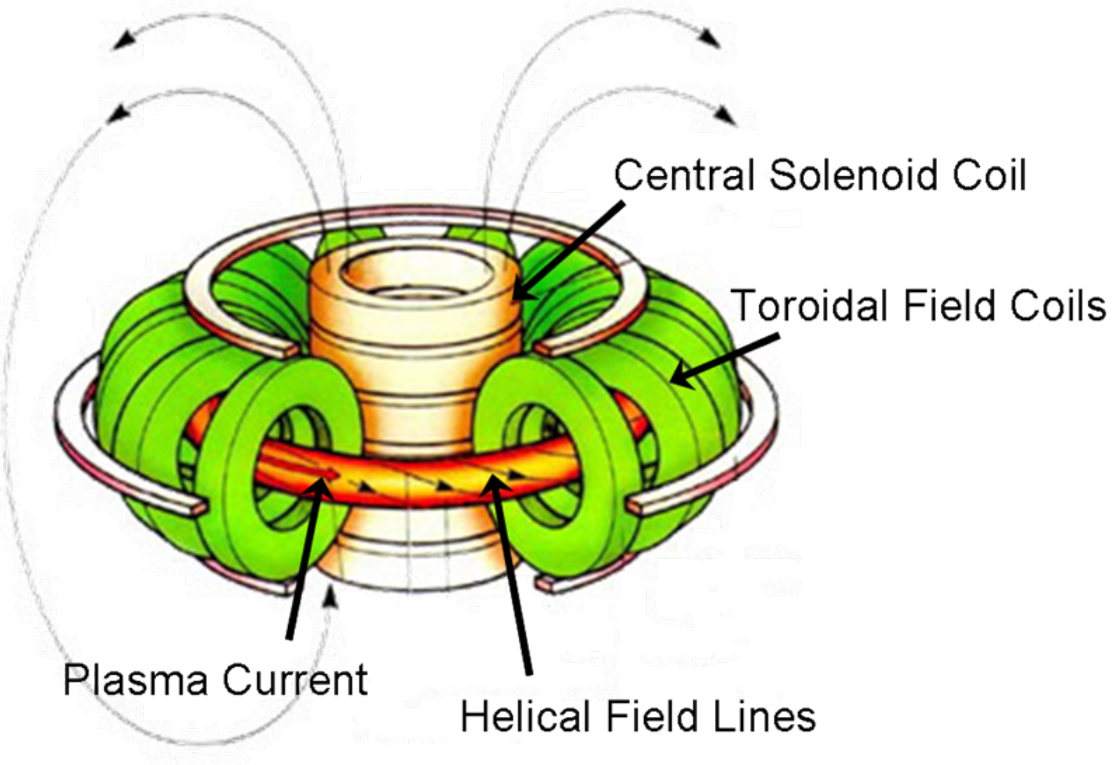

Figure 1.2: Tokamak. The central solenoid coil is the light yellow coil at the center of the torus. The toroidal field coils are colored in green. Image is courtesy of European Nuclear Society [11].

complexity to the design. Tokamaks also require auxiliary heating in order to achieve high temperatures. These auxiliary heating methods, such as neutral beam injection (NBI) and radio frequency (RF) heating are expensive and have low efficiencies [1].

Current drive is another issue in the tokamak device. The central solenoid is an inherently pulsed device and additional current drive methods will be necessary to achieve steady-state operation. Alternative current drive methods presently in use, such as lower hybrid current drive (LHCD), have predicted efficiencies for fusion reactors of up to $\eta_{cd} \sim 0.05$ A/W [1]. Thus 100 W of auxiliary power are required to drive 5 Amps of toroidal current. This would lead to a large fraction of the fusion power created in a reactor being necessary to drive the toroidal current.

1.3 Spheromak

A spheromak is a toroidal magnetic configuration within a simply-connected geometry, Fig. 1.3. Neither a central solenoid or toroidal field coil are needed to form a

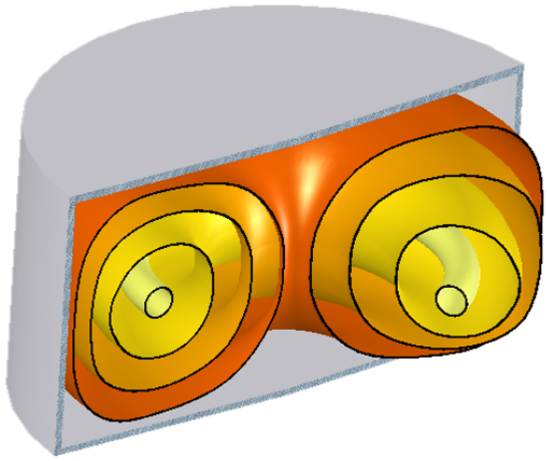

Figure 1.3: A drawing showing the flux surfaces of a spheromak within in a simply-connected geometry. Image courtesy of R. G. O'Neill [14].

spheromak. The toroidal and poloidal magnetic fields within the plasma are supplied by internal currents. The toroidal and poloidal fields are of similar magnitude with mostly poloidal field near the wall and toroidal field near the magnetic axis. For experiments operated on time scales short compared to the time for magnetic fields to diffuse into copper, a copper wall can be used to provide the stability and toroidal force balance of the spheromak configuration. For experiments operated on longer time scales external coils can be used for equilibrium and feedback stabilization.

For engineering purposes spheromaks, being simply connected, are simpler and cheaper to build than tokamaks. Spheromaks have the potential to achieve β on the order of 10% [15], compared to the 2-3% predicted by the Troyon limit in tokamaks [1]. Without a central solenoid coil steady-state operation is possible. With respect to

a fusion reactor the large internal currents, both toroidal and poloidal, could allow the spheromak to Ohmically heat to ignition [1]. This would provide an added cost savings as external heating methods would not be needed.

While cost and engineering complexity are limited without the central solenoid and toroidal field coils, the complexities in the physics of toroidal field and current formation are increased. Spheromaks are formed by self organization or relaxation of the magnetic fields to a minimum energy state. Ingenious methods have been developed to inject a quantity known as helicity, to be discussed in later chapters, to form the spheromak. The first spheromaks to achieve electron temperatures above 100 eV did so during the decay phase of the spheromak, after the helicity injection had been stopped [16]. A challenge that continues today for spheromak research is to achieve higher temperature and confinement times while injecting helicity into the spheromak.

1.4 Current drive

As mentioned earlier internal plasma currents are important for the heating and confinement of plasmas. Steady-state operations in tokamaks are limited by the ability to maintain a toroidal current in the plasma. Advances in current drive methods could lead to improvements in the steady-state operations of magnetic confinement devices.

HIT-SI is developing an alternative current drive mechanism called Steady Inductive Helicity Injection (SIHI). This method relies on dynamo action to form and sustain toroidal current. Spheromaks are a simpler device for testing this new current drive method. With an O-point in both the poloidal and toroidal magnetic field within the plasma volume, magnetic flux is not set in either direction by boundary conditions [5]. This allows plasma relaxation to form both the toroidal and poloidal fields within the plasma.

Chapter 2

HELICITY INJECTION CURRENT DRIVE

As discussed in the previous chapter an open issue in magnetic confinement plasma research is toroidal current drive. Spheromaks do not have a central solenoid coil for driving current, and tokamaks need additional current drive methods to achieve steady-state operation. Through helicity injection and magnetic relaxation toroidal current can be driven without a central solenoid coil [5]. Thus methods for injecting helicity are central in spheromak research and provide a path for steady-state operations in tokamaks. This chapter gives a review of the terminology used when discussing magnetic helicity and helicity injection. Also a review of the development of helicity injection current drive on spheromaks and tokamaks is given. HIT-SI uses a method of helicity injection called Steady Inductive Helicity Injection (SIHI), which will be discussed in the following chapter on HIT-SI.

2.1 Magnetic helicity

Magnetic helicity is the linkage of magnetic flux with magnetic flux [17] as shown in Fig. 2.1. It has been shown theoretically [18] and experimentally [5] that plasmas relax to a minimum energy state while conserving helicity. Helicity is conserved through magnetic reconnection and decays at a substantially slower rate than magnetic energy [19]. Helicity is a volumetric quantity and is not defined locally.

$$K = \int \vec{A} \cdot \vec{B} dV \tag{2.1}$$

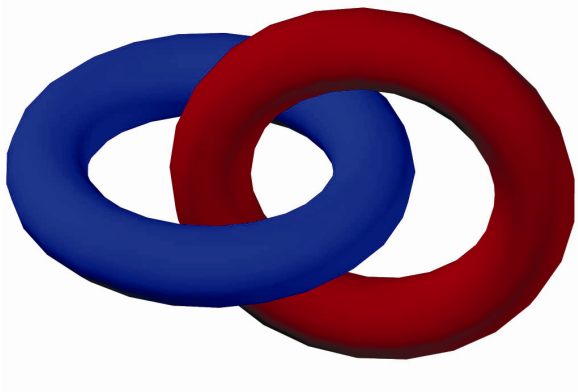

Figure 2.1: Magnetic helicity, K, is the self linkage of magnetic flux. The blue and red toroids are separate flux loops.

where $\vec{A}$ is the vector potential and $\vec{B}$ is the magnetic field. Choosing a volume that encloses both of the flux tubes in Fig. 2.1, the total helicity can be evaluated by performing the integral from Eqn. 2.1 over both of the flux tubes [19]. Evaluating the helicity in the volume of the blue flux tube shown in Fig. 2.1 using Eqn. 2.1

$$K = \oint \int \left(\vec{A} \cdot d\vec{l}\right) \left(\vec{B} \cdot d\vec{S}\right) \tag{2.2}$$

where $d\vec{l}$ is taken along the length of the blue flux tube and $d\vec{S}$ is the cross section of the flux tube. $\int \vec{B} \cdot d\vec{S} = \psi$, the flux in the blue tube and $\oint \vec{A} \cdot d\vec{l} = \phi$, the flux in the red tube. Thus $K = \psi\phi$ over the volume of the blue flux tube. Performing the integral over the red flux tube gives the same solution so the total helicity is

$$K = 2\psi\phi \tag{2.3}$$

which is the total helicity in the volume.

Magnetic helicity can also be thought of as current parallel to magnetic field. Currents driven along magnetic field lines generate flux that links the original field. Positive helicity has current in the direction of the magnetic field and negative helicity

has current anti-parallel to the magnetic field.

By minimizing the magnetic energy under the constraint of helicity conservation, Woltjer [20] showed that force-free magnetic fields with a constant λ represent the minimum energy state of a closed system.

$$\nabla \times \vec{B} = \lambda \vec{B} \tag{2.4}$$

where λ is a geometric constant (in units of m^{-1}) of the system. Taylor extended Woltjer's work by showing that helicity is conserved during the relaxation process to a minimum energy state [18]. The minimum energy states that satisfy Eqn. 2.4 are called Taylor states [19].

Isolated Taylor states within a closed volume are found by solving Eqn. 2.4, with $\vec{B} \cdot \hat{n} = 0$ over the surface of the volume. The Taylor state is the lowest λ solution to this equation. Thus the magnetic fields in the minimum energy state are determined by the geometry of the system.

Using Ampere's Law, $\nabla \times \vec{B} = \mu_0 \vec{j}$, with Eqn. 2.4 gives

$$\mu_0 \vec{j} = \lambda \vec{B} \tag{2.5}$$

From this it can be seen that λ is the ratio of the current density to the magnetic field. The higher λ is the more twisted a flux tube is. A geometry with a lower λ minimum energy state will have flux tubes with less writhe. Larger machines have a lower λ minimum energy state than smaller machines with the same shape.

2.2 Helicity injection

Helicity needs to be injected into a system to increase the helicity content of the toroidal configuration and to overcome the Ohmic dissipation of helicity. The helicity contained in a volume is well defined when there is no flux that links the boundary,

but is more difficult to define with flux linking the boundary. The problem arises because of the ambiguity in the choice of the gauge for the vector potential. This has been treated mathematically by Finn and Antonsen [21] with the development of relative helicity. In this section a more intuitive approach to understanding the total helicity in a volume with flux linking the boundary and helicity injection into that volume without the use of the vector potential will be outlined. This intuitive approach was developed by Jarboe [5].

Using the same arguments that led to Eqn. 2.3, the total helicity content in a closed volume can be expressed as

$$K = \oint^{\psi_t} \psi' d\psi \tag{2.6}$$

where ψ' is the amount of flux linking the incremental closed flux tube $d\psi$ and ψ_t indicates that the integral is performed on all flux tubes within the volume. Now if flux tube, $\Delta\psi$, is added to the system the helicity content will change by $\Delta K = 2\psi\Delta\psi$. From Faraday's law, the rate at which flux increases inside a flux tube is given by

$$\oint \vec{E} \cdot d\vec{l} = -\frac{\partial \phi}{\partial t} \tag{2.7}$$

where the integral is performed along the flux tube. The rate of change in helicity due to the change in the amount of linked flux is

$$-2 \oint \vec{E} \cdot d\vec{l} d\Psi \tag{2.8}$$

which gives the total change in helicity in the volume as

$$\dot{K} = -2 \int \oint \vec{E} \cdot d\vec{l} d\Psi \tag{2.9}$$

where the line integral is taken along the flux tube $d\Psi$ in the direction of the B field.

For a boundary which intersects these flux tubes the integral should be performed across the boundary and not along the external field. $\oint \vec{E} \cdot d\vec{l} = V$ along the boundary, where V is the voltage between the penetration points of the flux. $\oint \vec{E} \cdot d\vec{l}$ is path independent only if $d(\vec{B} \cdot \hat{n})/dt = 0$. When $d(\vec{B} \cdot \hat{n})/dt \neq 0$ the integral depends on how much changing flux the path links. The difficulty in having a well-defined path integral is resolved by subtracting the vacuum case from the integral

$$K = \oint^{\psi_t} \psi' d\psi - \oint \psi'_v d\psi_v \tag{2.10}$$

$$\dot{K} = -2 \int \oint \vec{E} \cdot d\vec{l} d\psi + 2 \int \oint \vec{E}_v \cdot d\vec{l}_v d\psi_v \tag{2.11}$$

where the subscript v indicates the vacuum fields. The boundary conditions are the same for the vacuum and plasma case so they cancel leaving

$$\dot{K} = -2 \int \vec{E} \cdot \vec{B} dV + 2 \int \vec{E}_v \cdot \vec{B}_v dV \tag{2.12}$$

The first term on the right hand side of the equation is due to dissipation of helicity in the plasma and the second term describes the injection of helicity into the volume.

Figs. 2.2 through 2.5 give an explanation for how helicity is injected in a plasma. The helicity injection rate is found from the second term in Eqn. 2.12, $\dot{K} = 2 \int \vec{E}_v \cdot \vec{B}_v dV$. In the figures $\vec{B}$ is parallel to $\vec{E}$. The flux through the end of the cylinder is $\Psi = AB_v$, where A is the area of the end of the cylinder, and the electric field can be expressed in terms of the applied voltage, $E_v = V/L$, where L is the length of the cylinder. Using these values in Eqn. 2.12 gives

$$\dot{K} = 2V\Psi \tag{2.13}$$

This equation is used to calculate the helicity injection rate for HIT-SI in Section 3.2.

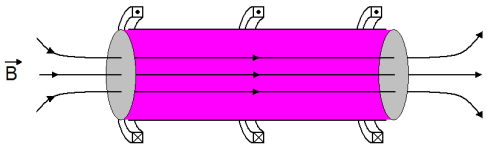

Figure 2.2: Initially there is longitudinal magnetic flux from the solenoid coil.

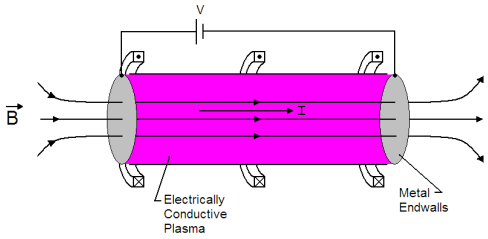

Figure 2.3: Applying a voltage across the cylinder drives a current in the plasma.

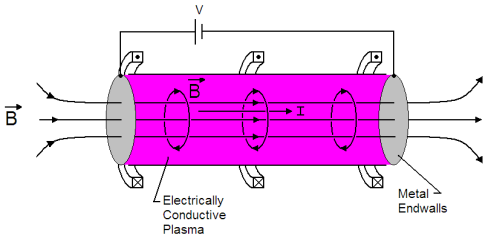

Figure 2.4: The plasma current creates azimuthal magnetic flux. The azimuthal flux links the longitudinal flux.

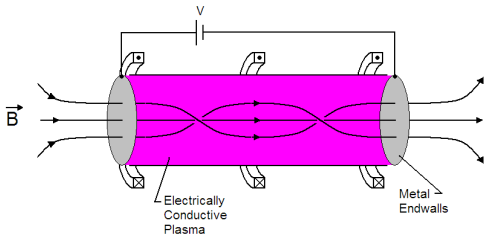

Figure 2.5: Helical field lines are formed as the plasma relaxes to its lowest energy configuration.

2.3 Coaxial helicity injection (CHI)

CHI is the most well-developed method of helicity injection current drive. It has been used for spheromak formation [5] and is an effective method for the startup of toroidal devices [22, 23, 24]. Fig. 2.6 illustrates how CHI is used to form a spheromak. Initially a solenoid coil inside the inner electrode forms magnetic fields, which link the

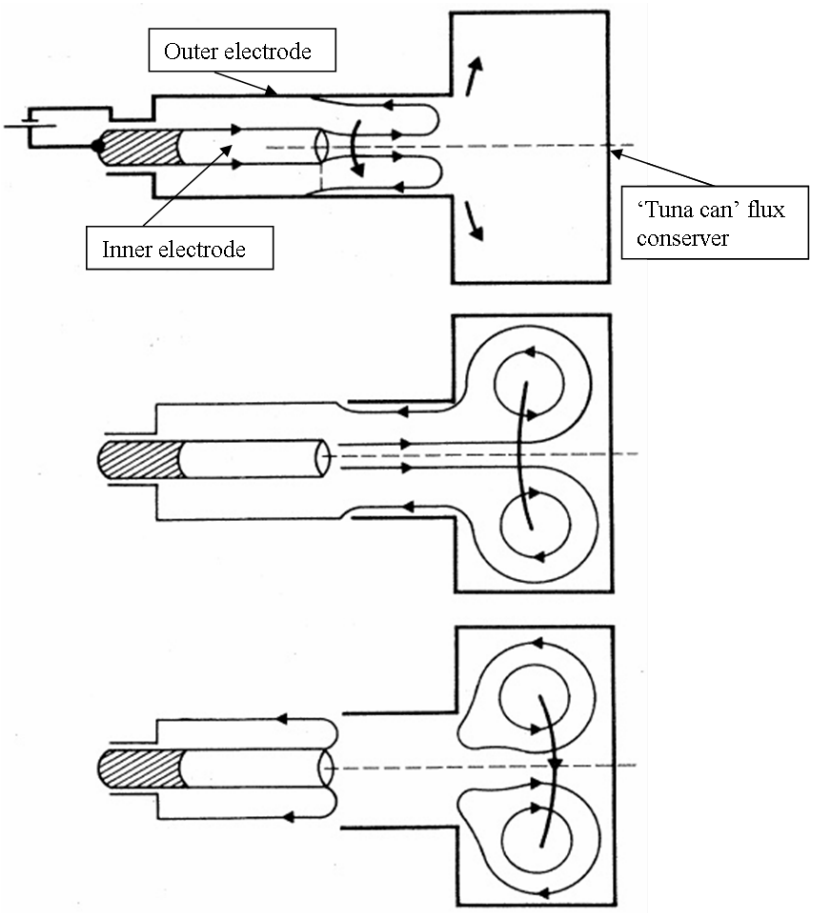

Figure 2.6: A 2-D representation of Coaxial Helicity Injection (CHI). Image adapted from Reference [25].

inner and outer electrodes. Voltage is applied between the electrodes, driving current along the magnetic field. Magnetic pressure forces the current path to expand to

the right. A toroidal plasma current is formed within the flux conserver through magnetic field reconnection and relaxation. CHI was developed on the compact torus experiment (CTX) where 600 kA of toroidal current and 100 eV electron temperatures were measured [26].

The development of CHI for spheromak formation was a precursor to the use of CHI as a start up method for tokamaks. CHI was first developed for use on tokamaks on the HIT and HIT-II experiments [23, 27]. In this scenario the central solenoid is used after a toroidal current is generated with CHI. A potential applied along vacuum magnetic flux between the outer shell and the central column generates helicity in the confinement volume. Similar to the use of CHI for forming spheromaks, the magnetic field relaxes and forms toroidal current in the confinement volume. CHI is currently used on the National Spherical Torus Experiment (NSTX) where it has produced 200 kA of additional current over inductive-only operations [24].

Chapter 3

OVERVIEW OF THE HIT-SI DEVICE

The Helicity Injected Torus with Steady Inductive Helicity Injection (HIT-SI) experiment investigates a method of current drive and spheromak formation through constant inductive helicity injection into a confinement volume of major radius 0.3 m. Magnetic helicity is injected on HIT-SI through the use of two injectors, which inductively drive current along field lines. Using Steady Inductive Helicity Injection (SIHI) [28, 29, 30] a DC plasma current is generated and formed in the confinement volume from the AC driven plasma injectors. Figure 3.1 shows a cross section of HIT-SI. The confinement volume is bordered by the teal and red parts, and the injectors

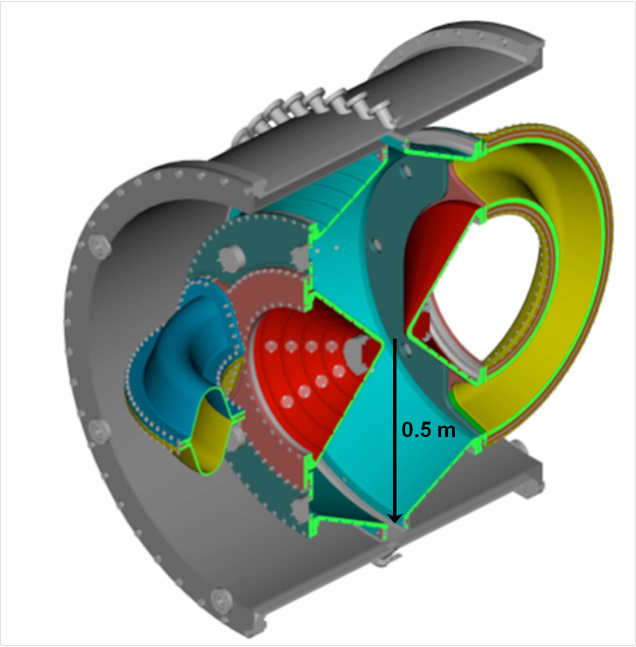

Figure 3.1: Cross section of HIT-SI. Drawing by John Rogers and Paul Sieck.

are bordered in yellow and blue.

3.1 Confinement volume

The region of the HIT-SI device where the spheromak is formed is known as the confinement volume. The confinement volume is bow-tie shaped to increase the predicted β limit of the spheromak equilibrium [15]. The confinement volume is bordered by the large cone (teal), the large plate (teal with the axial ports shown in grey), the small plate (pink), and the small cone (red) (see Fig. 3.1). Axial ports exist every 45° along the large plate (shown in gray in Fig. 3.1) for optical access to the confinement volume. A diagnostic ring provides electrical continuity between the two halves of the confinement volume while allowing access for a wide array of diagnostics.

3.2 Steady inductive helicity injection (SIHI)

SIHI was developed on HIT-SI. Using two inductively driven injectors, named the X- and Y-injectors, operated 90° out of phase steady-state helicity injection is achieved. The injectors are half toroids oriented so that their toroidal directions are perpendicular to each other. Each injector has two sets of coils: a voltage coil and a flux coil (see Fig. 3.2). The flux coil generates magnetic flux in the toroidal direction of the injector. The voltage coil creates a loop voltage around the injector and through the confinement volume to inductively drive current along the magnetic flux. The confinement volume and injectors are intimately coupled on the HIT-SI device. Electrical breaks are needed on the injectors and confinement volume to allow the flux and voltage to enter the machine. There is an electrical break around the injector mouths to prevent the copper from shorting out the injector loop voltage. A second electrical break extends around the inside of the injector, along the injector mouth, between one half of the large and small plates, and along the other injector mouth to the inside of the injector. This electrical break allows the flux into the confinement volume.

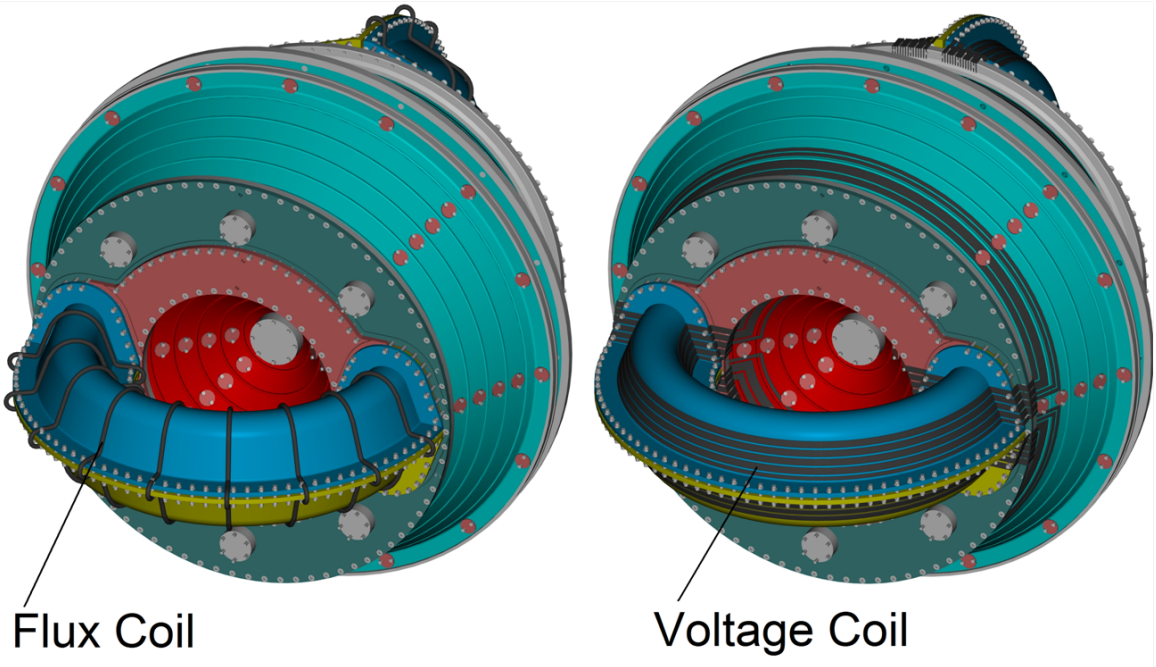

Figure 3.2: Flux and voltage coils on HIT-SI. Drawing by John Rogers and Paul Sieck.

Similar to Eqn. 2.13 the helicity injection rate on HIT-SI can be found from the flux through the injectors and the loop voltage around the injectors.

$$\dot{K} = 2V_{inj}\Psi_{inj} \tag{3.1}$$

where V_{inj} is the injector voltage and Ψ_{inj} is the injector flux. The voltage and flux coils on a given injector are driven in phase, generating a positive helicity injection rate at all times.

$$V_{inj} = V_{max}\sin(\omega t) \tag{3.2}$$

$$\Psi_{inj} = \Psi_{max}\sin(\omega t) \tag{3.3}$$

$$\dot{K} = 2V_{max}\Psi_{max}\sin^2(\omega t) \tag{3.4}$$

where $\omega = 2\pi f$ and f is the injector frequency. Injector frequencies of 5.8, 14.5 and 14.7 kHz have been used to date. Near constant helicity injection is achieved when the injectors operate 90° out of phase with equal voltage and flux.

$$\dot{K} = 2V_{max}\Psi_{max}(\cos^2(\omega t) + \sin^2(\omega t)) = 2V_{max}\Psi_{max} \tag{3.5}$$

SIHI is unique in that the injectors impose an n = 1 mode on the confinement volume to drive toroidal current. Helicity injection using CHI imposes an axisymmetric (n = 0) perturbation on the confinement volume. In both methods toroidal current is driven by the injection of helicity into the confinement volume [5, 28]. Cowling's theorem states that steady-state toroidal current cannot be driven by an axisymmetric perturbation [31]. Thus the axisymmetric perturbation from CHI cannot directly drive the toroidal current. In order to drive the toroidal current an instability in the injected current must develop that can then drive the toroidal current. SIHI does not require this intermediary step as the n = 1 injectors can directly drive the toroidal current.

3.3 HIT-SI Taylor state

The minimum energy state is the Taylor state found by solving $\nabla \times \vec{B} = \lambda \vec{B}$ with flux boundary conditions, where λ is a global constant [28]. In HIT-SI with no flux in the injectors, the Taylor state is a spheromak, with even symmetry, and the eigenvalue (λ_{sph}) is 10.3 m^{-1}. Adding toroidal flux in an injector allows any value of the injector λ to satisfy $\nabla \times \vec{B} = \lambda \vec{B}$ in the entire volume [28]. The injector solutions have odd symmetry. The superposition of Taylor states of equal λs is still a Taylor-state equilibrium. Since the injector solutions have odd symmetry solving $\nabla \times \vec{B} = \lambda \vec{B}$ with $\lambda = 10.3$ m^{-1} in the injectors does not couple to the even-symmetry spheromak [28]. Fig. 3.3 shows the magnetic field lines for a composite Taylor state with a ratio of toroidal current to injector current of 3. The blue field lines indicate flux that does

not link the injectors. At the time shown there is only current in one of the injectors. The Taylor state results on HIT-SI are from G. J. Marklin and C. J. Hansen.

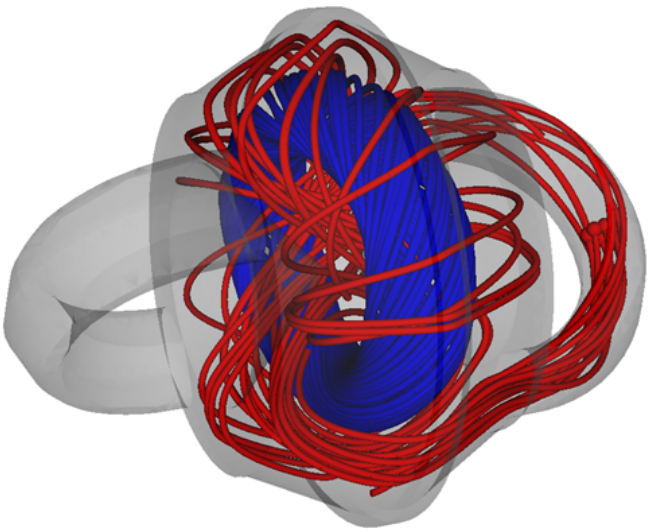

Figure 3.3: The composite Taylor state with a ratio of toroidal current to injector current of 3 in the HIT-SI device. Field lines that do not link the injector are blue and field lines that link the injector are red. Figure courtesy of C. J. Hansen.

Chapter 4
HIT-SI OPERATIONS

Operation of HIT-SI is achieved through the effective use of the injectors. The driving circuit for the voltage and flux coils (see Fig. 3.2) can be modified to operate the machine at different frequencies. Power is delivered to the circuits by charging the capacitors in the power supplies. Once the circuit is designed the injectors are operated by setting the charge voltage of the capacitors and the duty-cycle percentage (DCP) of each injector cycle. The gas inventory in the machine also affects the operation of the injector circuits. Gas injection is controlled by the plenum pressure, throttle settings, and trigger timing. In addition to injector and gas control settings RF pre-ionization enables repeatable plasma shots for the cleaning of the walls with low-power discharges. HIT-SI also has the capability of using a vertical field, but the use of the vertical field has not been shown to improve performance.

This chapter describes the injector circuits and gas injection systems, including the settings known to date to achieve the best machine performance. The focus of the discussion on operations here is with the injectors run at 14.5 kHz. A data set for all shots mentioned in this and subsequent chapters can be found in Appendix A. For details on operations at 5.8 kHz see Reference [32].

4.1 Injector settings

The HIT-SI injectors inject helicity and Ohmic power into the confinement vessel. The X- and Y-injectors are operated 90° out of phase for near constant helicity and power injection when the injectors are operated with similar power settings. Three important signals for each injector are the injector loop voltage, flux and current.

While the voltage and flux signals are largely determined by the bank charge and DCP, plasma interactions with the circuit and gas inventory in the vessel play a role in the resulting waveforms. Likewise, the injector current results from the circuit settings, gas injection and plasma interactions. Fundamentally, the injectors are operated so that they inject positive helicity and power at all times through the shot. Adjustments in the relative phase, named delta in the software settings, between each injector's voltage and flux circuits can be made to maximize the ratio of positive to negative helicity and power.

The voltage, flux, current, helicity injection, and power waveforms for both the X- and Y-injectors are shown in Fig. 4.1. For this shot the X-injector is leading, 90° ahead in phase, the Y-injector. The leading injector can be changed in the software settings [33], but typical operations for the data presented in this dissertation are with the X-injector as the lead injector. Frames 4 and 5 of Fig. 4.1 shows that the helicity and power injection is predominantly positive for this shot. After the plasma breaks down at 0.73 ms, the helicity injection traces show some negative helicity injection due to the relative phase change between the voltage and flux waveforms caused by the plasma load.

Past HIT-SI software controls [32] allowed only a single software setting for the injectors, meaning the X- and Y-injectors had to be operated at the same voltage and flux. Present injector controls allow each of the injectors voltage and flux signals to be adjusted individually. This increased flexibility led to new insights on the direction of current drive in the confinement volume and higher toroidal currents [30].

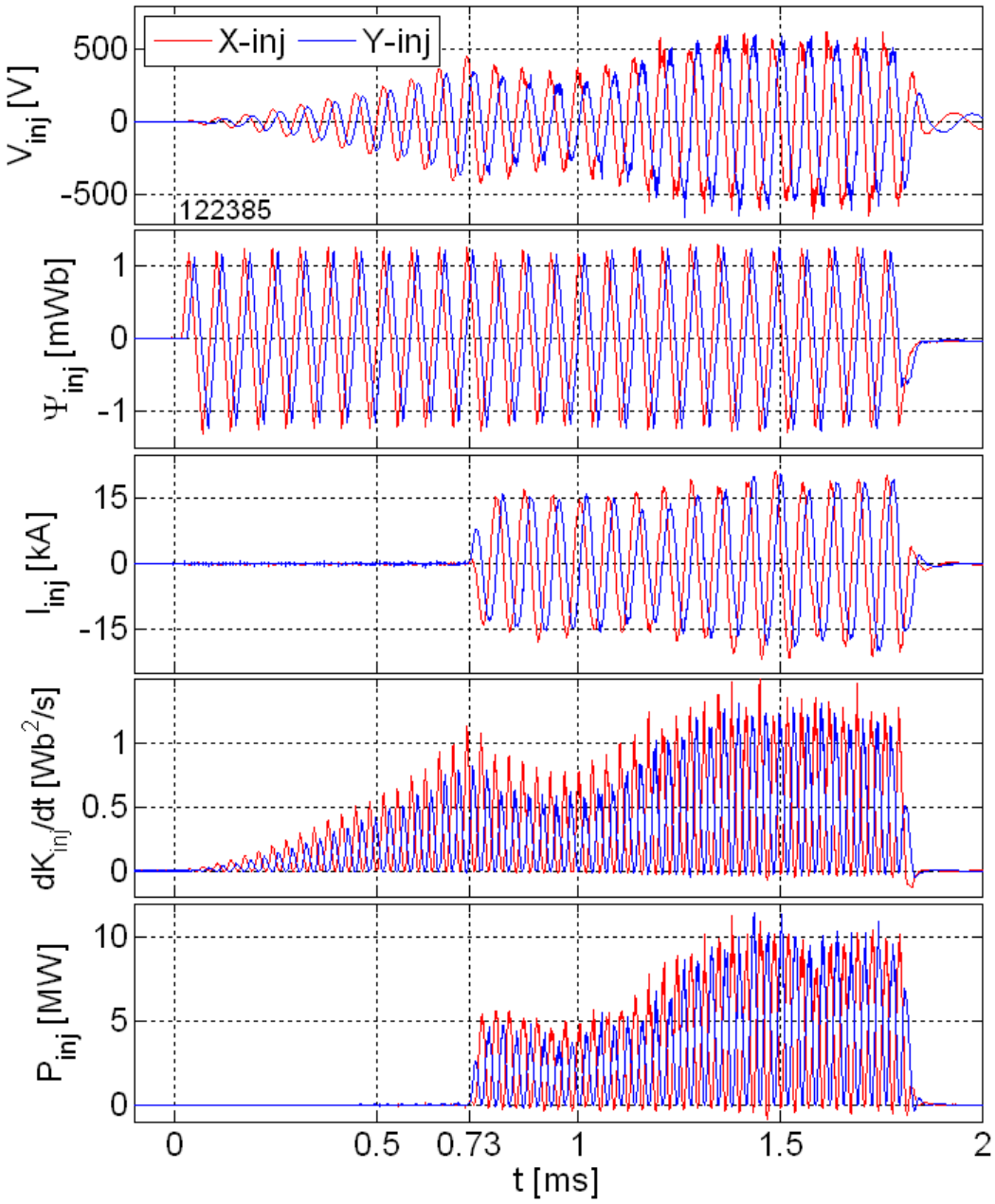

Figure 4.1: Injector voltage, flux, current, helicity injection, and power waveforms. The injector and gas injection settings for this shot are shown in Tables 4.1, 4.2 and 4.3. See Appendix C.3.1 for the location of the code used to make this figure.

4.1.1 Voltage circuit

The voltage coil is a 3 to 1 transformer, with the plasma as the secondary. A resonant LC, 'tank', circuit (Fig. 4.2) is used to oscillate current through the voltage coil. Power is supplied to the voltage circuits through 20 Switching Power Amplifiers [32] (SPAs, shown in Fig. 4.3) in parallel. Each SPA consists of four parallel pairs of Insulated Gate Bipolar Transistors (IGBTs, labeled S1-S4 in Fig. 4.3) in an H-bridge configuration. The H-bridge configuration enables the capacitors to drive an alternating circuit.

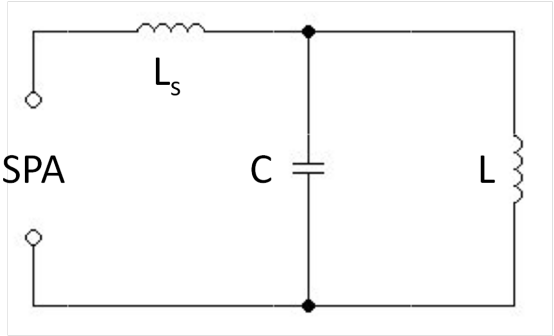

Figure 4.2: A simplified version of the voltage tank circuit. The inductor labeled as L represents the coil on the injector.

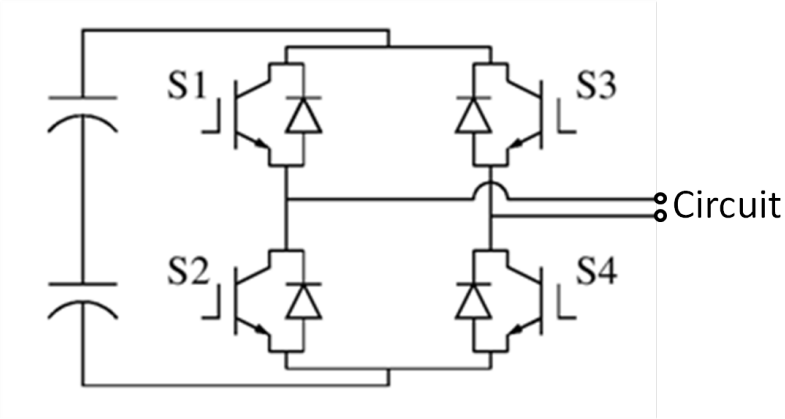

Figure 4.3: A diagram of a Switching Power Amplifier (SPA) showing the H bridge and capacitors.

HIT-SI injectors have been operated at 5.8, 14.5 and 14.7 kHz to date. The switch from 5.8 to 14.7 kHz occurred on 10/23/2009 (shot 118391). After running for a few months at 14.7 kHz the injector circuits were switched back to 5.8 kHz operations on 6/11/2010 (shot 119852). After a couple of months the injectors were switched back to higher frequency operations on 8/31/2010 (shot 120570). The voltage circuit for 5.8 kHz operations included a 650 μF capacitor bank as the parallel capacitor (C in Fig. 4.2) with a series inductor tuned to produce a resonant frequency in the circuit at 5.8 kHz. Software controls drove the circuit at 5.8 kHz. For 14.5 kHz operations, two 95 μF capacitors are used in parallel for the parallel capacitance (C in Fig. 4.2) with a 0.634 μH series inductor (L_s in Fig. 4.2) for a circuit resonant frequency of 15.8 kHz [34]. The driving frequency was adjusted to drive the circuits off resonance. The tank circuit is driven below the circuit resonance to limit the phase change in the flux and voltage waveforms caused by the plasma load and to maximize the ratio of coil to source current. For 14.5 kHz operations each injector circuit is controlled with a Blackfin processor [35].

Current is measured at the output of each of the SPAs with Hall-effect current transducers (known as LEMs) and digitized with our data acquisition system. A fault is tripped, ending the shot, if the current from any of the LEMs exceeds 1500 A. The collector-emitter voltage (V_{CE}) is measured at each IGBT and a fault is tripped if the voltage exceeds a threshold value. The fault system is in place to protect the IGBTs and the circuit.

4.1.2 Voltage circuit operations

There are three categories of shots typically taken on HIT-SI: low power helium shots with RF pre-ionization, higher power helium shots, and high power deuterium shots. Typical operating parameters for these three types of shots are shown in Table 4.1. The low power helium shots are the typical shots used for pulsed-discharge cleaning (PDC) and are the only class of shots that use RF pre-ionization. PDC shots are

run through a software program that can take shots in rapid succession with minimal diagnostics. PDC shots typically inject 2-3 MW of power and achieve less than 10 kA of peak toroidal current. Higher power helium shots are used to condition the walls with a higher toroidal current and to test injector settings for deuterium operations. Typical higher power helium shots inject around 5 MW of power and have 20 - 30 kA of peak toroidal current.

Table 4.1: Voltage circuit parameters for a typical low power helium shot (122368), higher power helium shot (122369) and high power deuterium shot (122385) with a tank circuit

Shot	Shot length	Freq (kHz)	X charge voltage	Y charge voltage	DCP vacuum	DCP plasma
122368	4 ms	14.5	360V (36%)	350V (33%)	X/Y 45/53%	100%
122369	2 ms	14.5	410V (42%)	380V (37%)	30%	100%
122385	1.8 ms	14.5	550V (56%)	500V (48%)	15%	100%

Peak operating conditions are achieved during deuterium operations. Settings must be chosen that achieve plasma breakdown and high injected power without exceeding the circuit limits or causing damage to the insulating walls of the plasma facing surface. There are two regimes that need to be considered when operating the voltage circuit for higher performing shots: the vacuum period of the shot before plasma breakdown and the period of the shot with plasma. Figure 4.4 shows the voltage traces for the X- and Y-injectors where breakdown occurred at 0.73 ms. During the vacuum period the injector voltage needs to ramp up to a level where the voltage is significant enough for breakdown (the transition from the gas to plasma state) to occur. Typical plasma breakdown occurs when the injector voltage gets above 400 V, which sets the minimum vacuum DCP needed with respect to the bank

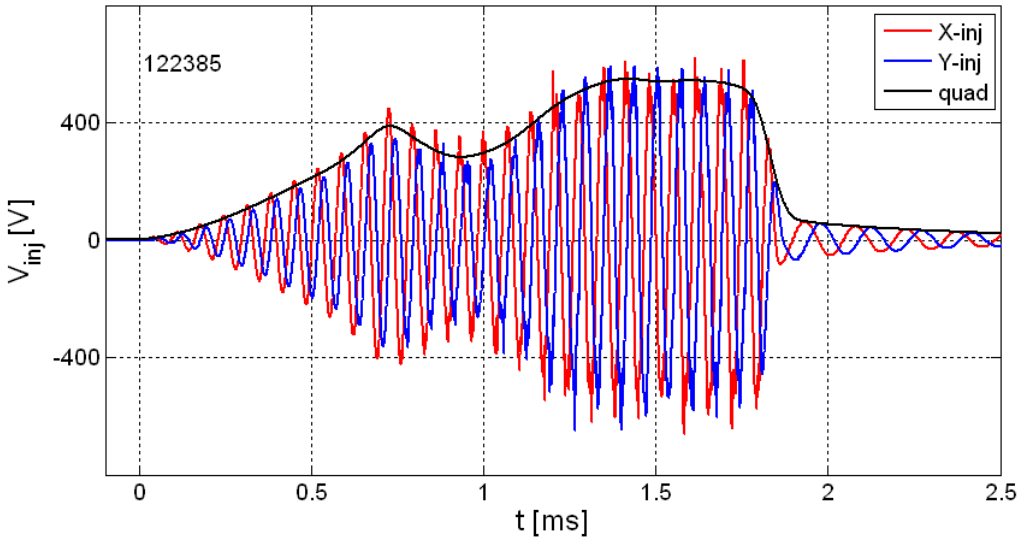

Figure 4.4: X- and Y-injector voltages with the quadrature value (the square root of the sum of the squares of the two signals averaged over an injector cycle). See Appendix C.3.1 for the location of the code used to make this figure.

charge settings. Care needs to be taken when ramping up the voltage as a DC offset in the injector voltage occurs if the voltage coils are ramped up to too high of a DCP too quickly [35]. For the circuit described for 14.5 kHz operations LEM faults occur (more than 1500 A from a single SPA) if the injector voltage increases much above 600 V. This sets the maximum DCP for a given bank charge setting. The operating frequency and circuit design can be adjusted so that LEM and V_{CE} faults occur at roughly the same injector voltage, but this has not been explored extensively to date.

After plasma breakdown the plasma introduces a load into the circuit. Left at the same DCP settings this load rapidly decreases the injected voltage. To increase the injected power the DCP needs to be increased after plasma breakdown. Software settings allow operators to control how fast the DCP changes after breakdown. Typically the DCP is ramped up so that it reaches 100% sometime before the end of the shot. As power is dissipated in the circuit voltage droop occurs. That is the

voltage across each supply slowly decreases over the course of the shot. For the short deuterium shots to date, with shot lengths of ∼2 ms, that is not a large problem, but it will need to be considered for longer length shots.

Another consideration when operating the voltage circuit is the amount of gas input into the system. Without enough gas there are not enough particles to carry the current (drift parameter limit) and large voltage spikes are seen in the injectors. These voltage spikes can lead to damage of the plasma facing walls near the injector mouths and to circuit faults. With too much gas the plasma is less dynamic. Gas injection will be discussed in more detail in Section 4.2, but it is important to consider the correlation between different machine settings.

4.1.3 Flux circuit

The flux coils are solenoidal coils that wrap around the injector half toroids [32]. Each flux coil consists of four overlapping 8-turn coils in parallel with 7-turn coils at each injector mouth. Power is supplied to each flux circuit with eight SPAs. Initial deuterium operations, including most of the shots for the data in this thesis, were with the direct drive of the flux circuit. Direct drive means that the switching power amplifiers (SPA) are connected directly to the flux coil, Fig. 4.5. The inductance of the flux coil is 1.85 μH [34].

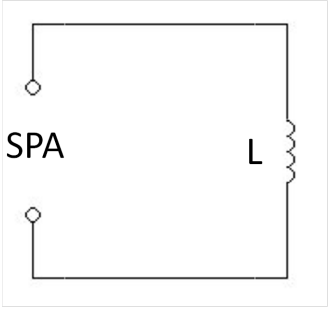

Figure 4.5: Initial operations with the flux circuit were with the SPAs driving the flux coil directly.

Fig. 4.6 shows the X- and Y-injector flux waveforms. Notice the triangular shape of the waveforms. This is roughly the maximum injectable flux when directly driving the flux coil. The peak flux reaches ∼1.2 mWb and the quadrature flux is ∼1 mWb. Plasma breakdown occurs at 0.73 ms and there is a slight change in the waveforms at this time, but not as large of a change as seen in the voltage waveforms.

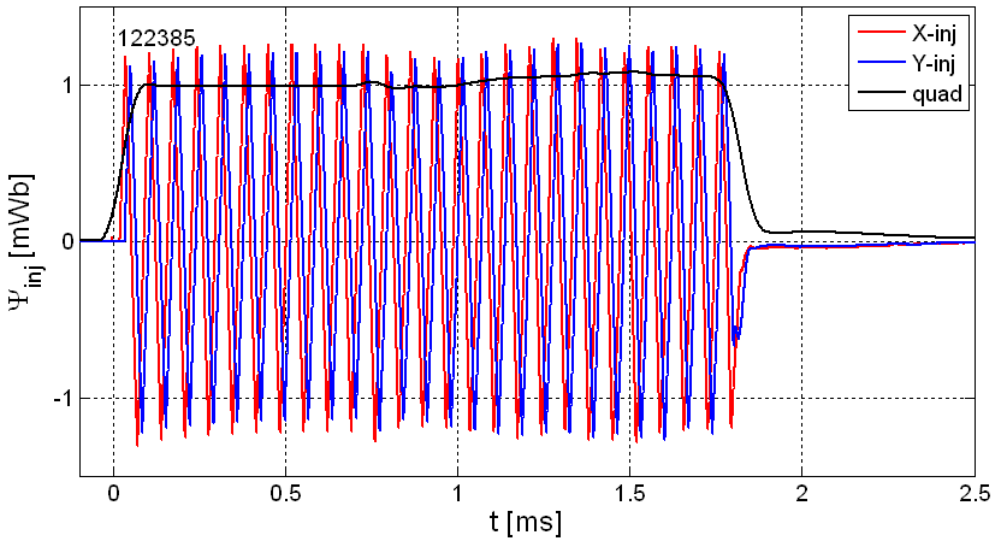

Figure 4.6: X- and Y-injector fluxes with the quadrature value. See Appendix C.3.1 for the location of the code used to make this figure.

Attempts to operate the flux circuit at 14.5 kHz using a tank circuit were unsuccessful initially due to a phase change in the flux waveform that occurs after plasma breakdown. Adding a phase adjustment to the software controls allowed operation of the flux circuit with a tank circuit. The flux circuits were changed to a tank circuit on Dec. 12, 2011, shot 124141. The present flux circuit is similar to the tank circuit shown in Fig. 4.2 with a series inductance of $L_s = 2.47$ μH and a series capacitance of $C = 95$ μF. The switch to the tank circuit has allowed the maximum flux in the injectors to increase from ∼1.2 mWb to ∼2 mWb at 14.5 kHz. In addition the flux circuit can now be run with a sinusoidal waveform as opposed to a triangular wave-

form with the direct-drive circuit. Additional work needs to be done to find the most appropriate settings for the flux circuit with the tank circuit.

Table 4.2 lists the flux coil settings for the three types of shots typically taken on HIT-SI: low power helium shots, higher power helium shots and high power deuterium shots. This table is for shots taken with direct drive of the flux circuit at 14.5 kHz.

Table 4.2: Flux circuit parameters for a typical low power helium shot (122368), higher power helium shot (122369) and high power deuterium shot (122385) with direct drive

Shot	Shot length	Freq (kHz)	X charge voltage	Y charge voltage	DCP vacuum	DCP plasma
122368	4 ms	14.5	700V (62%)	640V (54%)	100%	100%
122369	2 ms	14.5	790V (70%)	680V (57%)	100%	100%
122385	1.8 ms	14.5	830V (75%)	760V (65%)	100%	100%

4.2 Gas settings

Correct gas inventory in the confinement volume is imperative in achieving plasma discharges with high toroidal current. A minimum amount of gas is necessary to maintain the injector current while an excess of gas is detrimental to the plasma performance in the confinement volume. There are two methods of gas injection on HIT-SI. The gas injection points are shown in Fig. 4.7. Fill gas is used to maintain a constant gas pressure in the confinement volume for use with RF pre-ionization. Puff gas is gas injected into the injectors during the shot and is used to supply the gas needed to operate the injectors. Discharges at high density with fill gas and RF pre-ionization do not achieve significant current amplification. Helium discharges without fill gas and RF pre-ionization achieve improved performance without other changes

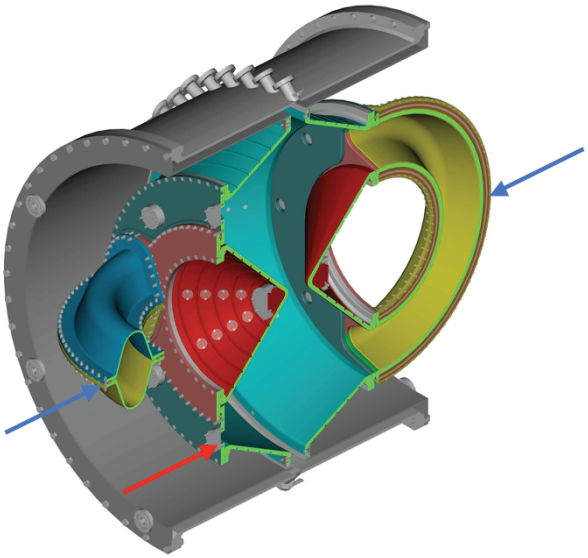

Figure 4.7: Gas injection points. Drawing by John Rogers and Paul Sieck

Red = Fill, Blue = Puff

in parameters. Initial 14.7 kHz operations achieved a toroidal current amplification of 1.7 at lower gas fueling rates (shot 118834). Further improvements in density control are achieved on HIT-SI by using helium operations to condition the machine for deuterium operations.

There are four adjustments that can be made to each of the puff gas systems: the puff pressure, the feed gas throttle, the control gas throttle and the puff trigger timing. In addition there is also a static fill gas injection system, which is now used strictly for conditioning shots.

4.2.1 Operating Gas

HIT-SI is typically operated with either helium or deuterium gas. Helium gas is used to clean the confinement volume walls for deuterium operations. The most common way to condition the walls is through a series of low power discharges, called Pulsed

Discharge Cleaning (PDC). PDC shots typically use fill gas and the RF antenna for pre-ionization. The necessary fill gas pressure required to maintain the glow creates too high of a gas inventory in the confinement volume for optimal plasma performance. Thus the fill gas system is only used for PDC level shots. Helium can also be used effectively to condition the walls with higher power shots without fill gas or the RF antenna.

Deuterium has been used for all of our higher performance shots. Helium conditioning of the alumina walls makes the walls act to pump the deuterium. The number of deuterium shots that can be taken after helium conditioning is dependent on the wall conditions and the amount of deuterium gas puffed into the machine. Typically the first two deuterium shots after helium conditioning perform well before the walls no longer act to pump the deuterium.

Pressure transducer measurements show that the gas flow rates are similar with both helium and deuterium as the operating gas (see Fig. 4.8). Diatomic deuterium

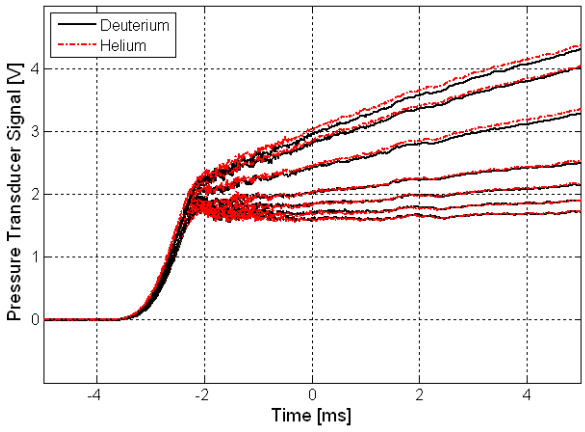

Figure 4.8: Helium and deuterium flow rates at seven different throttle settings. The flow rates for helium and deuterium are similar for each throttle setting (X-side shown). See Appendix C.6.1 for the location of the code used to make this figure.

gas injects the same number of electrons and protons per molecule as monotonic

helium gas.

Hydrogen and argon have also been used on HIT-SI. Hydrogen operations have been attempted on a number of occasions without achieving high toroidal currents in the confinement volume. More recently hydrogen has also been used to condition the machine to remove carbon. Evidence is inconclusive whether conditioning with hydrogen on HIT-SI is successful at removing carbon. Argon was used on HIT-SI during June of 2009 with 5.8 kHz operations. Argon shots did not show any significant toroidal current formation.

4.2.2 Puff gas

Puff gas is injected into the midpoint of each injector (see Fig. 4.7) and fuels the injectors for the duration of the shot. Without puff gas the injectors would have large spikes in the voltage and low injector current during the shot. The typical gas injection settings described in this section are obtained empirically. Some of the considerations when determining the optimal gas injection settings are the prevention of large voltage spikes on the injector voltage waveform, achieving plasma breakdown without RF pre-ionization and achieving large toroidal current amplification which tends to occur at lower plasma densities.

The puff gas injection system is shown in Fig. 4.9. The feed gas throttle is opened when we begin running so the plenum is maintained at the main gas supply pressure, typically 4000 to 5000 Torr. Shortly before the beginning of the shot, the solenoid valve is opened allowing He gas at 100 psi to begin flowing. This gas, flowing through the area shown in blue in Fig. 4.9, opens and closes the valves and is not injected into the machine. The increase in pressure opens the N/C valve and then, a short time later, closes the N/O valve. The feed gas throttle setting determines how quickly the main gas supply can flow into the plenum. Opening the throttle increases the flow rate during the shot. The interval between the opening of the N/C valve and the closing of the N/O valve is set by the control gas throttle. After the completion of

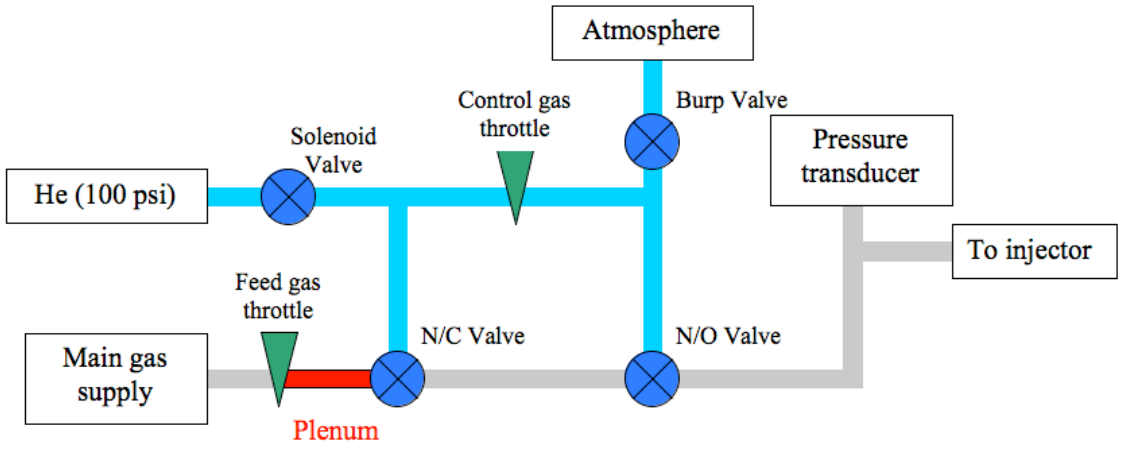

Figure 4.9: Puff gas injection system

the shot, the burp valve is opened, returning the N/C valve to the closed position and the N/O valve to the opened position.

Puff pressure

Typical operations use puff pressures between 4000 and 5000 Torr. Figures 4.10 and 4.11 show the effects of increasing the puff pressure from 4000 to 5000 Torr. The calculation of the gas flow rate from the pressure transducer voltage signal is made by assuming that the flow rate is proportional to the voltage. Then integrating the signal with the feed gas throttle closed and the N/O valve left open gives a number proportional to the total number of particles in the plenum.

$$\int P dt \propto N_{plenum} \tag{4.1}$$

$$P = K\frac{dN}{dt} \tag{4.2}$$

where N_{plenum} is the total number of particles in the plenum, and K is the constant of proportionality to convert between the pressure transducer signal and the particle flow rate. Thus the flow rate is $f = KV$ where V is the pressure transducer voltage. For the X-side puff measurement $K = 2.1 \times 10^{21}$ $\mathrm{V^{-1}s^{-1}}$. For the Y-side puff measurement $K = 2.5 \times 10^{21}$ $\mathrm{V^{-1}s^{-1}}$ [36]. Typical puff pressure settings are shown in Table 4.3.

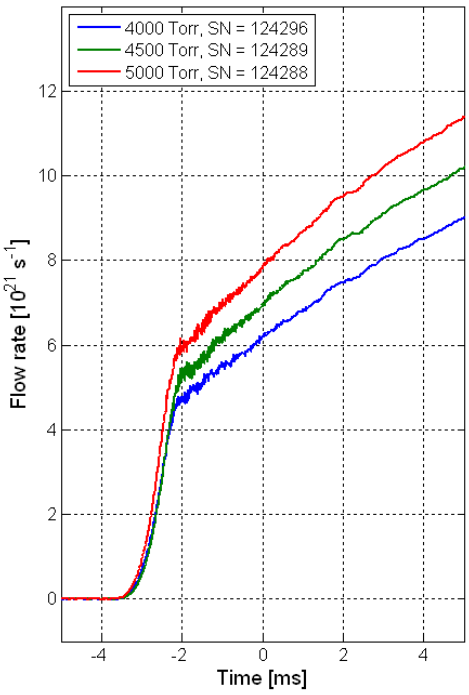

Figure 4.10: Gas flow into the X-injector with a throttle setting of 28 and variable pressure with deuterium gas.

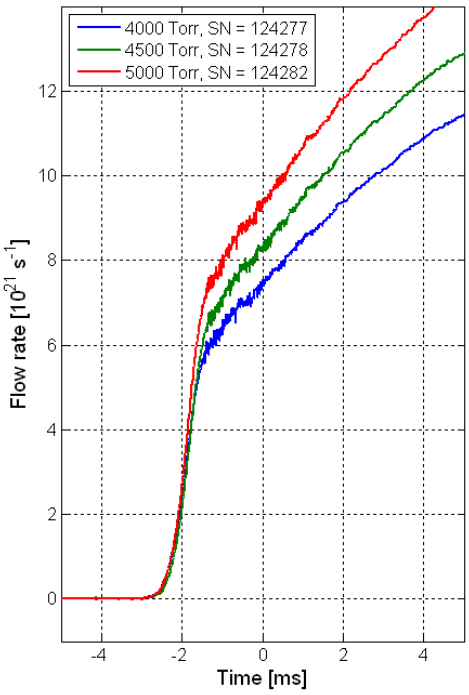

Figure 4.11: Gas flow into the Y-injector with a throttle setting of 33 and variable pressure with deuterium gas.

See Appendix C.6.2 for the location of the code used to make these figures.

Feed gas throttle

The feed gas throttle controls the rate of gas flow from the main gas supply to the plenum (see Fig. 4.9). Higher throttle settings are used on deuterium shots so that

the gas injection rate increases through the shot. Typical feed gas throttle settings are shown in Table 4.3.

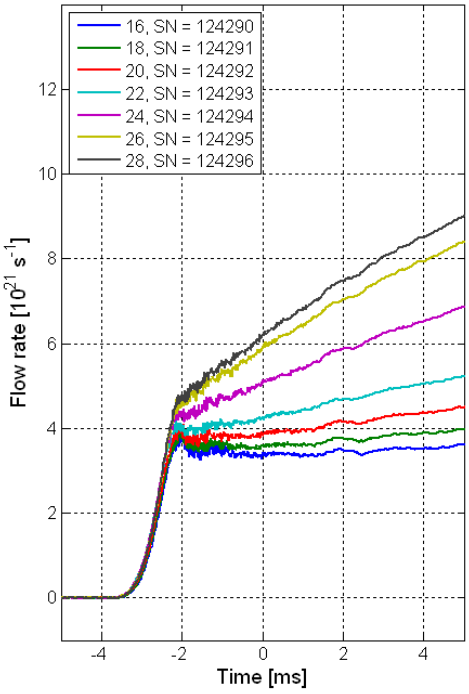

Figure 4.12: Gas flow into the X-injector with 4000 Torr pressure and variable throttle settings with deuterium gas.

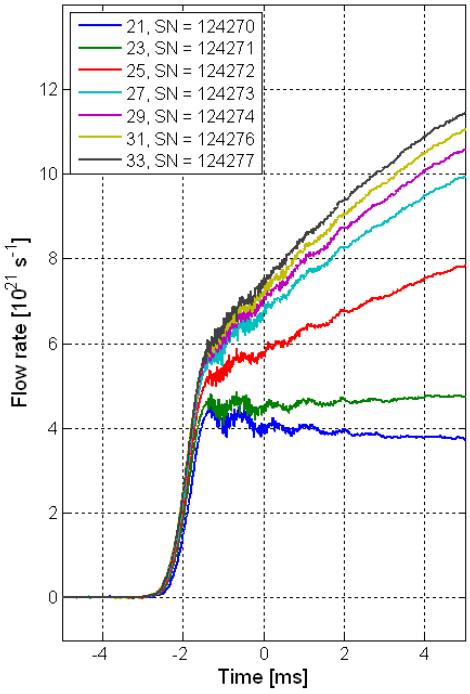

Figure 4.13: Gas flow into the Y-injector with 4000 Torr pressure and variable throttle settings with deuterium gas.

See Appendix C.6.3 for the location of the code used to make these figures.

Control gas throttle

The control gas throttle is used to close the N/O open valve (see Fig. 4.9) after the shot is over. Changes in the throttle setting effect the time when the flow of gas is cut off to the injectors. Throttle settings of 100 on the X-side and 75 on the Y-side close the N/O valve ∼25 ms after gas begins to flow into the injector. With the throttles fully open the N/O valve closes ∼7 ms after gas begins to flow into the injector.

Puff trigger timing

The opening of the N/C valve can be adjusted by a software setting. This setting is extremely important for achieving breakdown of the plasma. Puffing too early or too late in time will keep the plasma from breaking down. Typical puff trigger timings are shown in Table 4.3.

The puff timing triggers indicate (see Figs. 4.12 and 4.13) that the Y-injector gas is injected before the X-injector. It is unknown if this is actually the case though. The measurement of the flow rate is made before the gas enters the injector and there is not a free path for the gas to flow from the needle tip into the injector volume. The needle that is inserted into the injector does not extend past the location where the two injector halves come together. The alumina insulator that coats the copper extends into this gap between the injector halves and constrains the flow of gas by an unknown amount. Thus it is unknown at what time the gas actually enters the injector volume. It is possible that gas flows along the outer rim of the injector and diffuses into the injector through the gap between the two plates along the entire toroidal length of the injector.

Typical operating parameters

The following table lists the gas settings for the three types of shots typically taken on HIT-SI: low power helium shots, higher power helium shots and high power deuterium shots. This table is for shots taken at 14.5 kHz.

Table 4.3: Gas injection for typical operations

Shot	Shot length	Gas	RF	Puff timing	Puff pressure	Throttles
122368	4 ms	He	Yes	-9 ms	4000 Torr	X/Y 16/21
122369	2 ms	He	No	-9 ms	4000 Torr	X/Y 21/25
122385	1.8 ms	D	No	-8 ms	4500 Torr	X/Y 28/33

4.3 Voltage coil redesign

The paths of the voltage coils near the injector mouths have been redesigned to reduce the magnetizing inductance near the mouth. Figure 4.14 shows how the voltage coils crossed the gap between the injector and the confinement volume before the modification (red wires) and Fig. 4.15 shows the redesigned voltage coils (blue and yellow wires). The essential change is that the voltage coils no longer cross the gap between the injector and the confinement volume along the side of the injector, but rather they now cross the gap near the top and bottom of the injector mouth.

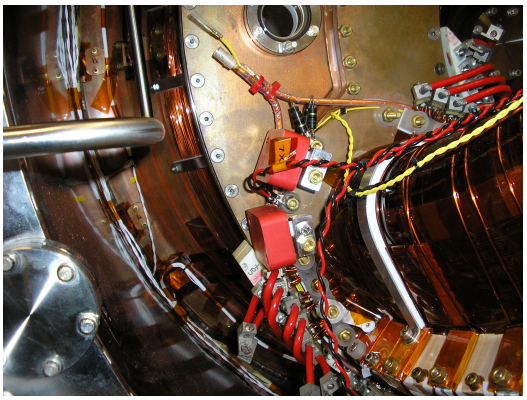

Figure 4.14: The original design for the voltage coil circuit near the injector mouth.

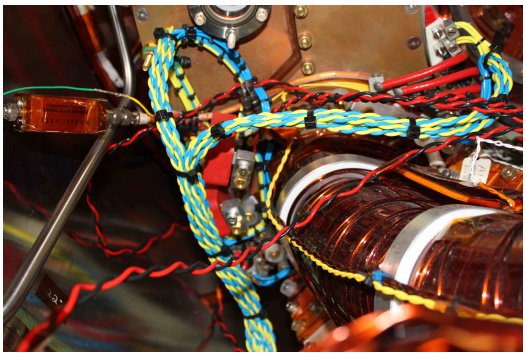

Figure 4.15: The redesigned shape of the voltage coil circuit.

The magnetic field (magnetizing inductance) from the voltage coil is measured with a magnetic probe similar in design to the 3D coils made for the internal magnetic probe. This measurement is done when the machine is open and there is access to the inside of the machine. The probe is placed at various locations (see Figs. 4.16 and 4.17) around the inside of the Y-injector mouths. The bases of the arrows indicate the location of the measurement. Each measurement is from a different vacuum shot with the same amount of current in the voltage coil. The magnetic field is also measured at the midpoint of the injector for a reference measurement. Figure 4.16 shows that

the magnetic field at the inside of the injector mouth is of similar magnitude to the magnetic field measured at the midpoint of the injector. After redesigning the voltage coils (Fig. 4.17) the magnetic field measured in the injector mouth is significantly less than the magnetic field at the midpoint of the injector. The goal is that by reducing the magnetizing inductance near the injector mouth that there would be less field errors near the injector mouth, which would limit wall interactions between the plasma and the injector mouth. After the modification there are still interactions between the plasma and the injector mouths so it is unknown whether this modification improved the performance of the injectors.

The magnetic field measured at the inside of the Y-injector mouths and at the center of the injector handle with current in the voltage coils.

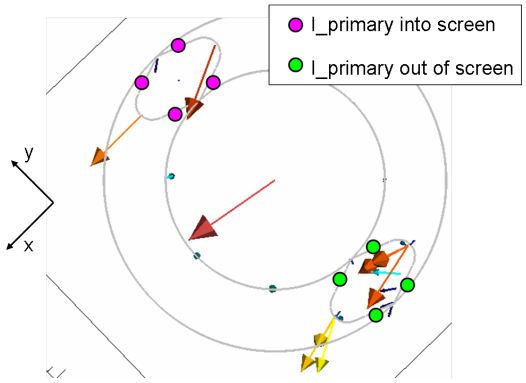

Figure 4.16: The voltage coils are in their original configuration. The magnitude of the field at the injector mouths is comparable to the field at the center of the injector.

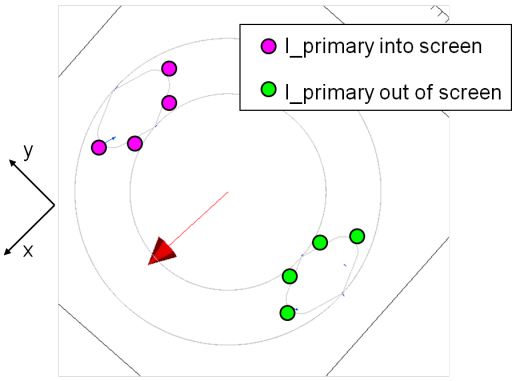

Figure 4.17: The voltage coils are in their new configuration. The pink and green dots show the new locations where the voltage coils cross the gap between the injector and the large plate at the injector mouth. The magnitude of the field at the injector mouths is now much smaller than the field at the center of the injector.

Chapter 5
DIAGNOSTICS

Multiple diagnostics are used to measure plasma parameters in the HIT-SI confinement volume. Magnetic signals are measured with probes and flux loops on the surface and internal to the plasma. Surface magnetic measurements are used to find the toroidal plasma current and mode structure of the plasma. Internal magnetic measurements give knowledge about the internal structure of the plasma and can be used to compare to computational results. Plasma light emission is measured using spectrometers, bandpass filters, and CCD cameras. Information on plasma temperature, velocity, impurity content, and structure can be found from the light emission measurements. In addition an interferometer is used to measure the electron density of the plasma, and a Langmuir probe is used to measure electron density and temperature.

The main focus of this chapter is on the far-infrared (FIR) interferometer and the internal magnetic probe. In addition, work to measure impurity line radiation with the vacuum ultraviolet (VUV) spectrometers and band pass filters will be discussed. Recent work with plasma imaging and spectroscopy has been done using a high-speed camera. This chapter outlines the set up of and shows typical data from these diagnostics.

5.1 Far-infrared (FIR) interferometer

Interferometry measures the index of refraction of a plasma, which is proportional to the electron density. This technique provides a non-perturbative, phase-based method of measuring the chord-averaged electron density. Due to the phase-based nature of

interferometry, the measurement can be made without calibration. One disadvantage of interferometry, however, is that it does not provide a local measurement. A more detailed description of the interferometer can be found in References [14] and [36]. A brief summary is given here.

Figure 5.1 shows the layout of the FIR interferometer.

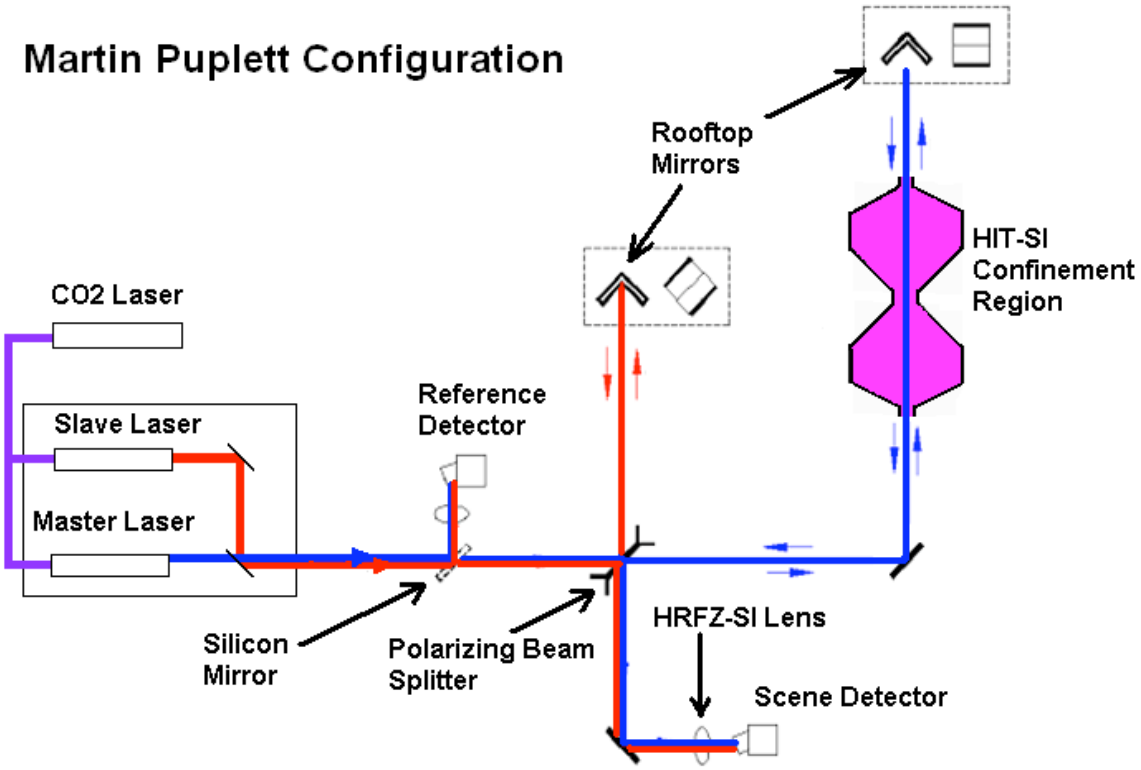

Figure 5.1: Design of the FIR interferometer.

The CO_2 laser operates at the 9R32 line to optically pump two difluoromethane FIR interferometers which lase at 184.3 μm. Due to the high frequency oscillations of the plasma density, a beat frequency between the lasers of 3 to 4 MHz is used. A Martin-Puplett configuration [37] is used to measure the phase change in the beat between the slave and master lasers from the changing index of refraction of the plasma. The plasma line-integrated density is derived using Ref. [38] for a double-

pass system.

$$\int n_e dl = -\frac{\Delta\phi 2\pi\epsilon_0 m_e c^2}{\lambda e^2} \tag{5.1}$$

where n_e is the electron density, ϵ_0 is the permittivity of free space, m_e is the electron mass, c is the speed of light, λ is the laser wavelength (184.3 μm), and e is the electronic charge. $\Delta\phi$, the phase change, is the only variable on the right-hand side of the equation which is not a constant.

5.1.1 Beam Path through the Spheromak Confinement Region

With the present diagnostic ring and mirror placement there are two possible beam paths for the laser through the confinement volume. One beam path has an impact parameter of 35.1 cm and the other has an impact parameter of 43.3 cm (see Fig. 5.2). An additional detector is needed to measure both chords simultaneously so a multiple-chord system cannot be implemented presently.

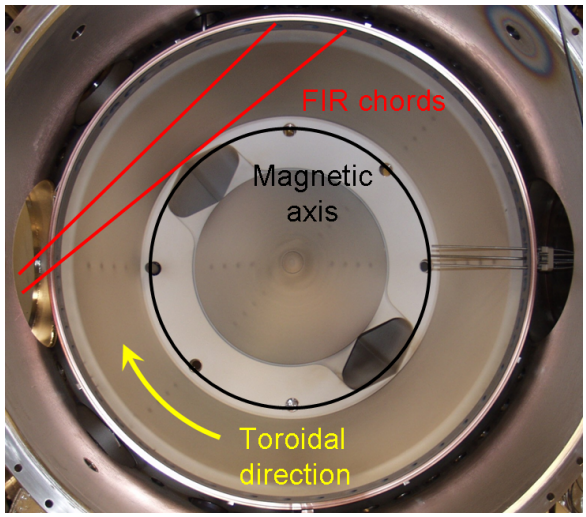

Figure 5.2: The toroidal cross-section of HIT-SI with the two possible chords of the FIR interferometer shown in red. Chord 7 has an impact parameter of 35.1 cm and chord 9 has an impact parameter of 43.3 cm.

5.1.2 Typical density trace

The line-averaged electron density of a typical deuterium shot is shown in Fig. 5.3. During the injector drive portion of the shot there are density fluctuations at the injector frequency of 14.5 kHz. After the injectors are shut off (2.0 ms) the line-averaged density increases up to ~3 x 10^{19} m^{-3} before it begins to decrease.

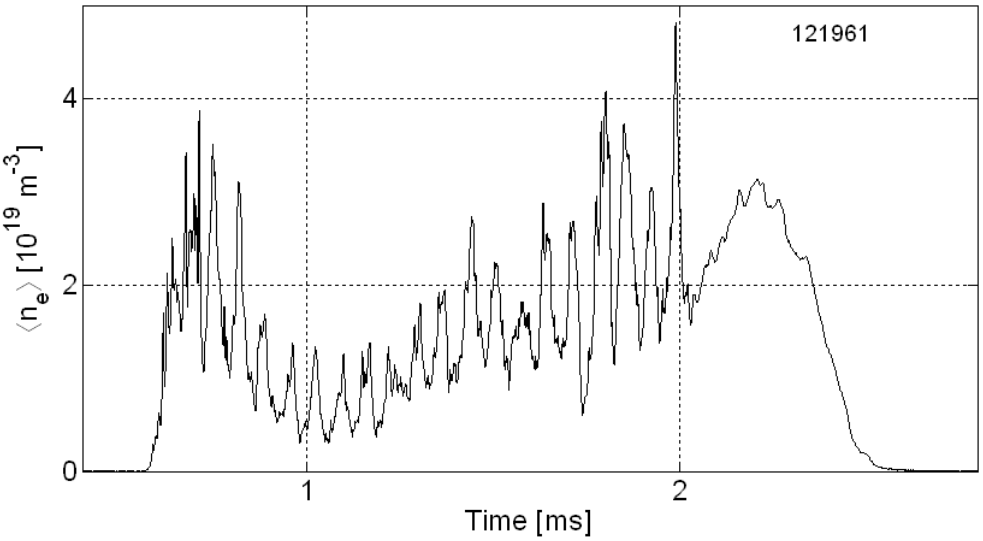

Figure 5.3: The line-averaged density along chord 7 for a 40 kA deuterium shot. See Appendix C.2.1 for the location of the code used to make this figure.

5.1.3 Chord comparison

Comparison of the density measurement along the two FIR chords is as accurate as the shot to shot repeatability of the plasma. Figure 5.4 compares the density along the two chords for two shots reaching about 40 kA of toroidal current. Figure 5.5 shows a similar comparison for two shots reaching about 35 kA of toroidal current.

The magnitude of the density is similar along both chords. In addition the phase of injector oscillations is similar along both chords. The differences between the

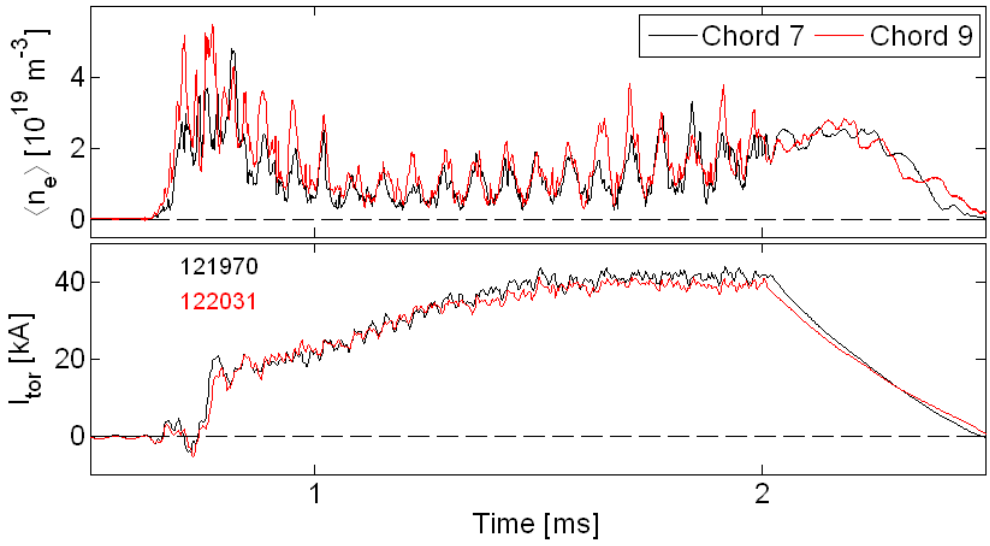

Figure 5.4: Comparison of line-averaged density for two similar shots along different chords. See Appendix C.2.1 for the location of the code used to make this figure.

chords can be attributed to differences in shot-to-shot repeatability. To distinguish differences between the two chords the measurements need to be made simultaneously.

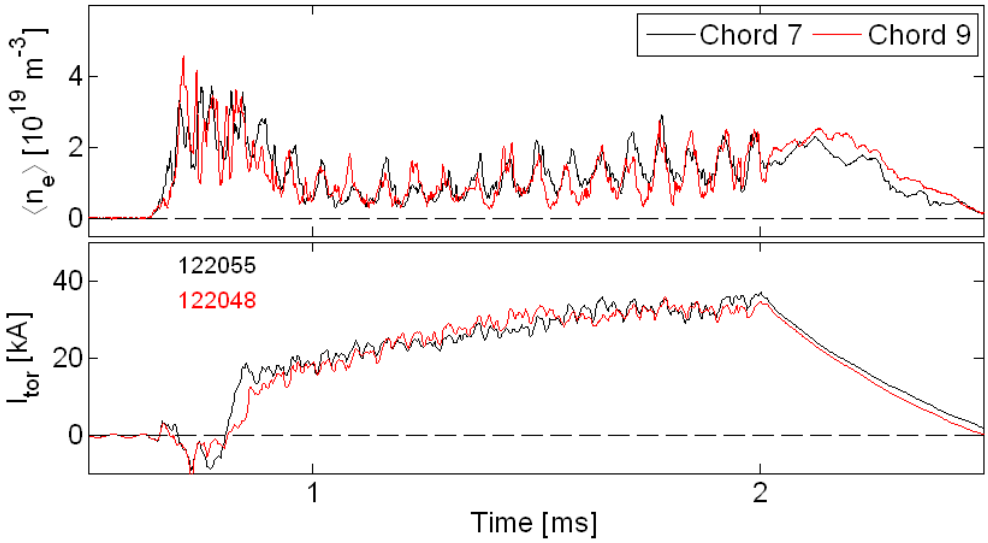

Figure 5.5: Comparison of line-averaged density for two similar shots along different chords. See Appendix C.2.1 for the location of the code used to make this figure.

5.2 Internal magnetic probe

Internal magnetic measurements are used to understand the magnetic field profile in the confinement volume. The internal magnetic probe used in HIT-SI was designed and built by R. J. Smith. The probe consists of three arrays of magnetic pickup coils that can be inserted through the diagnostic gap at a single toroidal location (see Fig. 5.6) to measure the magnetic field to a major radius of 33.1 cm (approximately the location of the magnetic axis). One advantage of the internal probe is that it provides local measurements of the magnetic field. A disadvantage of the probe is that it is a perturbative diagnostic; however, there is little evidence that the probe has had any deleterious effects on HIT-SI plasmas. Another difficulty is that each probe signal must be individually calibrated.

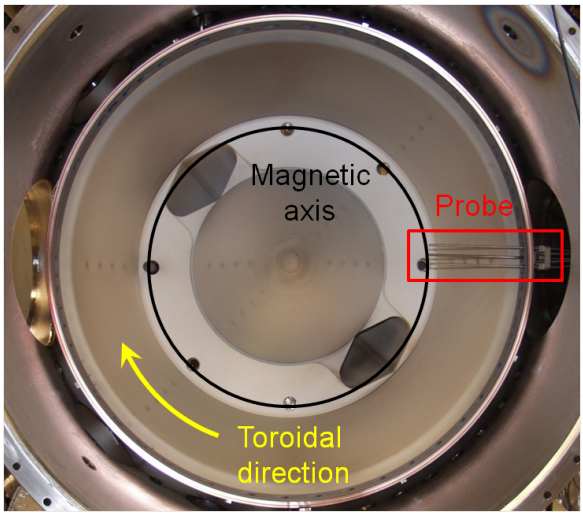

Figure 5.6: The location of the internal magnetic probe is boxed in red on a toroidal cross section of the HIT-SI confinement volume.

5.2.1 Theory

The theory behind a magnetic probe is relatively simple. A changing magnetic flux through a coil induces a voltage across the coil. In Fig. 5.7 the changing flux, repre-

sented by the blue arrows, produces a voltage across the coil.

$$V = NA\dot{B} \tag{5.2}$$

where NA is the effective area of the coils (the cross-sectional area multiplied by the number of turns) and $\dot{B}$ is the average value of the changing magnetic field. The measured voltage is integrated and divided by the effective area to give the local magnetic field. The actual coils are shown in Fig. 5.8.

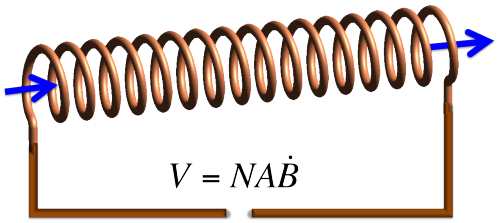

Figure 5.7: Simplified illustration of how a pickup coil works. Figure adapted from Wikipedia media commons. [10]

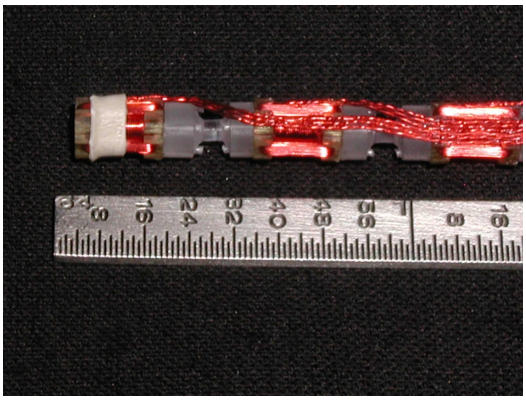

Figure 5.8: A close up picture of individual pickup coils. The radial coil is wrapped around the axis of the spool. The magnetic field transverse to the length of the stem is measured by the toroidal and poloidal coils. Diagnostic designed by R. J. Smith.

5.2.2 Construction

The internal magnetic probe is shown in Fig. 5.9. Arrays of 3D magnetic pickup

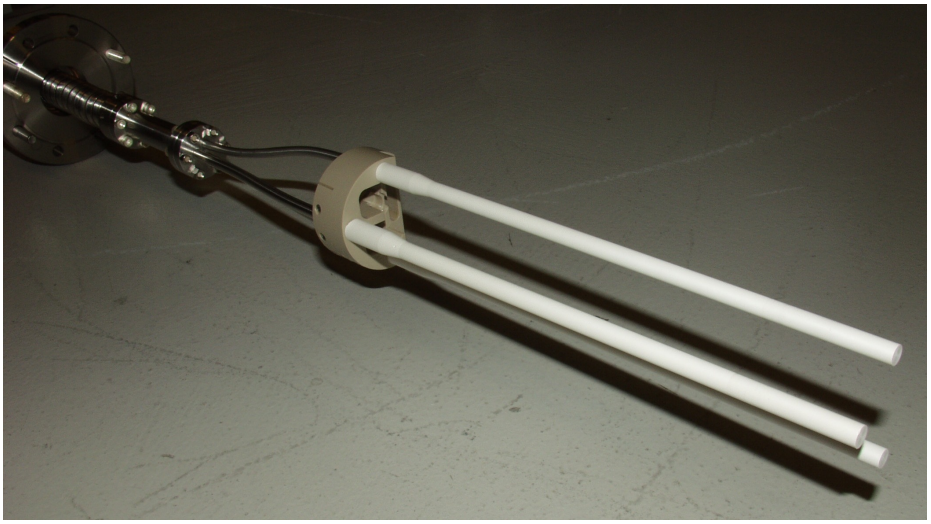

Figure 5.9: Picture of the internal magnetic probe before it was inserted into HIT-SI. The three stainless steel stems are protected from the plasma by boron nitride sheaths (white). The boron nitride sheaths are screwed onto threads extending from the PEEK piece (tan). The PEEK piece acts to position the stems and lock onto a key that extends from the diagnostic ring. Diagnostic designed by R. J. Smith.

coils (Fig. 5.8) are inserted into each of the three stainless steel stems. Each 3D coil consists of three overlapping windings and defines the local field at that location. The spools are 1/4 inch in length and each spool is spaced 1/4 inch apart along a thin plastic rod making the center of each probe 1/2 inch apart. The top stem has seven 3D coils, the middle stem has 17 3D coils, and the bottom stem has nine 3D coils. The stainless steel stems provide structural support and the vacuum break between the probes and the confinement volume. The stems are encased in boron nitride sheaths to insulate the stainless steel from the plasma. The bases of the boron nitride sheaths are threaded and screw onto threads that extend from the polyether ether ketone (PEEK) piece. The PEEK piece acts to stabilize the position of each stem and locks into a key that extends from the diagnostic ring. The probe is mounted onto a linear

actuator with a throw of about 25 cm.

During the installation of the probes into the stainless steel stems the toroidal probe nearest the end of the probe was damaged and there is no longer continuity through the coil. As of this writing no other probes are known to be damaged.

5.2.3 Calibration

A Helmholtz coil (Figs. 5.10 and 5.11) was used to calibrate each of the internal probe windings before the probe was inserted into the confinement volume. The Helmholtz

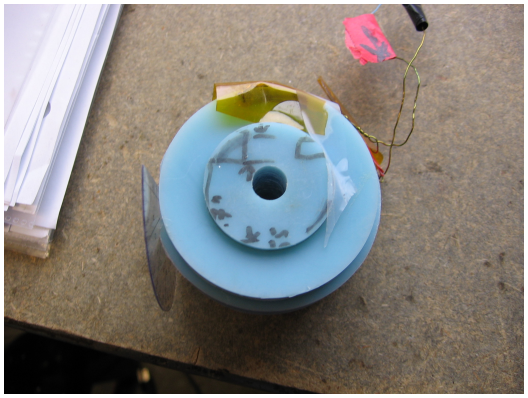

Figure 5.10: Orientation of the Helmholtz coil used for the calibration of the radial pickup coils. Coil designed by R. J. Smith.

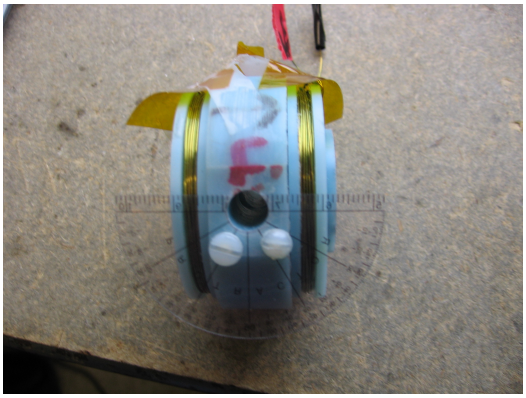

Figure 5.11: Orientation of the Helmholtz coil used for the calibration of the transverse pickup coils. Coil designed by R. J. Smith.

coil is designed so that it can be mounted onto the probe stem to generate magnetic fields either parallel or transverse to the stem. A detailed description of the calibration process and the calibration data are reported in Appendix D.

The calibration of the pickup coils is accurate in magnitude, but ambiguous in the overall sign of the signal. When the probe was inserted into the machine the overall sign of the probe signals matched the other magnetic diagnostics in the machine so it was believed the sign was correct. However, closer inspection of the internal magnetic fields in relation to the injector flux led to the discovery that the overall sign of the

probes was incorrect. That also implied that the overall sign of the flux loops on the confinement volume and the surface magnetic probes were also incorrect. The source of the error emanated from a mistake in understanding the direction of the vertical field, which was used to calibrate the overall sign of the flux loops. The overall sign of the magnetic signals is correct now.

The Helmholtz coil described in Figs. 5.10 and 5.11 has a resonance around 250 kHz. A second Helmholtz coil was made to determine the 3 dB point of the pickup coils in the stainless steel sleeve. The magnitude and phase of the signals are measured as a function of the input frequency to the Helmholtz coil. Fig. 5.12 shows that the 3 dB point for a selection of probes ranges between 666 and 911 kHz.

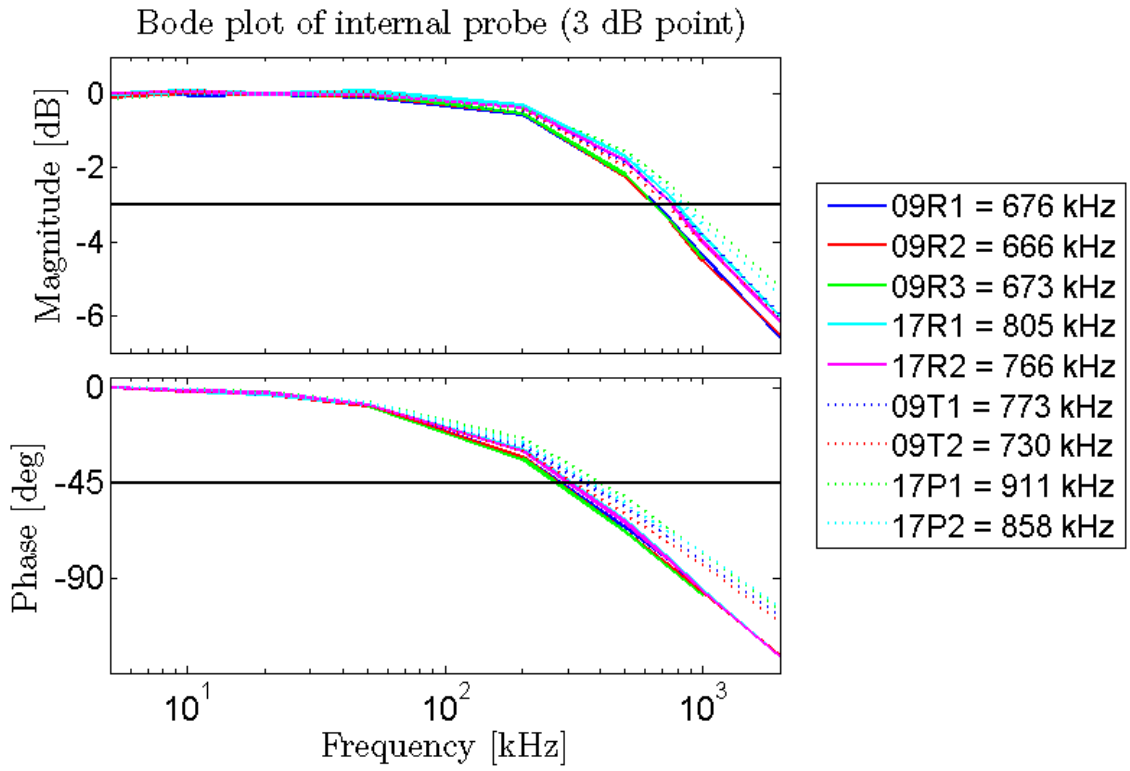

Figure 5.12: The 3 dB point of the pickup coils inside the stainless steel stems is ~700 kHz.

5.2.4 Measurements

Each step of the measurement process, from the pickup coil to the digitizer, needs to be understood to ensure the correct calibration of the magnetic signals. The leads from each pickup coil go to a junction box on the end of the probe stem. From this box BNC cables go to the patch panels above the HIT-SI device. BNC cables run between the patch panel above the HIT-SI device to panels above the data acquisition system in the control room. In the control room each cable is then connected to an integrator and then from the integrator to a digitizer. This section describes the creation of the final measurements from the original signals.

Baseline subtraction

The magnetic signals use integrators so it is critical to use a baseline subtraction when presenting the data. Baseline subtraction removes the result of integrating a constant voltage with the integrators over the course of the shot. In addition, a slanted baseline is used because occasionally the baseline will drift over the course of the day. The slanted baseline is thus a catch for the accuracy of the baseline subtraction. Figure 5.13 shows a raw signal compared to the signal after a baseline subtraction and slanted baseline have been performed. One issue with the slanted baseline is that occasionally the data has spurious points (large signals that are not real) that interfere with the calculation of the end points of the slanted baseline. Typically these spurious points occur at the beginning or end of the data collection. For this reason the slanted baseline program does not use the first or last data points in the calculation.

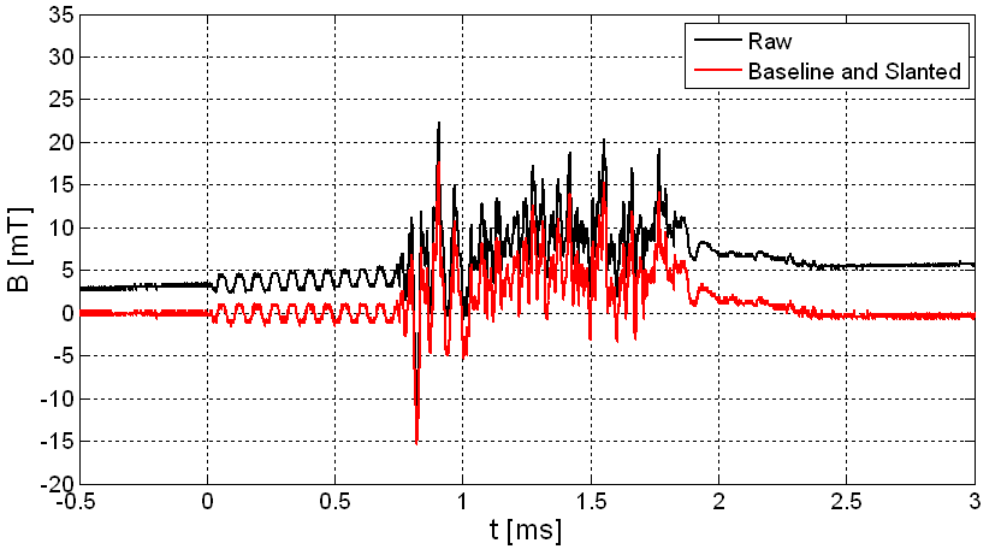

Figure 5.13: Correction of the internal probe signal due to a constant voltage drift in the integrator. See Appendix C.1.1 for the location of the code used to make this figure.

Matrix correction

The probe coils are slightly rotated with respect to the toroidal and poloidal directions in the machine. During the calibration process described in Appendix D the angle of maximum signal with respect to the toroidal and poloidal directions is measured. These angles are used to reconstruct the probe signals in the toroidal and poloidal directions in the machine. See Appendix C.7 for the location of the code used to write the matrix correction to the tree. Typically the rotation angle is a few degrees so the rotation angle is a minor correction to the data. Rotation of the probe stem does not affect the radial signal so no correction is needed for those signals. The toroidal and poloidal signals are given from the toroidal and poloidal winding signals, B_{T0} and B_{P0} respectively.

$$B_T = B_{T0}\cos\phi + B_{P0}\sin\phi \tag{5.3}$$

$$B_P = B_{P0}\cos\phi - B_{T0}\sin\phi \tag{5.4}$$

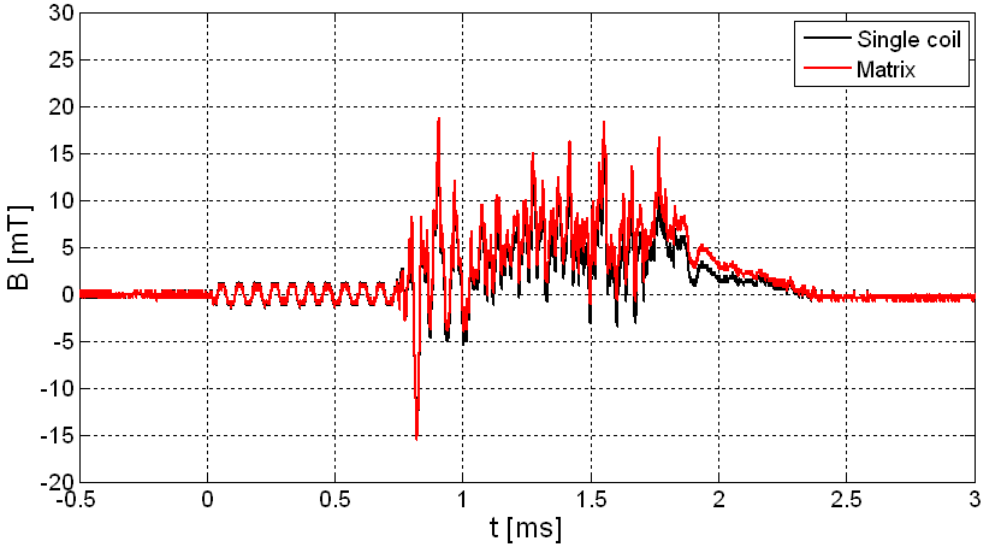

Figure 5.14: Correction of the internal probe signal due to the rotation of the probe windings. See Appendix C.1.1 for the location of the code used to make this figure.

Time shift

Studying the data from shots similar to the one shown in Fig. 5.15 one can notice a time lag between the bottom stem of probes compared to the top and middle stems. To test the source of the discrepancy a function is input into each digitizer used for the internal probe and the results recorded. It is found that the 2412 digitizer used here (HIT-2412-DD) lags the 1612 digitizers by 2.5 μs. The two 612 digitizers (HIT-612-ZZ1 and HIT-612-ZZ2) lag the 1612 digitizers by 5 μs. The result of adding a correction to the time base for signals on the 612 and 2412 digitizers is shown in Fig. 5.16.

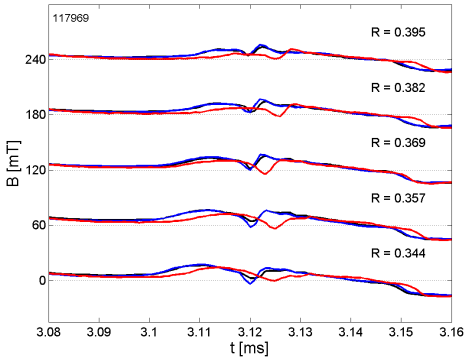

Figure 5.15: Internal magnetic probe signal at five radial locations along each of the three stems. The middle stem is shown in black, the top stem in blue and the bottom stem in red.

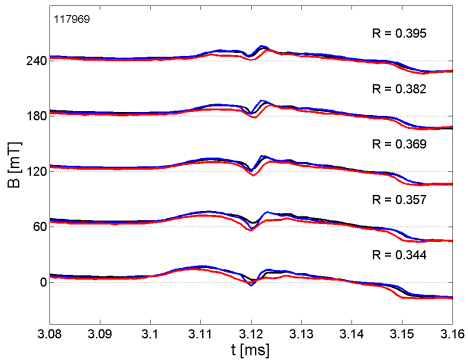

Figure 5.16: Internal magnetic probe signal at five radial locations along each of the three stems after the time base has been shifted for the 612 and 2412 digitizers. The middle stem is shown in black, the top stem in blue and the bottom stem in red.

See Appendix C.1.2 for the location of the code used to make these figures.

Variable integrator internal impedance

The calibration of the internal probe coils is made into a digital scope with 50 Ω termination. The magnitude of the actual digitized signal is affected by the internal resistance of the integrators. In addition the resistance of the cables from the internal probe junction box to the integrators could also cause a decrease in the measured voltage. Figure 5.17 shows the effect of adding this correction. The error in magnitude is <2%, on the order of the width of the lines used to make the plot.

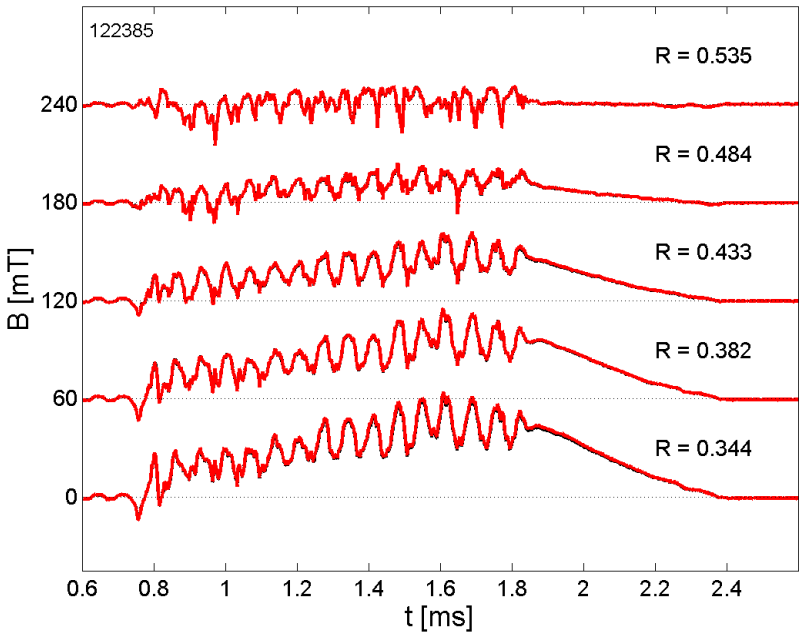

Figure 5.17: Plotting the toroidal magnetic field with (red) and without (black) adding a calibration factor due to the internal resistance of the integrators and the resistance of the cables from the internal probe junction box to the integrators. See Appendix C.1.3 for the location of the code used to make these figures.

5.2.5 Typical internal magnetic field traces

After the corrections described in the previous section the resulting poloidal, toroidal and radial signals are shown in Figs. 5.18, 5.19 and 5.20 respectively. Each figure shows the internal magnetic fields at five different radial locations with the traces in Figs. 5.18 and 5.20 offset by 40 mT and the traces in Fig. 5.19 offset by 60 mT.

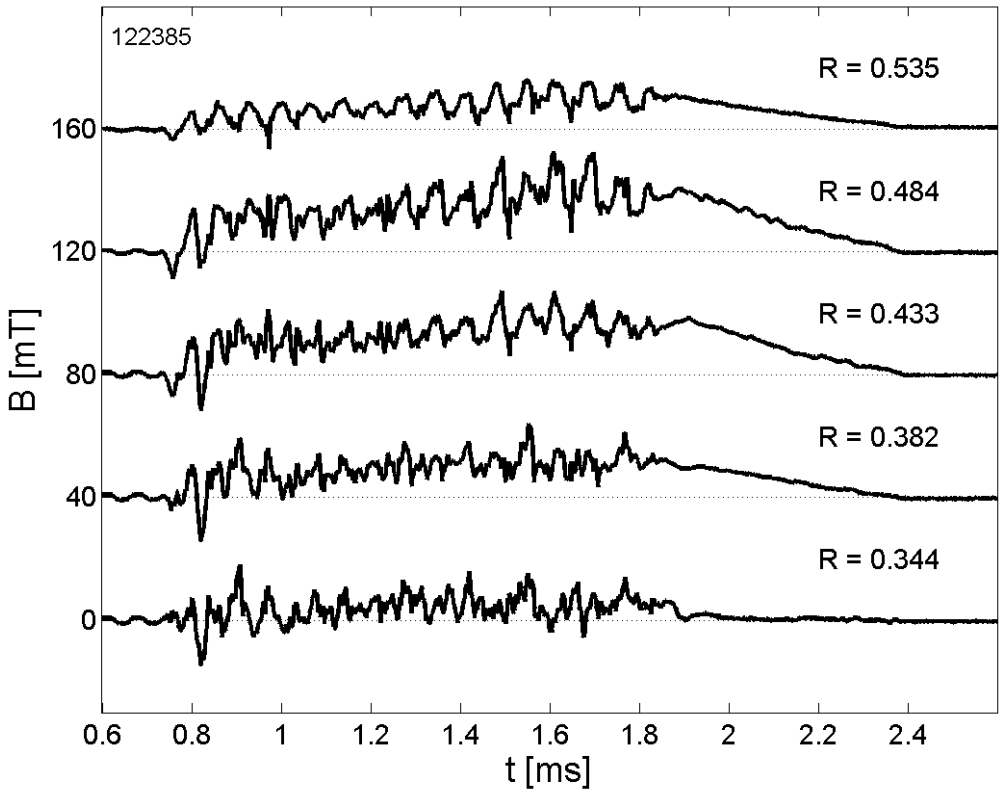

Figure 5.18: The poloidal magnetic field at five radial locations after the signals have been processed. See Appendix C.1.4 for the location of the code used to make this figure.

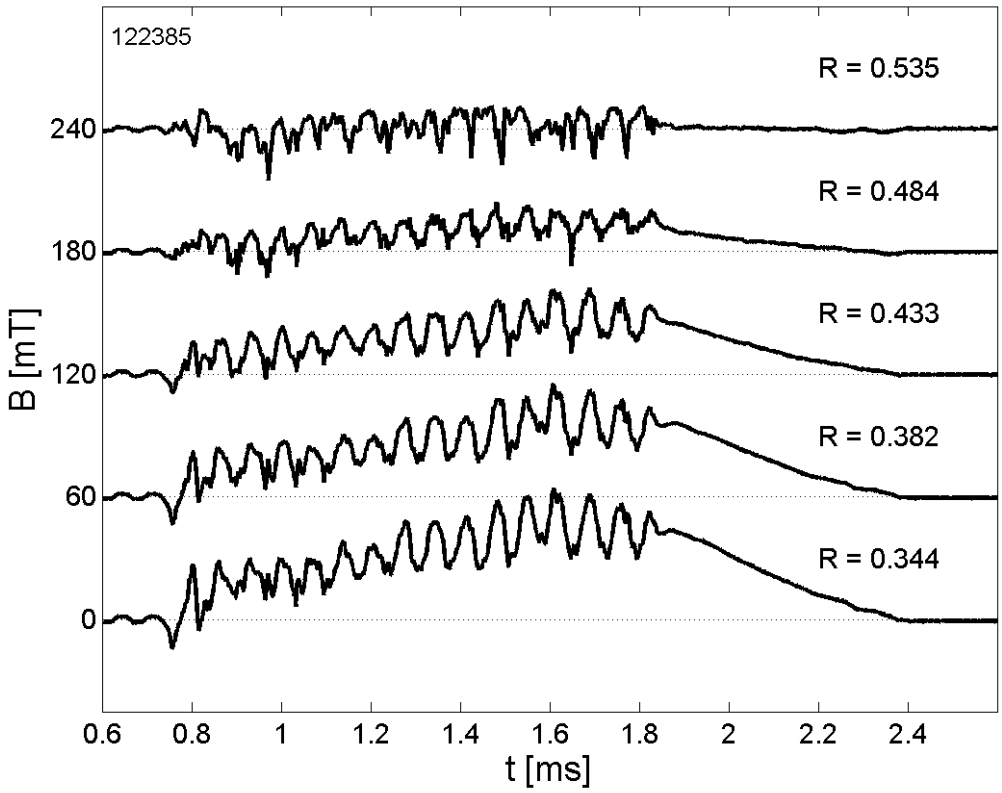

Figure 5.19: The toroidal magnetic field at five radial locations after the signals have been processed. See Appendix C.1.4 for the location of the code used to make this figure.

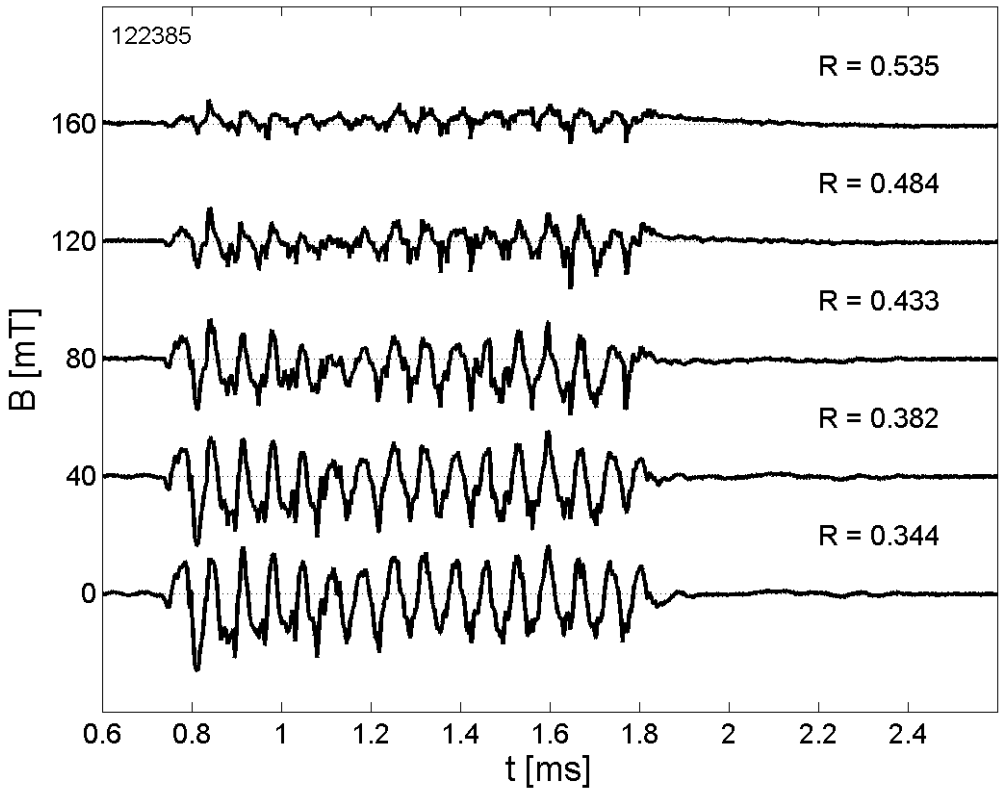

Figure 5.20: The radial magnetic field at five radial locations after the signals have been processed. See Appendix C.1.4 for the location of the code used to make this figure.

5.3 Spectroscopy

5.3.1 Vacuum ultraviolet (VUV) spectrometers

Two symmetrically viewing VUV spectrometers [39] are used to diagnose HIT-SI plasmas (see Fig. 5.21). The two spectrometers are used to compare the ratio of line radiation of impurity ion species. The relative abundance of different ionization states of atoms varies with the electron temperature so the ratio of the radiation between the two lines gives an indication of the temperature. The VUV spectrum is between the X-ray region (∼0.2 nm) and the UV region (∼200 nm). The spectrometers are located behind gate valves and employ their own turbo pump. The gate valves are controlled electronically to open just for a short period of time encompassing a plasma shot. This set up is necessary because VUV radiation is absorbed by oxygen and quartz.

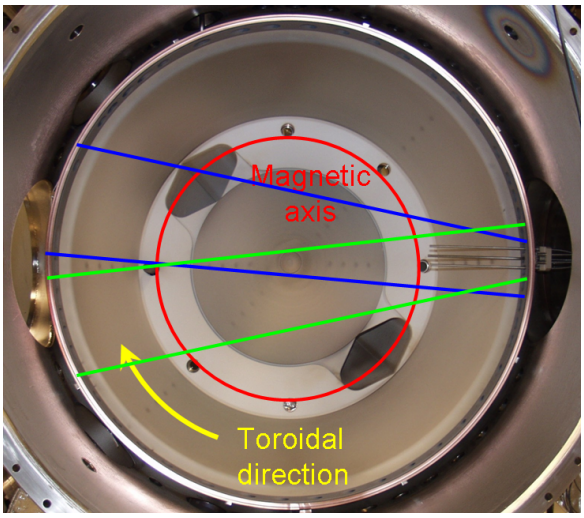

Figure 5.21: The maximum field of view of the VUV spectrometers is outlined in green (VUV upper) and blue (VUV lower). The actual field of view is limited by the holes in the diagnostic ring.

The VUV spectrometers were calibrated during a vacuum break when there was physical access to the confinement volume. A mercury pen lamp was positioned in the confinement volume at a location viewable by both spectrometers. The dial settings

of the spectrometers were adjusted around known mercury lines to test the accuracy of the wavelength measurement, the width of the line and the relative calibration between the two spectrometers (see Fig. 5.22 and Fig. 5.23). Measurements were made adjusting the spectrometer in both the clockwise (CW) and counter-clockwise (CCW) direction. The largest difference between the reported wavelength is 0.1 nm with the VUV lower at the 253.65 nm line. The full width half max of each curve is about 1 nm.

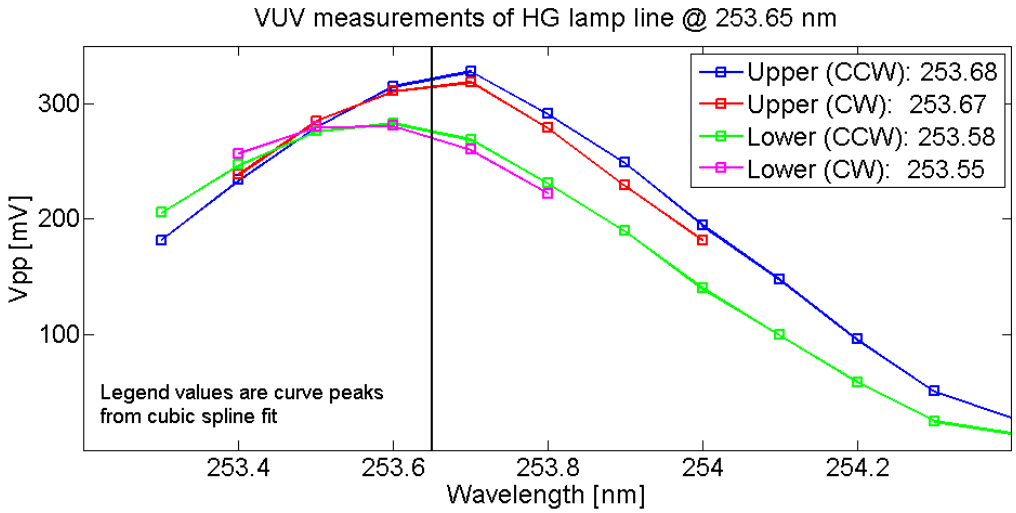

Figure 5.22: Calibration of the VUV spectrometers with a mercury pen lamp at 253.65 nm.

Charge state distributions are found by comparing the emission from two charge states of the same atomic species. Typically carbon III and carbon IV lines are used on HIT-SI. The absolute calibration is not crucial for this estimate so long as it is known that the correct line is being measured. The large full width half max means that slight deviations from the peak of the line profile will not adversely affect the measurement. Also the relative magnitudes between the two spectrometers is not enough of an issue to create any problems with the measurement.

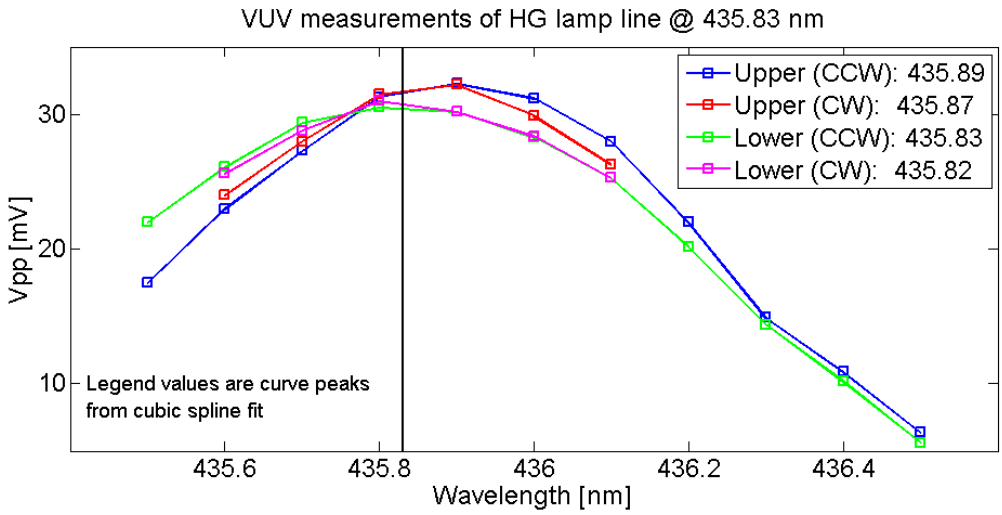

Figure 5.23: Calibration of the VUV spectrometers with a mercury pen lamp at 435.83 nm.

Typical VUV signals are shown in Fig. 5.24. One of the spectrometers is measuring line radiation from carbon III (117.6 nm) and the other line radiation from carbon IV (154.8 nm). When in equilibrium carbon III reaches its peak abundance of carbon ion species at an electron temperature of 8 eV and carbon IV has its peak abundant when the electron temperature is 10 eV [40]. The bottom of the figure shows the ratio between the two lines. After the injectors are shut off the relative abundance of CIV increases relative to CIII.

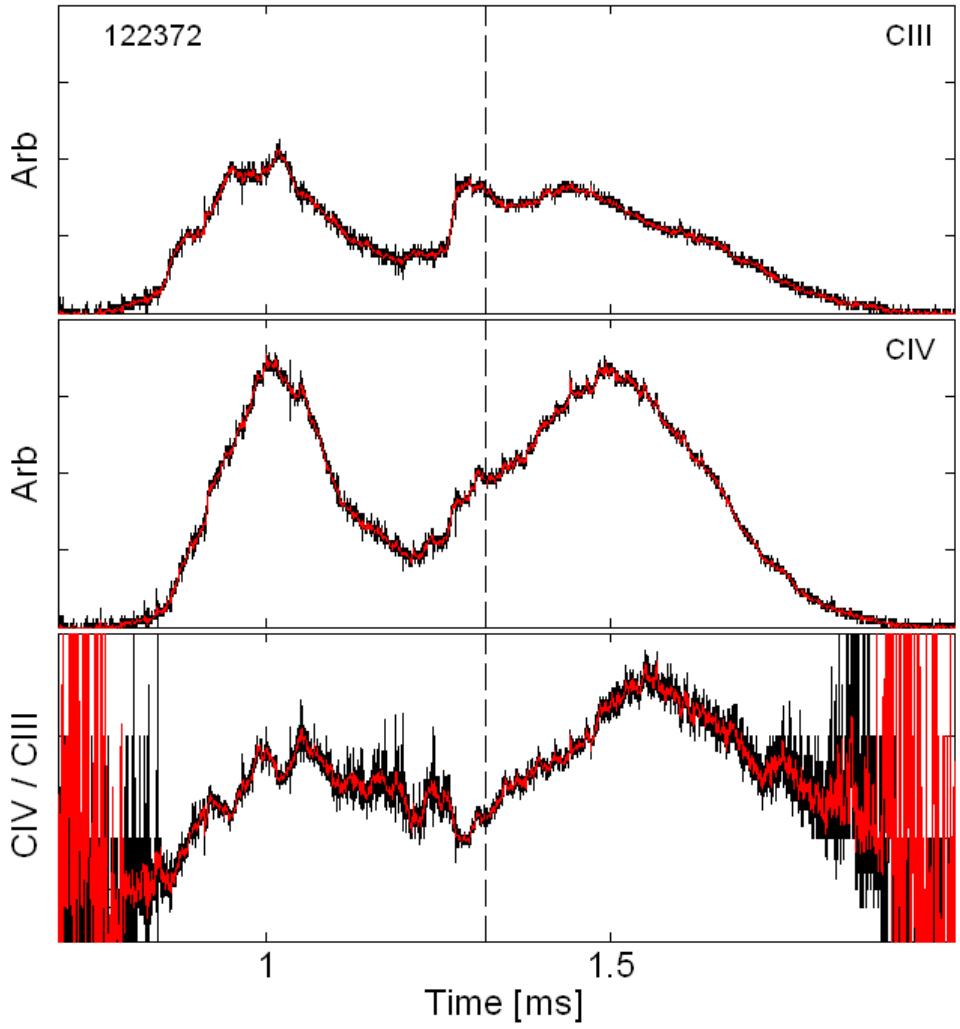

Figure 5.24: Typical VUV signals and the ratio between the signals. The black traces are the raw data and the red traces are the data smoothed over 15 data points. The vertical, dashed line indicates the time when the injectors are turned off. See Appendix C.3.2 for the location of the code used to make this figure.

5.3.2 Photomultiplier Tubes (PMTs)

PMTs are used on HIT-SI to measure plasma radiation through the bandpass filters mentioned in Appendix E. In addition to the filters mentioned in the appendix, there is also a bandpass filter for the H_α line (656.3 nm). Optical fibers designed to transmit low-wavelength light are used with the bandpass filters in the UV range. The bandpass filters are typically placed along the chords shown in Fig. 5.25.

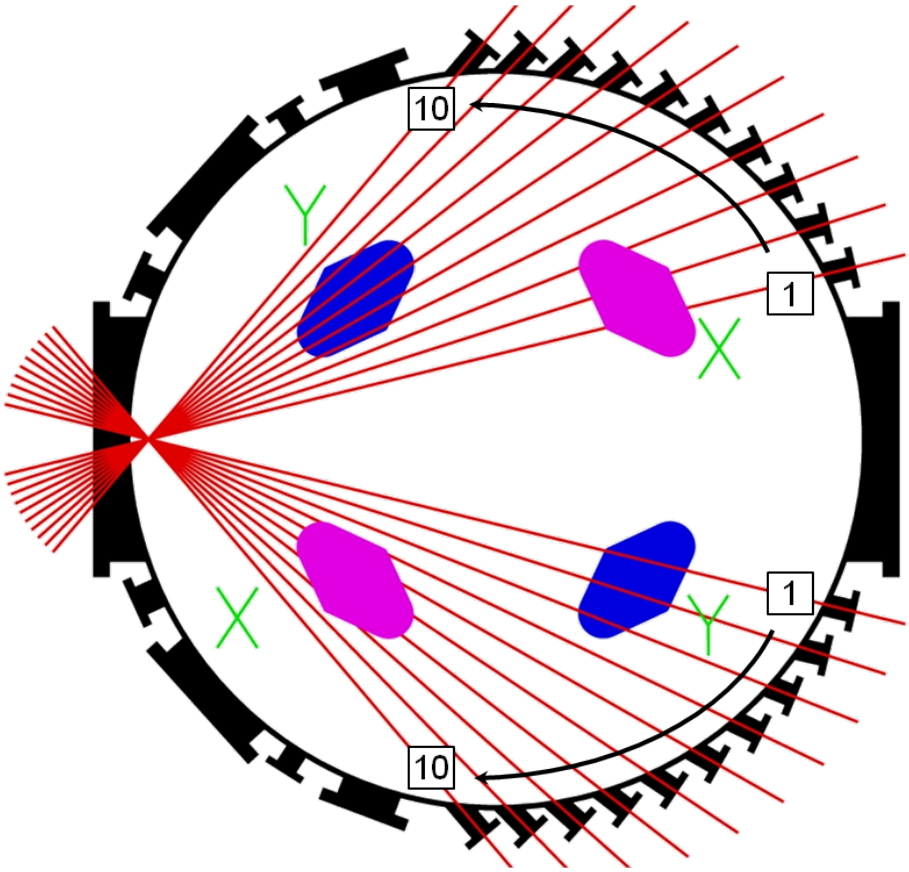

Figure 5.25: Location of the chords used with the PMT signals. There are 10 upper chords and 10 lower chords with the chord numbers as shown. Image courtesy of John Rogers and Aaron Hossack.

Figure 5.26 shows He I, H_α, C III and CII radiation for a deuterium shot that reaches 40 kA (see Fig. A.26). The H_α signal shows regular oscillations at the injector

frequency with the average light intensity similar at the beginning and end of the shot. Both the He I and C III signals increase over the duration of the shot and show a strong correlation in signal spikes. These spikes in light are not seen on the H_α signal.

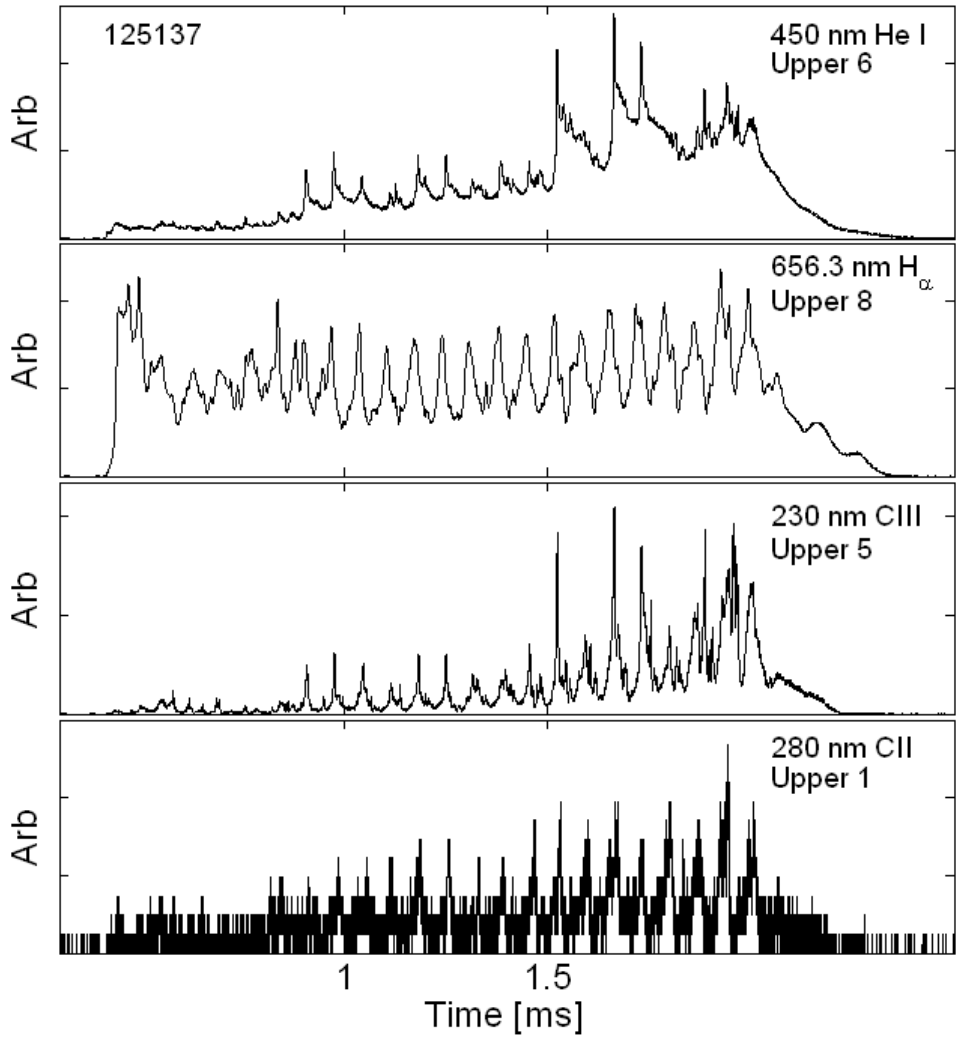

Figure 5.26: Typical PMT signals. See Appendix C.3.3 for the location of the code used to make this figure.

5.4 High speed camera imaging

HIT-SI recently purchased a Phantom model 710 high-speed camera with ARRA funding. This is a black and white camera capable of taking exposures as short as 300 ns. The smaller the area of the CCD used the faster the camera can be operated. Typical operations are at 150,000 frames per second (1 frame every 6.7 μs) with a resolution of 256 x 128 pixels. Using two coherent fiber bundles to simultaneously image the plasma from two angles stereoscopic movies can be made. Imaging spectroscopy has been done by imaging the output of a spectrometer with the high-speed camera. This section describes these two uses of the high-speed camera.

5.4.1 Stereoscopic imaging

The goal of stereoscopic imaging is to image the 3D structure of the plasma. A continuous view of a toroidal structure in the confinement volume during injector drive would be important in showing the efficacy of SIHI current drive. To achieve the widest possible view of the plasma two re-entrant ports are made to extend into the diagnostic ring. These ports are installed at 3° and 347° toroidally and spaced 15 cm apart (Fig. 5.27). As the figure shows, the re-entrant ports extend into the diagnostic ring. Before inserting the ports into the machine the metallic end of the ports is sprayed with an insulating spray. This is done to prevent the ports from acting as a ground for the plasma. The ports were originally sprayed with a boron nitride spray. However, when the ports were placed into the machine arcing occurred around the front edge of the port. Material from the arcing coated the windows and prevented the imaging of the plasma. The second attempt involves spraying the ports with an alumina spray. The alumina spray has performed better than the boron nitride spray, but has also suffered from arcing and the darkening of the re-entrant windows. For this reason new re-entrant ports have been purchased and will be used in the future. The last 10 cm of these re-entrant ports are made of quartz and will

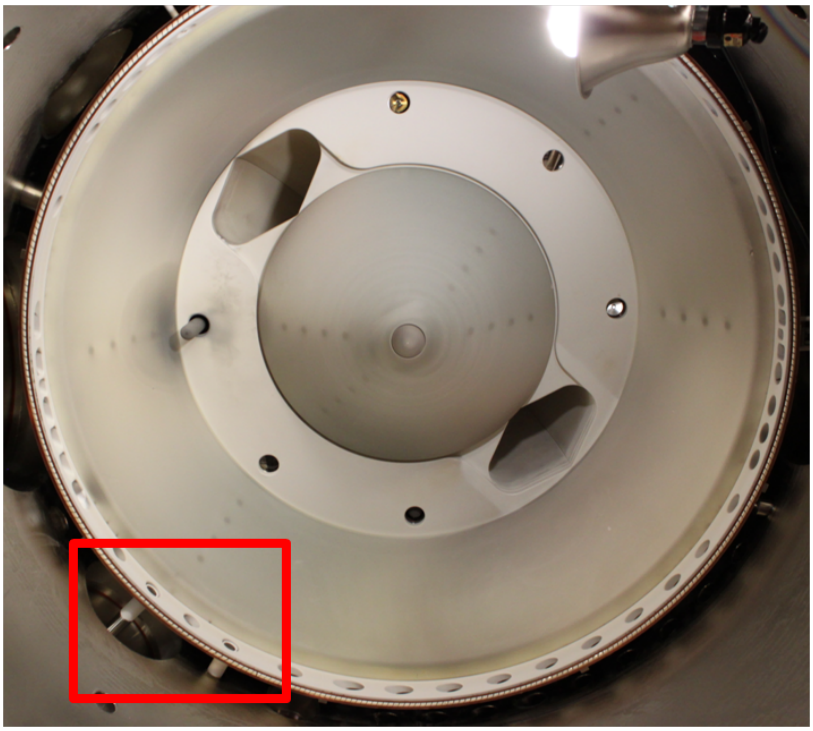

Figure 5.27: The re-entrant ports (boxed in red) used for stereoscopic imaging can be seen extending into diagnostic ring.

not need additional insulation.

Stereoscopic imaging is done through two coherent fiber bundles which extend into the re-entrant ports. Each fiber bundle consists of a square grid 4 mm x 4 mm made up of roughly 128 x 128 individual fibers. The numerical aperture (NA) of the fibers is 0.63. The two fiber bundles come back together into a single piece and are simultaneously imaged by the high-speed camera (Fig. 5.28). The images provide two views of the plasma which can be used to reconstruct a 3D image. Originally two completely separate coherent fibers were purchased. Later, it was decided to bring the fibers together into a single piece to simplify imaging both fibers simultaneously. During the process of bringing the two bundles together some of the fibers were damaged as can be seen in Figs. 5.29 and 5.30.

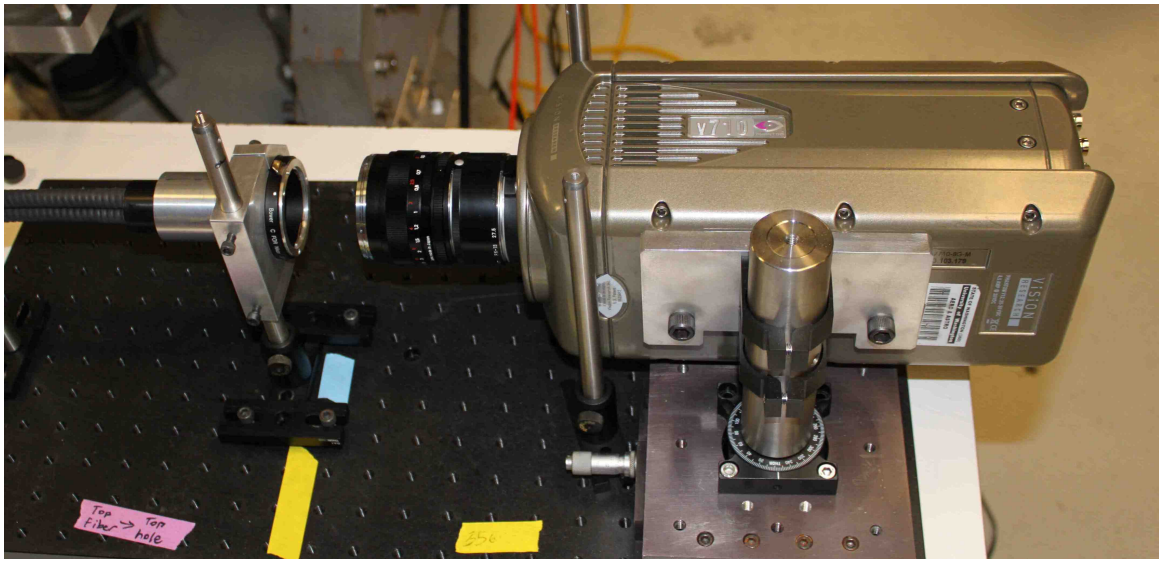

Figure 5.28: The high-speed camera images the output of both coherent fibers simultaneously.

After being brought together the two bundles make a rectangle of 256 x 128 fibers. The ideal setup with the fast camera is to use 256 x 128 pixels for no loss in resolution with the fastest imaging speed. Fig. 5.31 shows simultaneous images taken through the re-entrant ports. The images shown in Fig. 5.31 are of all visible light with a 4.88 μs exposure time near the initial plasma breakdown. Black spots from dead pixels are eliminated by interpolating over the spots with adjoining pixels. The opposite side of the diagnostic ring bisects the images. The conical shapes at the top and bottom of the figures are the small cones. A tube of light can be seen extending from one of the injector mouths.

Creation of stereoscopic images from the two images has not been tremendously successful. One issue is the space between the individual fibers shows up on each of the images (see the grid like patterns on the images in Fig. 5.31). When superimposing the images the black lines show up in different places on each of the images. Thus each eye sees black lines that are not part of the 3D image. Another difficultly is

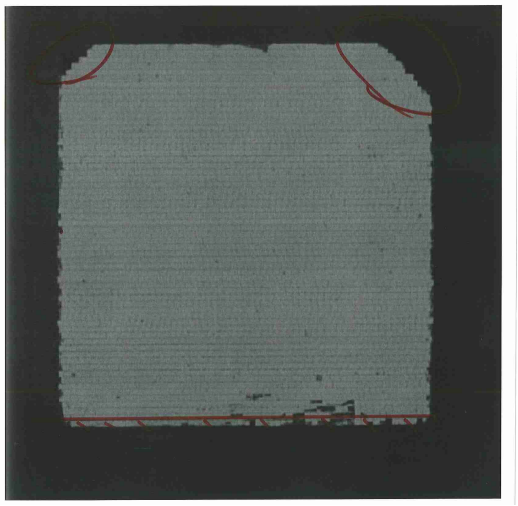

Figure 5.29: Fiber bundle 1. Black spots indicate dead fibers.

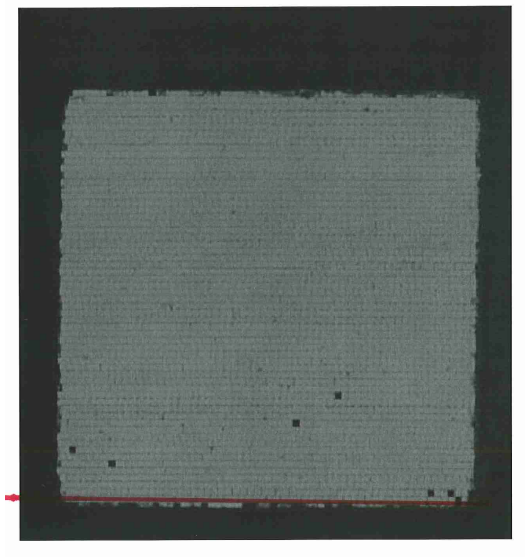

Figure 5.30: Fiber bundle 2. Black spots indicate dead fibers.

the low resolution of the images. Typically 3D images are made from high resolution images. In this case the 3D images need to be made from images that are 128 x 256 pixels. One way to overcome both of these problems is to use lenses and mirrors to bring the images from the re-entrant ports to the camera. This will be attempted in the future.

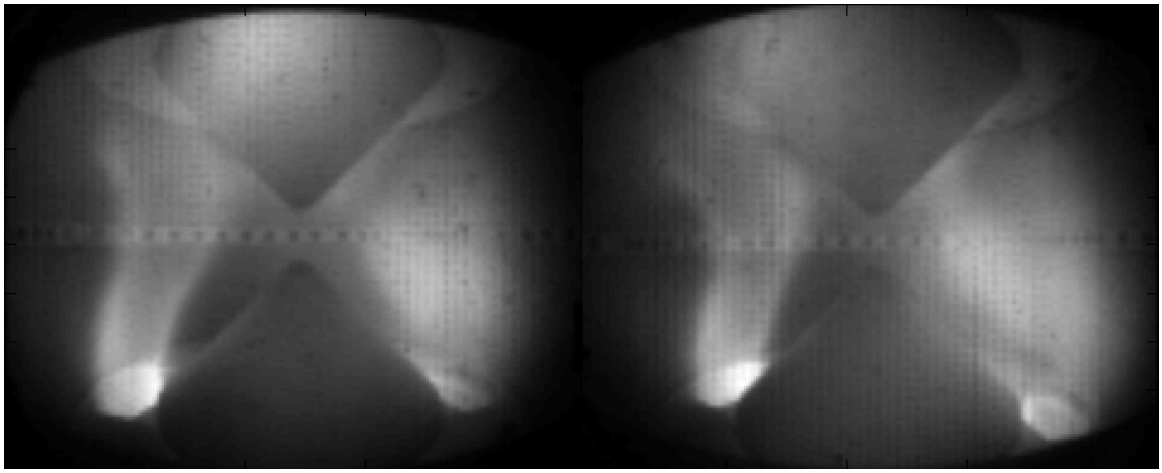

Figure 5.31: Visible light images taken with the high-speed camera through the diagnostic gap on shot 124241. Two coherent fiber bundles are used to image the plasma from two locations simultaneously. See Appendix B.9 for the code used to make this figure.

5.4.2 High Speed Spectroscopy (HISS)

The high-speed camera has been used in conjunction with a spectrometer to perform imaging spectroscopy. Figure 5.32 shows the design of HISS. Near the bottom right of the figure there is a 200 mm focal length lens. This lens is positioned in front of the axial port facing the Y-injector mouth at 270° for the data shown here. The lens is used to focus the light onto the entrance slit of the spectrometer. The exit slit of the spectrometer is removed and the fast camera images the output of the spectrometer. The black tube parallel to the front face of the spectrometer contains a diffuse light source behind a similar slit as the entrance slit of the spectrometer. This second slit is equidistant with the entrance slit of the spectrometer to a point where a mirror can be added to the system. Adding a 45° mirror in front of the exit slit allows the light to be used to create an image where the spectrometer is viewing in the machine. In Fig. 5.33 the spectrometer is being imaged across the lower part of the injector mouth at 270°.

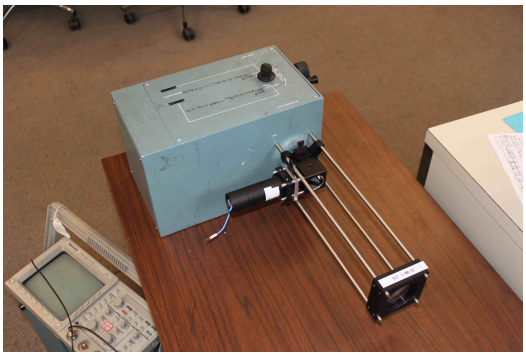

Figure 5.32: Entrance optics for the high speed spectrometer.

Figure 5.33: The spectrometer is imaged across the injector mouth as shown.

The goal of the diagnostic is to image with the fast camera spatial variation of light in one direction and wavelength variation of light in the other direction. Light entering

the entrance slit to the spectrometer varies spatially along the length of the slit. The grating in the spectrometer diffracts the light so that the wavelength variation of the light can be measured. The spectrometer is calibrated by comparing the output to the SPRED (Spectrometer-Poor Resolution Extended Domain) diagnostic that measures the spectral content of the plasma along a tangential chord integrated over the shot. Figure 5.34 shows the comparison between HISS and SPRED along the midpoint of the spatial resolution at the time when the peak amount of light is measured with the HISS diagnostic. Both diagnostics show the same spectral characteristics. The one

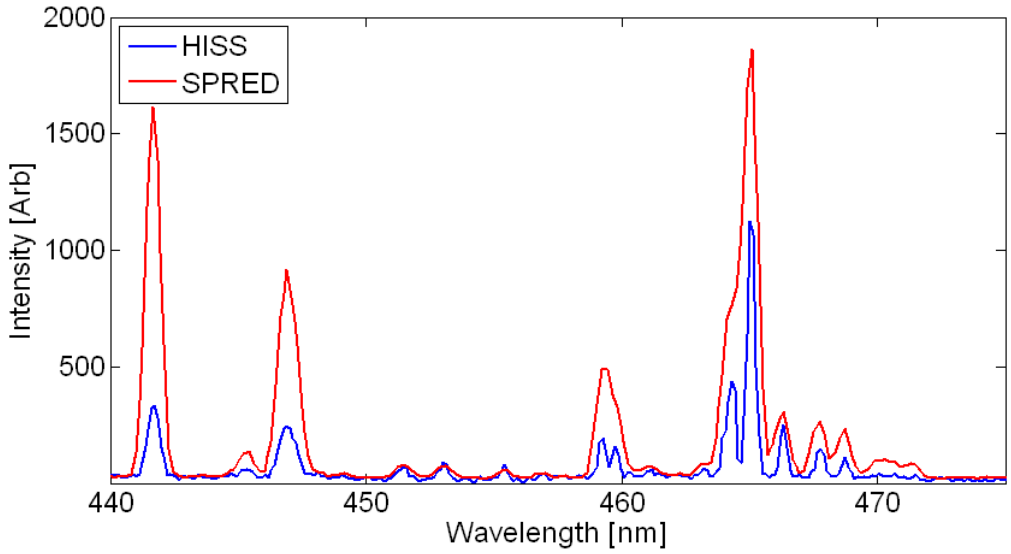

Figure 5.34: Comparison of spectral lines between HISS and SPRED. See Appendix C.3.5 for the location of the code used to make this figure.

difference being that the more dispersive HISS spectrometer allows higher spectral resolution. The fast camera is operated at 41,600 frames per second with 512 pixels of resolution in the spatial direction and 304 pixels of resolution in the wavelength direction. Line identification is done by comparing the measured lines to the NIST database and from differences in the SPRED spectrum for helium and deuterium shots.

Figures 5.35 through 5.38 show HISS data at four times during a deuterium shot that reaches a toroidal current of ∼40 kA. The vertical axis shows the variation in light with wavelength with some of the more prominent lines identified. The horizontal axis is the spatial dimension of the light shown in Fig. 5.33. The left side of the figure is the bottom of the light (confinement volume) and the right side the top of the light (injector mouth). The magnitude of the spectrum is plotted on the same log scale for each figure. Figure 5.35 shows the spectrum soon after breakdown. No He II light is measured during this time slice. Figure 5.36 is during the ramp up in toroidal current. More lines are visible now, including the He II line, but the light level of the lines from Fig. 5.35 have not increased appreciably by this time. Figure 5.37 is near the peak in toroidal current. A few new lines are visible and all of the lines are noticeably brighter by this time. Figure 5.38 shows the spectrum after the injectors have turned off. This spectrum is most similar to the spectrum from Fig. 5.35.

One thing to notice from the spatial data is that the highest intensity is near the midpoint of the spatial data. This seems to indicate that optical effects have a larger effect on the intensity than any effects measured by differences in the plasma spatially. In addition the figure is from line-integrated light across the confinement volume. Locally the area across the injector mouth might have different spectral characteristics, but that difference might not be enough to significantly alter its line-integrated characteristics.

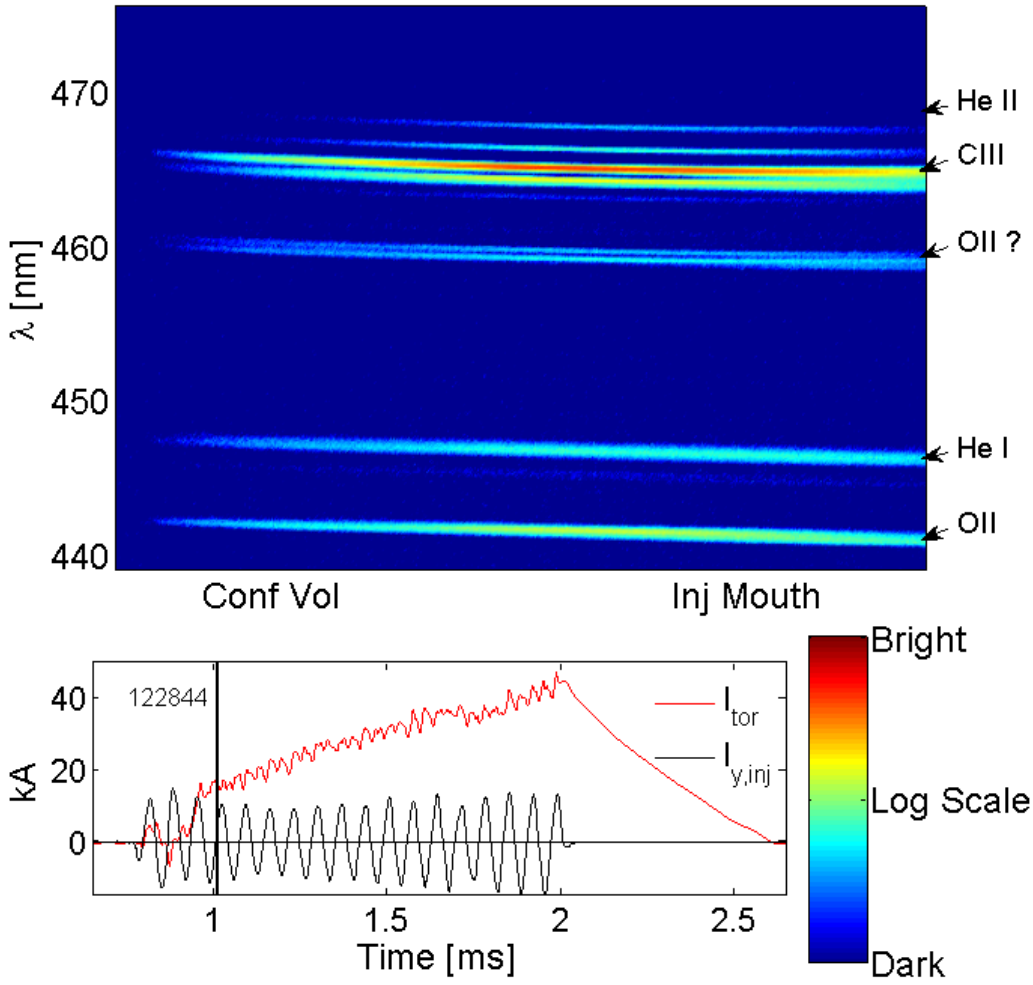

Figure 5.35: Spatial and wavelength measurement made with the HISS diagnostic at 1 ms. The toroidal current and Y-injector current are given as reference for the shot performance. The left side of the figure corresponds to the bottom of the light shown across the injector mouth in Fig. 5.33. See Appendix C.3.5 for the location of the code used to make this figure.

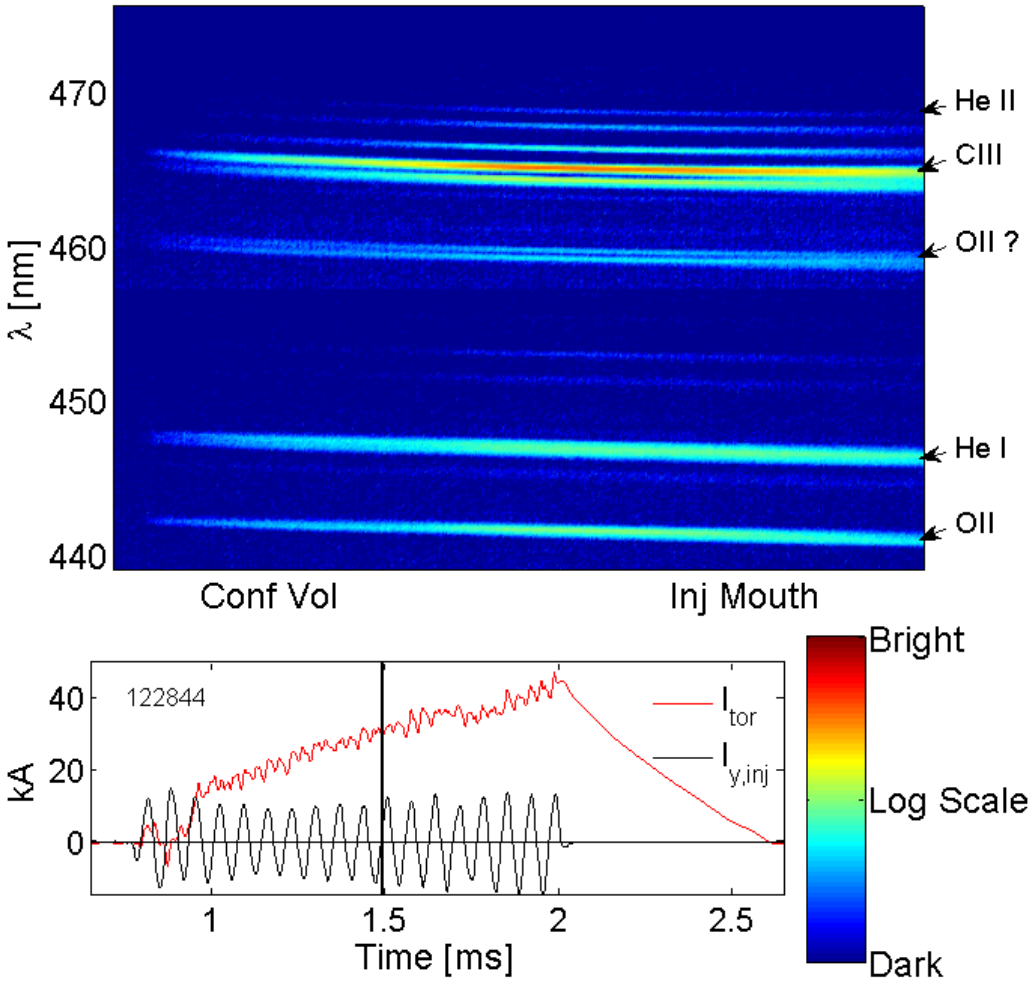

Figure 5.36: Spatial and wavelength measurement made with the HISS diagnostic at 1.5 ms. The toroidal current and Y-injector current are given as reference for the shot performance. The left side of the figure corresponds to the bottom of the light shown across the injector mouth in Fig. 5.33. See Appendix C.3.5 for the location of the code used to make this figure.

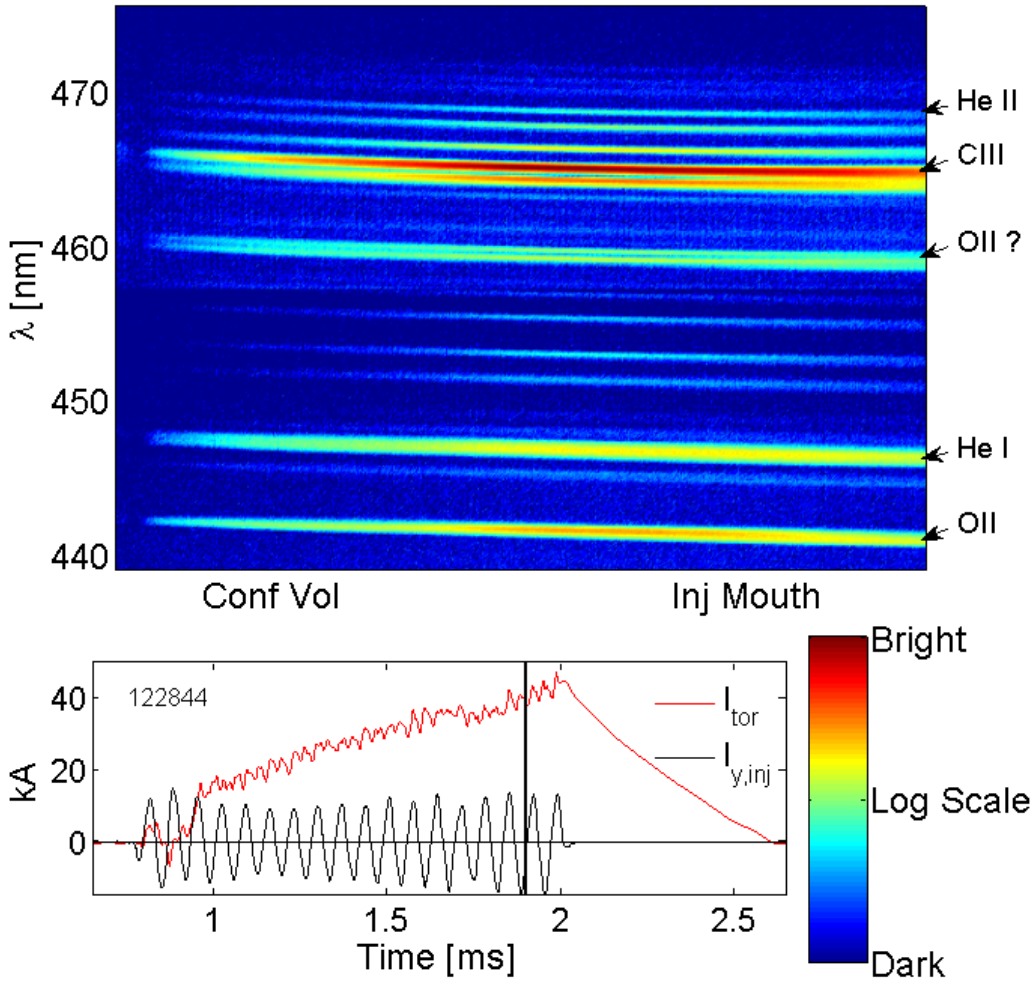

Figure 5.37: Spatial and wavelength measurement made with the HISS diagnostic at the peak in measured light. The toroidal current and Y-injector current are given as reference for the shot performance. The left side of the figure corresponds to the bottom of the light shown across the injector mouth in Fig. 5.33. See Appendix C.3.5 for the location of the code used to make this figure.

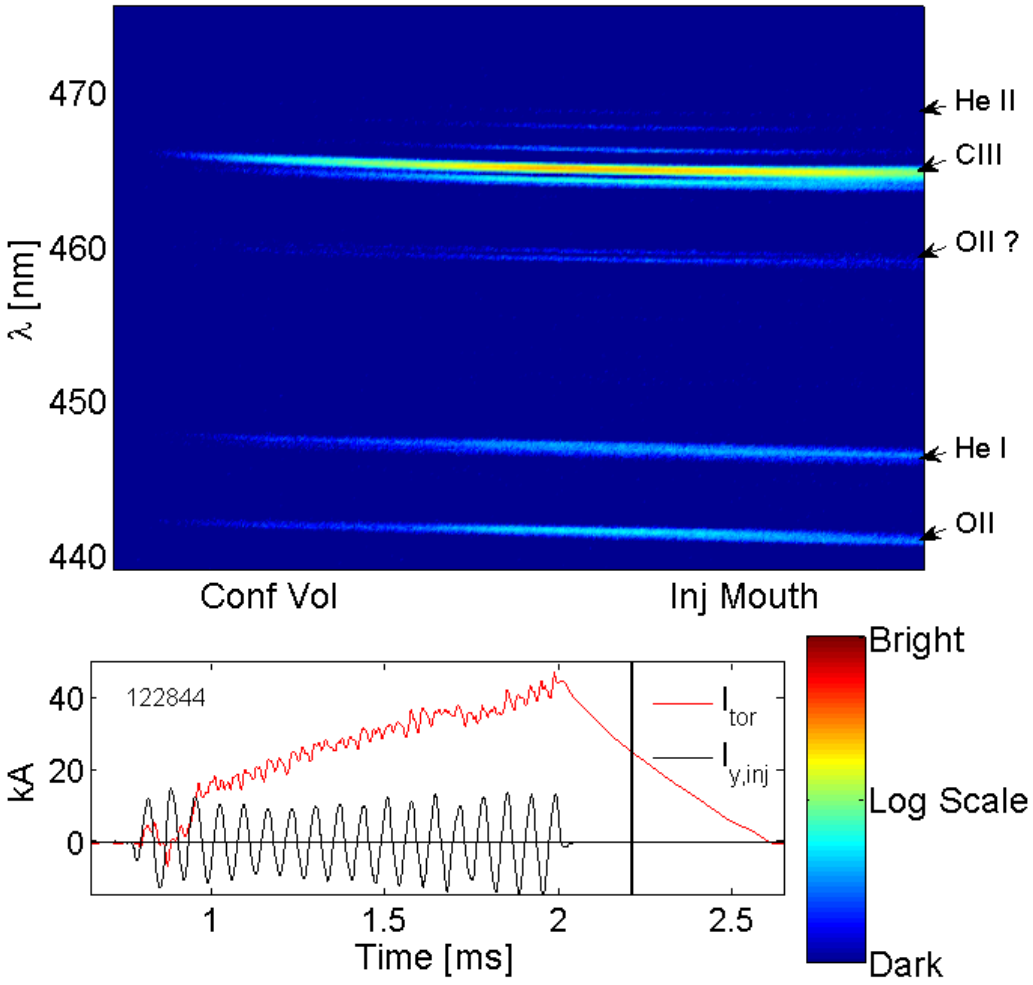

Figure 5.38: Spatial and wavelength measurement made with the HISS diagnostic at 2.2 ms. The toroidal current and Y-injector current are given as reference for the shot performance. The left side of the figure corresponds to the bottom of the light shown across the injector mouth in Fig. 5.33. See Appendix C.3.5 for the location of the code used to make this figure.

Chapter 6

DEUTERIUM OPERATIONS

A key to operating HIT-SI is to sufficiently fuel the injectors without over fueling the confinement volume. At low fueling rates the injectors become gas starved, meaning there is not enough gas to carry the current and causing spikes in the injector voltage. Additionally, shots with high power and low fueling rates tend to have problems with localized wall heating near the interface between the injector and the confinement volume. Wall heating is a key limiter of the injector voltage and the shot length. At higher fueling rates the buildup of density in the confinement volume becomes detrimental to plasma performance. Wall conditioning with helium plasmas followed by deuterium operations has allowed higher fueling rates while at the same time achieving lower density in the confinement volume [41]. Helium plasmas act to condition the alumina walls. The conditioned alumina walls then act as a pump for deuterium gas. The higher fueling rate allows the injectors to be operated at higher power and the wall pumping limits the plasma density in the confinement volume.

This chapter details the motivation for lower density operations, the steps taken to achieve density control on HIT-SI and the results achieved with this improved density control.

6.1 j/n

An important quantity in determining the quality of a spheromak plasma is the ratio of current density to electron density, j/n. Spheromaks and Reversed-Field Pinches (RFP) become radiation dominated when $j/n < 10^{-14}$ A·m [42]. Radiation losses limit the amount of energy that can go into driving current in the plasma. Previous

comparisons of the current density to electron density [36] indicated that HIT-SI plasmas were over fueled with $j/n < 0.5 \times 10^{-15}$ A·m. These results led to work to decrease the plasma density.

Current density in a plasma is given by

$$\vec{j} = n_e e(\vec{v_i} - \vec{v_e}) \tag{6.1}$$

where n_e is the electron density, e is the electron charge, v_i is the ion velocity, and v_e is the electron velocity. From this it can be seen that

$$\vec{j}/n_e = e(\vec{v_i} - \vec{v_e}) \equiv j/n \tag{6.2}$$

is a measure of the relative velocity between the electrons and ions. This is known as the drift velocity

$$v_{drift} = v_i - v_e. \tag{6.3}$$

Thus j/n is proportional to the drift velocity in a plasma. Since $j/n = 10^{-14}$ A·m is the ideal operating point the optimal relative velocity between ions and electrons is 160 km/s. The importance of j/n spans a wide variety of experiments with temperatures and magnetic field strengths that vary by many orders of magnitude.

A similar phenomenon when comparing current density to electron density is also seen on tokamak experiments. An empirically derived density limit seen on tokamak experiments known as the Greenwald limit [43] defines the maximum density for stable operations. The Greenwald limit is typically expressed as [43]

$$n_G = \frac{I_p}{\pi a^2} \tag{6.4}$$

where n_G is the density expressed in units of 10^{20} m^{-3}, I_p is the toroidal plasma current in units of MA and a is the minor radius of the torus. Tokamaks with a non-

circular cross section have a slightly different form for Eqn. 6.4. Recognizing that the right-hand side of Eqn. 6.4 is just the average current density, j, and rewriting the equation gives

$$\frac{j}{n} = 10^{-14} A \cdot m. \tag{6.5}$$

From this equation it can be seen that the Greenwald limit occurs at a similar ratio as the optimal operating point in RFPs and spheromaks. The Greenwald limit defines the operating space for tokamak operations at levels of $j/n > 10^{-14}$A·m. Tokamaks that operate above the Greenwald limit experience disruptions associated with the cooling of the edge of the plasma [43].

While the importance of j/n is seen in both tokamak and spheromak experiments, the effects of exceeding the Greenwald limit are different. In spheromaks the Greenwald limit defines the optimal operation point rather than a density limit for operations. Spheromaks can operate with densities above the Greenwald limit, but these over-fueled plasmas are radiation dominated and have poor toroidal current drive compared to plasmas with lower densities. In both tokamaks and spheromaks the problems associated with exceeding the Greenwald limit are associated with a cool, radiation dominated plasma.

j/n is calculated on HIT-SI using the toroidal current and the line-averaged electron density and is defined as

$$\frac{j}{n} \equiv \frac{\left|\overline{I_{tor}}\right|}{A\langle\overline{n_e}\rangle} \tag{6.6}$$

where $\overline{I_{tor}}$ is the toroidal current averaged over an injector cycle, $\langle\overline{n_e}\rangle$ is the line-averaged electron density average over an injector cycle and A, the area of a poloidal cross section, is 0.2 m^2.

6.2 Wall conditioning

Careful attention to fueling and wall conditioning are necessary to produce the desired plasma conditions in magnetic confinement experiments [44]. HIT-SI uses alumina

as a plasma-facing surface to insulate the plasma from the copper flux conserver and ensure that the current drive is completely inductive [28]. In addition, alumina reacts chemically with hydrogen isotopes, which makes it a good pump. However, the walls quickly become saturated with hydrogen isotopes, increasing wall recycling and radiated power. Past experiments performed in hydrogen and deuterium without helium conditioning achieved low toroidal currents. Without helium wall conditioning, adequate fueling of the injectors over fuels the confinement volume resulting in poor achieved toroidal current. Gas deficiencies in the injectors cause voltage spikes and localized wall heating near the injector mouths. The potential for localized wall heating limits the shot length. Helium wall conditioning allows higher gas injection rates while still achieving lower density in the confinement volume through the pumping of deuterium by the alumina walls.

The typical cleaning procedure is to take approximately 30 lower power ($\sim$3 MW of injected power) PDC helium shots to condition the walls for deuterium operations. Then a couple of higher power helium shots ($\sim$5 MW of injected power) are taken to condition the walls with a higher toroidal current discharge. This helium cleaning allows one to two high performance deuterium shots, with up to 10 MW of injected power, before the performance begins to degrade.

Three shots of a typical sequence—higher power helium shot, high performance deuterium shot and deuterium shot with poor wall pumping—are shown in Figs. 6.1 and 6.2 [41]. Operating settings are similar for all three shots. The first shot is a typical helium shot with an average electron density of $\sim$4 x 10^{19} m^{-3} and a toroidal current of magnitude 20 kA (toroidal current polarity is not controllable for dual injector shots). For the first deuterium shot, the toroidal current reaches 40 kA with lower electron density than the helium shot. The total injected power on this deuterium shot is $\sim$25% higher than the helium shot despite the similar operating settings. Higher plasma impedance, from the lower density, causes a larger increase in injected voltage compared to the decrease in injected current resulting in increased power injection.

Continued deuterium operations lead to an oscillating toroidal current of lower magnitude. A large increase in impurity hydroxide radiation as measured by the SPRED diagnostic occurs after repeated deuterium shots as the walls no longer pump the deuterium (see Fig. 6.2). For these shots SPRED is viewing along the midplane of the confinement volume at an impact parameter of 29 cm.

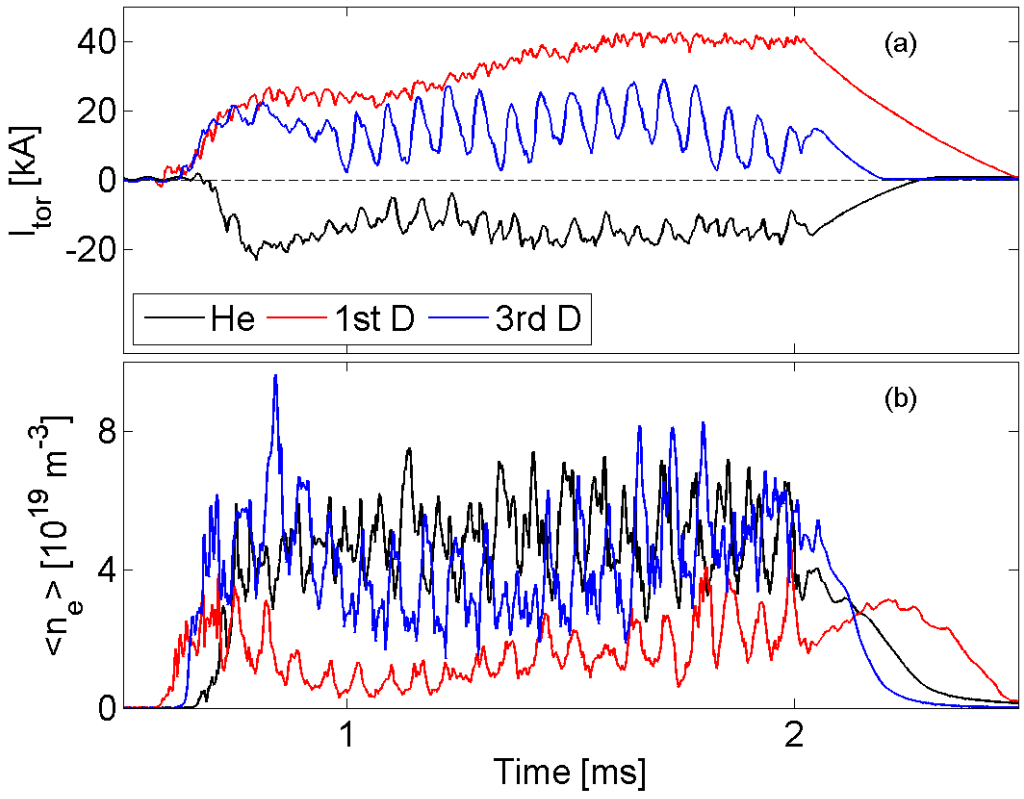

Figure 6.1: a) The toroidal current and b) line-averaged electron densities for a helium shot (121959) and subsequent deuterium shots (121961 and 121963) [41].

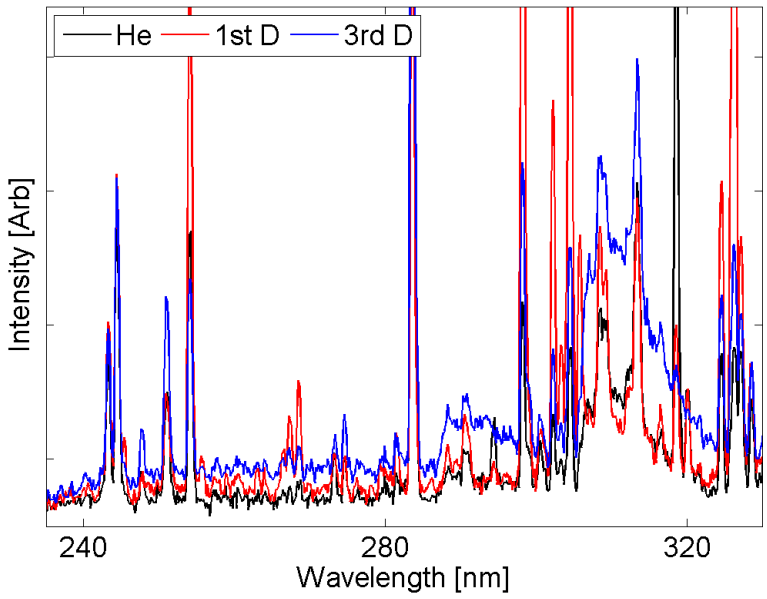

Figure 6.2: Line radiation of a helium shot (121959) and subsequent deuterium shots (121961 and 121963) [41].

This process of conditioning the walls with helium discharges followed by deuterium operations has produced the first HIT-SI discharges with ratios of $j/n > 10^{-14}$ A·m. Figure 6.3 compares the performance of the helium and first deuterium shot from Figs. 6.1 and 6.2. The initial formation of toroidal current is similar for both

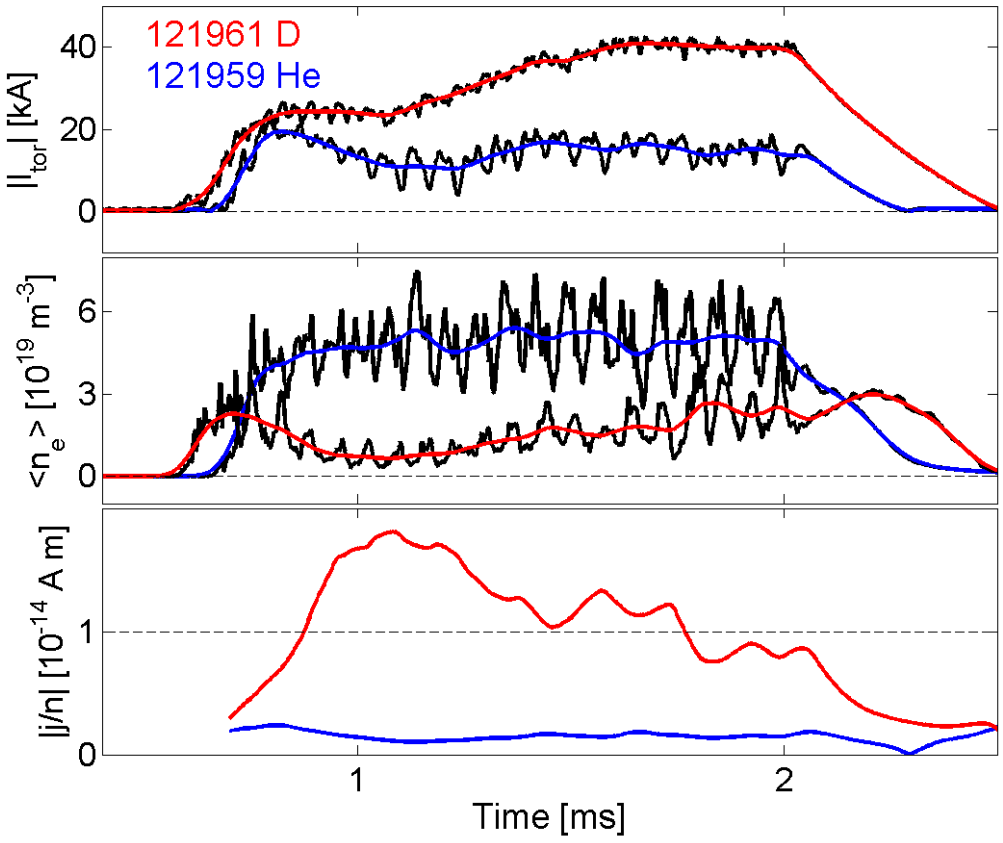

Figure 6.3: Comparison of toroidal current (top), line-averaged electron density (mid) and j/n for a deuterium and helium shot [45].

shots. However the current on the lower density deuterium shot continues to increase after the initial formation of toroidal current. The ratio of j/n exceeds the Greenwald limit for much of the deuterium shot and has more than a sevenfold improvement in peak j/n compared to the helium shot.

6.3 Performance results achieved during deuterium operations

Deuterium operations with the conditioned walls have achieved the best performance on HIT-SI, achieving the highest toroidal currents (> 50 kA) and current amplification ratios ($I_{tor}/I_{inj} \sim 3$) [41]. Toroidal currents persist for up to 0.64 ms after the injectors are turned off. Additionally, the measured n = 1 toroidal Fourier mode of the poloidal magnetic field decreases at higher current amplification ratios indicating more direct drive of the toroidal current.

6.4 Toroidal current and current amplification

The primary goal of HIT-SI operations is to drive toroidal current in the confinement volume. Without a central solenoid coil there is no direct means for driving this current and the current drive occurs through dynamo action. Figure 6.4 shows the toroidal current for a deuterium shot that reaches 50 kA. In addition to higher achieved toroidal current, a new feature of the toroidal current growth is the steady growth of the current through multiple injector cycles after the initial formation of current. Between 0.9 and 1.5 ms of the shot shown in Fig. 6.4 the toroidal current increases from ∼20 to ∼50 kA. This indicates that the toroidal current is being steadily built up by the injector drive.

Toroidal current amplification is the ratio of toroidal current to injector current. Surface probes measure the poloidal magnetic field at 18 locations around each of four poloidal cross sections located at toroidal angles of 0°, 45°, 180° and 225° [46]. Using the surface probes and the assumption of zero magnetic field at the corners in the poloidal cross section (two poloidal cross sections are shown in Fig. 3.1), Amperian loops are constructed to measure the toroidal current (the simply-connected confinement volume precludes the use of an external Rogowski coil for this measurement). The toroidal current reported in this paper is the average toroidal current from these four locations. Both injector currents are measured with Rogowski coils. Current

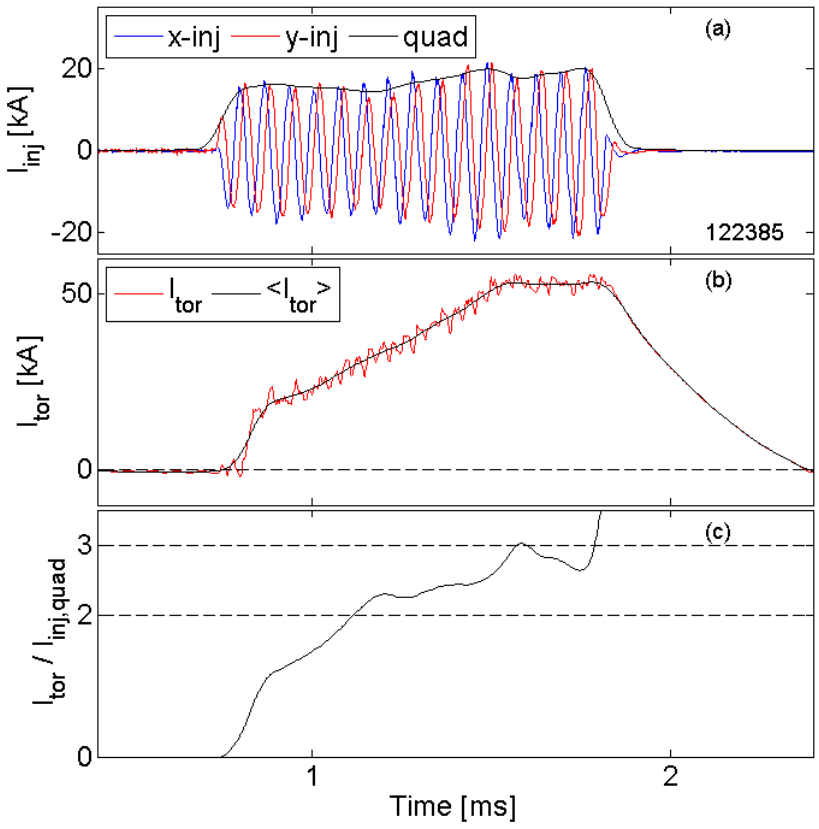

Figure 6.4: a) X- and Y-injector currents with the quadrature current; b) toroidal current and current time-averaged over and injector cycle; c) current amplification of the time-averaged signals [41].

amplification is calculated on HIT-SI by dividing the toroidal current time averaged over an injector cycle by the injector currents added in quadrature (the square root of the sum of the squares of the two signals). The signals are smoothed over an injector cycle to eliminate spurious amplifications that are the result of rapid changes in either toroidal or injector currents. Part c) of Fig. 6.4 shows current amplification greater than 2 achieved from 1.1 ms until the injectors are shut off at 1.8 ms with peak amplification during injector drive of 3.

Figure 6.5 shows toroidal current persistence of 0.64 ms from the time of peak

toroidal current. The toroidal current persistence for this shot is especially long be-

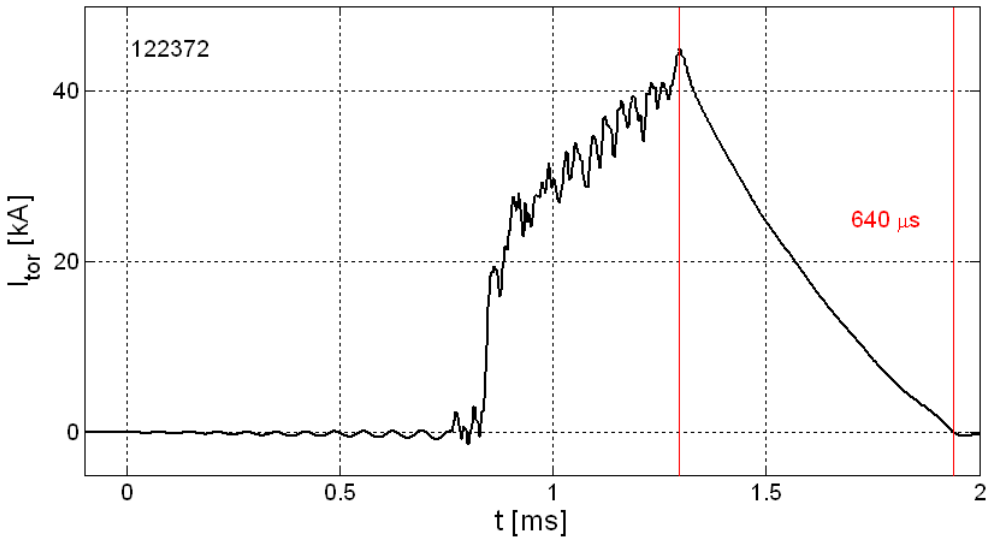

Figure 6.5: Deuterium shots have achieved a toroidal current decay time of up to 0.64 ms.

cause the injectors are turned off while the toroidal current is still increasing compared to the shot shown in Fig. 6.4 where the injectors are turned off after the toroidal current has plateaued. Deuterium shots typically use a shot length of about 2 ms. Longer shots with deuterium show decreases in the toroidal current after about 2 ms. It is suspected that the build up of density in the confinement volume causes the roll off in toroidal current, but this is still under investigation.

6.5 n = 1 mode analysis

In addition to the higher toroidal currents and current amplifications, deuterium operations also show different mode activity. Using toroidal Fourier mode analysis of the poloidal magnetic fields measured by the surface probes at 16 locations on both sides (z = +/- 3 cm) of the midplane diagnostic gap [46], the injector magnetic fields appear predominantly as an n = 1 mode. In addition to the injector n = 1 mode there are n = 1 eigenmodes of the confinement volume. The magnitude of the n = 1 Fourier mode measured by the surface probes increases before axisymmetric toroidal current is measured in the confinement volume (see Fig. 6.6). As the toroidal current increases the n = 1 mode decreases. The amplitude of the injected current is relatively constant during the shot.

At the beginning of the shot the n = 1 magnitude measured by the surface probes is much larger than the n = 1 magnitude predicted by the Taylor equilibrium calculation. At the end of the shot the measured n = 1 magnitude is in better agreement with the Taylor equilibrium. This implies the decrease in the measured n = 1 magnitude is the result of less energy in the n = 1 eigenmode of the confinement volume. It is proposed that as the toroidal current increases the injectors begin to transfer helicity directly to the toroidal current without driving the n = 1 eigenmode of the confinement volume. The inverse correlation of toroidal current with measured n = 1 Fourier mode for six deuterium shots is summarized in Fig. 6.7.

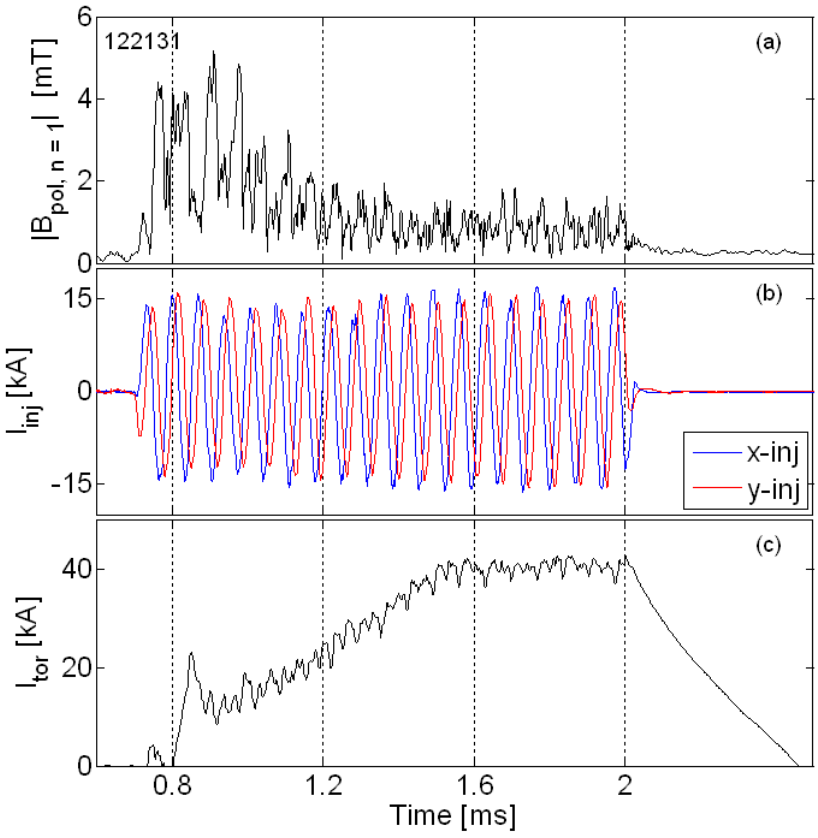

Figure 6.6: a) The magnitude of the n = 1 toroidal Fourier mode of the poloidal magnetic field, b) the injector currents and c) the toroidal current [41]. See Appendix C.3.6 for the location of the code used to make this figure.

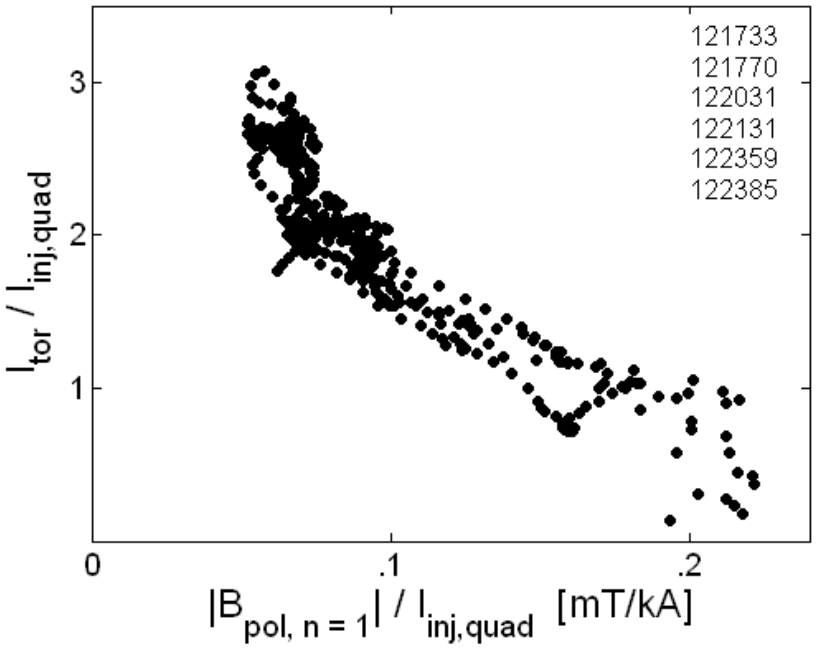

Figure 6.7: Scatter plot of the current amplification compared to the magnitude of the n = 1 toroidal mode of the poloidal magnetic field averaged over an injector cycle and normalized by the quadrature injector signal for six shots [41]. See Appendix C.3.7 for the location of the code used to make this figure.

6.6 Injector λ

With high wall pumping and a low fueling rate the first deuterium shot taken on HIT-SI after helium conditioning had low injector current and injector λ (see Fig. 6.8). This shot shows that a minimum injector λ is needed to form a spheromak in the confinement volume. As discussed in Section 2.1 injector λ is proportional to the ratio of injector current to injector flux, $\lambda = \mu_0 I_{inj}/\Psi_{inj}$. For a spheromak to form the injected λ needs to be greater than the λ of the confinement volume [28]. $\lambda = 10.3$ m^{-1} for the HIT-SI confinement volume. This property is illustrated nicely in the first deuterium shot. The effects of wall pumping were not known at this time so this shot had an initial $\lambda < 10.3$ m^{-1}. Despite high levels of helicity injection, toroidal current does not form on this shot until λ increases above 10.3 m^{-1}, Fig. 6.8.

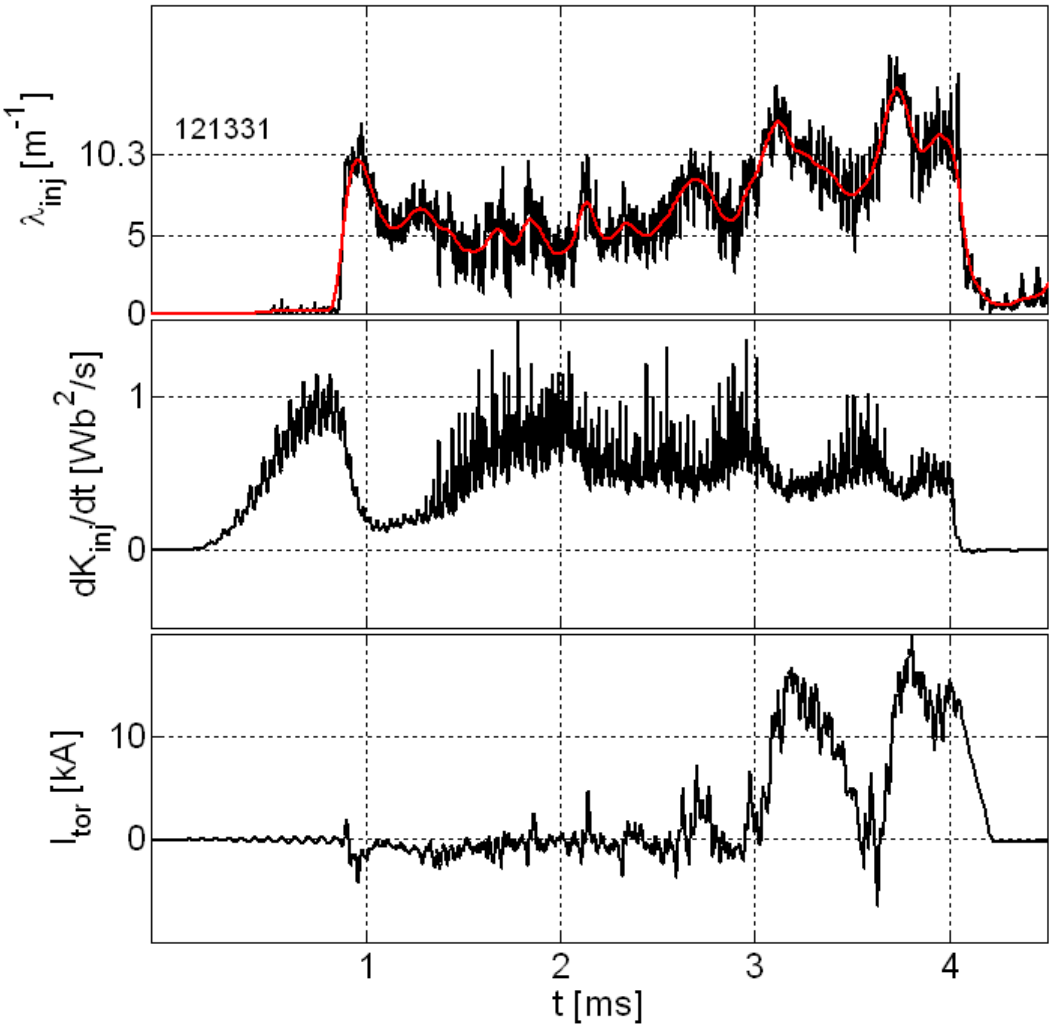

Figure 6.8: Injector λ, helicity injection rate ($\dot{K}_{inj}$) and toroidal current. See Appendix C.3.4 for the location of the code used to make this figure.

6.7 Comparison to H_α

Density measurements on HIT-SI are characterized by large oscillations, $\delta n/n$, of order unity. Other than the correlation to the injector frequency, the source of these density oscillations is not well known. To investigate the source of the density oscillations bandpass filter diagnostics are set up on chords neighboring the FIR chord (upper chord 7). H_α is measured along upper chord 8 and He I is measured along upper chord 6 (Fig. 6.9) The location of the chords along the midplane of the confinement volume is shown in Fig. 5.25.

H_α measures a large increase in radiation slightly before the initial density spike. As the shot progresses oscillations in H_α radiation and electron density track well. The beginning of the gradual rise in the density at the end of the shot coincides with a large increase in the He I radiation. The beginning of the toroidal current ramp up also occurs near the large increase in He I radiation. A larger data set needs to be considered before conclusions about the source of the density oscillations can be made from these data.

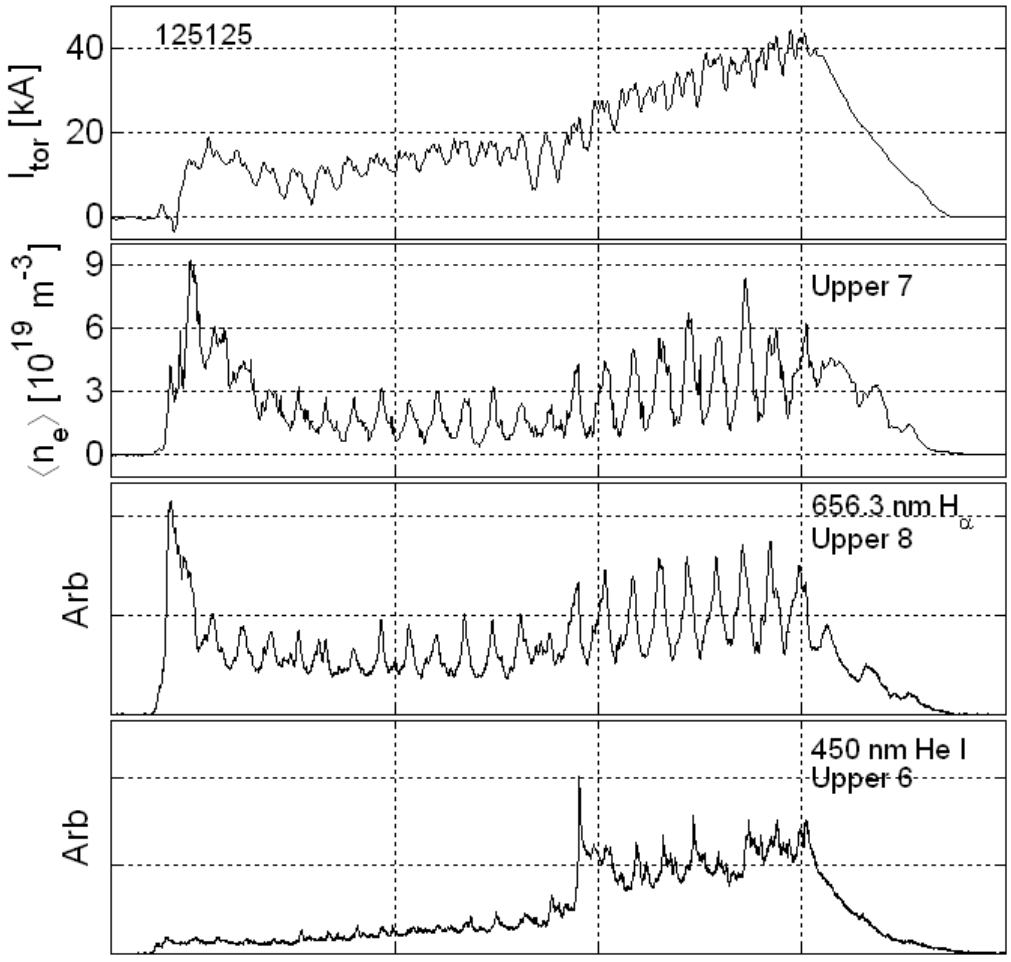

Figure 6.9: Toroidal current, line-averaged density along upper chord 7, H_α line-radiation along chord 8 and He I line-radiation along chord 6 for a deuterium shot. See Appendix C.2.2 for the location of the code used to make this figure.

6.8 Discussion

The success of deuterium operations is the result of improved density control. Helium operations condition the alumina walls, which then act to pump deuterium. Thus density control is achieved because the walls pump deuterium. Wall pumping is capable of controlling the density for a limited number of shots (typically two) before the walls need to be reconditioned with helium operations (Fig. 6.1). Improved density control has produced the first HIT-SI plasmas with $j/n \geq 10^{-14}$ A·m (Fig. 6.3). This corroborates past results on spheromaks and RFPs [42] that saw radiation dominated plasmas when $j/n \leq 10^{-14}$ A·m.

Deuterium operations have produced the best performing shots on HIT-SI, achieving over 50 kA of toroidal current and current amplifications (I_{tor}/I_{inj}) of 3 (Fig. 6.4). These high performance shots have also achieved current decay times of up 0.64 ms (Fig. 6.5). In addition, these shots are characterized by an initially large n = 1 mode that decreases as the current amplification increases (Figs. 6.6 and 6.7). This decrease in n = 1 activity indicates that the injectors are no longer coupling to an n = 1 eigenmode in the confinement volume, but rather are coupling directly to the spheromak eigenmode. Thus the injector perturbations are less disrupting as the equilibrium grows.

The importance of the injector λ has also been reinforced from deuterium operations. With an injector $\lambda < 10.3$ m^{-1} toroidal current does not form in the confinement volume despite high helicity injection rates (Fig. 6.8). H_α radiation measured on a chord near the interferometer chord shows oscillations in radiation that correlate with oscillations in the electron density (Fig. 6.9). While more data is needed to verify this result over a larger number of shots, this measurement indicates that the density oscillations are the result of the ionization and recombination of the majority gas species.

Chapter 7

INTERNAL MAGNETIC FIELD PROFILES

The internal magnetic probe has provided important insights into the performance of HIT-SI. Initial comparisons of the internal probe signals to the Taylor-state equilibrium helped to validate the Taylor model in HIT-SI [28]. More recent results from internal probe measurements of high performance deuterium shots show that the field is suppressed relative to the Taylor equilibrium indicating that the plasma can no longer be described by a zero pressure, constant λ, equilibrium. To better understand the new magnetic field configuration a Grad-Shafranov solver [47] is used to fit the probe signals to an equilibrium with non-constant λ and plasma pressure. After the injectors have turned off, called the decay phase of the shot, Taylor equilibria are a subset of Grad-Shafranov equilibria with constant λ and zero pressure. During the decay phase Grad-Shafranov equilibria indicate plasma pressure and the transition from a hollow to a peaked λ profile as the toroidal current decays. The transition from a hollow to a peaked current profile on a spheromak was first seen by Knox et al. on the Compact Toroid Experiment (CTX) [48]. In addition the internal current density and λ profile are explored using calculations from the three-stem probe. Qualitative agreement of the λ profile during the decay phase of the shot is seen between the Grad-Shafranov equilibrium and the calculation of $\nabla \times \vec{B}$ using the three internal probe stems.

This chapter describes comparisons between the measured internal magnetic fields and equilibrium reconstructions of the magnetic field. The calculation of current densities from the internal probe signals is described and the results of these calculations are given.

7.1 Comparison to Taylor-state equilibrium

Section 3.3 describes the calculation of the Taylor-state equilibrium in HIT-SI. Using the toroidal current measured by the surface probes along with the X- and Y-injector currents, the magnetic fields based upon the Taylor equilibrium can be calculated at all locations in HIT-SI [28]. These predicted fields from the Taylor equilibrium are then compared to the experimentally measured magnetic fields without the use of a fitting parameter. Past results on HIT-SI [28] and present low current amplification shots (Figs. 7.1, 7.2 and 7.3) show good agreement between the internal magnetic fields and the Taylor equilibrium for plasma dynamics at and below the injector frequency of 14.5 kHz. Since the Taylor equilibrium is calculated from the toroidal and injector currents any frequency content not seen in those current measurements will not be seen in the reconstructed Taylor equilibrium. Magnetic fields measured interior to the plasma have higher frequency content than the toroidal or injector currents. This is especially evident at the beginning of the shot when a large n = 1 mode is present (see Figs. 6.6 and 6.7 showing the n = 1 content).

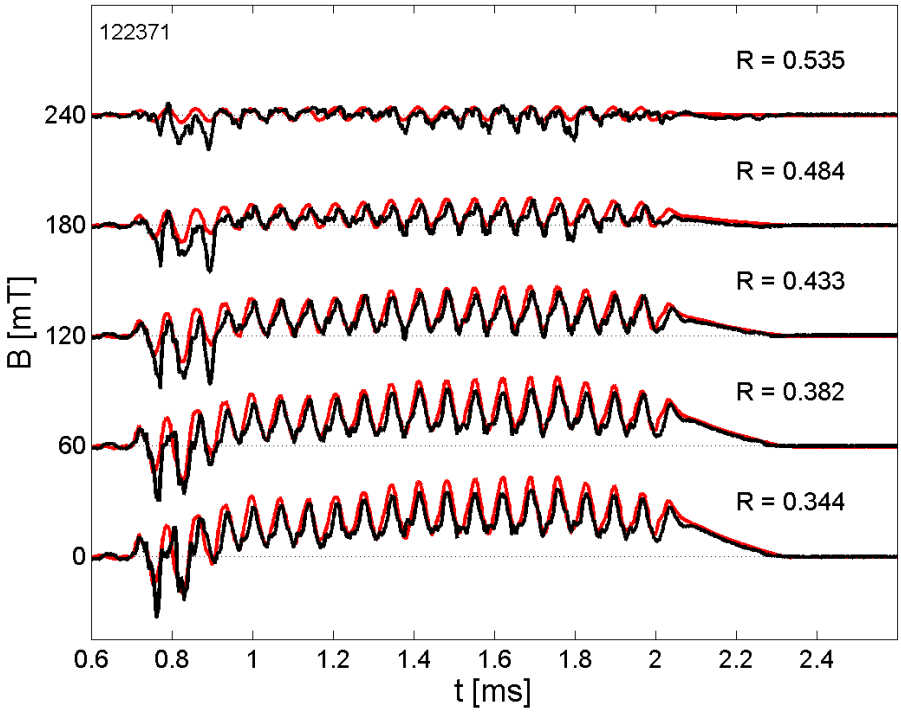

Figure 7.1: Comparison of the internal toroidal magnetic probe signals (black) to the fields predicted by the Taylor equilibrium reconstruction (red) at five locations for a helium shot with peak current amplification reaching 1.4. The bottom trace is near the magnetic axis and the top trace is near the wall with the zero value of each successive probe shifted up by 60 mT [45]. See Appendix C.1.5 for the location of the code used to make these figures.

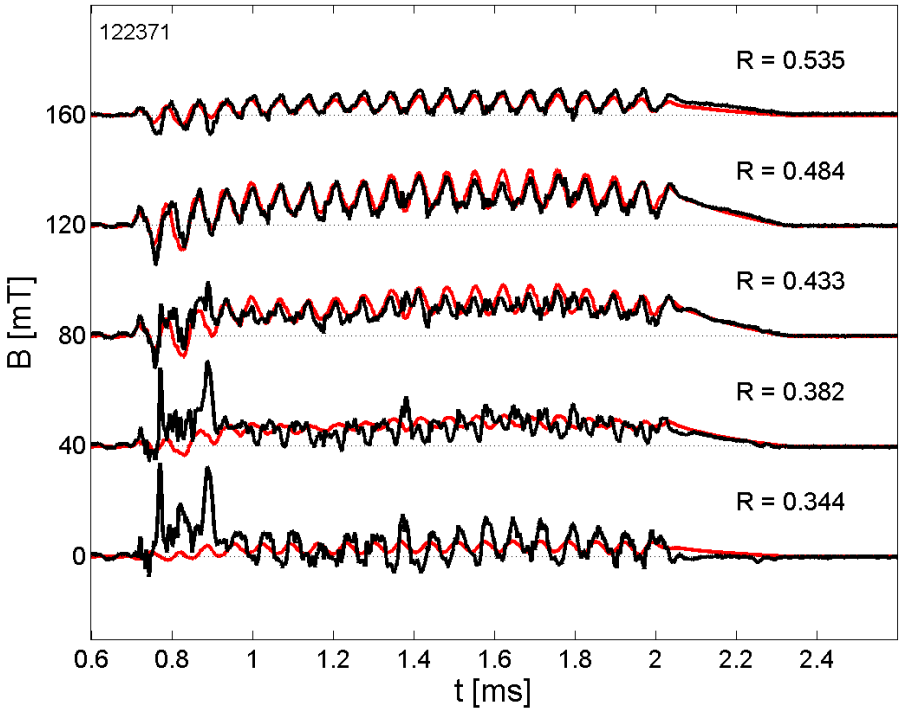

Figure 7.2: Comparison of the internal poloidal magnetic probe signals (black) to the fields predicted by the Taylor equilibrium reconstruction (red) at five locations for a helium shot with peak current amplification reaching 1.4. The bottom trace is near the magnetic axis and the top trace is near the wall with the zero value of each successive probe shifted up by 40 mT [45]. See Appendix C.1.5 for the location of the code used to make these figures.

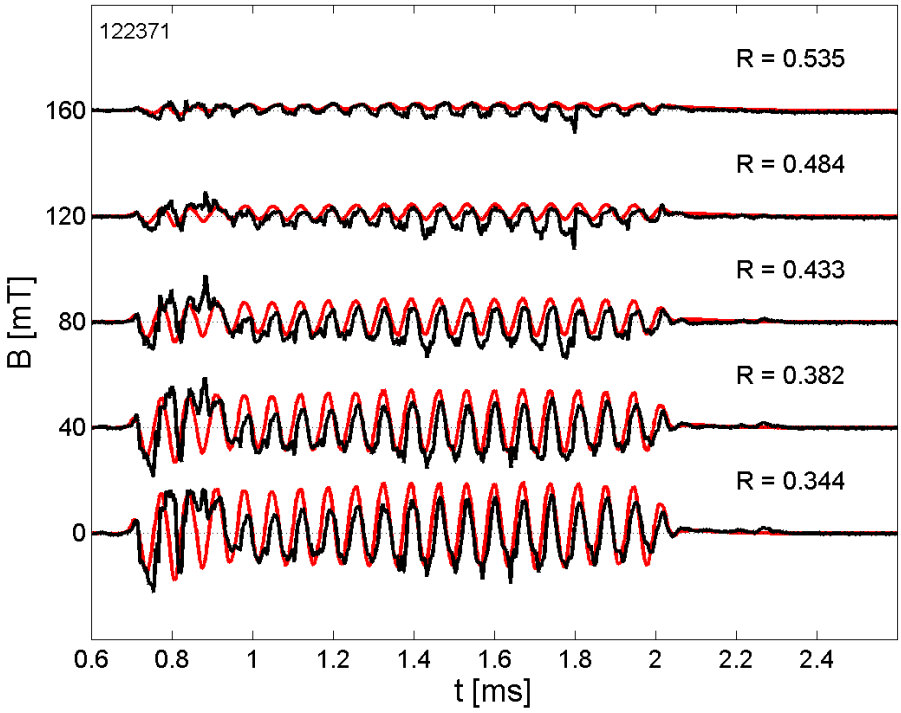

Figure 7.3: Comparison of the internal radial magnetic probe signals (black) to the fields predicted by the Taylor equilibrium reconstruction (red) at five locations for a helium shot with peak current amplification reaching 1.4. The bottom trace is near the magnetic axis and the top trace is near the wall with the zero value of each successive probe shifted up by 40 mT. See Appendix C.1.5 for the location of the code used to make these figures.

Figures 7.4, 7.5 and 7.6 show the same comparison between the Taylor equilibrium and the fields measured by the internal probe for a high performance deuterium shot. There are two differences that are readily apparent on the deuterium shots: the DC

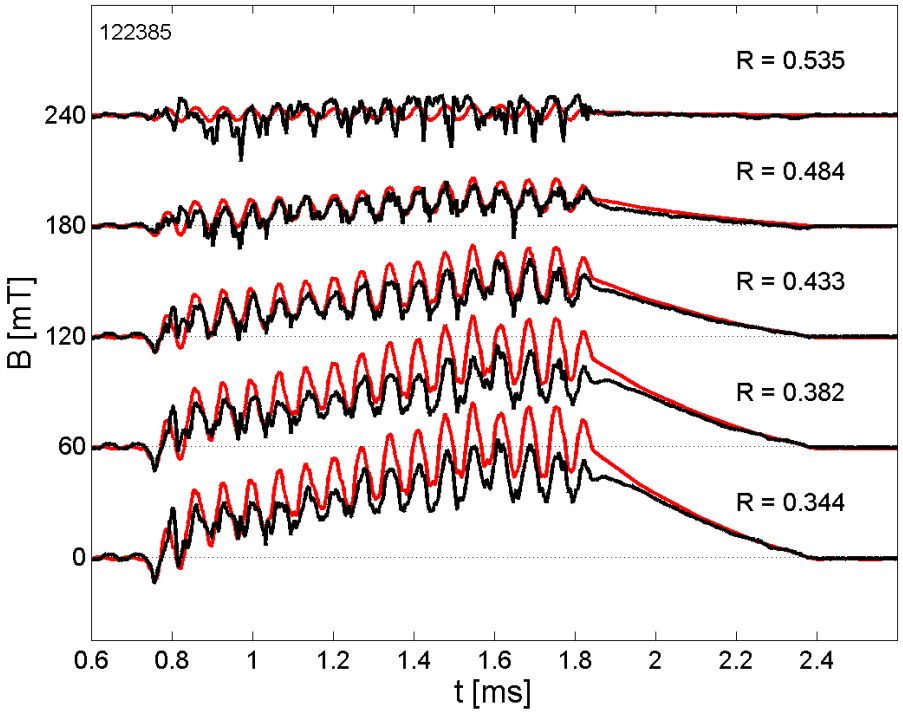

Figure 7.4: Comparison of the internal toroidal magnetic probe signals (black) to the fields predicted by the Taylor equilibrium reconstruction (red) at five locations for a deuterium shot with the current amplification reaching 3 at 1.6 ms. The bottom trace is near the magnetic axis and the top trace is near the wall with the zero value of each successive probe shifted up by 60 mT [45]. See Appendix C.1.5 for the location of the code used to make these figures.

level of the magnetic field is suppressed relative to Taylor (see the innermost toroidal signals and the poloidal signals between 38 and 49 cm) and the magnetic fields have higher frequency content (see the outermost toroidal signal and the innermost poloidal signal).

The DC field measured by the probes is suppressed compared to the field predicted

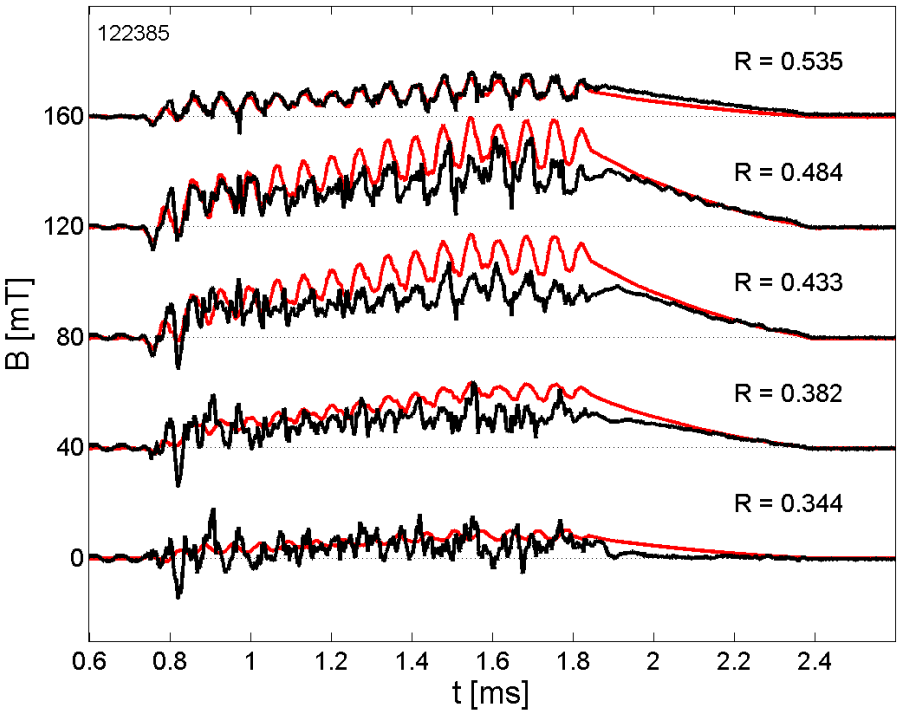

Figure 7.5: Comparison of the internal poloidal magnetic probe signals (black) to the fields predicted by the Taylor equilibrium reconstruction (red) at five locations for a deuterium shot with the current amplification reaching 3 at 1.6 ms. The bottom trace is near the magnetic axis and the top trace is near the wall with the zero value of each successive probe shifted up by 40 mT [45]. See Appendix C.1.5 for the location of the code used to make these figures.

by the Taylor equilibrium. This difference indicates that the zero pressure, constant λ, Taylor equilibrium is no longer a valid model for predicting the internal DC fields. To accurately model the internal magnetic fields a pressure gradient or hollow λ profile is needed. A hollow λ profile has $\lambda > 10.3$ m^{-1} near the edge of the plasma and $\lambda < 10.3$ m^{-1} near the magnetic axis with the overall average of λ in the confinement volume of 10.3 m^{-1}. Internal density or temperature profiles are needed to confirm if a pressure gradient is present. Either scenario is an indication that a region of plasma separate from the injector flux exists. A pressure gradient would indicate particle

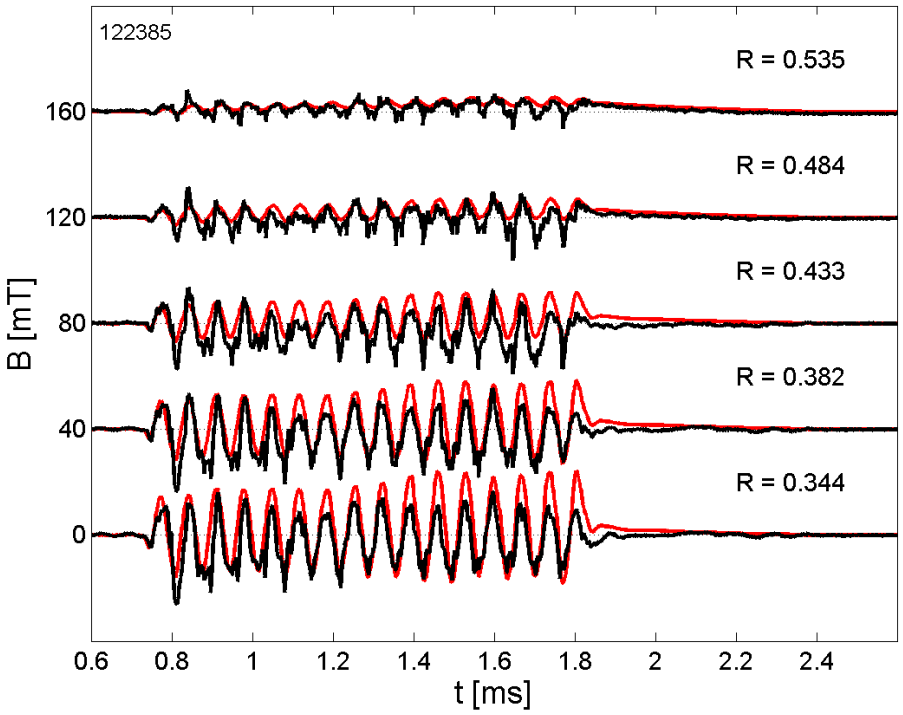

Figure 7.6: Comparison of the internal radial magnetic probe signals (black) to the fields predicted by the Taylor equilibrium reconstruction (red) at five locations for a deuterium shot with the current amplification reaching 3 at 1.6 ms. The bottom trace is near the magnetic axis and the top trace is near the wall with the zero value of each successive probe shifted up by 40 mT. See Appendix C.1.5 for the location of the code used to make these figures.

confinement, which needs closed flux surfaces to maintain the particle pressure. A hollow λ profile would indicate the injectors are driving a region of high λ near the edge of the confinement volume and sustaining a region of plasma with lower λ near the magnetic axis.

7.2 Comparison to Grad-Shafranov equilibrium

Equilibrium calculations are valid during the decay phase when the plasma is axisymmetric according to the toroidal current calculations made by the surface probes.

The HIT-SI Grad-Shafranov solver is developed and maintained by C. J. Hansen. 2-D equilibria with pressure and variable λ profiles are obtained through solutions of the Grad-Shafranov equation [49] using all 16 of the internal toroidal probes and all 17 of the poloidal probes, the toroidal current, and the poloidal surface probes as fitting parameters. Fig. 7.7 shows that the Grad-Shafranov solution matches the internal magnetic signals better—with an error in the total toroidal current of less than 1%—than the constant λ, zero pressure Taylor equilibrium during the decay of a high performance deuterium shot.

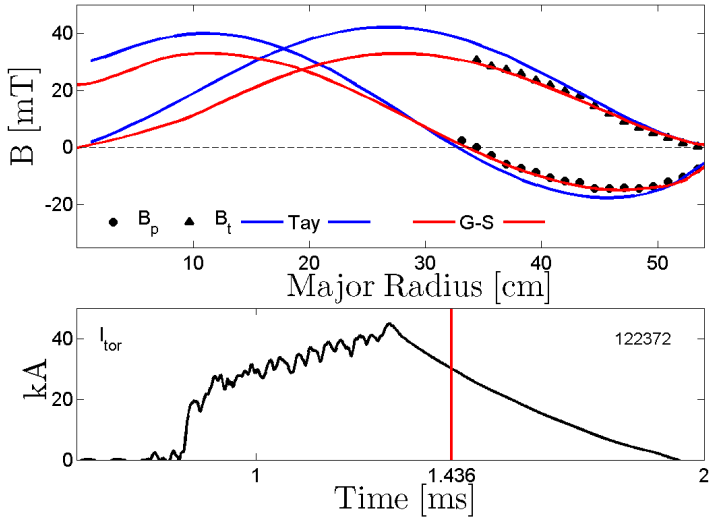

Figure 7.7: Comparison between the internal magnetic signals, the Taylor equilibrium based upon the toroidal current, and the Grad-Shafranov equilibrium. See Appendix C.4 for the location of the code used to make this figure.

The Grad-Shafranov equation can be written as [10]

$$\Delta^* \psi = -\mu_0 R^2 p' - FF' \tag{7.1}$$

where ψ is the flux function, R is the major radius, p is the plasma pressure, $F = RB_\phi$

and $'$ denoting derivatives with respect to ψ. B_ϕ is the toroidal magnetic field. The Grad-Shafranov equilibrium is found by minimizing the error in the toroidal current and magnetic probe signals. The chi-squared error of the user defined p' and FF' profiles is minimized through an automated routine to fit the data. p' and FF' are piecewise linear and tanh functions. The user profiles are determined through multiple iterations of the code and by selecting profiles that improve upon the accuracy of previous iterations of the solver until a satisfactory solution is found. Figure 7.8 shows the profiles for p' at four times during the decay of shot 122372. Figure 7.9 shows the profiles for FF' at four times during the decay of shot 122372.

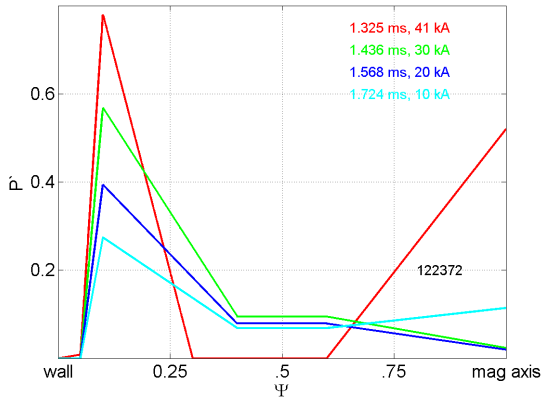

Figure 7.8: p' profiles at four times during the decay of shot 122372.

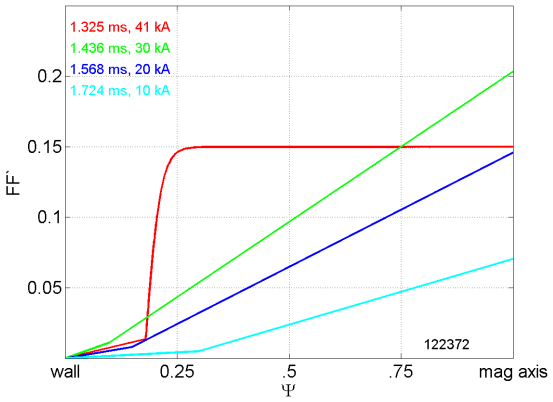

Figure 7.9: FF' profiles at four times during the decay of shot 122372.

Once the equilibrium has been found by fitting to the probe signals other information about the plasma is available. Fig. 7.10 compares the flux surfaces for the Taylor equilibrium and the Grad-Shafranov equilibrium at the time shown in Fig. 7.7. The flux surfaces for the Grad-Shafranov solution are elongated and shifted toward

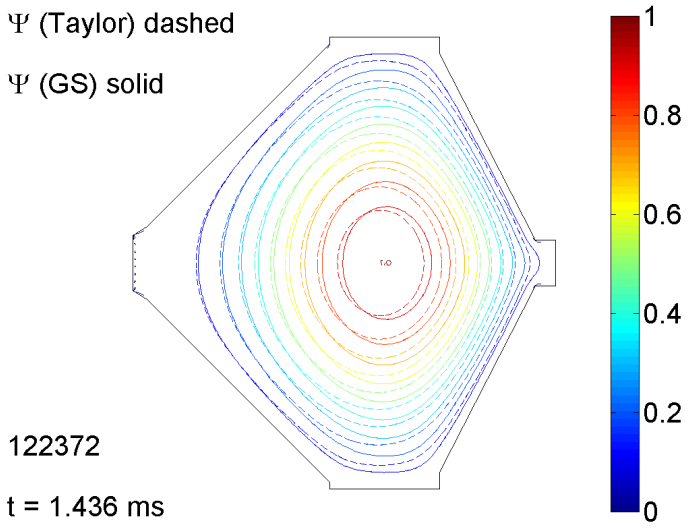

Figure 7.10: Comparison of the flux surfaces for the Taylor and Grad-Shafranov equilibria. See Appendix C.4 for the location of the code used to make this figure.

the wall of the confinement volume. This is an example of a Shafranov shift [49] where the flux surfaces are shifted outward due to plasma pressure effects. A hollow profile with an outward shift is an example of an equilibrium with pressure. Without pressure a hollow profile would be shifted inward [50].

Figure 7.11 shows the λ profile at four times during the decay phase of shot 122372. Initially, soon after the injectors are turned off, the λ profile shows regions of high λ near the geometric axis ($R = 0$ cm) and the outer wall of the confinement volume ($R = 55$ cm), which is indicative of a hollow λ profile. As the toroidal current decays the λ profile flattens and then becomes peaked near the end of the shot. This occurs

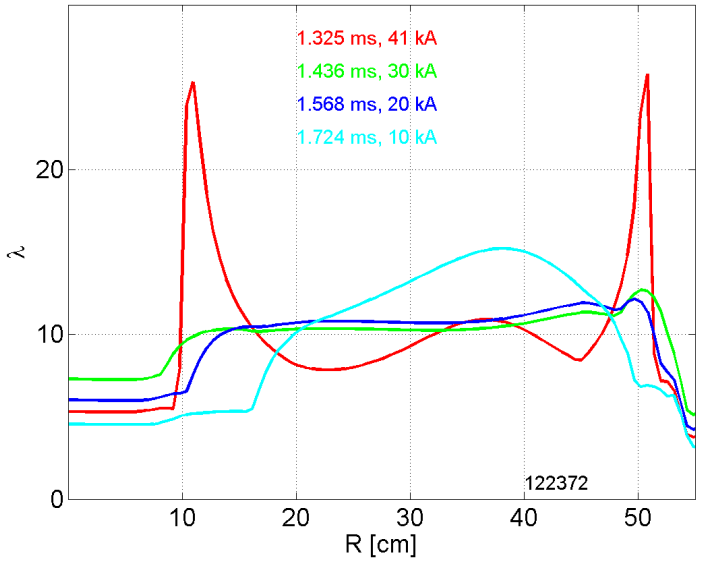

Figure 7.11: λ plotted as a function of major radius at four times during the decay phase of shot 122372. See Appendix C.4 for the location of the code used to make this figure.

because the edge of the plasma is more resistive than the core of the plasma. In the edge region the poloidal current dominates and in the core the toroidal current dominates. Thus resistive decay effects the poloidal currents more than the toroidal currents. Near the magnetic axis $\lambda \sim j_{tor}/B_{tor}$ and since B_{tor} is sustained by the poloidal current λ near the magnetic axis increases.

β is also calculated from the Grad-Shafranov equilibria. The volume averaged β at the four times shown in Fig. 7.11 are shown in Table 7.1.

Table 7.1: β at four times during the decay of shot 122372

Time [ms]	β [%]
1.325	25
1.436	38
1.568	41
1.724	72

These β values are higher than the Mercier β limits calculated in Reference [15]. The Maryland spheromak also reported results with high β [51]. The reason for these high β results on HIT-SI and the Maryland spheromak is because of the slow growth rate of pressure driven modes compared to the plasma lifetime in cold spheromaks [50].

7.3 Current density and λ

The purpose of having a magnetic probe with three stems is to use the offset magnetic measurements to calculate current density and λ. However, the measurement accuracy needed to make this calculation is difficult to achieve. The current density is calculated by taking the difference between adjacent probe signals so small errors in the position or calibration of a given probe can adversely affect the accuracy of the calculation. Another complicating issue is the lack of enough digitizers for the all of the signals on each of the probe stems. Also three different types of digitizers are used to collect the data from the internal probe. Each type of digitizer has a slightly different zero time (on the order of 5 μs), which needs to be corrected (see Appendix B.3). When taking the difference between two signals, this large of a time difference can destroy the accuracy of the calculation.

This section gives a description of the calculation and the resulting current density and λ. A comparison of the calculated results to the current density and λ profiles from a Grad-Shafranov equilibrium is made in the second subsection in an attempt to quantify the accuracy of the calculation.

7.3.1 Current density calculation

The current density is calculated using Ampere's law in the differential form.

$$\vec{j} = \frac{1}{\mu_0} \nabla \times \vec{B} \tag{7.2}$$

In the coordinate system used on HIT-SI, the positive radial direction is defined out of the machine. The positive Z-direction is defined as pointing from the X-side of the machine to the Y-side. The positive toroidal direction is defined using the right-hand rule with your thumb pointing in the positive Z-direction along the geometric axis (see Fig. 5.6). The positive poloidal direction is defined using the right-hand rule with your thumb in the positive toroidal direction.

The distances between probes are small in relation to the size of the machine so a Cartesian coordinate system can be used. For the location of the probe, a right-handed coordinate system can be constructed with the direction $\hat{i}$ in the direction of positive radial field, $\hat{j}$ in the direction of positive poloidal field, and $\hat{k}$ in the direction of positive toroidal field. It should also be noted that B_z is sometimes used instead of the poloidal field. For the location of the probe B_z = -B_p. Using this notation $\nabla \times \vec{B}$ can be written as

$$\nabla \times \vec{B} = \left(\frac{\partial B_t}{\partial j} - \frac{\partial B_p}{\partial k}\right)\hat{i} + \left(\frac{\partial B_r}{\partial k} - \frac{\partial B_t}{\partial i}\right)\hat{j} + \left(\frac{\partial B_p}{\partial i} - \frac{\partial B_r}{\partial j}\right)\hat{k} \tag{7.3}$$

The discrete nature of the probes leads to taking numerical derivatives where in general

$$\frac{\partial B}{\partial x} \approx \frac{\Delta B}{\Delta x} \tag{7.4}$$

In the radial direction a first order approximation is used to calculate toroidal and poloidal derivatives for the first and last digitized probe signals (see Appendix B.4).

$$\frac{\partial B}{\partial i} \approx \frac{B^{n+1} - B^n}{\Delta i} \tag{7.5}$$

where Δi is the radial distance between probes, 0.5 inches or 0.0127 m when consecutive probes are digitized, and n is the probe number. A second order derivative is used for the remaining radial locations

$$\frac{\partial B}{\partial i} \approx \frac{B^{n+1} - B^{n-1}}{2\Delta i} \tag{7.6}$$

In the poloidal direction, calculating the derivative from the middle array can be done with the second probe from either the top or middle array (see Appendix B.5)

$$\frac{\partial B}{\partial j} \approx \frac{B^n_{t,b} - B^n_m}{\Delta j} \tag{7.7}$$

where Δj is the distance in the poloidal, $\hat{j}$, direction between the arrays, 0.875 inches or 0.0222 m. The subscripts t, b, and m refer to the the top, bottom, and middle arrays respectively. For the data presented here the poloidal derivates are calculated as

$$\frac{\partial B}{\partial j} \approx \frac{B_t^n + B_b^n - 2B_m^n}{2\Delta j} \tag{7.8}$$

In the toroidal direction, there are three ways of calculating the derivative: using the top array and the middle array, using the middle array and the bottom array, and using the top and bottom arrays (see Appendix B.6).

$$\frac{\partial B}{\partial k} \approx \frac{B_m^n - B_t^n}{\Delta k} \tag{7.9}$$

$$\frac{\partial B}{\partial k} \approx \frac{B_b^n - B_m^n}{\Delta k} \tag{7.10}$$

$$\frac{\partial B}{\partial k} \approx \frac{B_b^n - B_t^n}{2\Delta k} \tag{7.11}$$

where Δk is the distance in the toroidal, $\hat{k}$, direction between the middle array and either of the other two arrays, 0.875 inches or 0.0222 m. The top and bottom arrays are located at the same z coordinate and are displaced a larger distance apart so they are used to calculate the toroidal derivatives here.

Putting this together at a given insertion depth and noting that $\Delta j = \Delta k$ gives the current density, $\vec{j}$, as (see Appendix B.8)

$$j_{rad}(n) = \frac{1}{2\mu_0}\left(\frac{B_t^{n,tor} + B_b^{n,tor} - 2B_m^{n,tor} - B_b^{n,pol} + B_t^{n,pol}}{\Delta k}\right) \tag{7.12}$$

$$j_{pol}(n) = \frac{1}{2\mu_0}\left(\frac{B_b^{n,rad} - B_t^{n,rad}}{\Delta k} - \frac{B_m^{n+1,tor} - B_m^{n-1,tor}}{\Delta i}\right) \tag{7.13}$$

$$j_{tor}(n) = \frac{1}{2\mu_0}\left(\frac{B_m^{n+1,pol} - B_m^{n-1,pol}}{\Delta i} - \frac{B_t^{n,rad} + B_b^{n,rad} - 2B_m^{n,rad}}{\Delta k}\right) \tag{7.14}$$

Fig. 7.12 shows the toroidal, poloidal and radial current densities at a major

radius of 34.4 cm for a deuterium shot that reaches 46 kA. For this shot the current

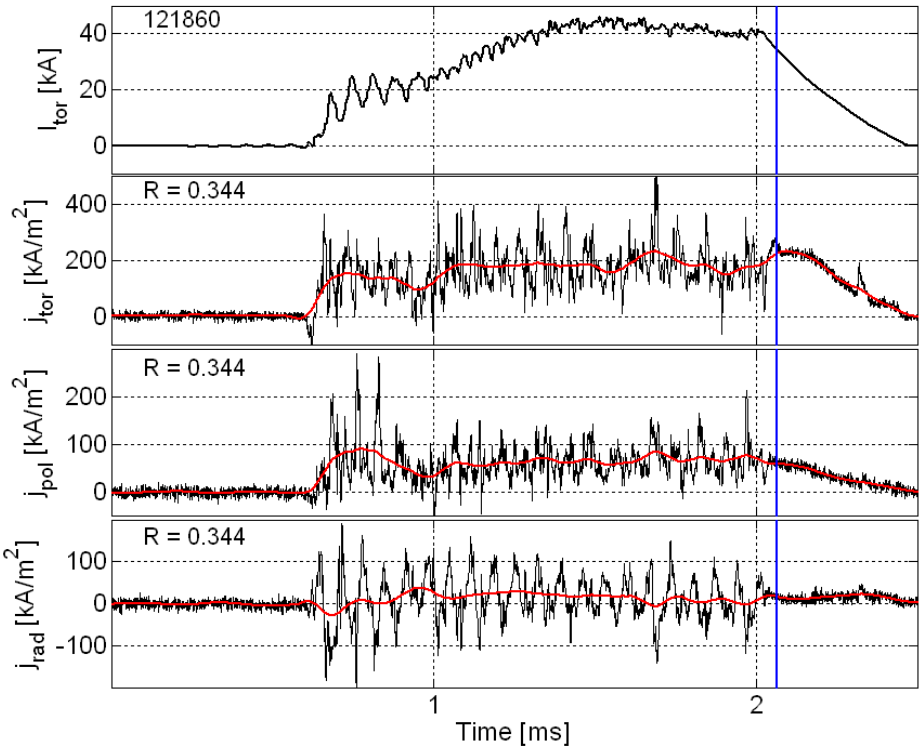

Figure 7.12: Toroidal current and current density calculated with the internal probe for shot 121860. The red traces are the current densities calculated after averaging the signals over an injector cycle. The blue line indicates a time point that will be studied in more detail later in this chapter. See Appendix C.1.6 for the location of the code used to make this figure.

density calculation is made with only signals digitized with Joerger Model TR1612 digitizers to avoid any issues with discrepancies in the time base between digitizers. All three directions of probes 2, 4, and 6 on all three stems along with probe 8 on the middle and bottom stem are used for the calculation. The black traces are made with the full-bandwidth data and show the variation of the current density over an injector cycle. The red traces are made with the probe signals averaged over an injector cycle. Interesting to note is the time between 1 and 1.5 ms when the toroidal

current increases from ∼25 to ∼45 kA. During this time period the average toroidal current density at the location shown does not increase. As $\lambda \sim j/B$ constant j with increasing B is consistent with the formation of a hollow λ profile.

With local values of $\vec{j}$ and $\vec{B}$ known, λ can be calculated.

$$\lambda = \frac{\mu_0 \vec{j} \cdot \vec{B}}{B^2} \tag{7.15}$$

Figure 7.13 shows λ as a function of time at three locations for the shot shown in Fig. 7.12. The high-frequency traces include the full-bandwidth data and the average

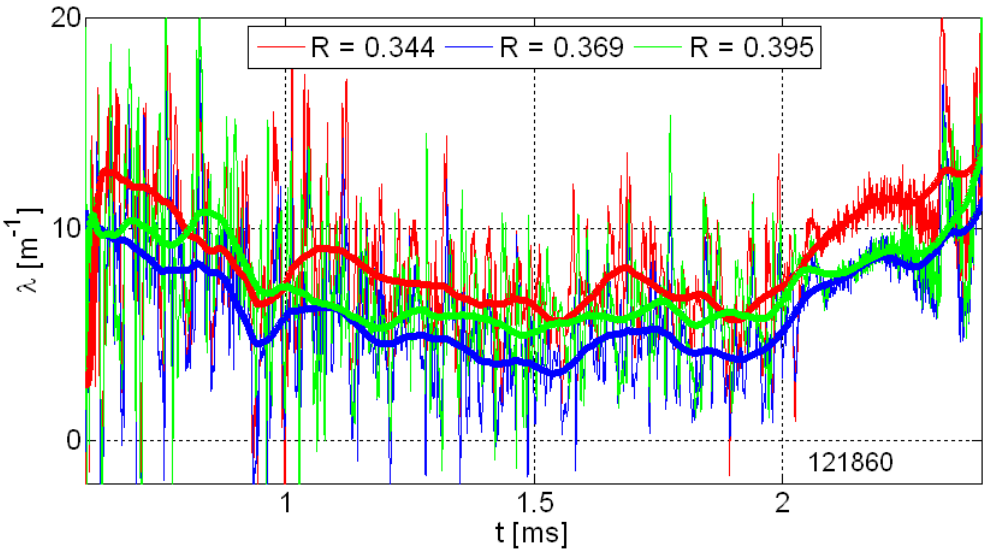

Figure 7.13: λ calculated with the internal probe signals at three locations. The smooth traces are the λ traces calculated after averaging the signals over an injector cycle. See Appendix C.1.6 for the location of the code used to make this figure.

values are made by making the calculation of λ and $\vec{j}$ with the magnetic fields averaged over an injector cycle.

While the calculated λ shows large oscillations, the general trend of the data is consistent with the interpretation of a hollow λ profile during the time when the

injectors are on and moving toward a peaked λ profile during the decay. After the initial toroidal current is formed $\lambda \sim 10$ m^{-1}. As the toroidal current increases (see Fig. 7.12) the calculated λ decreases to ~ 5 m^{-1}. When the injectors are turned off at 2 ms, λ increases until the plasma decays completely away. This would seem to corroborate the indications of a hollow λ profile from the depressed values of the DC magnetic field when compared to the Taylor equilibrium. However, lower λ values are also calculated on lower current amplification shots, Fig. 7.14. These lower

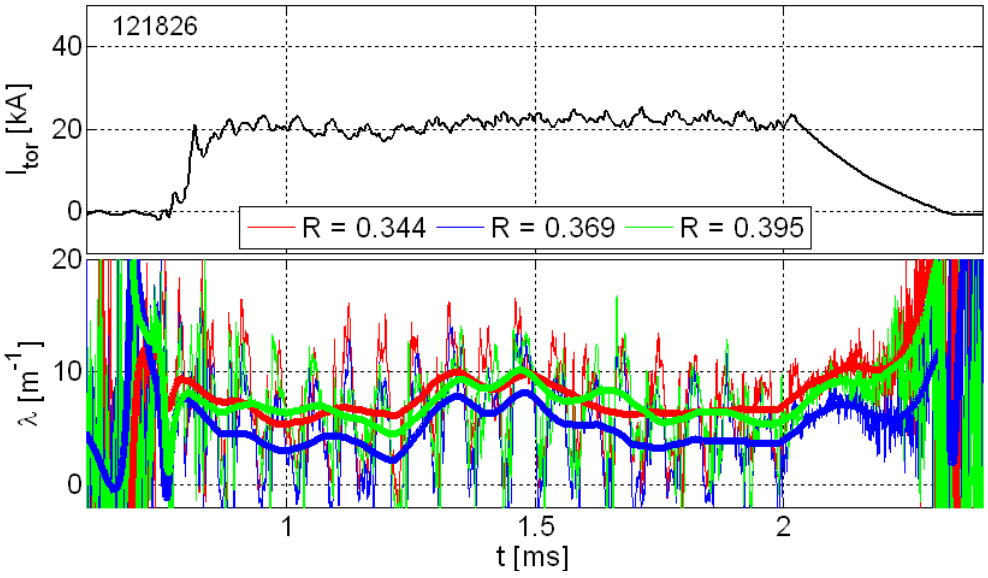

Figure 7.14: λ calculated with the internal probe signals at three locations for a helium shot. The smooth traces are the λ traces calculated after averaging the signals over an injector cycle. See Appendix C.1.6 for the location of the code used to make this figure.

current amplification shots match the predicted Taylor equilibrium with a constant $\lambda = 10.3$ m^{-1}, see Figs. 7.1, 7.2 and 7.3, so there is a disconnect in the predicted and calculated λ values here.

The most apparent difference in the λ traces between the low and high current amplification shots is in the high frequency content of the traces. For the low current amplification shot the majority of the frequency content is at the injector frequency,

14.5 kHz. The higher current amplification shot has higher frequency content. This is also apparent when comparing the current density traces for the two shots, Figs. 7.12 and 7.15. The toroidal current density in Fig. 7.15 oscillates at the injector frequency

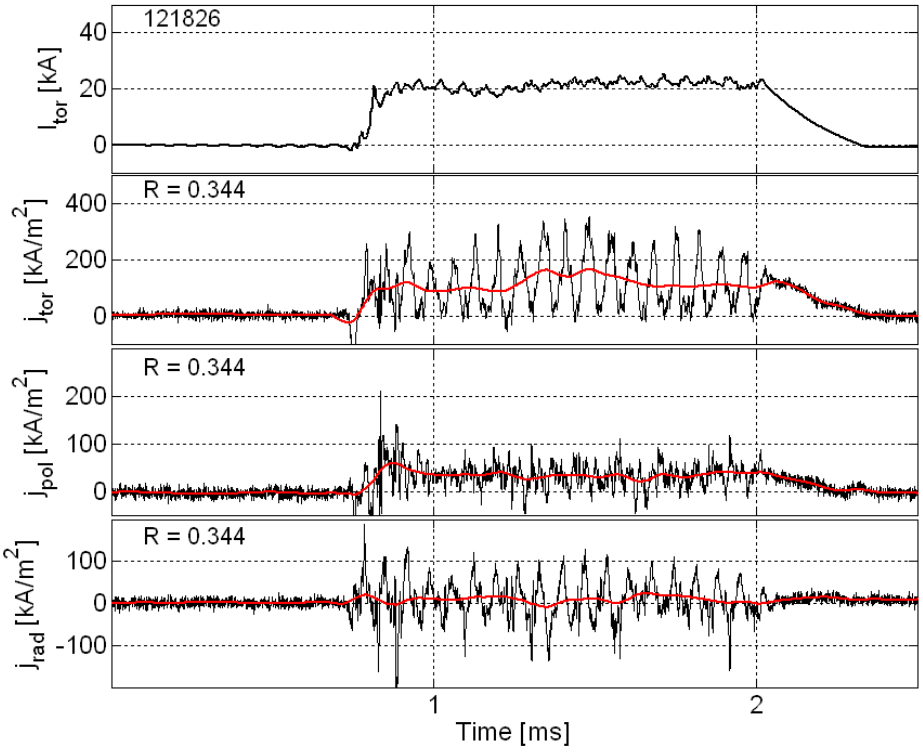

Figure 7.15: Toroidal current and current density calculated with the internal probe for shot a typical helium shot. The red traces are the current densities calculated after averaging the signals over an injector cycle. See Appendix C.1.6 for the location of the code used to make this figure.

and the minimum toroidal current density is ∼0 for each injector cycle. For the deuterium shot shown in Fig. 7.12 the current density oscillates at a higher frequency and the minimum toroidal current remains above 0 for the majority of the shot.

Partially retracting the internal probe provides λ measurements at larger major radii. This is used to test the effect seen in Fig. 7.11 where λ goes from a hollow to a peaked profile during the decay phase of the shot. Fig. 7.16 shows λ calculated at

an intermediate region between the magnetic axis and the wall of the confinement volume. During the decay phase of the shot λ remains relatively constant for the

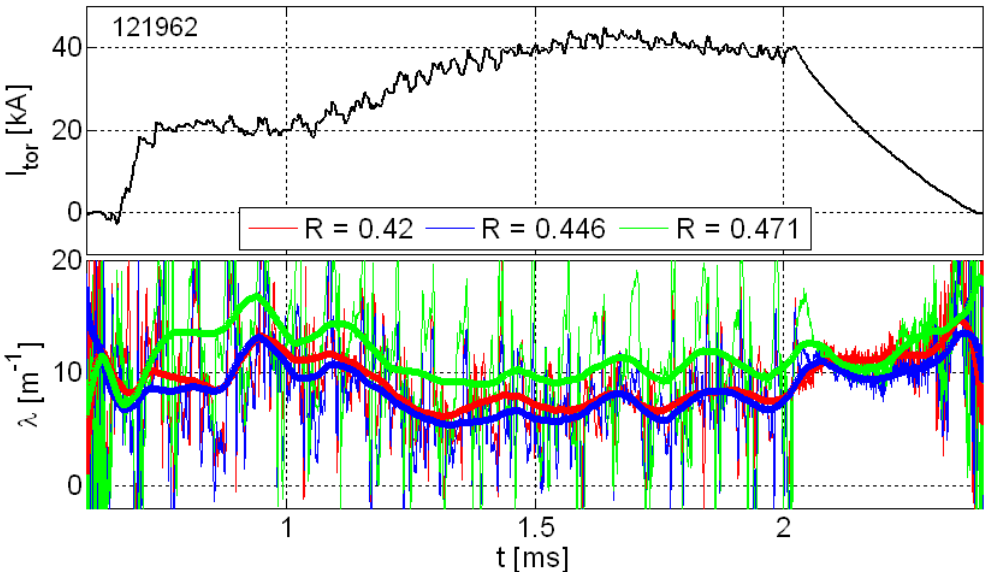

Figure 7.16: λ calculated with the internal probe signals at three locations. The smooth traces are the λ traces calculated after averaging the signals over an injector cycle. See Appendix C.1.6 for the location of the code used to make this figure.

first $\sim$250 μs after the injectors are turned off. Fig. 7.17 shows λ calculated near the wall of the confinement volume. During the first $\sim$250 μs of the decay phase λ decreases. Figs. 7.13, 7.16 and 7.17 provide a consistent view which agrees with Fig. 7.11. Initially during the decay phase the value of λ is high near the edge and low near the magnetic axis. As the toroidal current decays λ increases near the magnetic axis and decreases near the wall.

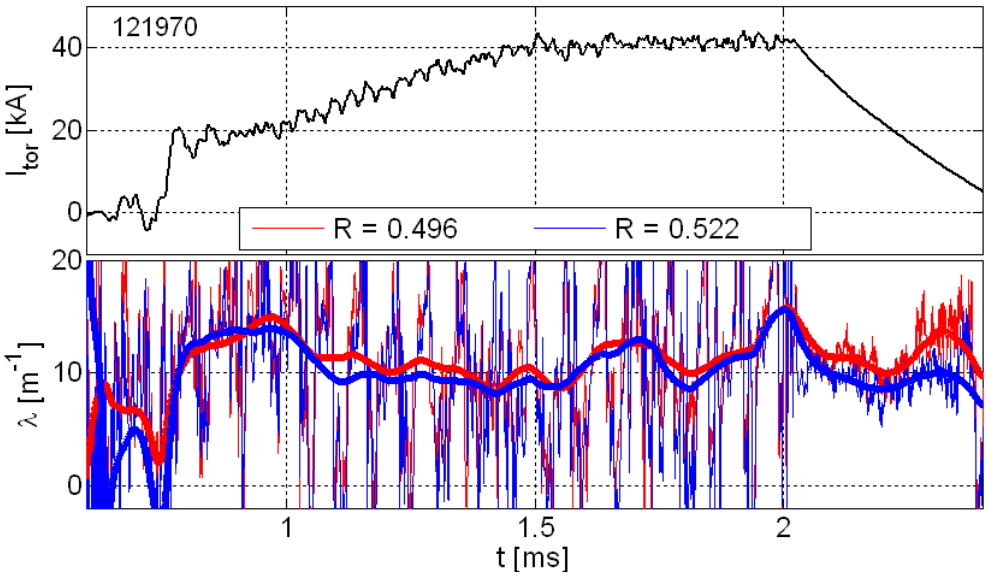

Figure 7.17: λ calculated with the internal probe signals at two locations. The smooth traces are the λ traces calculated after averaging the signals over an injector cycle. See Appendix C.1.6 for the location of the code used to make this figure.

7.3.2 Comparison of current density calculation to current density from the Grad-Shafranov equilibrium

A similar computation of the Grad-Shafranov equilibrium as in Section 7.2 is done on a shot when signals from all three probe stems are digitized. Fig. 7.18 shows the Grad-Shafranov equilibrium, the Taylor equilibrium and the poloidal and toroidal probe signals from the main stem plotted during the decay phase of the shot.

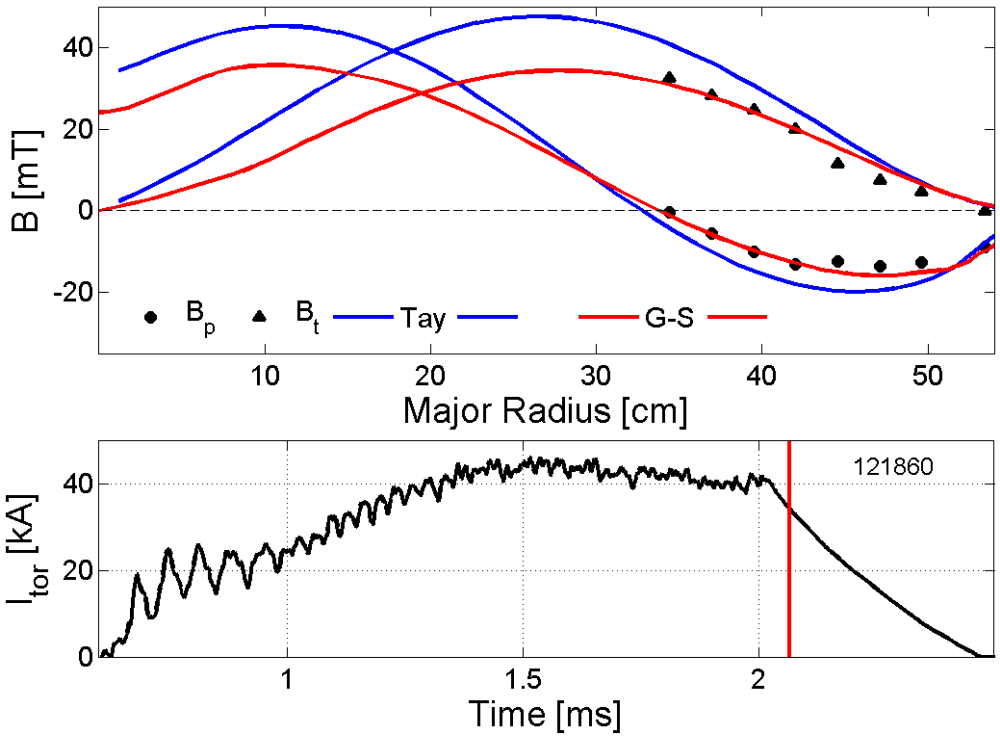

Figure 7.18: Comparison between the internal magnetic signals, the Taylor equilibrium based upon the toroidal current, and the Grad-Shafranov equilibrium. See Appendix C.4 for the location of the code used to make this figure.

The Grad-Shafranov equilibrium, shown in red, matches the internal probe signals better than the Taylor equilibrium, shown in blue. From the Grad-Shafranov equi-

librium current density and λ can be calculated at the probe locations. The values from the Grad-Shafranov equilibrium can then be compared to the calculation of $\vec{j}$ and λ using the three probe stems. Fig. 7.19 shows the comparison of these two calculations. The values calculated from the internal probe signals averaged over an

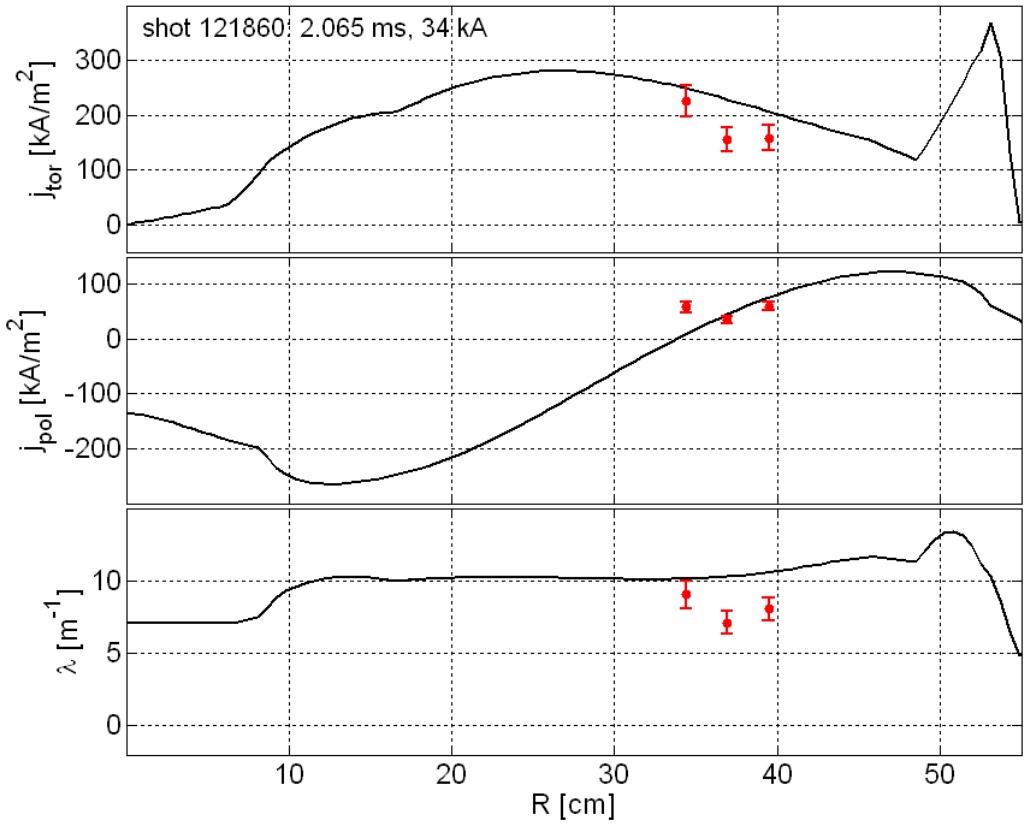

Figure 7.19: The black traces are the fields from the Grad-Shafranov equilibrium. The red data points are the values calculated from the internal probe signals averaged over an injector cycle. The error bars are the RMS value of the oscillations in the signal compared to the calculation made with the signals time-averaged over an injector cycle. See Appendix C.4 for the location of the code used to make this figure.

injector cycle are shown in red with the error bars the RMS value of the oscillations in the full-bandwidth signal. With the exception of the inner most poloidal current density measurement, which is predicted to be nearly zero from the Grad-Shafranov

equilibrium, all of the comparisons are within a factor of 2 of each other. Each of the λ values is below the value predicted by the Grad-Shafranov equilibrium.

7.4 Discussion

Comparisons of the internal probe signals to the Taylor equilibrium for helium shots show good agreement without the use of a fitting parameter (Figs. 7.1, 7.2 and 7.3). This is important because it shows continuity with past measurements [28] and indicates the accuracy of the probe calibration, which has been redone since the measurements presented in Reference [28]. Results of probe measurements from deuterium operations show that the DC level of the field is suppressed from the level predicted by the Taylor equilibrium during the sustainment and decay phases of the shot (Figs. 7.4 and 7.5). The suppressed field indicates either a pressure gradient in the plasma or a hollow λ profile with $\lambda < 10.3$ m^{-1} at the magnetic axis.

To investigate these new profiles a Grad-Shafranov solver is used to fit to the internal probe signals with finite β, variable λ equilibria during the decay phase of the shot. Grad-Shafranov equilibria show a transition from a hollow to a peaked λ profile (Fig. 7.11) and a shifting of the equilibria towards the outer wall from plasma pressure effects (Fig. 7.10). In addition, $\beta \geq 25\%$ is calculated during the decay phase of the shot (Table 7.1). These high β values are possible because of the slow growth rate of pressure driven modes compared to the plasma lifetime in cold spheromaks [50].

Results are also presented from current density calculations using all three stems of the internal probe (Fig. 7.12). Calculations show a hollow λ profile during the sustainment phase of both deuterium and helium shots (Figs. 7.13) where the comparison to Taylor only indicates a hollow profile during deuterium operations. The source of the discrepancy could be that a larger low λ region is needed to see depressed field measurements. For example the toroidal field measured at the magnetic axis is affected by poloidal current along the entire major radius of the plasma. In contrast the current density is a local quantity. A significant difference in the frequency con-

tent of the λ and toroidal current densities is seen when comparing the deuterium and helium shots (Figs. 7.12 and 7.15). Presumably the higher frequency content is important in the sustainment of the higher toroidal current seen in the deuterium shot. Retracting the internal probe shows that the behavior of λ changes moving from the magnetic axis to the wall of the confinement volume (Figs. 7.16 and 7.17). Near the magnetic axis λ increased during the decay phase of the shot while near the wall λ decreased during the decay phase. This is consistent with the transition from a hollow to a peaked λ profile and an average $\lambda = 10.3\ \mathrm{m}^{-1}$ in the confinement volume.

Finally, comparisons between the Grad-Shafranov equilibrium and the current density calculation with the three stems are made to quantify the accuracy of taking the $\nabla \times \vec{B}$ with the internal probe signals (Fig. 7.19). The current density and λ calculated with the three probe stems agree with the values from the Grad-Shafranov equilibrium within a factor of 2. In general it appears that the current density calculations using the three stems are qualitatively accurate.

Chapter 8

IMPOSED-DYNAMO CURRENT DRIVE (IDCD)

Deuterium operations have led to the first HIT-SI plasmas with toroidal current sustained at more than twice the quadrature injector current through multiple injector cycles. The sustainment of current at these levels indicates the formation of separatrix current—current not linking the helicity injectors—in the confinement volume at up to 40 kA. Using the model of separatrix and injector currents the toroidal current drive can be explained by the imposed fluctuations of the injectors [52]. This result is important for dynamo theory as the fluctuations driving the dynamo can be controlled as opposed to resulting from instabilities in the plasma.

This chapter discusses the local toroidal current measurements and explains the currents described in the model. In addition the theoretical development of the imposed-dynamo current drive (IDCD) model [52] is given along with a comparison of the predictions of the model to measured data.

8.1 Separatrix current

Toroidal current that does not link the injectors is defined as separatrix current. Surface probes measure the toroidal current at four toroidal angles: 0°, 45°, 180° and 225° [46]. During higher performing shots the average toroidal current is approximately equal at each toroidal angle. In addition the magnitudes of oscillating toroidal current are approximately equal at each toroidal angle. Oscillations in the local toroidal currents are at the injector frequency (14.5 kHz). The toroidal current measured at each toroidal angle is shown in Fig. 8.1. In addition to the local toroidal current measurements, the average toroidal current and separatrix current

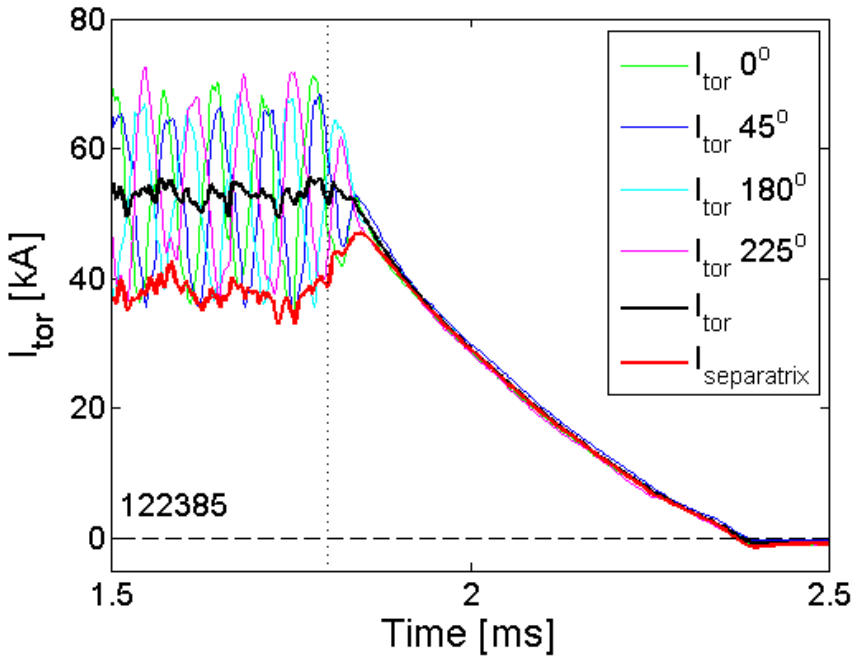

Figure 8.1: The separatrix current as bounded by the toroidal current measured at four toroidal angles [41].

are plotted in Fig. 8.1. The separatrix current (I_{sep}) is calculated by subtracting the average of the instantaneous amplitude of the local current oscillations at the four toroidal locations from the average toroidal current. The instantaneous amplitude of the oscillations at a given toroidal angle is calculated by subtracting the local current time-averaged over an injector cycle from the original signal. The amplitude is found by taking the Hilbert transform of the resulting trace. After the injectors turn off the separatrix current increases as the helicity in the injectors is transferred, through magnetic relaxation, to the separatrix current.

8.2 Model of separatrix current

The local toroidal current measurements can be explained by separatrix current along with injector currents (see Figs. 8.2 and 8.3) [41]. Both figures show the same current

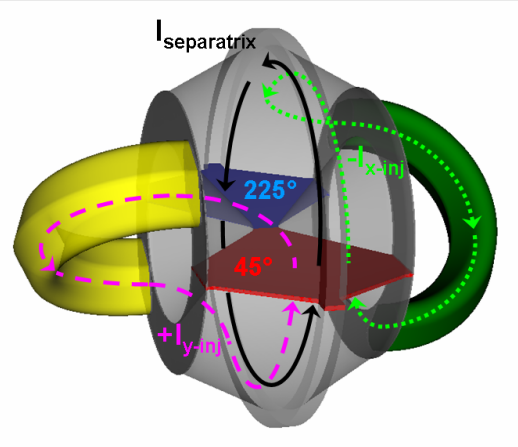

Figure 8.2: Separatrix and injector current paths are shown on a 3D model of HIT-SI when the peak injector current is at 45° [41].

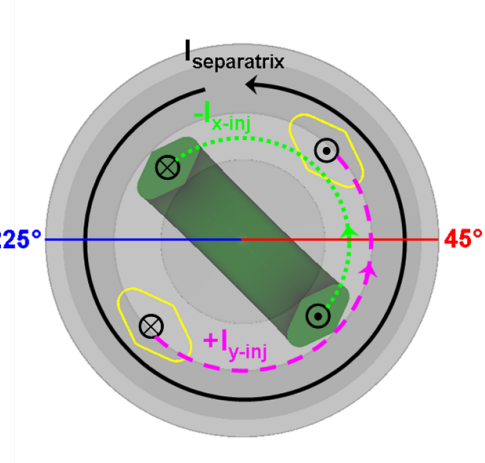

Figure 8.3: Separatrix and injector current paths are shown when the peak injector current is at 45° [41].

paths. The 2D view is a toroidal cross section looking from the Y-side of the machine to the X-side. The circle with the dot in Fig. 8.3 represents current into the plane of the paper and the circle with the x represents current out of the plane of the paper. Current into the plane of the paper represents current entering the X-injector and exiting the Y-injector. (Note the X-injector mouths are below and the Y-injector mouths are above the plane of the paper.) The time slice shown in the figures is when there is negative X-injector and positive Y-injector current. With separatrix current in the positive toroidal direction both injector currents cross the 45° degree plane. At this time just the separatrix current is measured at 225°, and the separatrix current plus both injector currents is measured at 45°.

Figure 8.4 shows the reconstruction of the local toroidal current at 45° from the separatrix current and the injector currents. This is largely a test of how the local oscillations at 45° relate in magnitude and phase to the injector currents. The top trace is the magnitude of the X-injector current that crosses 45°. When the X-injector current is positive it crosses the 225° plane and when it is negative it crosses the 45°

plane. Thus the top trace is the magnitude of negative X-injector current. The second trace is the magnitude of positive Y-injector current. The third trace is the separatrix current as calculated in Fig. 8.1. In the bottom trace the reconstructed current (the sum of the current in the top three traces) is compared to the current measured by the surface probes at 45°. Similar results are achieved by reconstructing the local toroidal current at 225°. The reconstruction does not work as well at 0° and 180°. The calculation is complicated by the fact that the Amperian loops bisect the X-injector mouths at those locations and work is ongoing to explain the current oscillations at those locations.

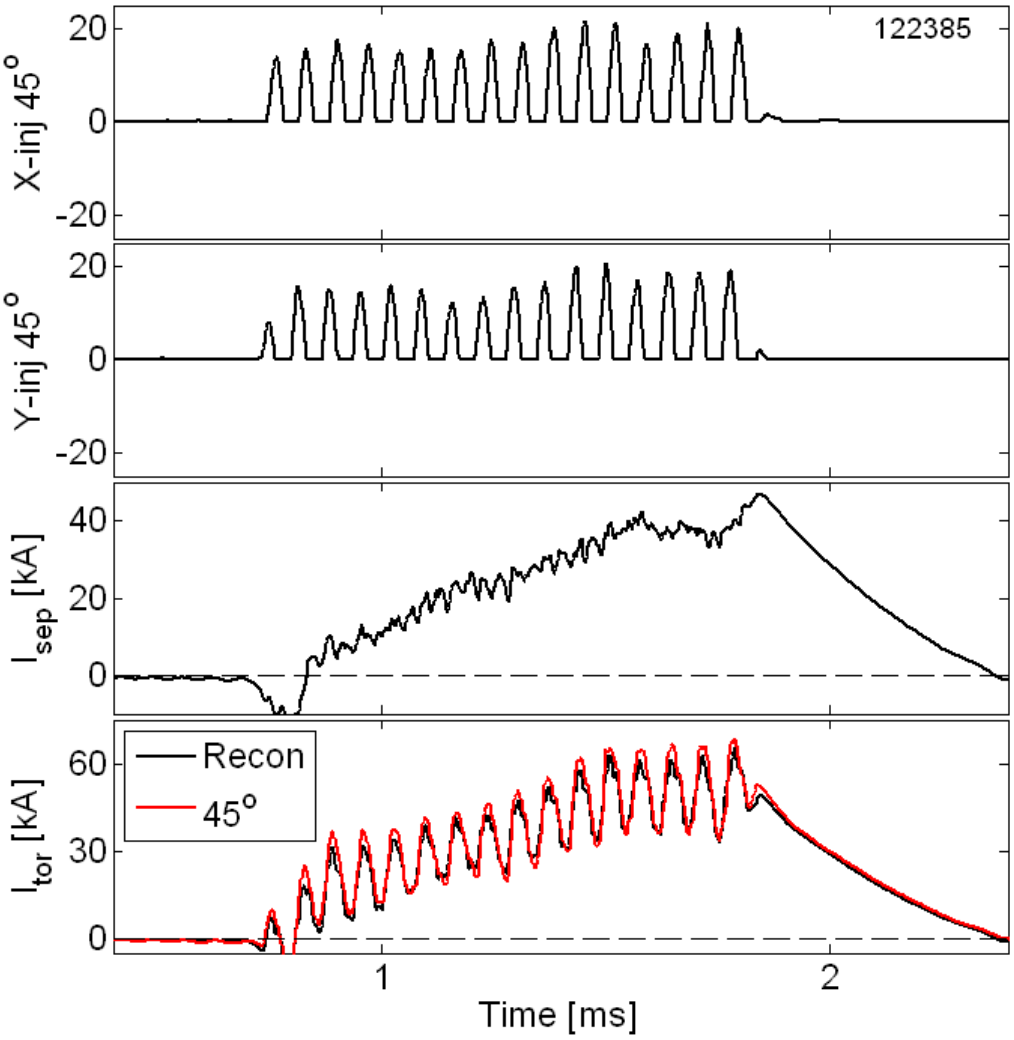

Figure 8.4: Reconstruction of the local toroidal current from the injector currents and the separatrix current. See Appendix C.5.1 for the location of the code used to make this figure.

8.3 Derivation of the IDCD equation

Dynamos are interesting and important because they provide a means for generating and sustaining a toroidal current in a plasma without a central solenoid. The Earth's magnetic field is an example of a field sustained by dynamo action. The source of dynamos is seen by studying the generalized Ohm's law [53, 54]

$$\vec{E} + \vec{v} \times \vec{B} - \frac{\vec{j} \times \vec{B}}{en} + \frac{\nabla P_e}{en} = \eta \vec{j} \tag{8.1}$$

where E is the electric field, B is the magnetic field, v is the ion velocity, j is the current density, n is the electron density, P_e is the electron pressure, η is the plasma resistivity and the electron inertial term $(-m_e/(e^2 n)\partial\vec{j}/\partial t)$ has been neglected because it is small in our plasmas.

Higher order effects are studied by breaking each of the terms into a mean field and fluctuating field quantity

$$x = x_0 + \delta x \tag{8.2}$$

Toroidal field sustainment is studied by looking at the parallel components $(\vec{x} \cdot \vec{B})$. Only terms that do not average to zero over a flux surface are considered (this eliminates first order terms).

$$\eta_\parallel \vec{j}_{\parallel 0} - \vec{E}_{\parallel 0} = \left\langle \delta\vec{v} \times \delta\vec{B} \right\rangle_\parallel - \frac{\left\langle \delta\vec{j} \times \delta\vec{B} \right\rangle_\parallel}{en} \tag{8.3}$$

The first term on the right-hand side is commonly known as the MHD dynamo and the second term is known as the Hall dynamo. It should be noted that

$$\left\langle \delta\vec{v} \times \delta\vec{B} \right\rangle_\parallel - \frac{\left\langle \delta\vec{j} \times \delta\vec{B} \right\rangle_\parallel}{en} = \left\langle \delta\vec{v}_e \times \delta\vec{B} \right\rangle_\parallel \tag{8.4}$$

Thus it can be seen that the MHD and Hall dynamo terms combine to give a term

that is defined in terms of the fluctuating electron velocity. In order to simplify the derivation of the IDCD equation the full dynamo will be estimated by just the Hall dynamo term

$$\delta\vec{v}_e \times \delta\vec{B} \approx -\delta\vec{j} \times \delta\vec{B}/en \tag{8.5}$$

The error introduced by this approximation can be estimated by comparing the magnitude of δj and δv. Figure 8.1 shows fluctuations in the toroidal current at the injector frequency of ∼30 kA, which translates to a $\delta j \sim 150$ kA/m^2. The average electron density is $\sim 2\times10^{19}$ m^{-3} giving $\delta j/ne \sim 50$ km/s. Ion fluctuations on HIT-SI have been measured at ≤ 10 km/s [55]. From this it can be seen that using just the Hall dynamo term and neglecting the MHD dynamo term introduces an error of $\leq$ 20% into the calculation. With this approximation Eqn. 8.3 becomes

$$-\left\langle \delta\vec{j} \times \delta\vec{B} \right\rangle_{\parallel} /en = \eta_{\parallel}\vec{j}_{\parallel 0} - \vec{E}_{\parallel 0} \tag{8.6}$$

Integrating this equation over the volume of interest gives

$$-\int \frac{\left\langle \delta\vec{j} \times \delta\vec{B} \right\rangle_{\parallel}}{en} dV = \int \eta_{\parallel}\vec{j}_{\parallel 0} - \vec{E}_{\parallel 0} dV \tag{8.7}$$

Since plasmas are essentially charge neutral, the Maxwell stress tensor can be defined as [56]

$$\nabla \cdot \overleftrightarrow{T} \equiv \vec{j} \times \vec{B} \tag{8.8}$$

Making a perturbation analysis, the off-diagonal terms that survive the flux-surface averaging are

$$T_{\perp\parallel} = \delta\vec{B}_{\perp}\delta\vec{B}_{\parallel}/\mu_0 \tag{8.9}$$

where $\delta\vec{B}_{\perp}$ is the fluctuating field perpendicular to the mean field and $\delta\vec{B}_{\parallel}$ is the

fluctuating field parallel to the mean field. Since

$$\int \frac{\delta\vec{j}\times\delta\vec{B}}{en}dV = \int \frac{\nabla\cdot\overleftrightarrow{T}}{en}dV = \int \frac{\overleftrightarrow{T}}{en}\cdot d\vec{S} = \int \frac{\delta\vec{B}_\perp\delta\vec{B}_\parallel}{\mu_0 en}\cdot d\vec{S}, \tag{8.10}$$

Eqn. 8.7 can be rewritten as

$$-\int \frac{\delta\vec{B}_\perp\delta\vec{B}_\parallel}{\mu_0}\cdot d\vec{S} = en\int \eta_\parallel\vec{j}_{\parallel 0} - \vec{E}_{\parallel 0}dV. \tag{8.11}$$

The parallel terms in Eqn. 8.11 can be separated into toroidal, B_{tor}, and poloidal, B_{pol}, components to be analyzed separately.

$$-\int \frac{\delta\vec{B}_\perp\delta\vec{B}_{tor}}{\mu_0}\cdot d\vec{S} = en\int \eta\vec{j}_{tor} - \vec{E}_{tor}dV \tag{8.12}$$

where for simplicity η, $\vec{j}_{tor}$ and $\vec{E}_{tor}$ replace η_{tor}, $\vec{j}_{tor,0}$ and $\vec{E}_{tor,0}$. For a toroidal surface $d\vec{S} = Rd\phi rd\theta\hat{r}$ and $dV = Rd\phi rd\theta dr$ with ϕ the toroidal angle, θ the poloidal angle, R the major radius and r the minor radius of the torus. The term on the left-hand side is a flux surface averaged quantity and the terms on the right-hand side are toroidally symmetric mean values so evaluation of the integral is trivial

$$-\frac{\delta B_\perp\delta\vec{B}_{tor}}{\mu_0}2\pi R2\pi r = en\left(\eta\vec{j}_{tor} - \vec{E}_{tor}\right)2\pi R\pi r^2 \tag{8.13}$$

which further reduces to

$$-2\frac{\delta B_\perp\delta\vec{B}_{tor}}{\mu_0} = enr\left(\eta\vec{j}_{tor} - \vec{E}_{tor}\right) \tag{8.14}$$

The physical picture is of a fluctuation across a mean field becoming distorted by a difference in the shear flow of the electron fluid across the surface. Without any shear flow the perpendicular fluctuation will not become distorted and $\delta B_{tor} = 0$. With too much shear flow the fluctuation will not be able to penetrate the surface and

$\delta B_\perp = 0$. In either case Eqn. 8.14 is no longer valid. The direction of the momentum transport is determined by the gradient in the shear and the direction of the imposed perturbation. If the electron flow is higher in the region inside the mean flux surface then the fluctuation will act to slow down the electron velocity inside the mean flux surface. However, if the electron flow is lower in the region inside the mean flux surface then the fluctuation will act to increase the electron velocity inside the mean flux surface.

To test the validity of the model each variable needs to be approximated by a measurable quantity. As can be seen in both deuterium (Fig. 7.6) and helium (Fig. 7.3) shots the magnitude of the fluctuating field is proportional to the injector current, giving $\delta B_\perp \sim \delta B_{tor} \sim \mu_0 I_{inj}$ where $I_{inj} = \sqrt{I_{x,inj}^2 + I_{y,inj}^2}$ is the quadrature injector signal. The toroidal current density can be found from the toroidal current, $j_{tor} = I_{tor}/\pi a^2$. The line-averaged density from the interferometer is used for the density measurement. Modeling the mean field inside the toroidal surface as a single turn solenoid with uniform j_{tor} the inductance per unit length is $L/l = \mu_0/4\pi$ and the resistance per unit length is $R/l = \eta/\pi r^2$ giving

$$\tau_{L/R} = L/R = \frac{\mu_0 r^2}{4\eta} \tag{8.15}$$

where $\tau_{L/R}$ can be found from helicity balance. The electric field can also be found using the inductance per unit length

$$E_{tor} = -\frac{\mu_0}{4\pi}\dot{I}_{tor} \tag{8.16}$$

Putting these values into Eqn. 8.14 gives

$$2\mu_0 I_{inj}^2 \propto enr\left(\frac{\mu_0 r^2}{4\tau_{L/R}}\frac{I_{tor}}{\pi a^2} + \frac{\mu_0}{4\pi}\dot{I}_{tor}\right) \tag{8.17}$$

which reduces to

$$I_{inj}^2 \propto \frac{enr}{8\pi}\left(\frac{I_{tor}}{\tau_{L/R}}\frac{r^2}{a^2} + \dot{I}_{tor}\right) \tag{8.18}$$

Assuming that $r = a$ and rolling the constants into a single fitting parameter, C gives

$$I_{inj}^2 = Cn\left(\frac{I_{tor}}{\tau_{L/R}} + \dot{I}_{tor}\right) \tag{8.19}$$

Assuming that $r = a$ is equivalent to assuming that resistive dissipation happens over the entire poloidal cross section, which is a fair assumption because the toroidal current density was assumed to be constant over the poloidal cross section. Solving for $\dot{I}_{tor}$ with arbitrary constant C gives

$$\dot{I}_{tor} = \frac{C}{n}I_{inj}^2 - \frac{I_{tor}}{\tau_{L/R}} \tag{8.20}$$

The first term on the right-hand side of the equation is a source term proportional to the injector current squared and inversely proportional to the density. The second term describes the decrease in toroidal current due to resistive dissipation.

As mentioned above the L/R time can be calculated from the helicity decay time, $\tau_{L/R} = 2\tau_K$. The helicity decay time is calculated from the total helicity content of the plasma divided by the helicity injection rate.

$$\tau_K = \frac{K}{2V_s\Psi_{inj} - \dot{K}} \tag{8.21}$$

where V_s is the voltage delivered to the spheromak

$$V_s = V_{inj} - R_{inj}I_{inj} \tag{8.22}$$

V_{inj} is the injector loop voltage and $R_{inj}I_{inj}$ is the voltage drop in the injectors, which is measured to be 150 V at 20 kA so $R_{inj} = 7.5$ mΩ [57]. The helicity in the plasma

is calculated according to the Taylor model.

$$K = \left(3.5 \times 10^{-14} Wb^2/A^2\right) I_{tor}^2 + \left(5.0 \times 10^{-14} Wb^2/A^2\right) I_{x,inj}^2 + \left(5.0 \times 10^{-14} Wb^2/A^2\right) I_{y,inj}^2 + \left(4.0 \times 10^{-14} Wb^2/A^2\right) I_{x,inj} I_{y,inj} \quad (8.23)$$

A seeming inconsistency is that the total helicity content is found from the Taylor model while results from high-performance deuterium shots show that the Taylor model does not accurately predict the measured internal profiles. Locally λ varies in the confinement volume causing the difference between the measured fields and the constant λ Taylor profile. However, the globally averaged $\lambda = 10.3$ m^{-1} in both cases and the Taylor model provides an accurate prediction of the total helicity in the confinement volume.

Figure 8.5 shows the steps involved in the calculation of τ_k. The top frame shows the helicity injection rate including the average value and the helicity injection rate into the spheromak volume. The second frame shows the total helicity content calculated from Eqn. 8.23 including the value time averaged over an injector cycle. The third frame shows the time rate of change of the average total helicity. The final frame is the helicity decay time.

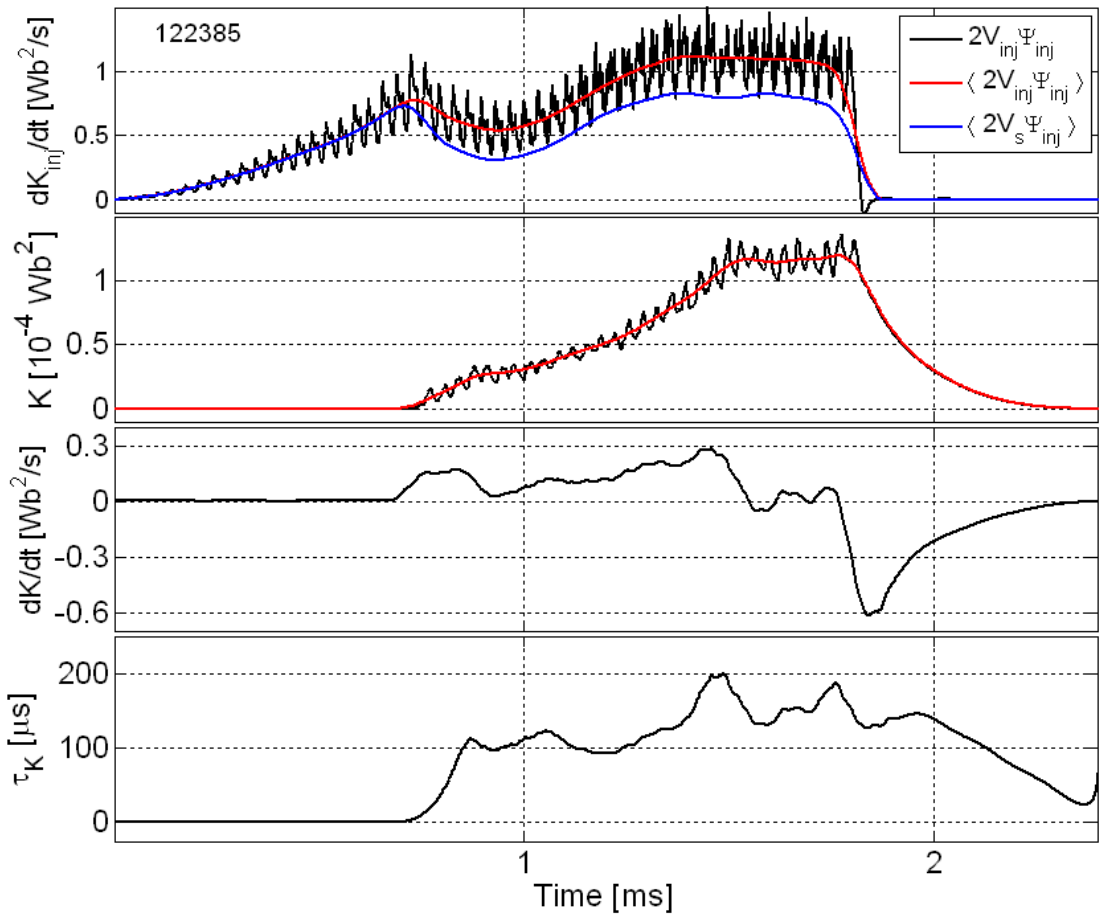

Figure 8.5: Calculation of τ_K: helicity injection rate, total helicity, time rate of change of helicity and helicity decay time. See Appendix C.5.2 for the location of the code used to make this figure.

The next step is to apply Eqn. 8.20 to HIT-SI plasmas. Figure 8.6 compares the predicted toroidal current with a user-defined value for C. The width of the

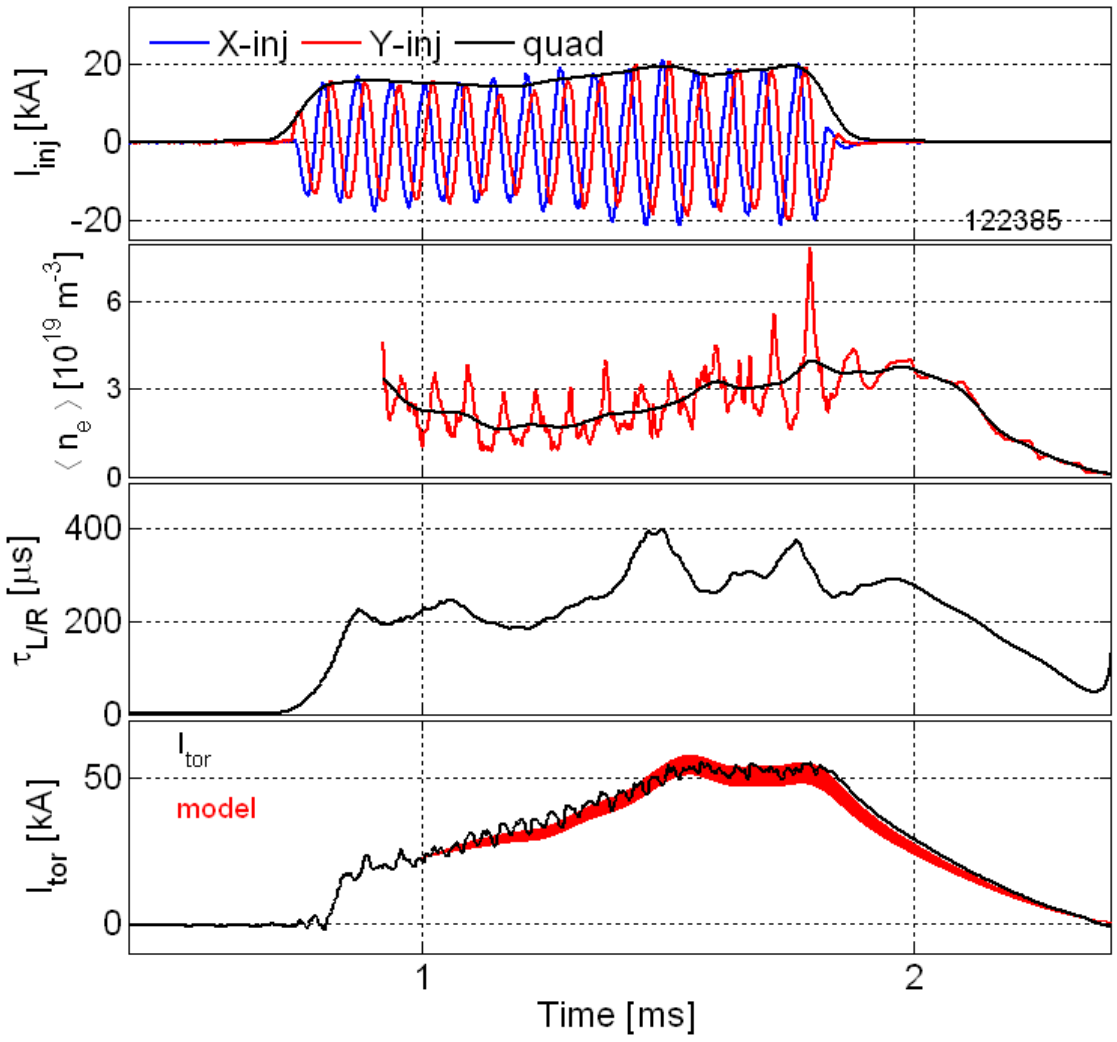

Figure 8.6: Comparison of the current predicted by the IDCD to the measured toroidal current. See Appendix C.5.3 for the location of the code used to make this figure.

predicted toroidal current trace is from the uncertainty in the helicity injection into the confinement volume compared to the helicity injected into the injector. The width is based upon adding and subtracting 20% to the injector resistance in Eqn. 8.22. The

constant found to best match the data is $C = 1.5 \times 10^{19}$.

Using the constant found in the fit to shot 122385, the IDCD equation can be applied to other shots of variable conditions without the use of a fitting parameter. Figure 8.7 shows the application of the constant found from shot 122385 to three other shots. These three shots cover a wide range of densities, injector currents, and

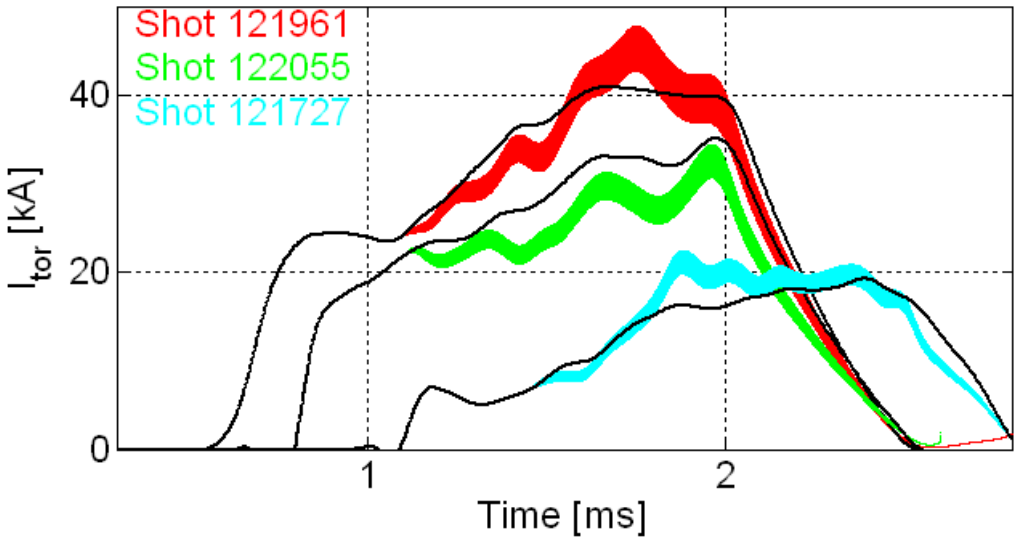

Figure 8.7: Comparison of the current predicted by the IDCD to the measured toroidal current using the fitting parameter from shot 122385. Appendix C.5.4 for the location of the code used to make this figure.

toroidal currents (see Figs. A.4, A.10 and A.16). This comparison shows that the IDCD model, Eqn. 8.20, predicts the overall behavior of the toroidal current from the plasma density and injector current.

8.4 Discussion

The local toroidal current measurements can be explained by a separatrix current along with injector currents (see Figs. 8.2 and 8.3) [41]. When the average toroidal current is greater than the total injected current, all of the current in the confinement

volume will flow in the same toroidal direction (the injector currents will flow in the same direction as the separatrix current). The oscillations in the locally measured currents are from the oscillating injector currents passing that location. This interpretation is confirmed by the magnitude and phase of the measured current oscillations shown in Fig. 8.1. The minima in the local current measurements occur when no injector current passes a given toroidal location and therefore measures only separatrix current. Thus, the minimum level of toroidal current at each of the four toroidal locations is attributed to the current inside the separatrix (Fig. 8.1) with the oscillations the result of the injector currents passing by a given toroidal location. This result indicates a sustained region of separatrix current through multiple injector cycles.

An alternative explanation for the current amplification is injector current making multiple toroidal passes in the confinement volume. This explanation also requires the injector currents to transit in the same toroidal direction of the confinement volume each half cycle. The toroidal current would then be scaled by the sum of the injector current magnitudes, which has significant fourth harmonic content. At current amplifications greater than 2 the magnitude of this fourth harmonic content is approximately half of the magnitude of the first harmonic. The local toroidal current measurements do not suggest the presence of large oscillations at four times the injector frequency (see Fig. 8.1). In addition, each injector turns off every half cycle, forcing closure of the injector flux. It seems unlikely that every half cycle injector field lines making multiple toroidal transits would be produced or handed off to the other injector. However, the data do not preclude some injector current making multiple toroidal passes.

Research into the effects of 3D perturbations on tokamak equilibria is a popular topic now [58]. Some effects seen in tokamak experiments are similar to the IDCD model. Neoclassical toroidal viscosity (NTV) torque is proportional to the square of the applied coil current [59]. Density dependence has also been shown to affect the plasma response to 3D field effects [60, 61]. The threshold for the formation of locked

modes scales with density [62, 63].

The IDCD equation models the toroidal current growth from the injector current and electron density (Figs. 8.6 and 8.7) [52]. The implication of this model is that the toroidal current growth is the result of applied perturbations rather than instabilities in the plasma. In other words, the dynamo can be controlled by varying the injector current and electron density.

Chapter 9

CONCLUSION

With its inductive helicity injectors HIT-SI is in a unique position to test the effects of 3D perturbations on magnetic equilibria. In addition the size and temperature of the plasmas allow probing of the internal fields which is not possible on high power tokamak experiments. Localized internal magnetic field measurements are leading to insights on the effects of 3D perturbations on the magnetic field structures. These measurements indicate that the injectors are driving a region of low λ and that this region is built up and sustained during the injector drive (Figs. 7.4 and 7.5). In addition the internal fluctuations are proportional to the injector current leading to the development of the IDCD model.

New results on HIT-SI are achieved using deuterium operations. Wall-conditioning with helium plasmas followed immediately by deuterium operations has produced plasmas with improved density control. These deuterium plasmas are the first HIT-SI plasmas with $j/n \geq 10^{-14}$ A·m (Fig. 6.3). Deuterium operations have produced record toroidal currents (> 50 kA) and current amplifications ($\sim$3) on HIT-SI (Fig. 6.4). High performance shots have also achieved current decay times of up 0.64 ms (Fig. 6.5). Grad-Shafranov equilibria during the decay phase of the shot show a transition from a hollow to a peaked λ profile and a shifting of the equilibria towards the outer wall from plasma pressure effects. In addition, $\beta \geq 25\%$ is calculated during the decay phase of the shot. Achieving the record current amplification for a spheromak of 3 with current persistence after the injectors are off proves that SIHI is an effective solenoid-free and electrode-free plasma startup method.

High performance deuterium shots sustain a minimum toroidal current—called

separatrix current—of up to 40 kA through multiple injector cycles (Fig. 8.1). As the current amplification (and the separatrix current) grows the n = 1 mode decreases in the confinement volume (Figs. 6.6 and 6.7) indicating the axisymmetric field is the dominant magnetic structure in the confinement volume. During this time the toroidal current is sustained through the direct coupling of the injectors to the axisymmetric field. Thus the injector perturbations are less disrupting as the equilibrium grows.

Finally the IDCD model is developed. This model accurately predicts the build up of toroidal current from the electron density and injector current (Figs. 8.6 and 8.7) [52]. The implication of this model is that dynamo current drive is applied directly by the injectors and does not need to result from instabilities in the plasma.

Chapter 10

SUGGESTIONS FOR FUTURE WORK

Future work with the most wide-ranging implications involves the testing of the IDCD model to discover if insights from the model can be used to improve machine performance. Two areas of immediate interest are the effects of higher frequency injector operations on the equilibrium in the confinement volume and whether the fluctuation levels can be controlled at different locations within the confinement volume.

In addition, advances in the diagnostics for HIT-SI will improve the understanding of the plasma structure and current drive mechanism. Information on the internal magnetics near the geometric axis of the machine will help to define the Grad-Shafranov equation and provide better understanding of the high performance deuterium shots. A new internal probe is under construction that will measure the magnetic fields through the geometric axis. Additional work with the high-speed camera should help to determine the structure of the equilibrium from the emitted light. Limitations on the resolution set by the coherent fiber bundles could be overcome by using lenses and mirrors to bring the image to the fast camera from the re-entrant ports.

Comparisons of the internal probe measurements to computation results from NIMROD will help to validate the accuracy of the computation. With a valid model the current density and λ profile during the entire shot will be known. This could provide further insights to better utilize the injectors to improve the toroidal current drive.

Further improvements in density control are needed to continue to increase the

toroidal current for longer shot lengths. There are two ways of improving the density control: either the injectors need to better utilize the injected gas or the confinement volume needs to better pump the injected gas. Further increasing the injector operating frequency could help to limit the outgassing of the injectors. Improved pumping in the confinement volume is difficult to achieve on HIT-SI, but could be implemented on the HIT-SI3 (Fig. 10.1), which is under construction. On HIT-SI3 there are three injectors on one side of the machine. The flux conserver on the opposite wall could be perforated to allow better pumping of gas from the confinement volume.

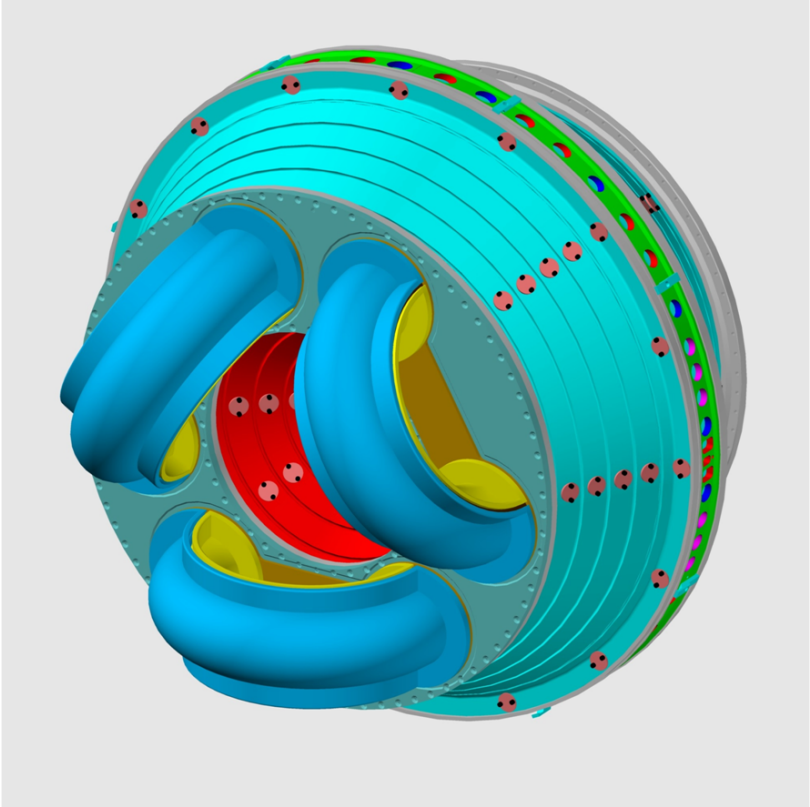

Figure 10.1: HIT-SI3. Drawing by John Rogers.

BIBLIOGRAPHY

[1] J.P. Freidberg. *Plasma Physics and Fusion Energy*. Cambridge University Press, Cambridge, 2007.

[2] J. Wesson. *Tokamaks*. Clarendon Press, Oxford, England, 1987.

[3] L. Spitzer. The stellarator concept. *Physics of Fluids*, 1:253, 1958.

[4] H.A.B. Bodin and A.A. Newton. Reversed-field-pinch research. *Nuclear Fusion*, 20(10):1255, 1980.

[5] T. R. Jarboe. Review of spheromak research. *Plasma Physics and Controlled Fusion*, 36:945–990, 1994.

[6] Loren C. Steinhauer. Review of field-reversed configurations. *Physics of Plasmas*, 18(7):070501, 2011.

[7] U. Shumlak, R. P. Golingo, B. A. Nelson, and D. J. Den Hartog. Evidence of stabilization in the Z-pinch. *Phys. Rev. Lett.*, 87:205005, Oct 2001.

[8] S. Ohi, T. Minato, Y. Kawakami, M. Tanjyo, S. Okada, Y. Ito, M. Kako, S. Gotô, T. Ishimura, and H. Itô. Quadrupole stabilization of the $n = 2$ rotational instability of a field-reversed theta-pinch plasma. *Phys. Rev. Lett.*, 51:1042–1045, Sep 1983.

[9] R.F. Post. The magnetic mirror approach to fusion. *Nuclear Fusion*, 27(10):1579, 1987.

[10] Wikipedia. `http://en.wikipedia.org`.

[11] European Nuclear Society. `http://www.euronuclear.org`.

[12] International Thermonuclear Experimental Reactor (ITER). `http://www.iter.org/`.

[13] M. Keilhacker, A. Gibson, C. Gormezano, P.J. Lomas, P.R. Thomas, M.L. Watkins, P. Andrew, B. Balet, D. Borba, C.D. Challis, I. Coffey, G.A. Cottrell, H.P.L. De Esch, N. Deliyanakis, A. Fasoli, C.W. Gowers, H.Y. Guo, G.T.A. Huysmans, T.T.C. Jones, W. Kerner, R.W.T. Knig, M.J. Loughlin, A. Maas, F.B. Marcus, M.F.F. Nave, F.G. Rimini, G.J. Sadler, S.E. Sharapov, G. Sips, P. Smeulders, F.X. Sldner, A. Taroni, B.J.D. Tubbing, M.G. von Hellermann, D.J. Ward, and JET Team. High fusion performance from deuterium-tritium plasmas in JET. *Nuclear Fusion*, 39(2):209, 1999.

[14] R.G. O'Neill. *An Experimental Study of Helicity Injection Current Drive in the HIT-SI Spheromak*. PhD thesis, University of Washington, 2007.

[15] U. Shumlak and T. R. Jarboe. Stable high beta spheromak equilibria using concave flux conservers. *Physics of Plasmas*, 7:2959–2963, 2000.

[16] T. R. Jarboe, Cris W. Barnes, I. Henins, H. W. Hoida, S. O. Knox, R. K. Linford, and A. R. Sherwood. The Ohmic heating of a spheromak to 100 eV. *Physics of Fluids*, 27(1):13–15, 1984.

[17] H.K. Moffatt. *Magnetic Field Generation in Electrically Conducting Fluids*. Cambridge University Press, Cambridge, 1978.

[18] J. B. Taylor. Relaxation of toroidal plasma and generation of reverse magnetic fields. *Phys. Rev. Lett.*, 33:1139–1141, Nov 1974.

[19] P.M. Bellan. *Spheromaks*. Imperial College Press, Covent Gardens, London, 2000.

[20] L. Woltjer. A theorem on force-free magnetic fields. *Proceedings of the National Academy of Sciences*, 44:489–491, 1958.

[21] J. M. Finn and T. M. Antonsen. Magnetic helicity: what is it, and what is it good for? *Comments Plasma Physics and Controlled Fusion*, 9:111, 1985.

[22] M. Ono, G. J. Greene, D. Darrow, C. Forest, H. Park, and T. H. Stix. Steady-state tokamak discharge via dc helicity injection. *Phys. Rev. Lett.*, 59:2165–2168, Nov 1987.

[23] B. A. Nelson, T. R. Jarboe, D. J. Orvis, L. A. McCullough, J. Xie, C. Zhang, and L. Zhou. Formation and sustainment of a 150 kA tokamak by Coaxial Helicity Injection. *Physical Review Letters*, 72:3666–3669, 1994.

[24] R. Raman, D. Mueller, B. A. Nelson, T. R. Jarboe, S. Gerhardt, H. W. Kugel, B. LeBlanc, R. Maingi, J. Menard, M. Ono, S. Paul, L. Roquemore, S. Sabbagh, and V. Soukhanovskii. Demonstration of Tokamak Ohmic Flux Saving by Transient Coaxial Helicity Injection in the National Spherical Torus Experiment. *Phys. Rev. Lett.*, 104:095003, Mar 2010.

[25] W. C. Turner, G. C. Goldenbaum, E. H. A. Granneman, J. H. Hammer, C. W. Hartman, D. S. Prono, and J. Taska. Investigations of the magnetic structure and the decay of a plasma-gun-generated compact torus. *Physics of Fluids*, 26(7):1965–1986, 1983.

[26] T. R. Jarboe, F. J. Wysocki, J. C. Fernandez, I. Henins, and G. J. Marklin. Progress with energy confinement time in the CTX spheromak. *Physics of Fluids B: Plasma Physics*, 2(6):1342–1346, 1990.

[27] T. R. Jarboe, P. Gu, V. A. Izzo, P. D. Jewell, K. J. McCollam, B. A. Nelson, R. Raman, A. J. Redd, P. E. Sieck, R. J. Smith, M. Nagata, and T. Uyama. Current drive experiments in the HIT–II spherical tokamak. *Nuclear Fusion*, 41:679, 2001.

[28] T. R. Jarboe, W. T. Hamp, G. J. Marklin, B. A. Nelson, R. G. O'Neill, A. J. Redd, P. E. Sieck, R. J. Smith, and J. S. Wrobel. Spheromak formation by Steady Inductive Helicity Injection. *Phys. Rev. Lett.*, 97:115003, 2006.

[29] P. E. Sieck, T. R. Jarboe, V. A. Izzo, W. T. Hamp, B. A. Nelson, R. G. O'Neill, A. J. Redd, and R. J. Smith. Demonstration of steady inductive helicity injection. *Nuclear Fusion*, 46:254–261, 2006.

[30] D.A. Ennis, B.S. Victor, J.S. Wrobel, C. Akcay, T.R. Jarboe, G.J. Marklin, B.A. Nelson, and R.J. Smith. New understandings and achievements from independent-injector drive experiments on HIT-SI. *Nuclear Fusion*, 50(7):072001, 2010.

[31] T. G. Cowling. The present status of dynamo theory. *Ann. Rev. Astron. Astrophys.*, 19:115–35, 1981.

[32] P.E. Sieck. *Spheromak Formation Using Steady Inductive Helicity Injection*. PhD thesis, University of Washington, 2006.

[33] A. J. Redd, T. R. Jarboe, W. T. Hamp, B. A. Nelson, R. G. O'Neill, P. E. Sieck, R. J. Smith, G. L. Sutphin, and J. S. Wrobel. Overview of the Helicity Injected Torus (HIT) program. *Journal of Fusion Energy*, 26:163–168, 2007. Paper DOI 10.1007/s10894-006-9049-y.

[34] B. A. Nelson, T. Moser, and D. Bryant. DRAFT: HIT-SI Tank Circuit State-Space Model. Private communication, 2012.

[35] B. A. Nelson, A. B. Bourdages, D. Bryant, T. R. Jarboe, Y. Kikuchi, M. Mesbahi, T. Moser, and A. S. Nelson. Progress on Digital Control of the HIT-SI Power Supply Systems. In *Proceedings of the Workshop on Innovation in Fusion Science (ICC2011) and US-Japan Workshop on Compact Torus Plasma (August 16-19, 2011, Seattle, Washington USA)*, 2011. Archived at www.iccworkshops.org/icc2011/uploads/217/nelsonproceedings.pdf.

[36] B. S. Victor. Density analysis of the HIT-SI spheromak. Master's thesis, University of Washington, 2009.

[37] P. D. Jewell, R. J. Smith, and T. R. Jarboe. Martin-Puplett multichannel far infrared heterodyne interferometer on the Helicity Injected Torus II. *Review of Scientific Instruments*, 74:80–87, 2003.

[38] I.H. Hutchinson. *Principles of Plasma Diagnostics*. Cambridge University Press, Cambridge, 2nd edition, 2002.

[39] L.A. McCullough. A Study of Selected Impurities on the Helicity Injected Tokamak Using Two Vacuum Ultraviolet Monochromators. Master's thesis, University of Washington, 1995.

[40] P. G. Carolan and V. A. Piotrowicz. The bahaviour of impurities out of coronal equilibrium. *Plasma Physics*, 25:1065–1086, 1983.

[41] B. S. Victor, T. R. Jarboe, A. C. Hossack, D. A. Ennis, B. A. Nelson, R. J. Smith, C. Akcay, C. J. Hansen, G. J. Marklin, N. K. Hicks, and J. S. Wrobel. Evidence for Separatrix Formation and Sustainment with Steady Inductive Helicity Injection. *Phys. Rev. Lett.*, 107:165005, Oct 2011.

[42] S. Ortolani and G. Rostagni. Density limits and scaling in reversed field pinches. *Nuclear Instruments and Methods*, 207:35–48, 1983.

[43] Martin Greenwald. Density limits in toroidal plasmas. *Plasma Physics and Controlled Fusion*, 44(8):R27, 2002.

[44] J Winter. Wall conditioning in fusion devices and its influence on plasma performance. *Plasma Physics and Controlled Fusion*, 38(9):1503, 1996.

[45] B. S. Victor, T. R. Jarboe, A. C. Hossack, D. A. Ennis, B. A. Nelson, C. J. Hansen, and J. S. Wrobel. Advances in Steady Inductive Helicity Injection for Plasma Startup and Toroidal Current Drive. *IEEJ Transactions*, 2012.

[46] J.S. Wrobel. *A study of HIT-SI plasma dynamics using surface magnetic field measurements*. PhD thesis, University of Washington, 2011.

[47] C. J. Hansen. Grad Shafranov solver. Private communication, 2011.

[48] S. O. Knox, Cris W. Barnes, G. J. Marklin, T. R. Jarboe, I. Henins, H. W. Hoida, and B. L. Wright. Observations of spheromak equilibria which differ from the minimum-energy state and have internal kink distortions. *Phys. Rev. Lett.*, 56:842–845, Feb 1986.

[49] V. D. Shafranov. Plasma Equilibrium in a Magnetic Field. *Reviews of Plasma Physics*, 2:103, 1966.

[50] T. R. Jarboe. Pressure driven modes. Private communication, 2012.

[51] R.S. Shaw and J.M. Finn. Axisymmetric equilibria in the Maryland Spheromak. *Nuclear Fusion*, 27(8):1309, 1987.

[52] T. R. Jarboe, B. S. Victor, B. A. Nelson, C. J. Hansen C. Akcay, D. A. Ennis, A. C. Hossack, G. J. Marklin, and R. J. Smith. Imposed-Dynamo Current Drive. *Submitted*, 2012.

[53] H. Ji, A. F. Almagri, S. C. Prager, and J. S. Sarff. Time-resolved observation of discrete and continuous magnetohydrodynamic dynamo in the reversed-field pinch edge. *Phys. Rev. Lett.*, 73:668–671, Aug 1994.

[54] Hantao Ji. Turbulent dynamos and magnetic helicity. *Phys. Rev. Lett.*, 83:3198–3201, Oct 1999.

[55] A. C. Hossack. Ion velocity. Private communication, 2012.

[56] Allen H. Boozer. Error field amplification and rotation damping in tokamak plasmas. *Phys. Rev. Lett.*, 86:5059–5061, May 2001.

[57] T.R. Jarboe, C. Akcay, M.A. Chilenski, D.A. Ennis, C.J. Hansen, N.K. Hicks, R.Z. Aboul Hosn, A.C. Hossack, G.J. Marklin, B.A. Nelson, R.G. O'Neill, P.E. Sieck, R.J. Smith, B.S. Victor, J.S. Wrobel, and M. Nagata. Recent results from the HIT-SI experiment. *Nuclear Fusion*, 51(6):063029, 2011.

[58] J.D. Callen. Effects of 3D magnetic perturbations on toroidal plasmas. *Nuclear Fusion*, 51(9):094026, 2011.

[59] A. M. Garofalo, W. M. Solomon, M. Lanctot, K. H. Burrell, J. C. DeBoo, J. S. deGrassie, G. L. Jackson, J.-K. Park, H. Reimerdes, M. J. Schaffer, and E. J. Strait. Plasma rotation driven by static nonresonant magnetic fields. *Physics of Plasmas*, 16(5):056119, 2009.

[60] S. M. Wolfe, I. H. Hutchinson, R. S. Granetz, J. Rice, A. Hubbard, A. Lynn, P. Phillips, T. C. Hender, D. F. Howell, R. J. La Haye, and J. T. Scoville. Non-axisymmetric field effects on Alcator C-Mod. *Physics of Plasmas*, 12(5):056110, 2005.

[61] A. J. Cole, C. C. Hegna, and J. D. Callen. Neoclassical toroidal viscosity and error-field penetration in tokamaks. *Physics of Plasmas*, 15(5):056102, 2008.

[62] J.E. Menard, R.E. Bell, D.A. Gates, S.P. Gerhardt, J.-K. Park, S.A. Sabbagh, J.W. Berkery, A. Egan, J. Kallman, S.M. Kaye, B. LeBlanc, Y.Q. Liu, A. Sontag, D. Swanson, H. Yuh, W. Zhu, and the NSTX Research Team. Progress in understanding error-field physics in NSTX spherical torus plasmas. *Nuclear Fusion*, 50(4):045008, 2010.

[63] Jong-Kyu Park, Jonathan E. Menard, Stefan P. Gerhardt, Richard J. Buttery, Steve A. Sabbagh, Ronald E. Bell, and Benoit P. LeBlanc. Sensitivity to error fields in NSTX high β plasmas. *Nuclear Fusion*, 52(2):023004, 2012.

Appendix A

DATA FROM IMPORTANT SHOTS

A.1 Data set for all shots used in this dissertation

This section contains plots of the injector voltage, injector flux, injector current, helicity injection rate, injected power, toroidal current, n = 1 mode amplitude and density (if available) for each shot mentioned in this dissertation.

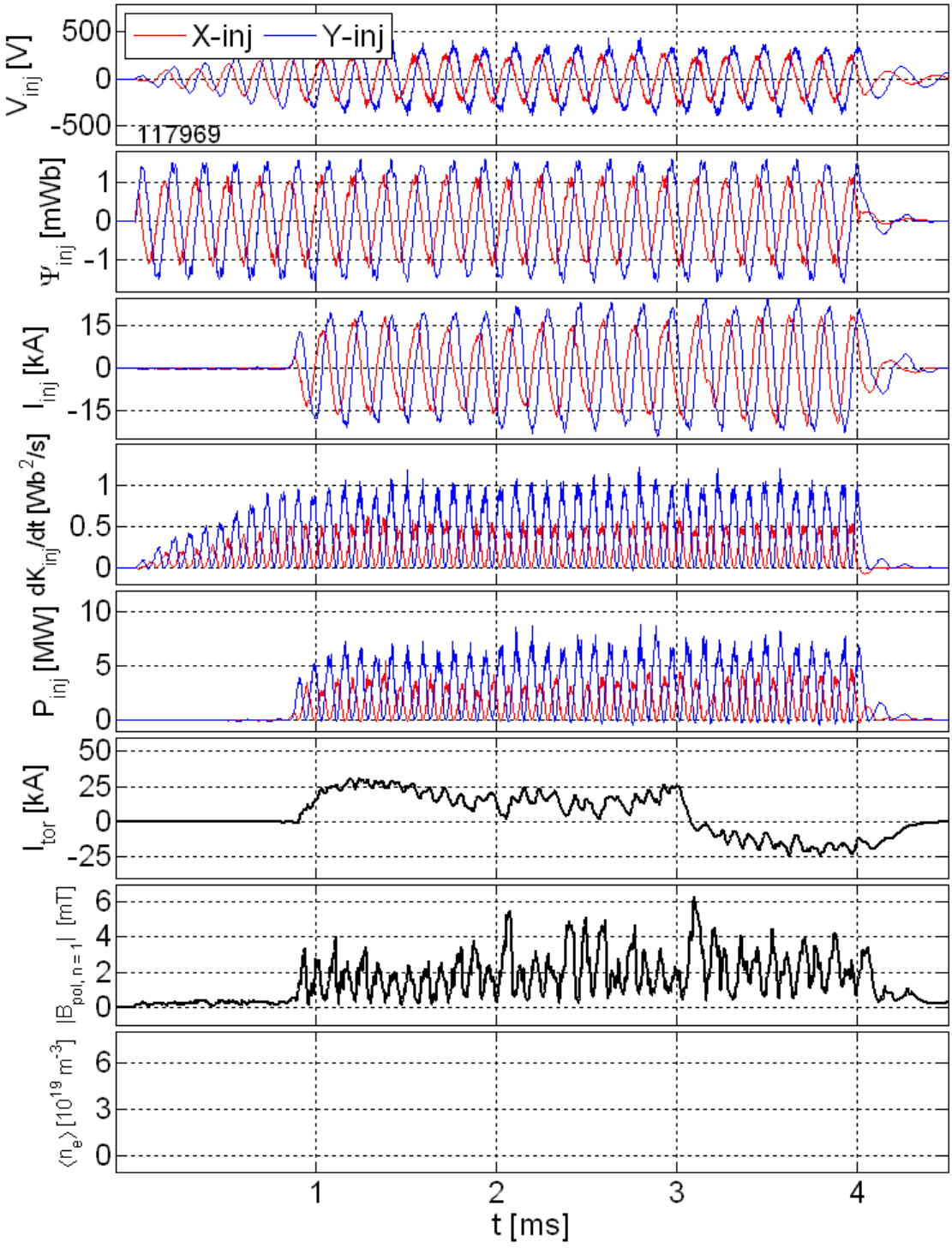

Figure A.1: Injector voltage, injector flux, injector current, helicity injection rate, injected power, toroidal current and n = 1 mode amplitude for shot 117969.

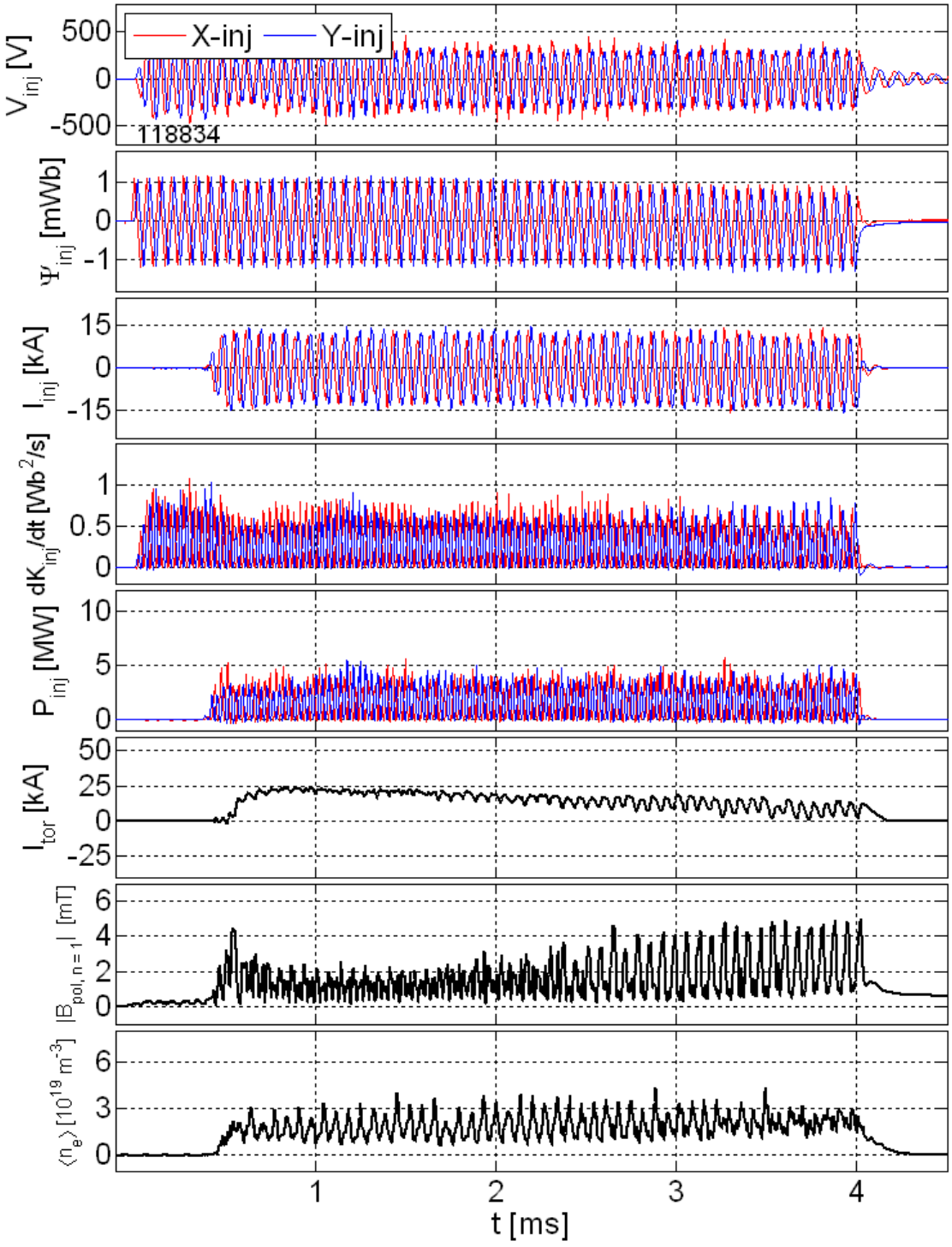

Figure A.2: Injector voltage, injector flux, injector current, helicity injection rate, injected power, toroidal current, n = 1 mode amplitude and density for shot 118834.

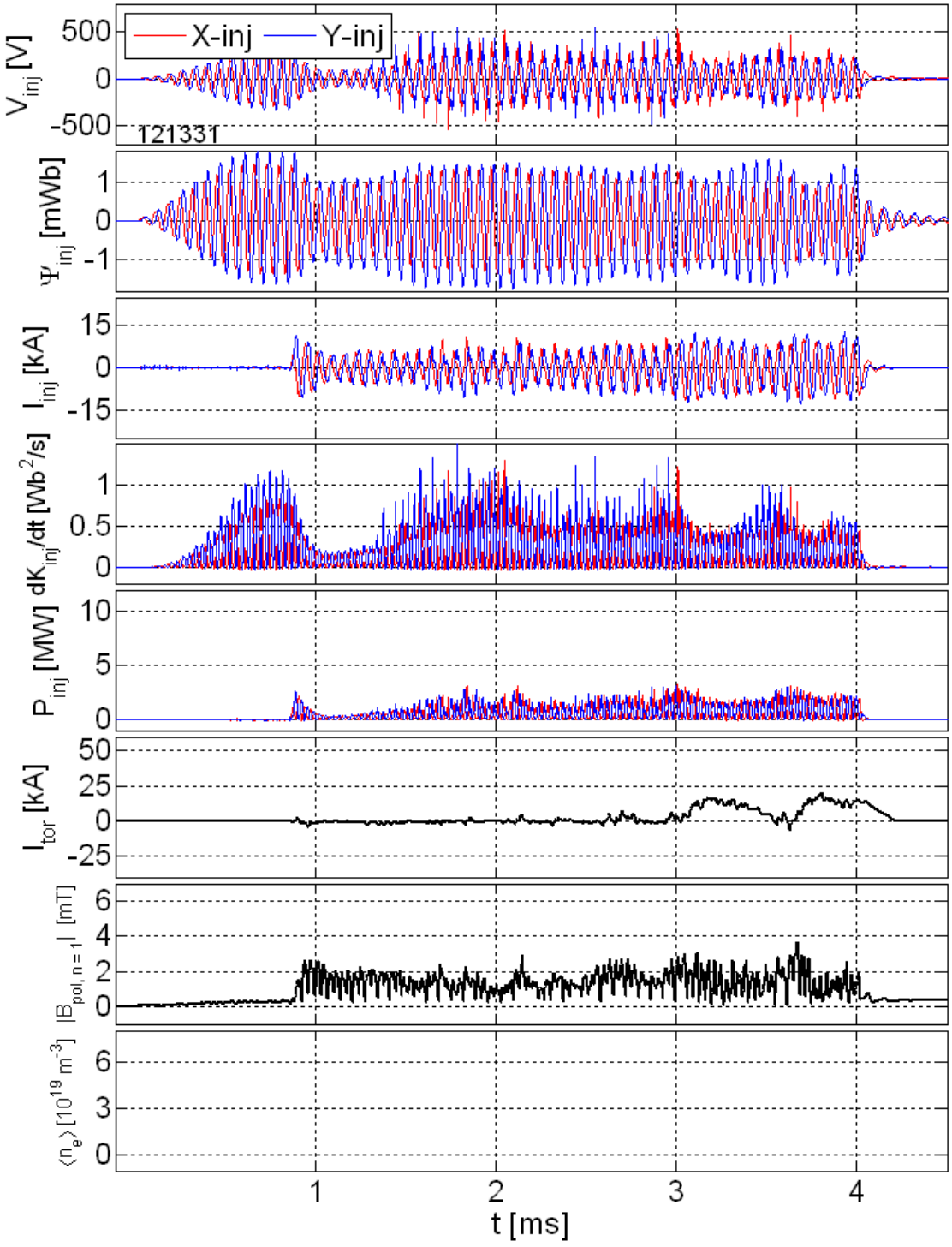

Figure A.3: Injector voltage, injector flux, injector current, helicity injection rate, injected power, toroidal current and n = 1 mode amplitude for shot 121331.

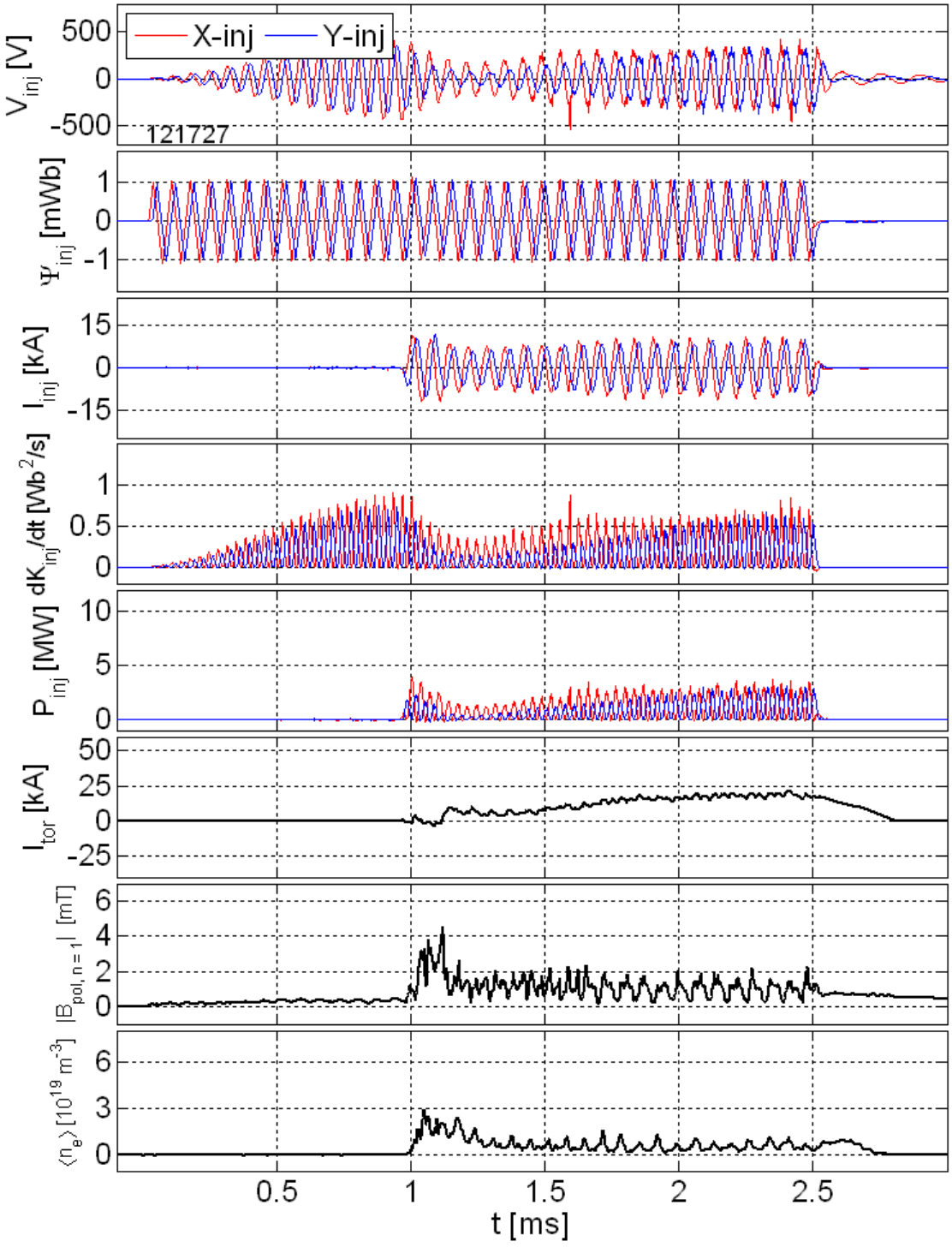

Figure A.4: Injector voltage, injector flux, injector current, helicity injection rate, injected power, toroidal current, n = 1 mode amplitude and density for shot 121727.

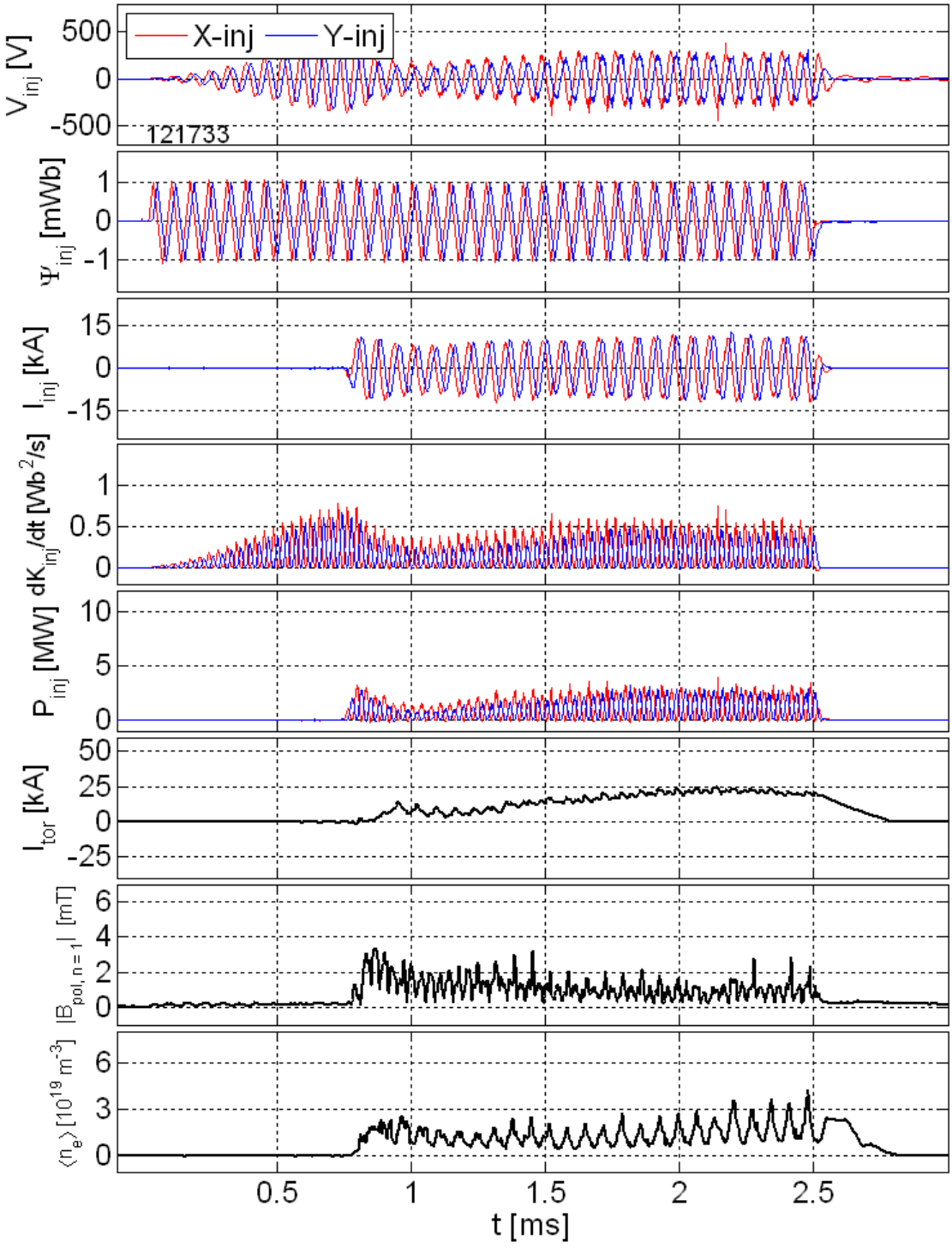

Figure A.5: Injector voltage, injector flux, injector current, helicity injection rate, injected power, toroidal current, n = 1 mode amplitude and density for shot 121733.

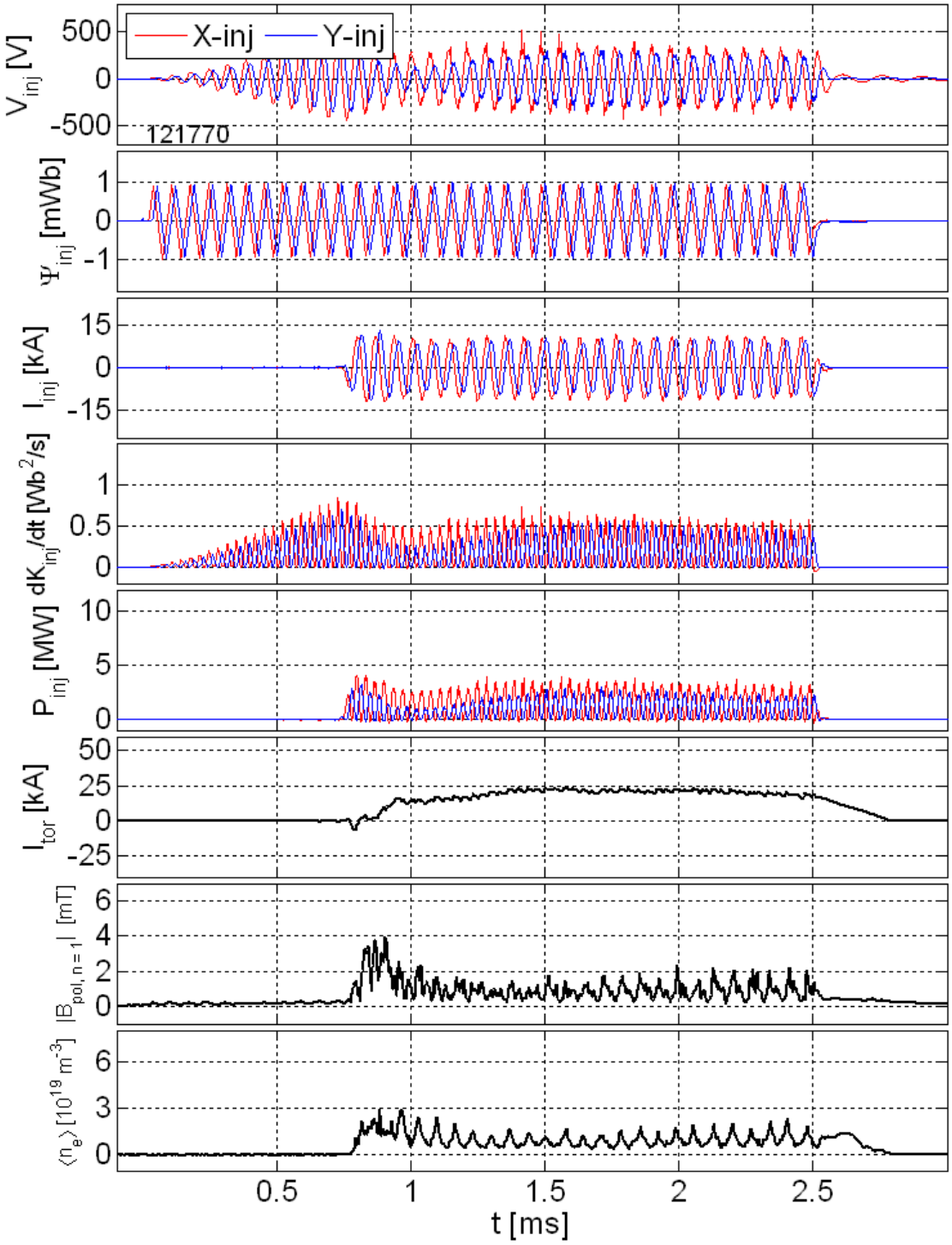

Figure A.6: Injector voltage, injector flux, injector current, helicity injection rate, injected power, toroidal current, n = 1 mode amplitude and density for shot 121770.

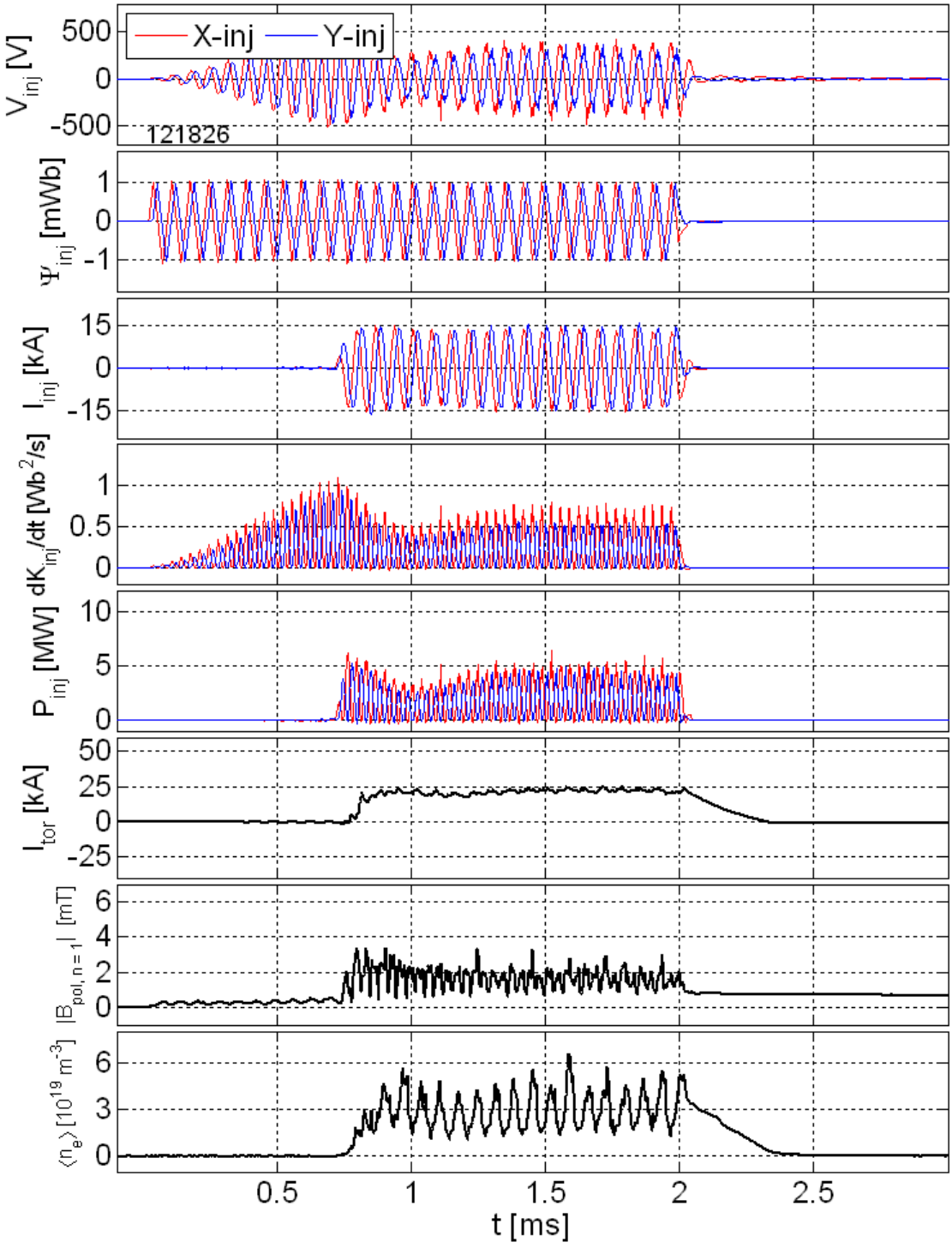

Figure A.7: Injector voltage, injector flux, injector current, helicity injection rate, injected power, toroidal current, n = 1 mode amplitude and density for shot 121826.

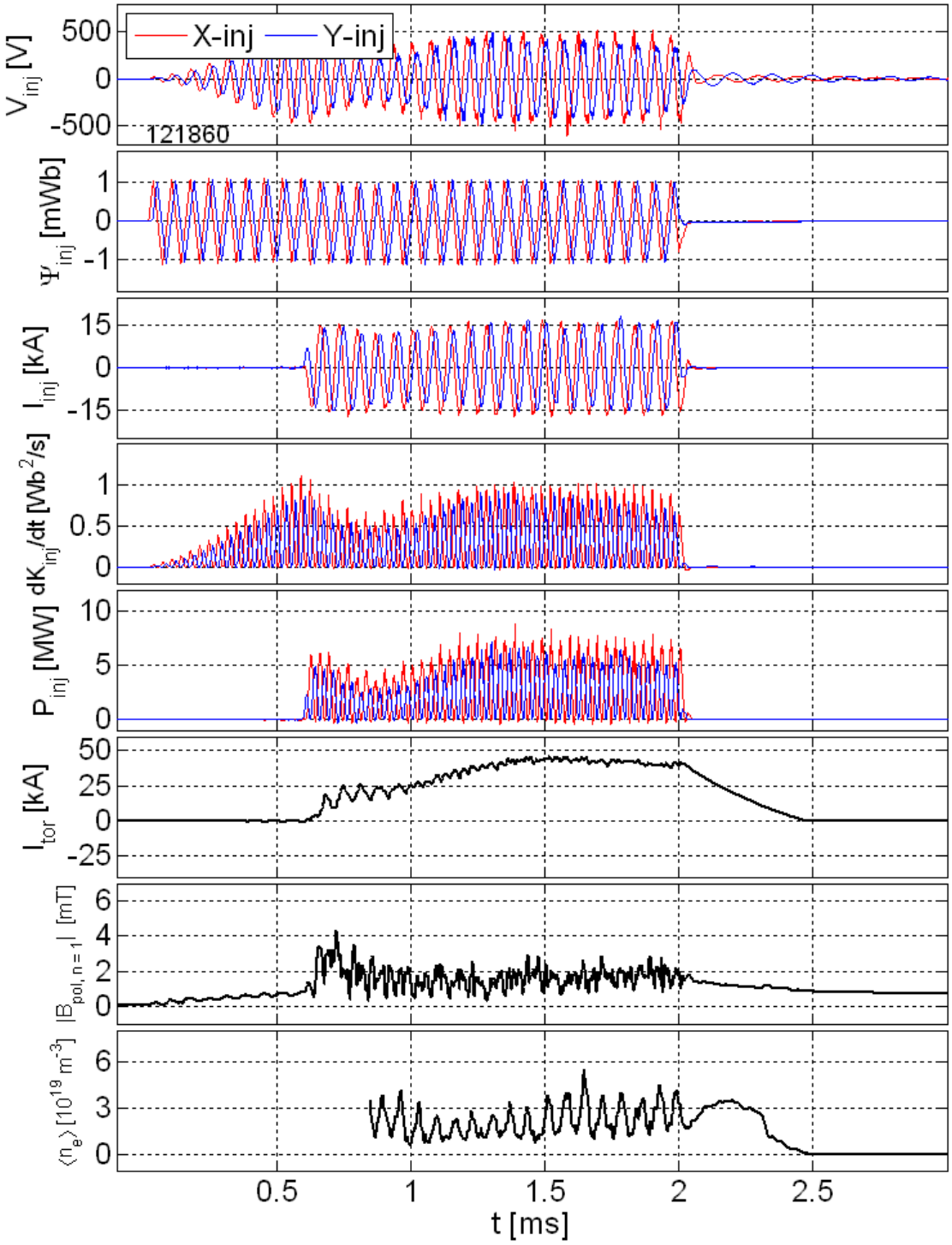

Figure A.8: Injector voltage, injector flux, injector current, helicity injection rate, injected power, toroidal current, n = 1 mode amplitude and density for shot 121860.

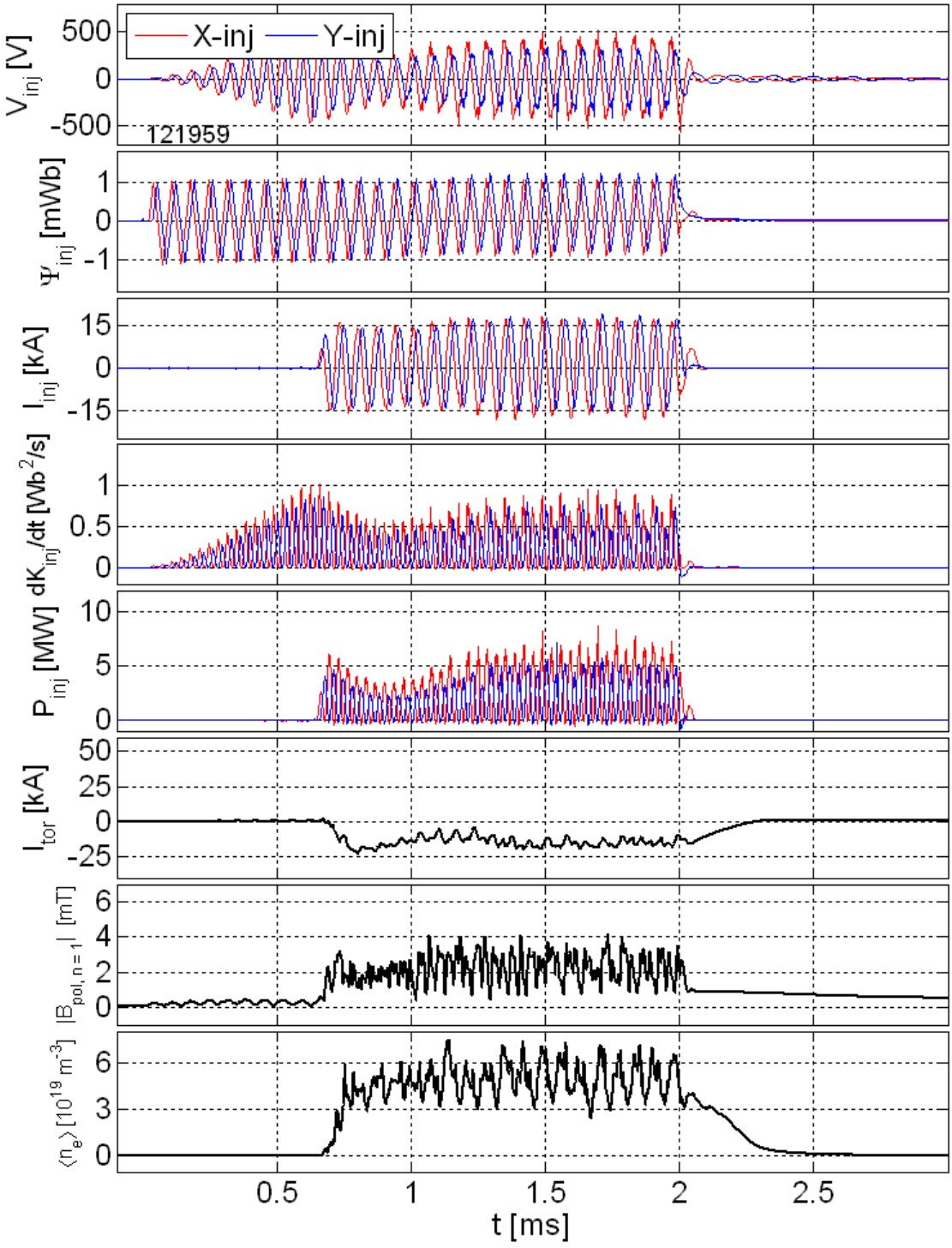

Figure A.9: Injector voltage, injector flux, injector current, helicity injection rate, injected power, toroidal current, n = 1 mode amplitude and density for shot 121959.

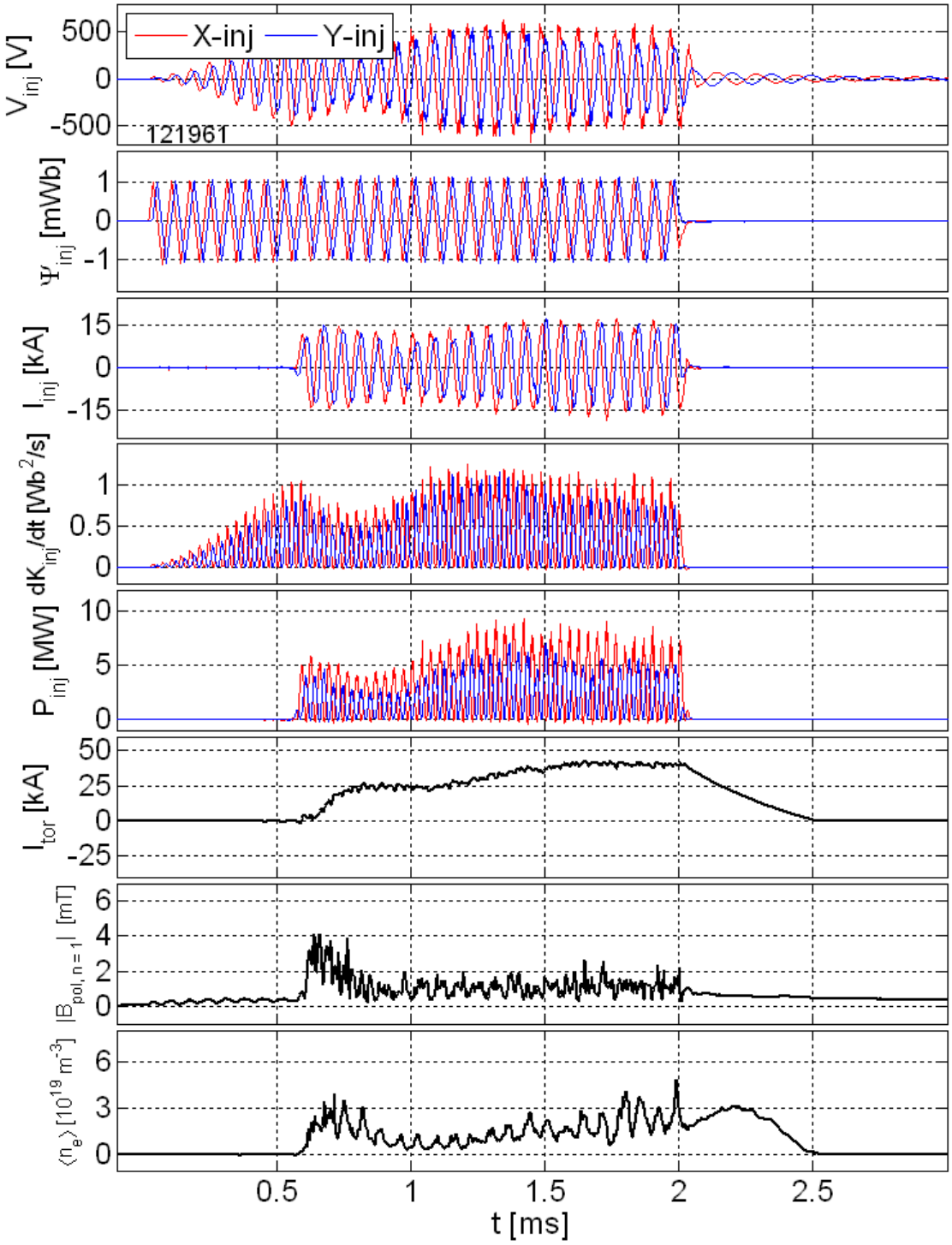

Figure A.10: Injector voltage, injector flux, injector current, helicity injection rate, injected power, toroidal current, n = 1 mode amplitude and density for shot 121961.

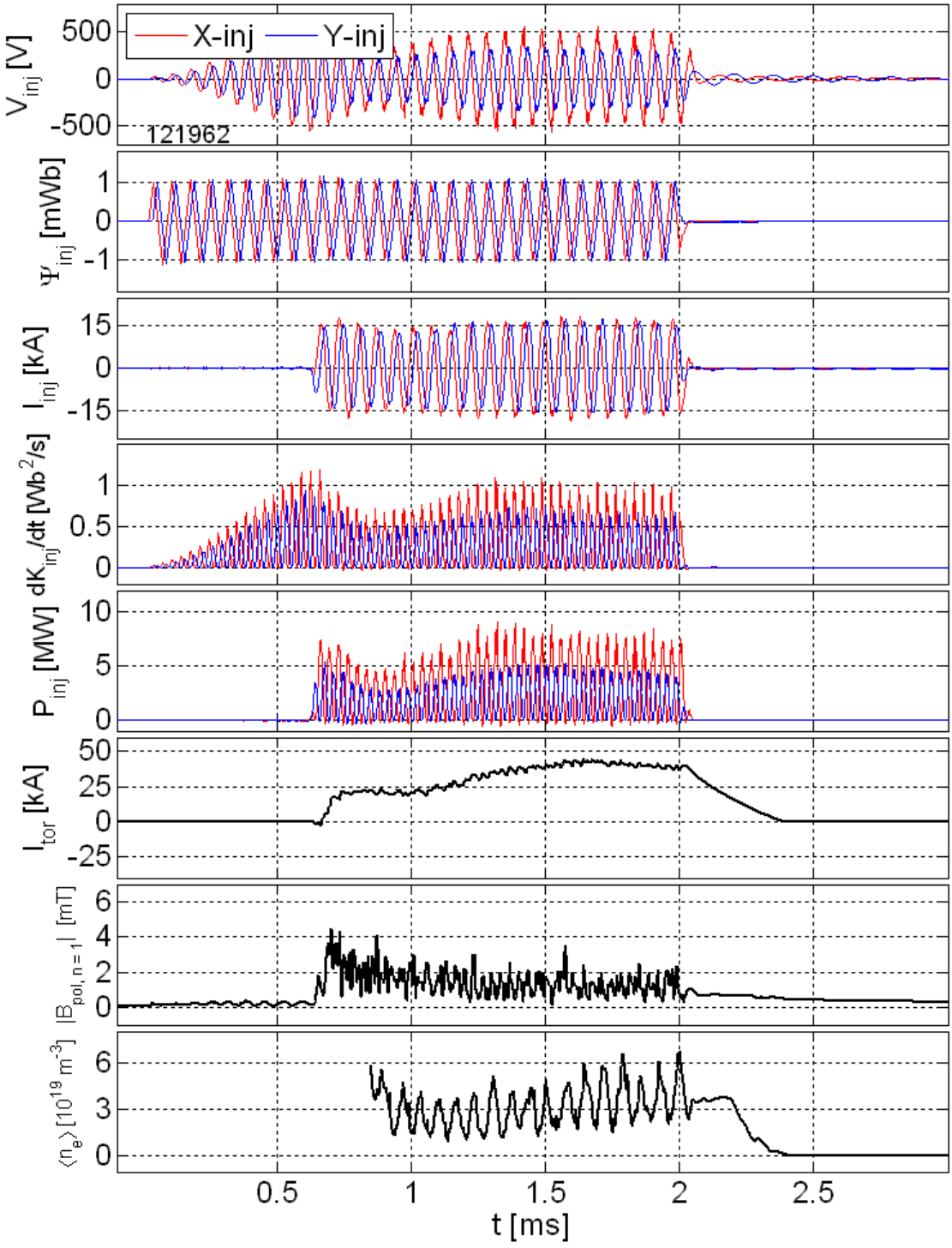

Figure A.11: Injector voltage, injector flux, injector current, helicity injection rate, injected power, toroidal current, n = 1 mode amplitude and density for shot 121962.

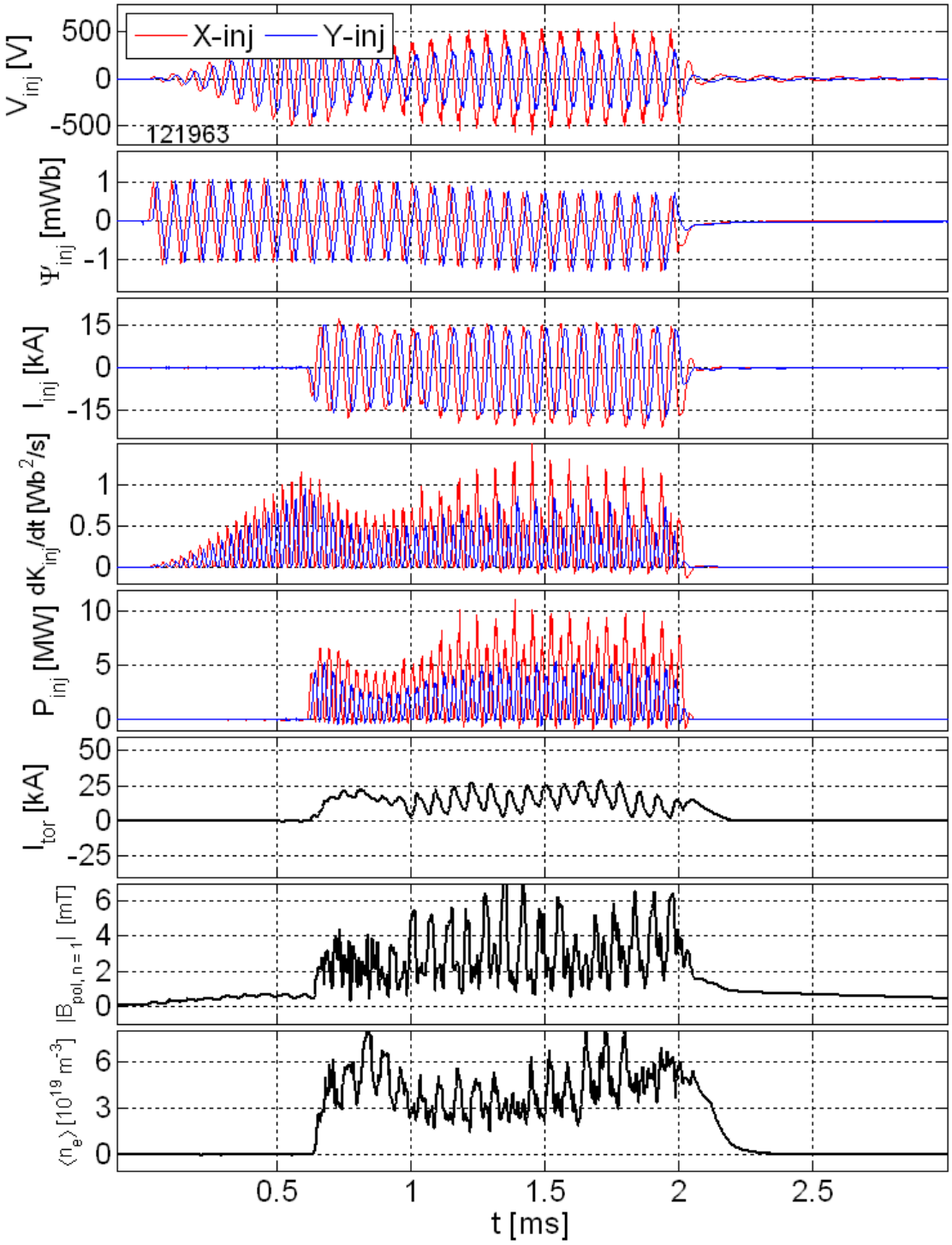

Figure A.12: Injector voltage, injector flux, injector current, helicity injection rate, injected power, toroidal current, n = 1 mode amplitude and density for shot 121963.

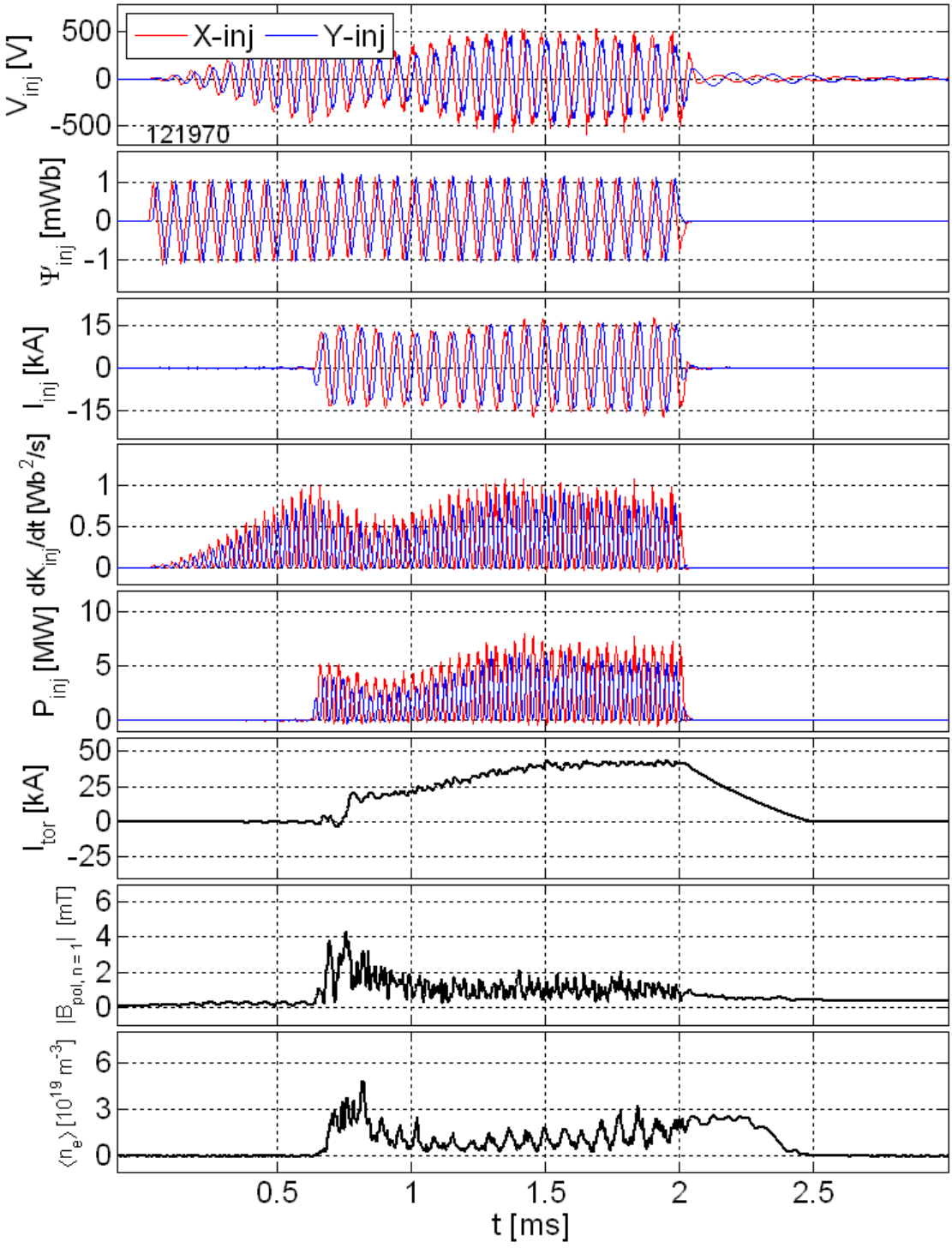

Figure A.13: Injector voltage, injector flux, injector current, helicity injection rate, injected power, toroidal current, n = 1 mode amplitude and density for shot 121970.

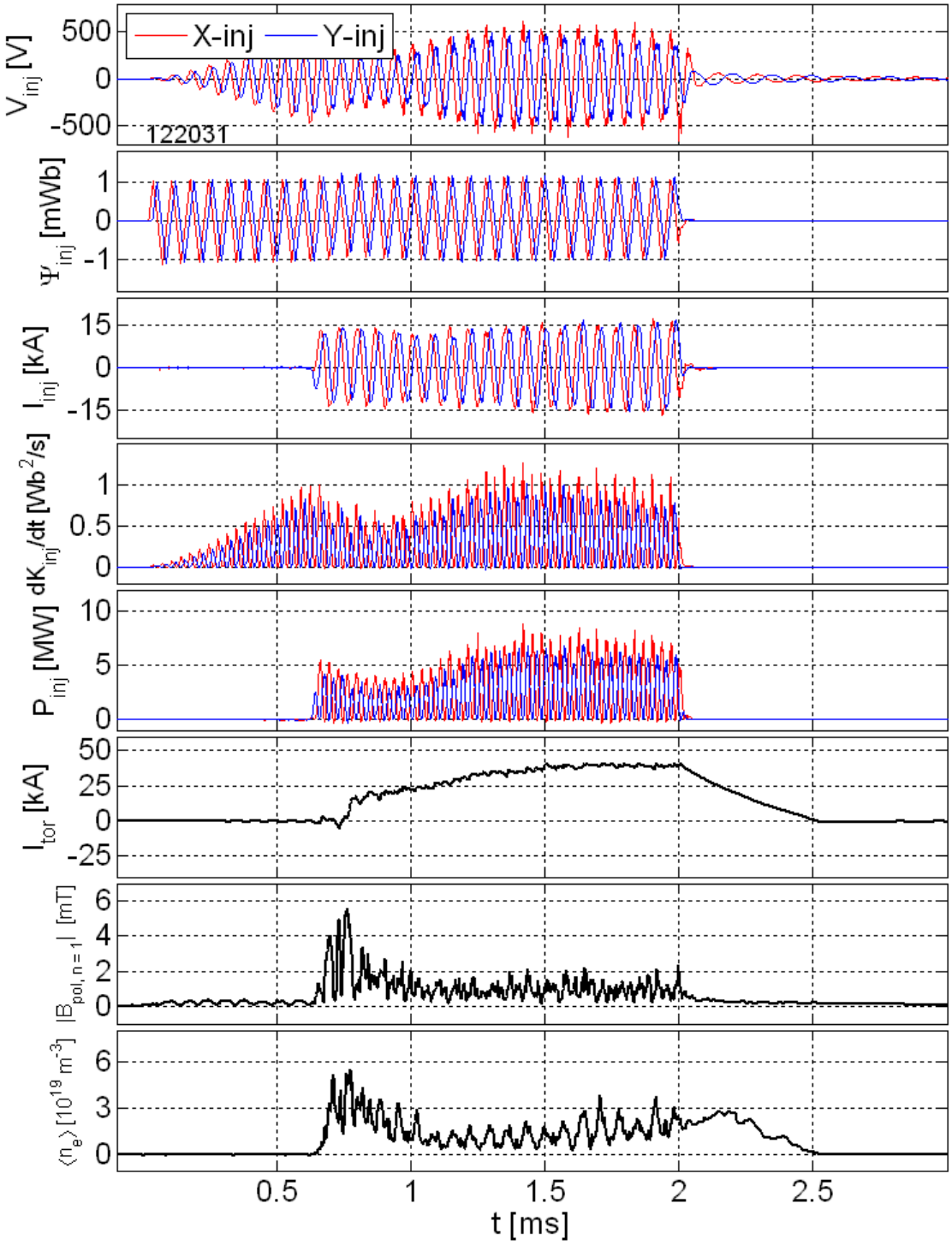

Figure A.14: Injector voltage, injector flux, injector current, helicity injection rate, injected power, toroidal current, n = 1 mode amplitude and density for shot 122031.

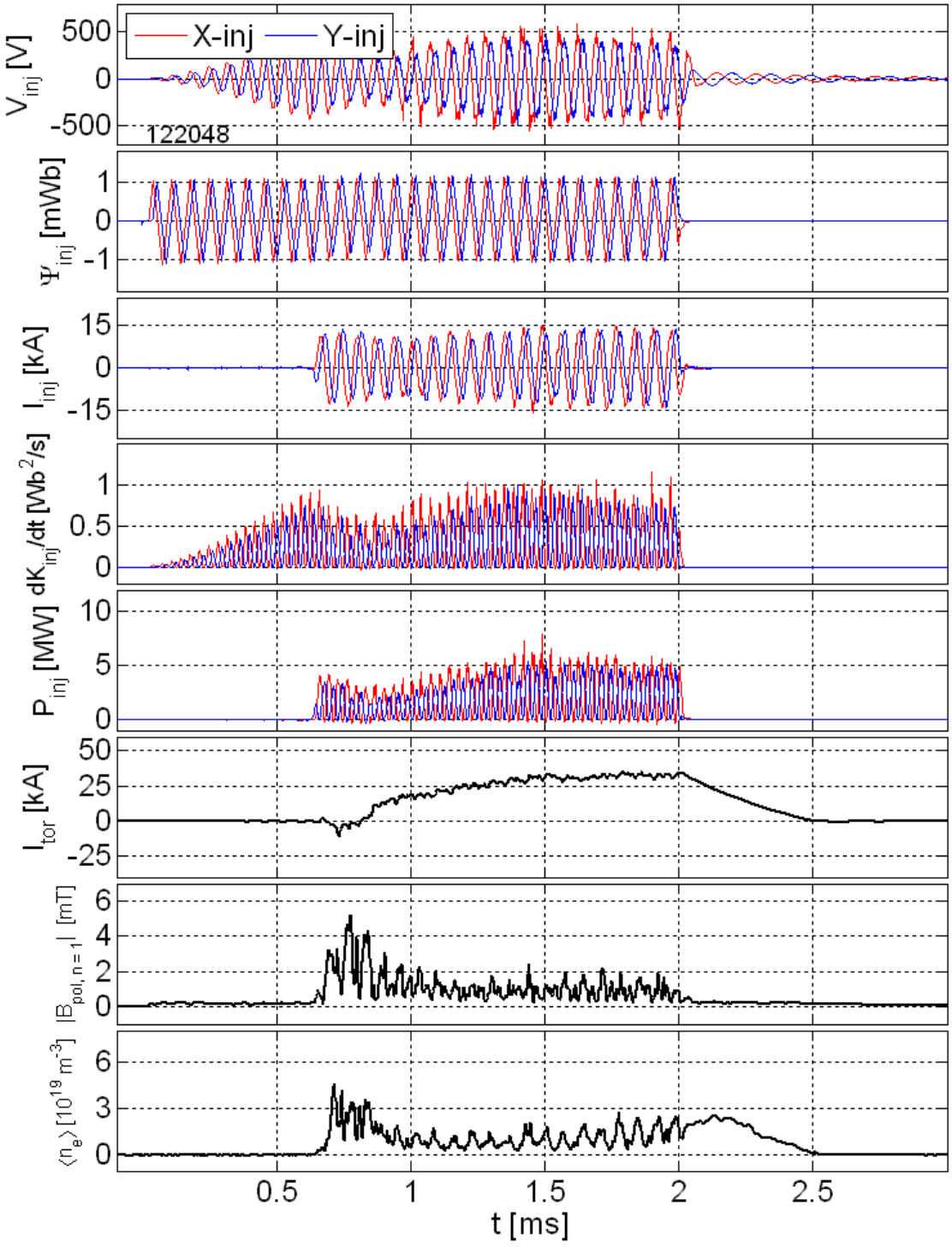

Figure A.15: Injector voltage, injector flux, injector current, helicity injection rate, injected power, toroidal current, n = 1 mode amplitude and density for shot 122048.

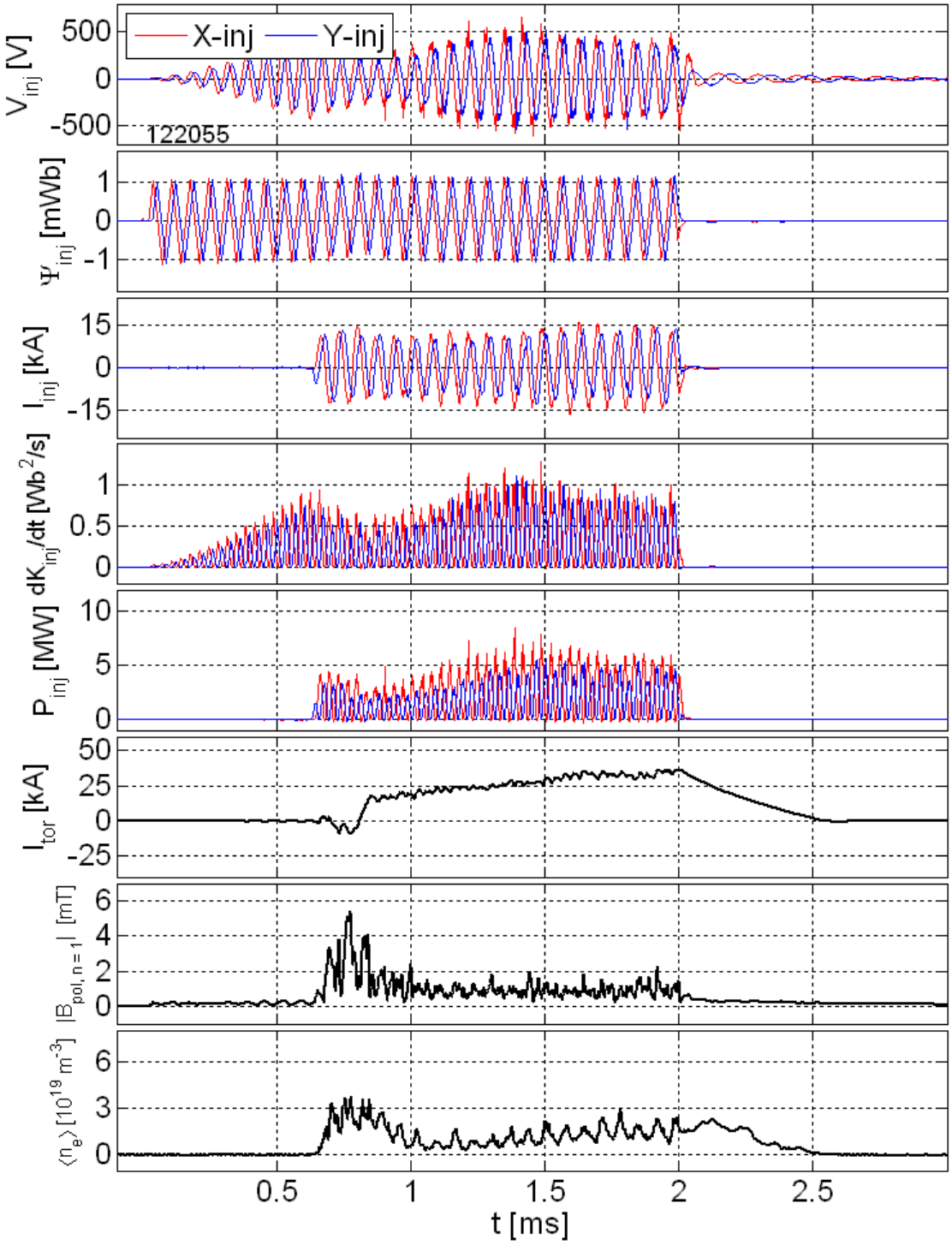

Figure A.16: Injector voltage, injector flux, injector current, helicity injection rate, injected power, toroidal current, n = 1 mode amplitude and density for shot 122055.

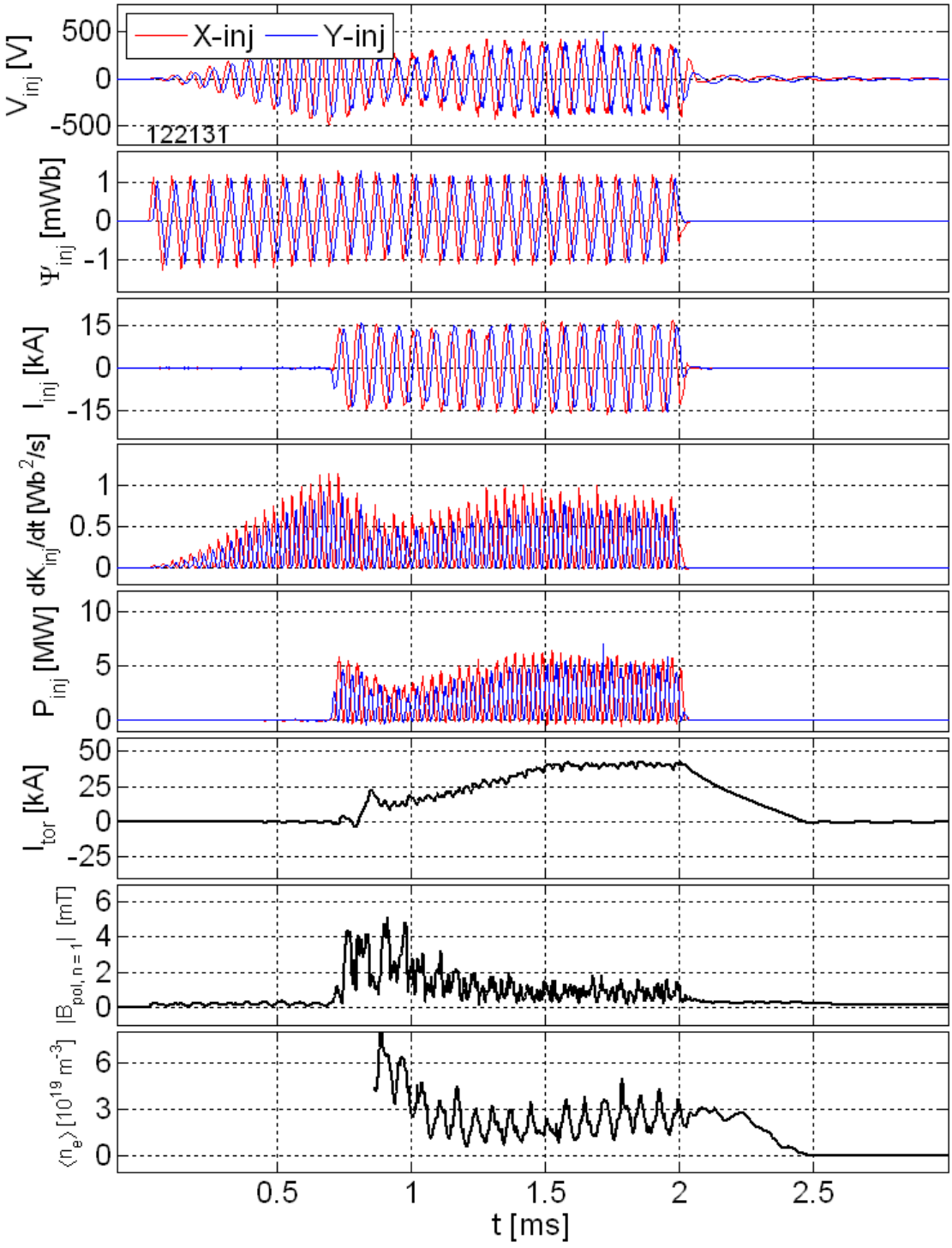

Figure A.17: Injector voltage, injector flux, injector current, helicity injection rate, injected power, toroidal current, n = 1 mode amplitude and density for shot 122131.

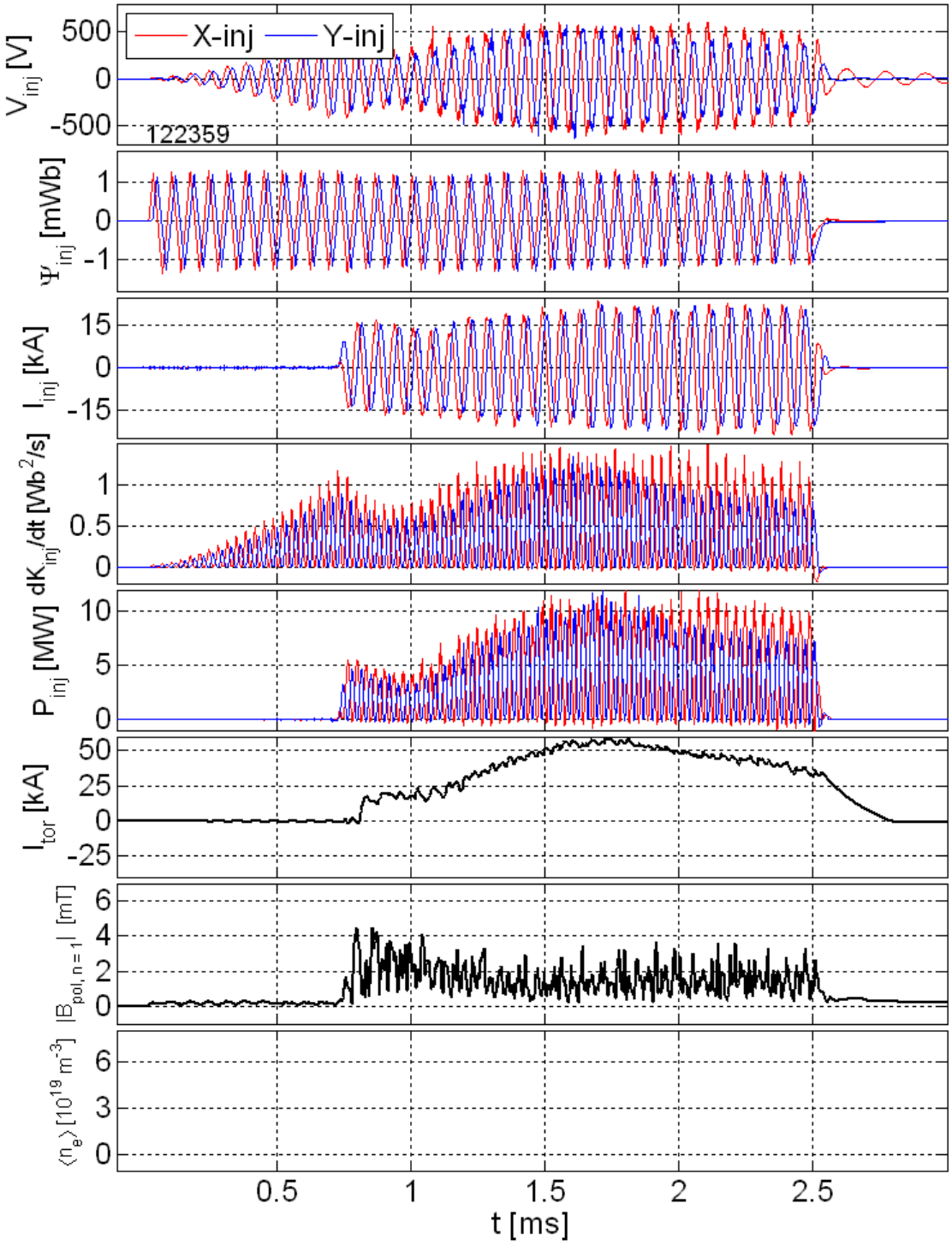

Figure A.18: Injector voltage, injector flux, injector current, helicity injection rate, injected power, toroidal current and n = 1 mode amplitude for shot 122359.

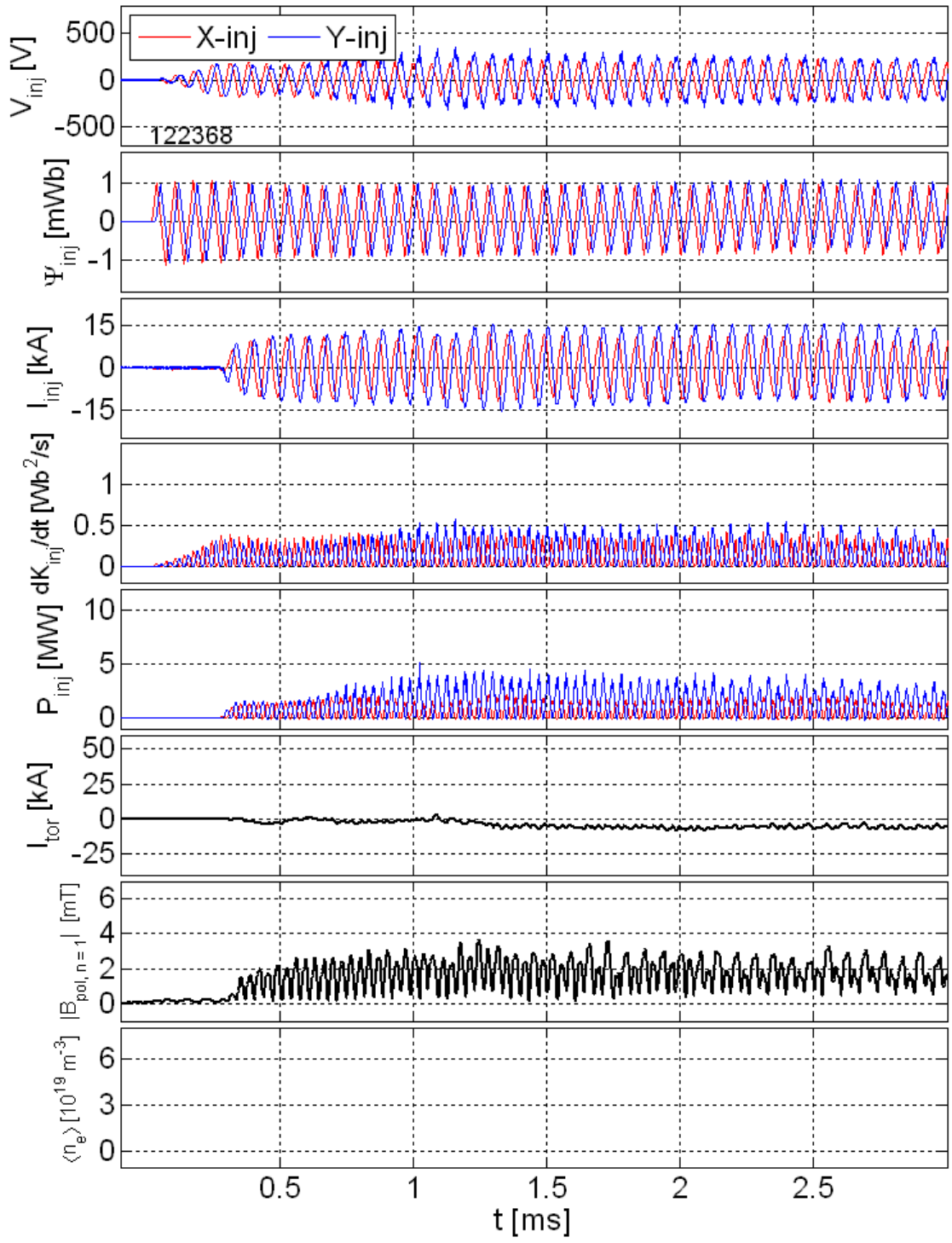

Figure A.19: Injector voltage, injector flux, injector current, helicity injection rate, injected power, toroidal current and n = 1 mode amplitude for shot 122368.

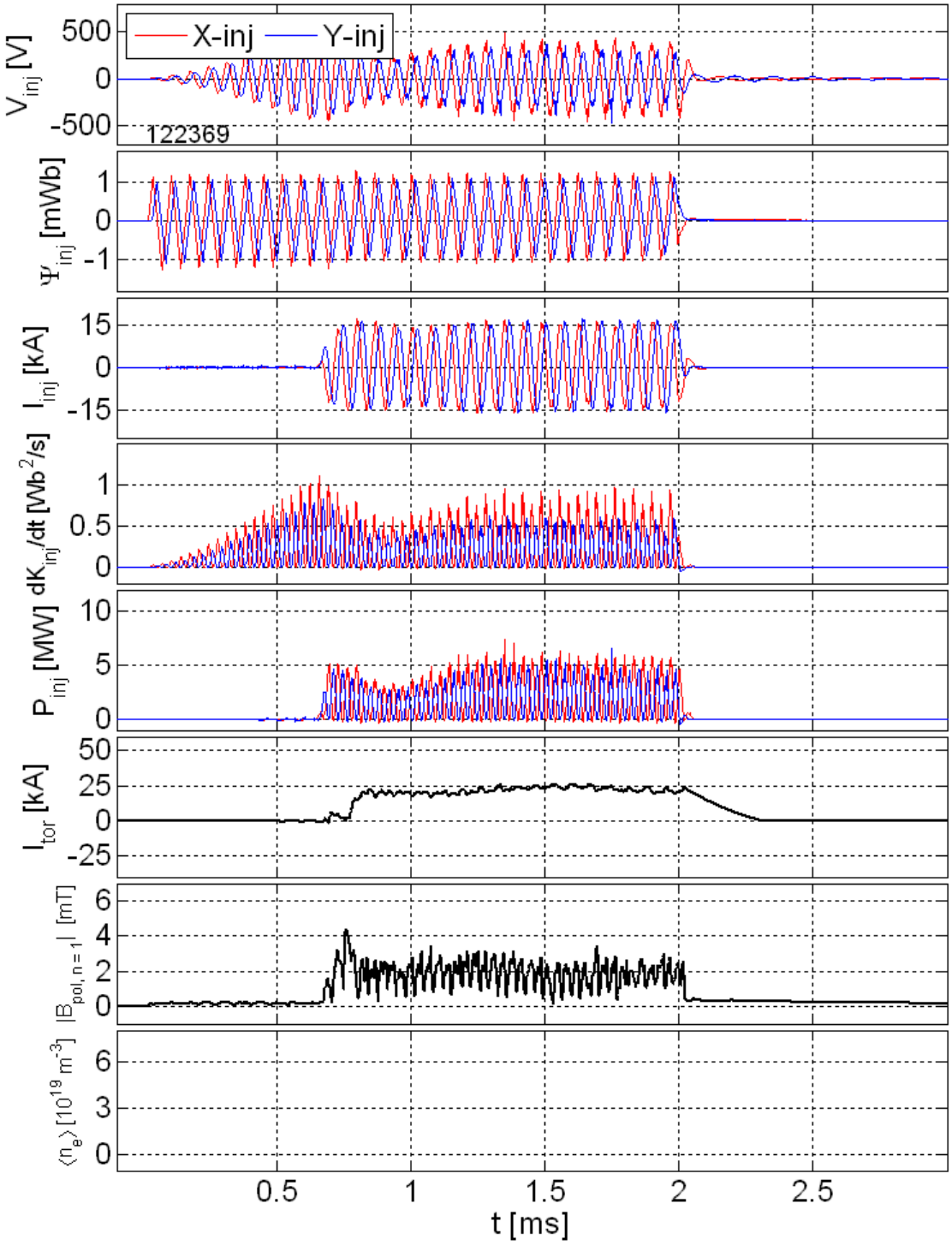

Figure A.20: Injector voltage, injector flux, injector current, helicity injection rate, injected power, toroidal current and n = 1 mode amplitude for shot 122369.

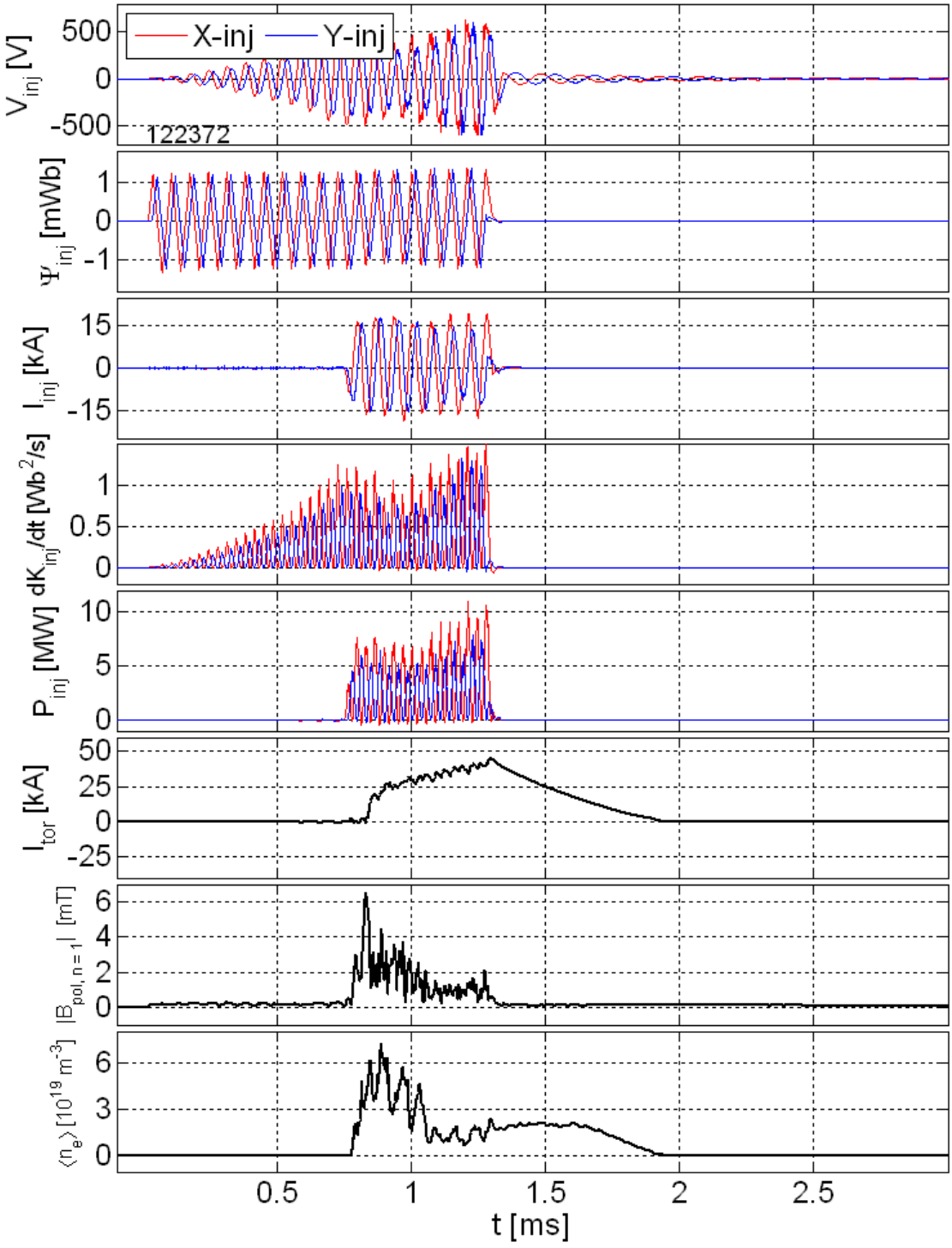

Figure A.21: Injector voltage, injector flux, injector current, helicity injection rate, injected power, toroidal current, n = 1 mode amplitude and density for shot 122372.

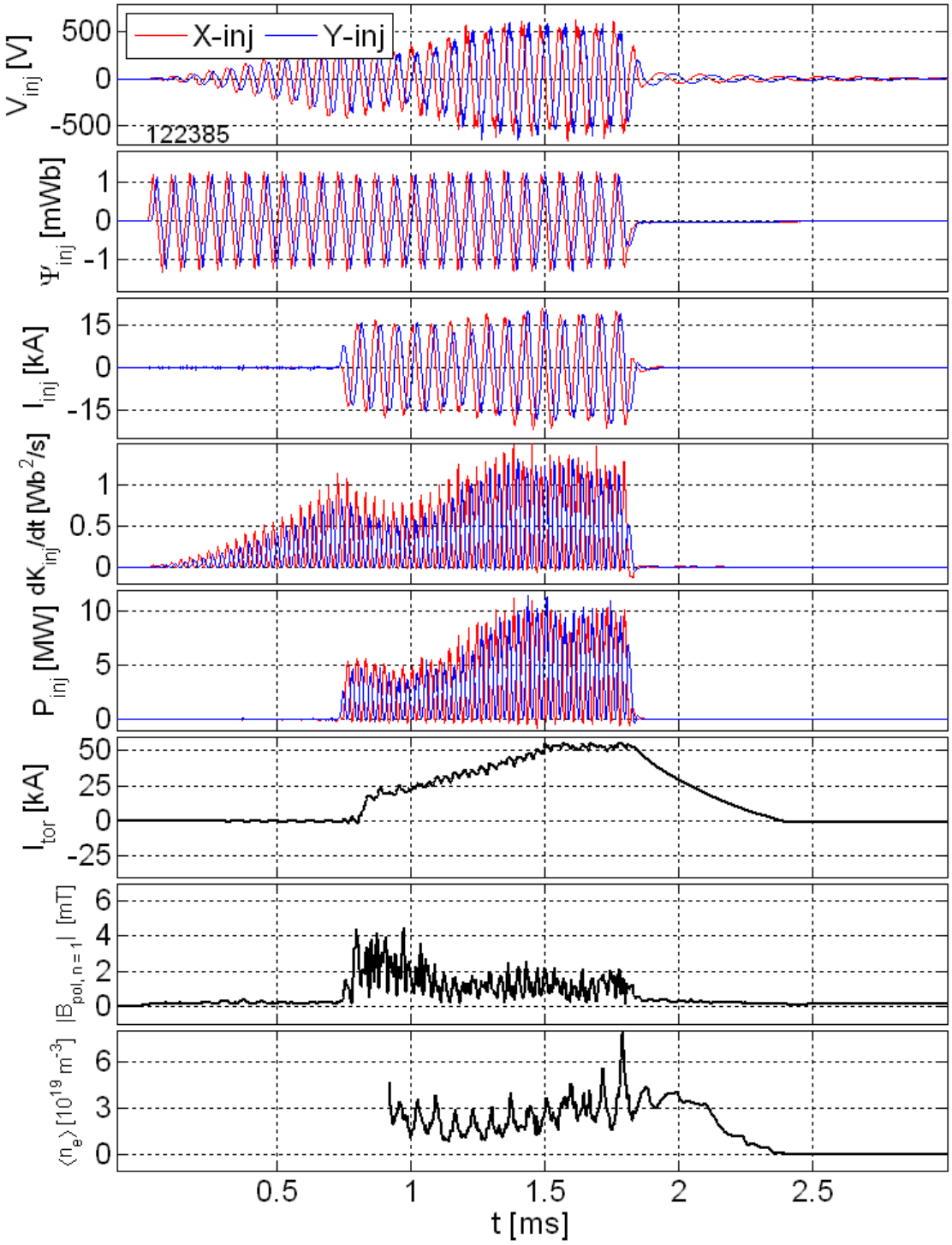

Figure A.22: Injector voltage, injector flux, injector current, helicity injection rate, injected power, toroidal current, n = 1 mode amplitude and density for shot 122385.

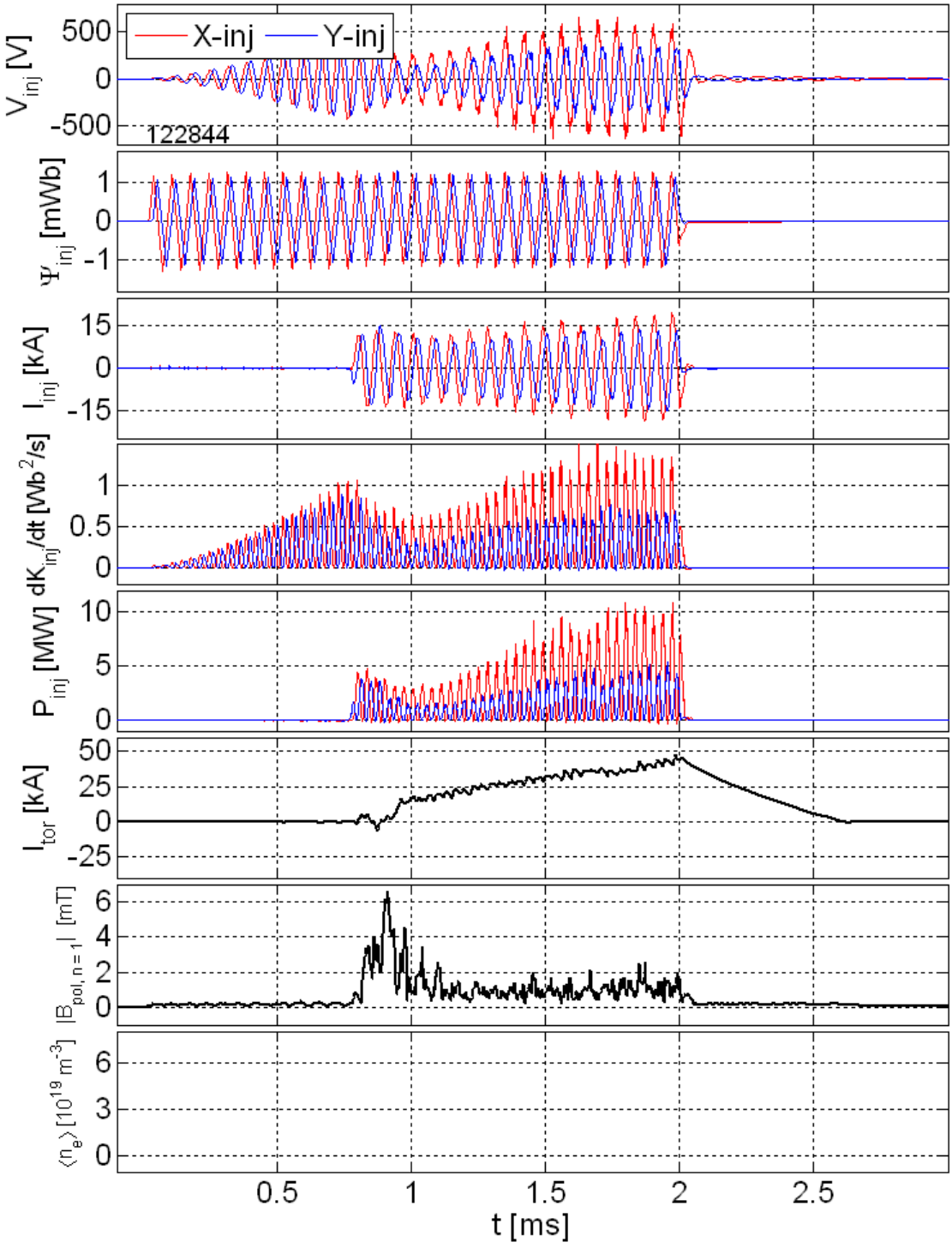

Figure A.23: Injector voltage, injector flux, injector current, helicity injection rate, injected power, toroidal current and n = 1 mode amplitude for shot 122844.

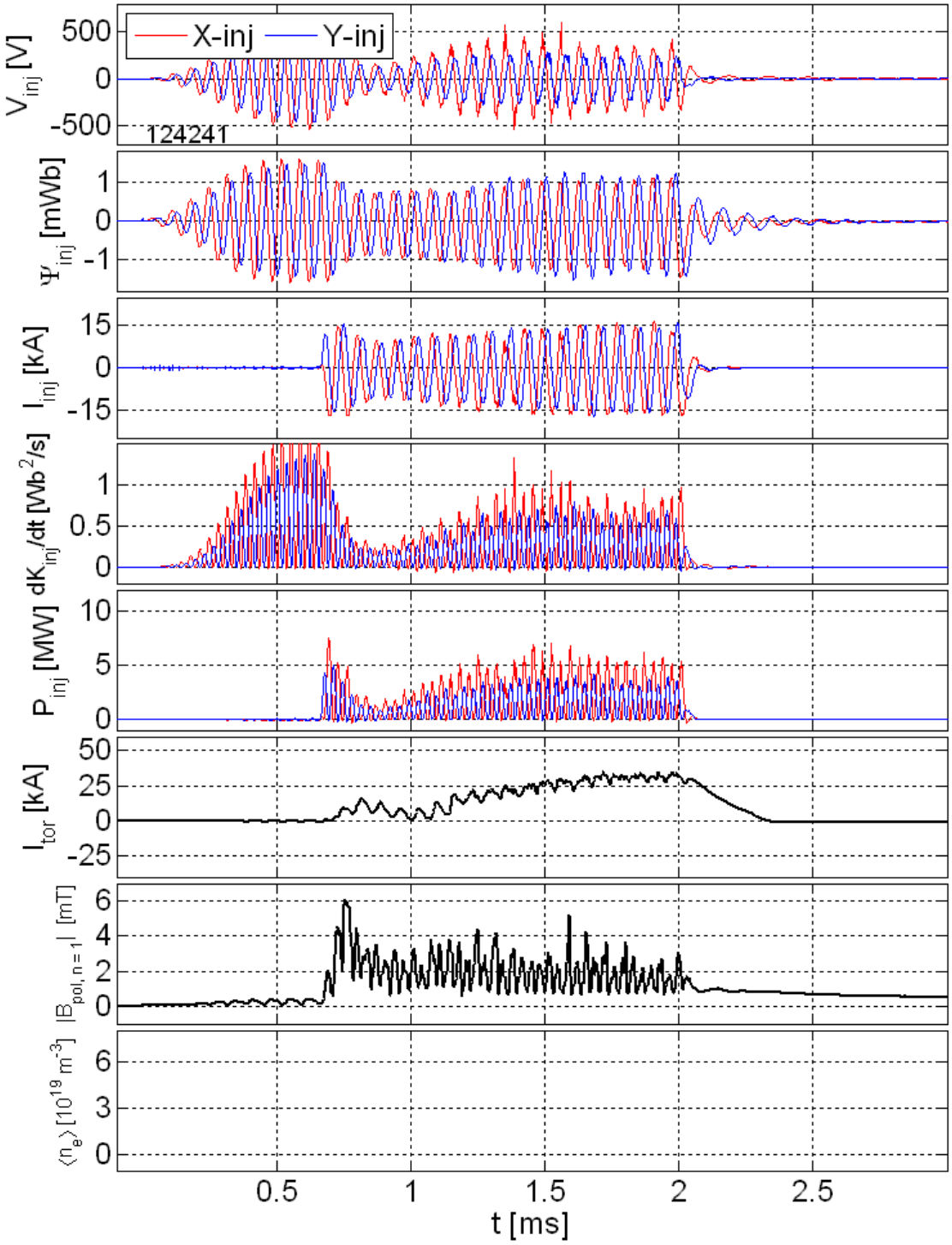

Figure A.24: Injector voltage, injector flux, injector current, helicity injection rate, injected power, toroidal current and n = 1 mode amplitude for shot 124241.

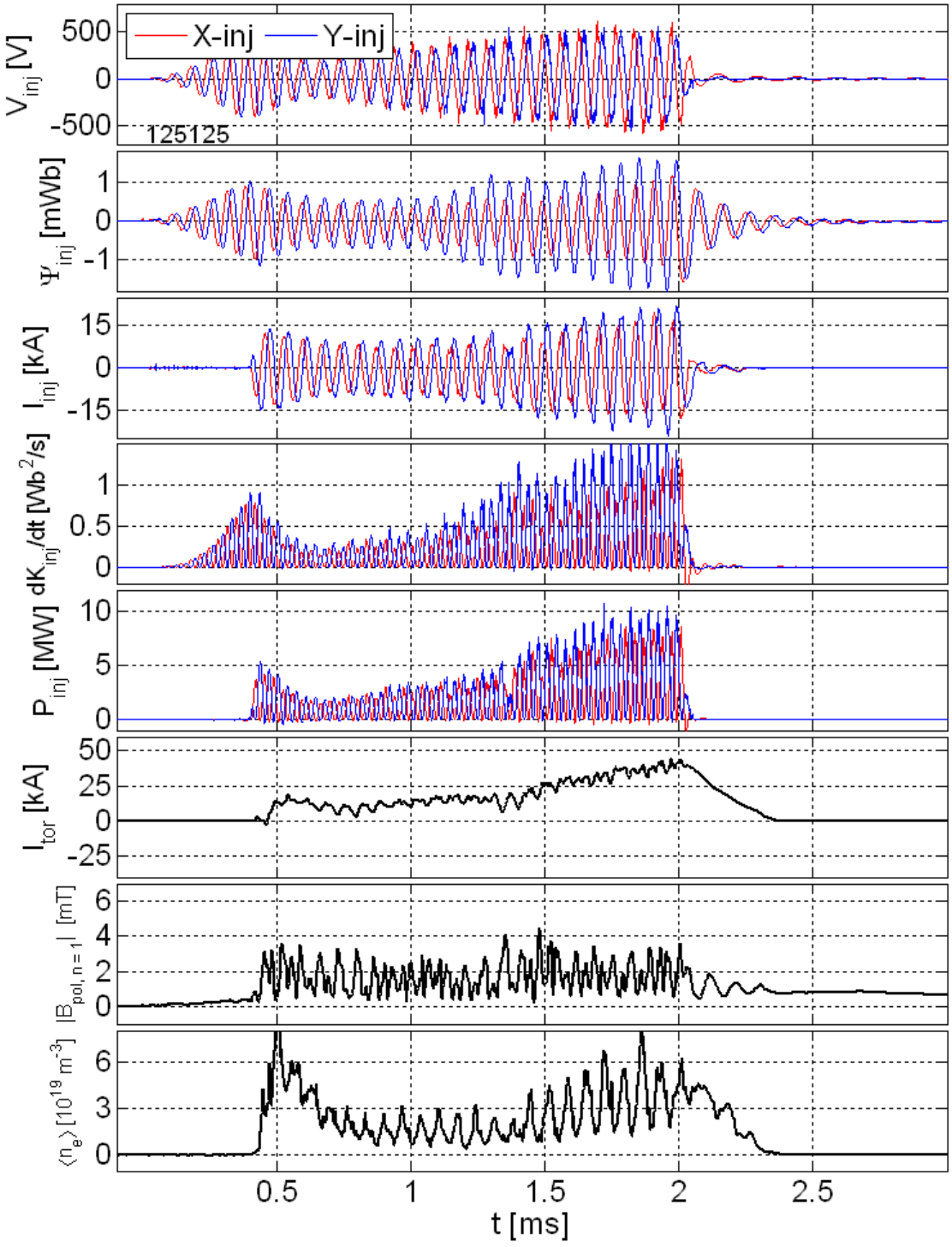

Figure A.25: Injector voltage, injector flux, injector current, helicity injection rate, injected power, toroidal current, n = 1 mode amplitude and density for shot 125125.

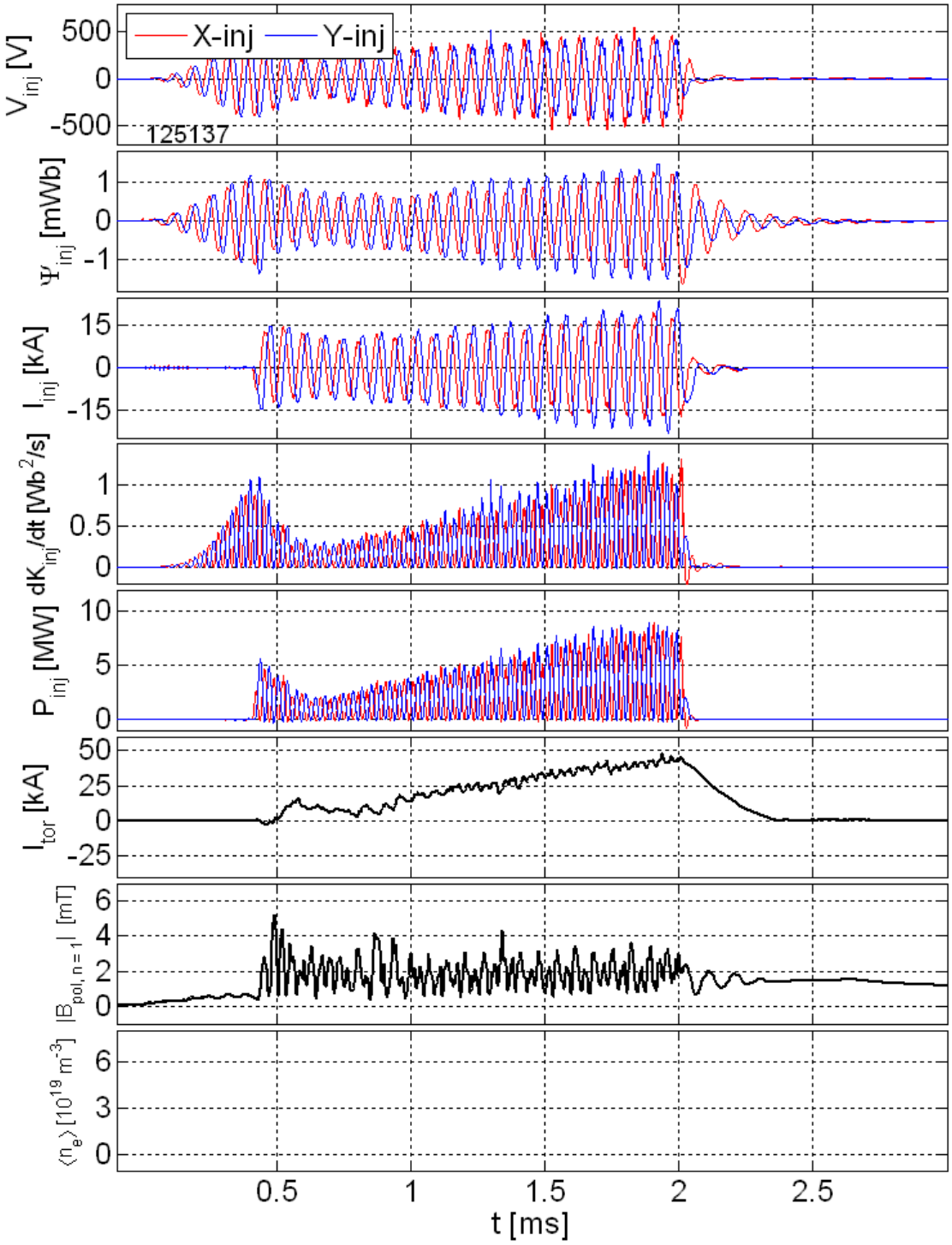

Figure A.26: Injector voltage, injector flux, injector current, helicity injection rate, injected power, toroidal current and n = 1 mode amplitude for shot 125137.

A.2 Extended data set for shot 122385

Shot 122385 is the most heavily studied shot in this thesis. A full data set from the magnetic and spectral diagnostics is presented in this section.

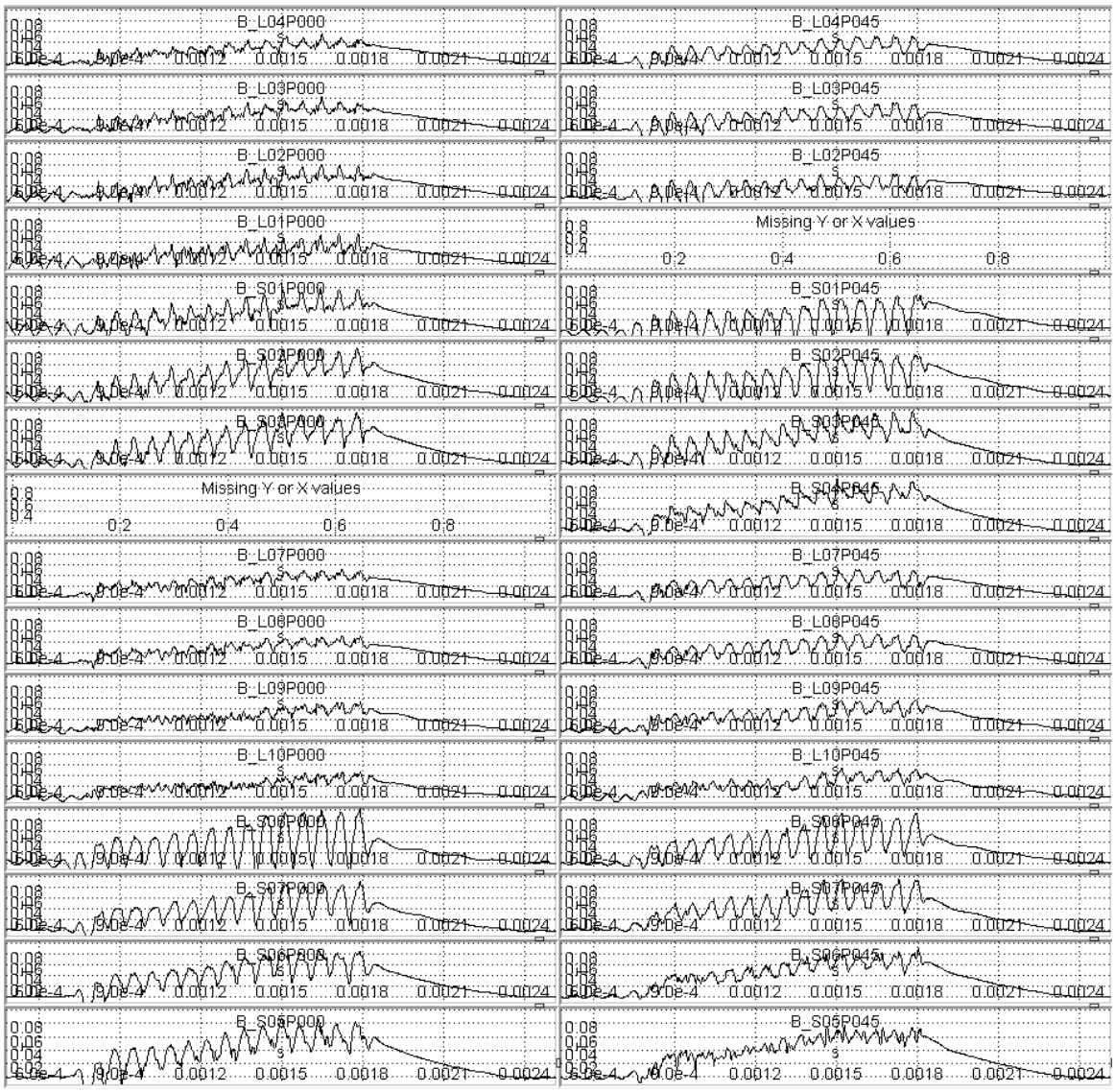

Figure A.27: Poloidal surface probe data at 0° and 45° for shot 122385. All plots are from 0.5 to 2.5 ms and -0.01 to 0.1 T.

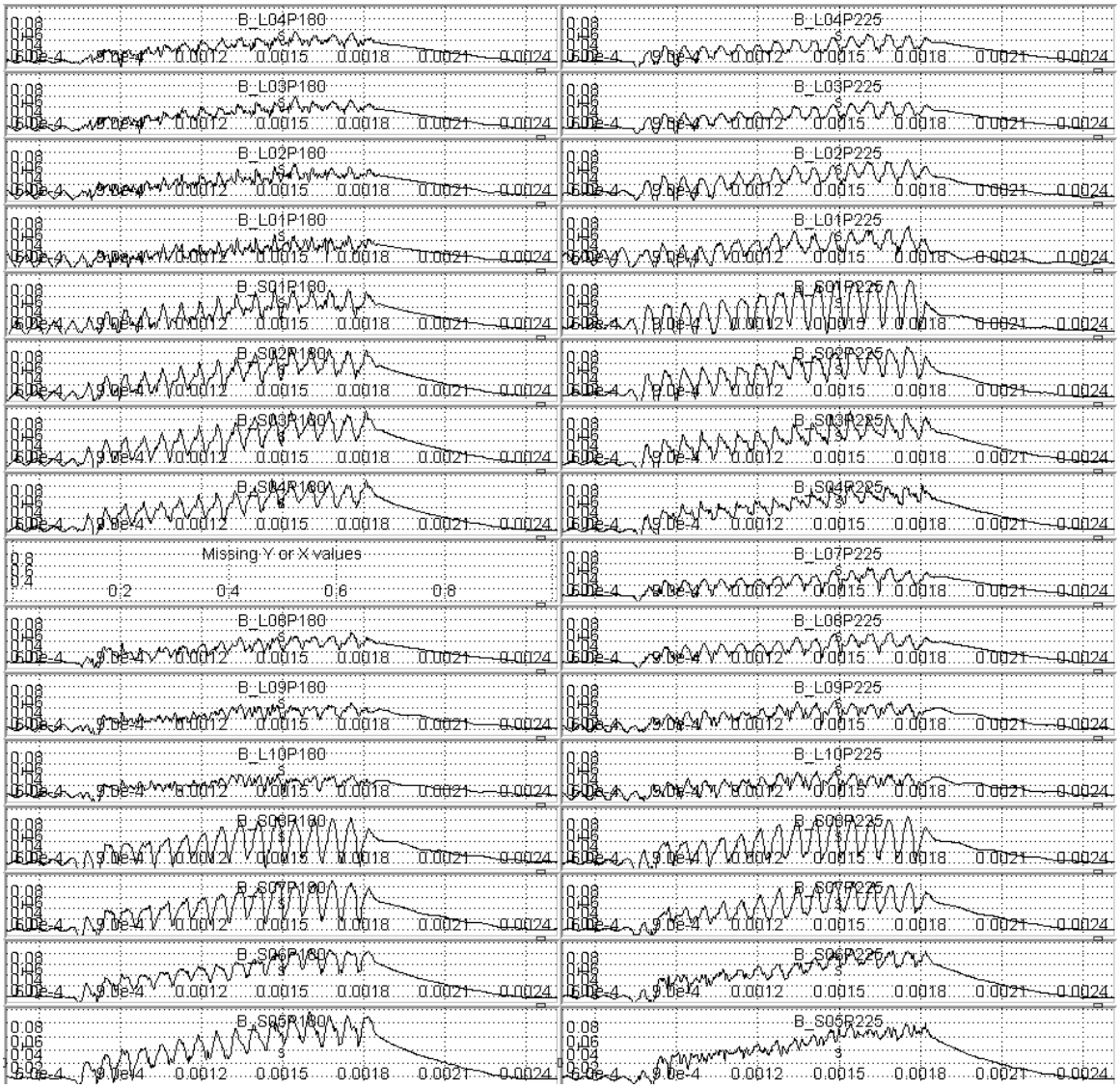

Figure A.28: Poloidal surface probe data at 180° and 225° for shot 122385. All plots are from 0.5 to 2.5 ms and -0.01 to 0.1 T.

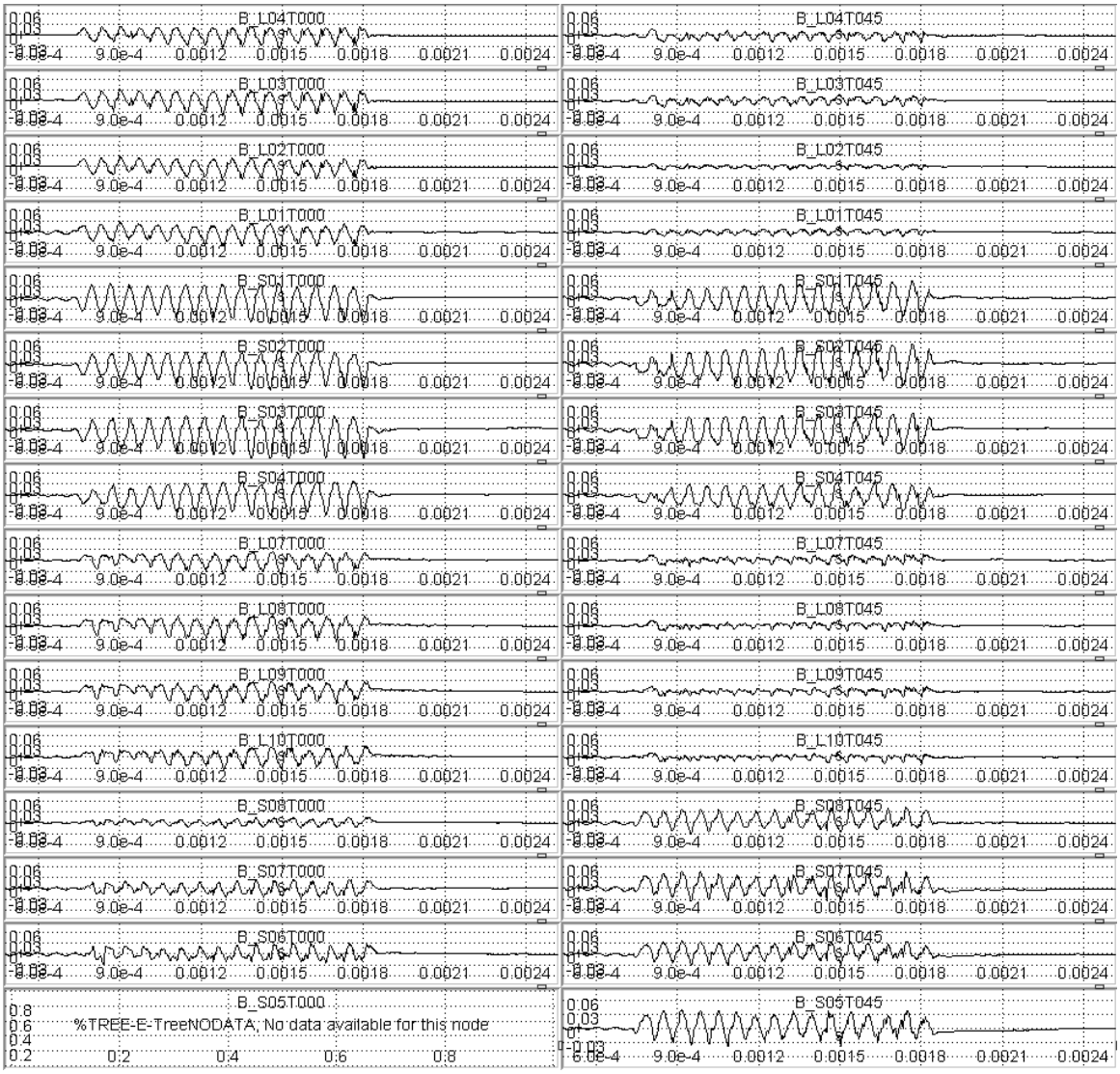

Figure A.29: Toroidal surface probe data at 0° and 45° for shot 122385. All plots are from 0.5 to 2.5 ms and -0.08 to 0.08 T.

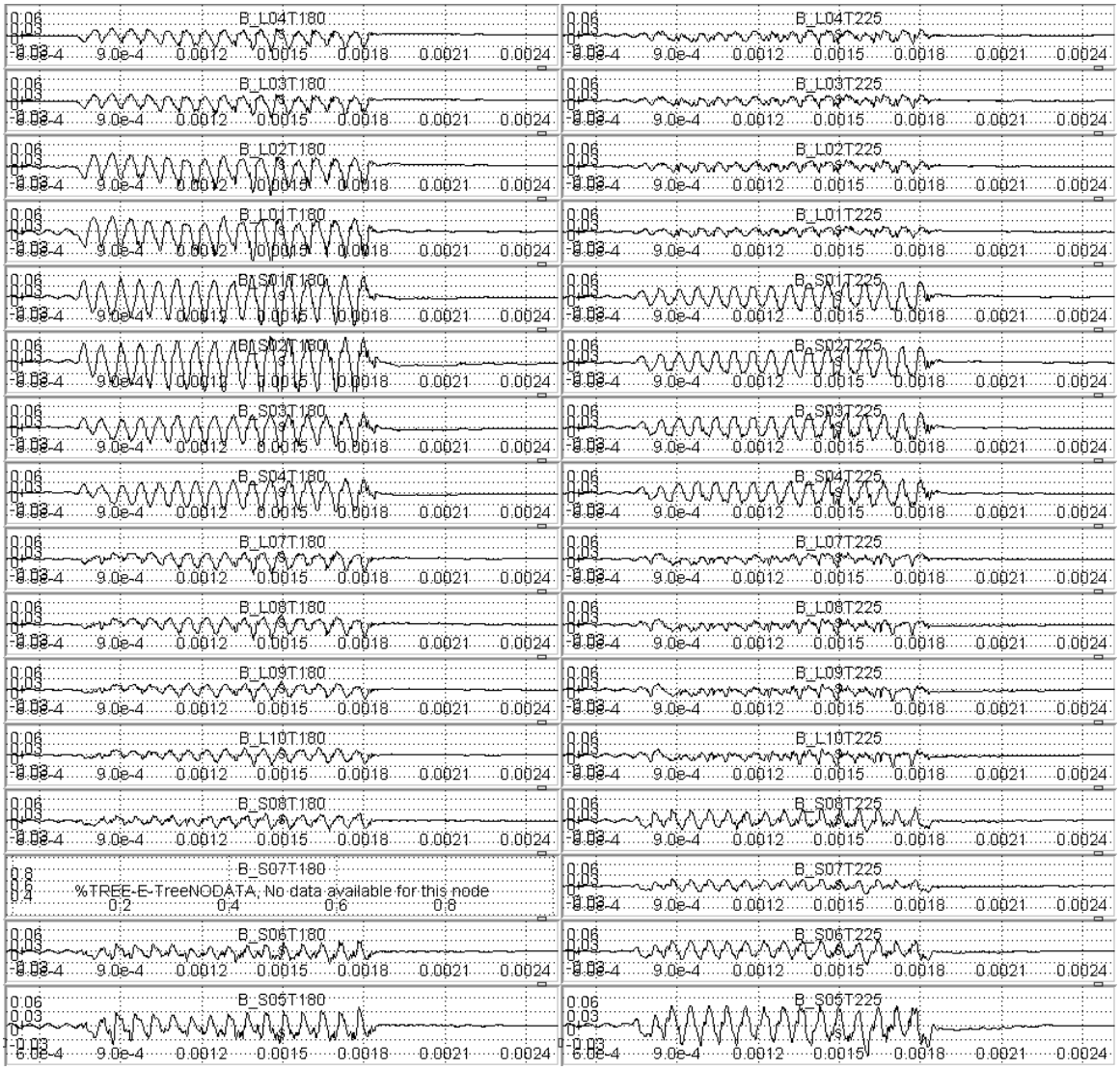

Figure A.30: Toroidal surface probe data at 180° and 225° for shot 122385. All plots are from 0.5 to 2.5 ms and -0.08 to 0.08 T.

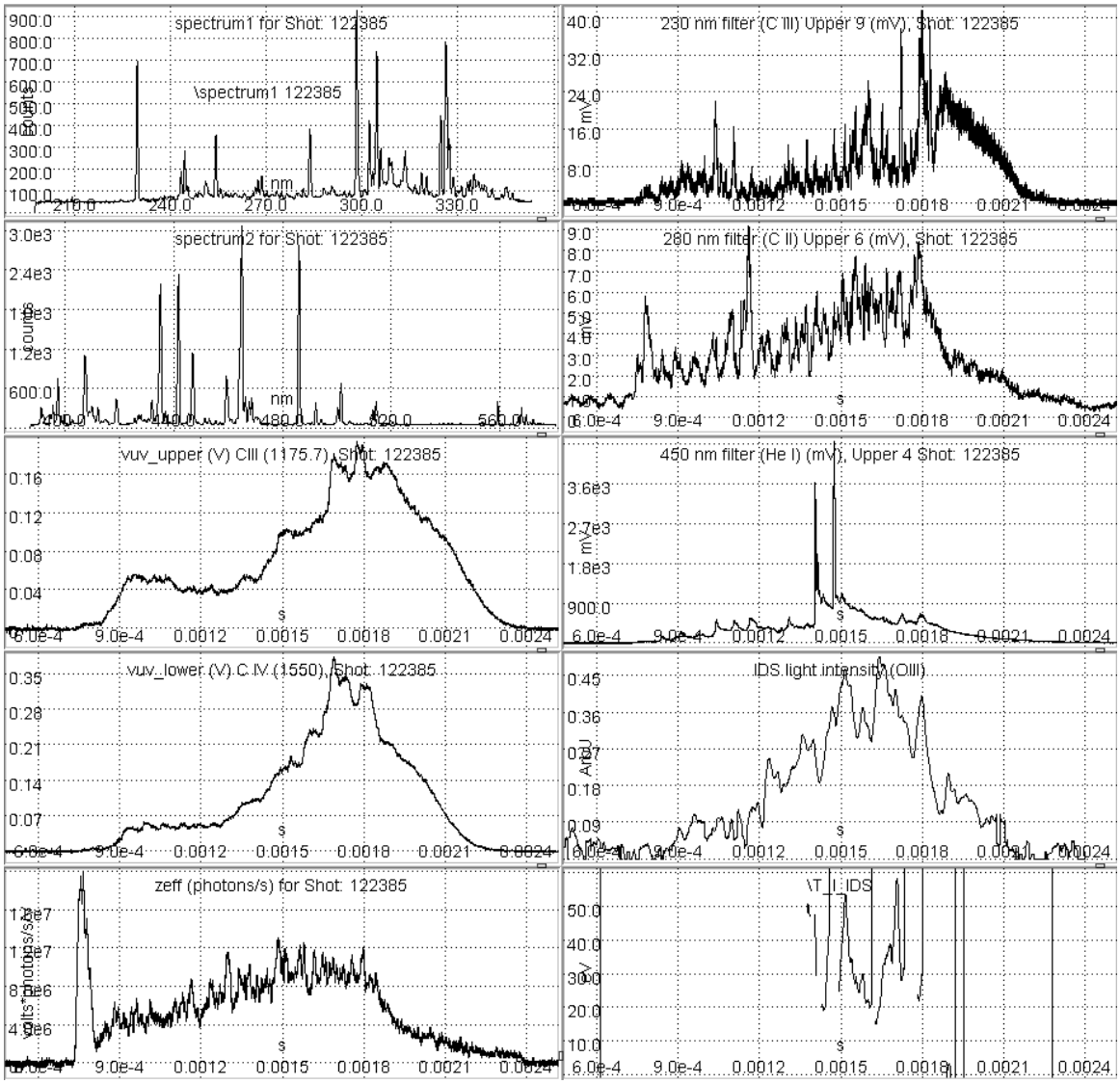

Figure A.31: Spectroscopic data for shot 122385.

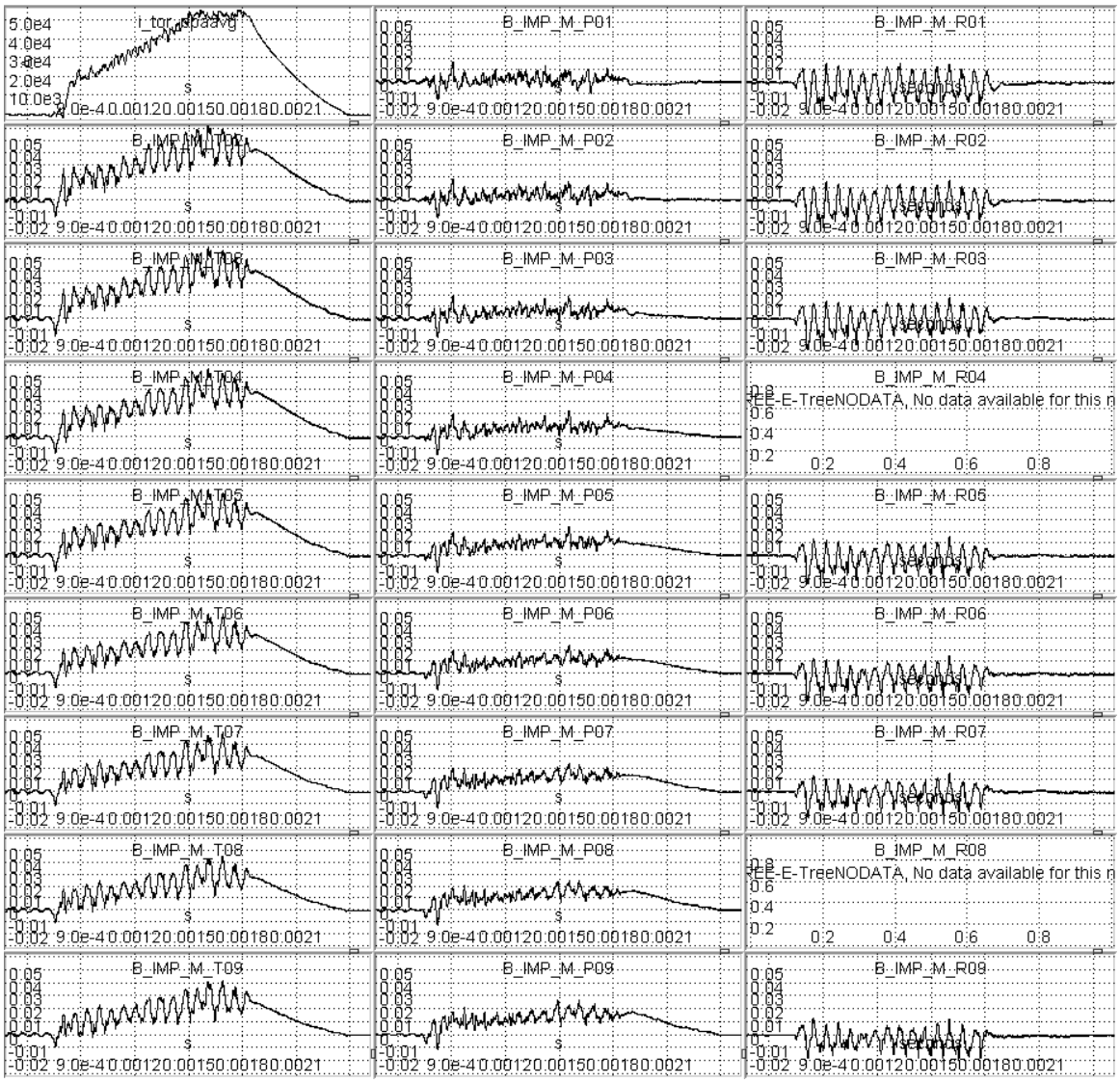

Figure A.32: Internal probe data for probes 1 - 9 for shot 122385. All plots are from 0.5 to 2.5 ms and -0.03 to 0.06 T.

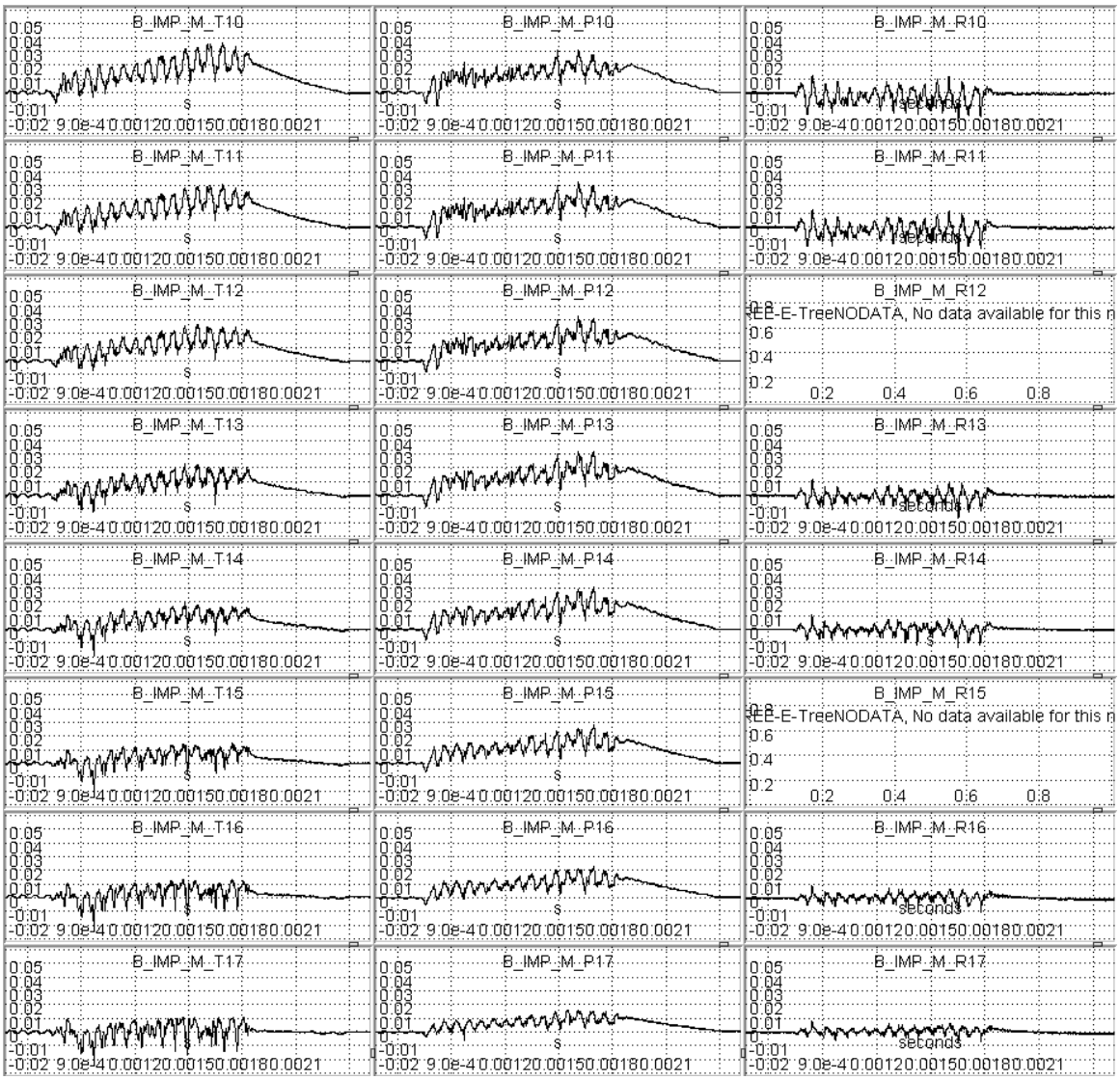

Figure A.33: Internal probe data for probes 10 - 17 for shot 122385. All plots are from 0.5 to 2.5 ms and -0.03 to 0.06 T.

Appendix B

MATLAB ANALYSIS CODE

This appendix has the MATLAB code used for the data analysis in this dissertation.

B.1 Read in generic data from the HIT-SI MDSPlus database

This function is located at

`bvictor\Matlab\filters\gen_data_in_smart.m`

```
function [t, dt, x] = gen_data_in_smart(sig)

% this gets generic data from landau

x = mdsvalue(sig);
if isa(x, 'char')
    t = NaN;
    dt = NaN;
    x = NaN;
elseif isa(x, 'numeric')
    dt = mdsvalue(['samplinginterval(' sig ')']);
    tmin = mdsvalue(['minval(dim_of(' sig '))']);
    tlength = mdsvalue(['size(dim_of(' sig '))']);
    t = tmin + dt*((1: tlength) - 1);
end
```

B.2 Reads in internal probe data from the HIT-SI MDSPlus database

This function is located at

```
bvictor\Matlab\filters\imp_data_in_construct.m
```

```
function [cb_field, ins_depth] = imp_data_in_construct(array, ...
    tin, filterdata, f_order, low_filt, high_filt, shot, shift, dafi)

% using a slanted baseline and matrix

% this gets the IMP data from landau

probe = ['01'; '02'; '03'; '04'; '05'; '06'; ...
    '07'; '08'; '09'; '10'; '11'; '12'; ...
    '13'; '14'; '15'; '16'; '17'];

N = length(probe(:,1));

dir = ['R'; 'P'; 'T'];
% r is in the i direction
% p is in the j direction
% t is in the k direction

cb_field = zeros(length(dir), N, length(tin));
ins_depth = zeros(1, N);

% calibration factors based on dafi impedence.
% these values good from shot 121973
pol_scale = [1.02;
    1.016;
    1.014;
    1.018;
    1.013;
    1.022;
    1.027;
    1.024;
    1.025;
    1.022;
    1.02;
    1.028;
    1.029;
    1.022;
    1.022;
    1.024;
    1.021];

% there is no first toroidal probe
```

```
tor_scale = [0;
    1.025;
    1.012;
    1.014;
    1.008;
    1.022;
    1.024;
    1.024;
    1.023;
    1.012;
    1.019;
    1.02;
    1.022;
    1.019;
    1.021;
    1.026;
    1.025];


for j = 1: N
    pnode = ['\B_IMP_' array '_P' probe(j, :) ':b_winding'];
    tnode = ['\B_IMP_' array '_T' probe(j, :) ':b_winding'];
    rnode = ['\B_IMP_' array '_R' probe(j, :)];
    dtp = mdsvalue(['samplinginterval(' pnode ')']);
    dtt = mdsvalue(['samplinginterval(' tnode ')']);
    dtr = mdsvalue(['samplinginterval(' rnode ')']);
    tminp = mdsvalue(['minval(dim_of(' pnode '))']);
    tmint = mdsvalue(['minval(dim_of(' tnode '))']);
    tminr = mdsvalue(['minval(dim_of(' rnode '))']);
    tlengthp = mdsvalue(['size(dim_of(' pnode '))']);
    tlengtht = mdsvalue(['size(dim_of(' tnode '))']);
    tlengthr = mdsvalue(['size(dim_of(' rnode '))']);
    if isa(tminr, 'char')
        cbw_rad = zeros(1, length(tin))*NaN;
    elseif isa(tminr, 'numeric')
        trad = tminr + dtr*((1: tlengthr) - 1);
        % shifting time base here for digi differences
        if strcmp(shift, 'shift_time') == 1
            trad = imp_time_shift(trad, shot, array, probe(j,:), 'R');
        end
        bw_rad = mdsvalue(['slanted_baseline2(sub_baseline_string("\'
            rnode '"))']);
        if filterdata == 2;
            % bandpass filter
            bw_fil_r = bp_filt(f_order, low_filt, ...
                high_filt, bw_rad, dtr);
        elseif filterdata == 1;
            % lowpass filter
            bw_fil_r = lp_filt(f_order, low_filt, ...
                bw_rad, dtr);
```

```
    elseif filterdata == 0;
        bw_fil_r = bw_rad;
    elseif filterdata == 3;
        % filter at half Nyquist
        bw_fil_r = lp_filt(f_order, 1/dtr/4, ...
            bw_rad, dtr);
    elseif filterdata == 4;
        % inverse bandpass filter
        bw_fil_r = ibp_filt(f_order, low_filt, ...
            high_filt, bw_rad, dtr);
    end
    cbw_rad = interp1(trad, bw_fil_r, tin);
end
if isa(tminp, 'char')
    cbw_pol = zeros(1, length(tin))*NaN;
elseif isa(tminp, 'numeric')
    tpol = tminp + dtp*((1: tlengthp) - 1);
    % shifting time base here for digi differences
    if strcmp(shift, 'shift_time') == 1
        tpol = imp_time_shift(tpol, shot, array, probe(j,:), 'P');
    end
    bw_pol = mdsvalue(['slanted_baseline2(sub_baseline_string("\'
        pnode '"))']);
    if filterdata == 2;
        % bandpass filter
        bw_fil_p = bp_filt(f_order, low_filt, ...
            high_filt, bw_pol, dtp);
    elseif filterdata == 1;
        % lowpass filter
        bw_fil_p = lp_filt(f_order, low_filt, ...
            bw_pol, dtp);
    elseif filterdata == 0;
        bw_fil_p = bw_pol;
    elseif filterdata == 3;
        % filter at half Nyquist
        bw_fil_p = lp_filt(f_order, 1/dtp/4, ...
            bw_pol, dtp);
    elseif filterdata == 4;
        % inverse bandpass filter
        bw_fil_p = ibp_filt(f_order, low_filt, ...
            high_filt, bw_pol, dtp);
    end
    cbw_pol = interp1(tpol, bw_fil_p, tin);
    if strcmp(dafi, 'dafi_cf') == 1
        if shot >= 121973
            cbw_pol = cbw_pol*pol_scale(j);
        end
    end
end
if isa(tmint, 'char')
```

```
    cbw_tor = zeros(1, length(tin))*NaN;
elseif isa(tmint, 'numeric')
    ttor = tmint + dtt*((1: tlengtht) - 1);
    % shifting time base here for digi differences
    if strcmp(shift, 'shift_time') == 1
        ttor = imp_time_shift(ttor, shot, array, probe(j,:), 'T');
    end
    bw_tor = mdsvalue(['slanted_baseline2(sub_baseline_string("\'
        tnode '"))']);
    if filterdata == 2;
        % bandpass filter
        bw_fil_t = bp_filt(f_order, low_filt, ...
            high_filt, bw_tor, dtt);
    elseif filterdata == 1;
        % lowpass filter
        bw_fil_t = lp_filt(f_order, low_filt, ...
            bw_tor, dtt);
    elseif filterdata == 0;
        bw_fil_t = bw_tor;
    elseif filterdata == 3;
        % filter at half Nyquist
        bw_fil_t = lp_filt(f_order, 1/dtt/4, ...
            bw_tor, dtt);
    elseif filterdata == 4;
        % inverse bandpass filter
        bw_fil_t = ibp_filt(f_order, low_filt, ...
            high_filt, bw_tor, dtt);
    end
    cbw_tor = interp1(ttor, bw_fil_t, tin);
    if strcmp(dafi, 'dafi_cf') == 1
        if shot >= 121973
            cbw_tor = cbw_tor*tor_scale(j);
        end
    end
end
cb_field(1,j,:) = cbw_rad;
if strcmp(array, 'M') == 1
    if j == 1 % there is no rot ang for the 1st probe
        % b/c there is no toroidal probe
        cb_field(2,j,:) = cbw_pol;
        cb_field(3,j,:) = cbw_tor;
    elseif j > 1
        rotnode = ['\B_IMP_' array '_T' probe(j, :) ':ROT_ANG'];
        rot_ang = mdsvalue(rotnode);
        cb_field(2,j,:) = cbw_pol*cos(rot_ang) - cbw_tor*sin(rot_ang
            );
        cb_field(3,j,:) = cbw_tor*cos(rot_ang) + cbw_pol*sin(rot_ang
            );
    end
else
```

```
        rotnode = ['\B_IMP_' array '_T' probe(j, :) ':ROT_ANG'];
        rot_ang = mdsvalue(rotnode);
        if isa(rot_ang, 'char')
            cb_field(2,j,:) = cbw_pol;
            cb_field(3,j,:) = cbw_tor;
        elseif isa(tmint, 'numeric')
            cb_field(2,j,:) = cbw_pol*cos(rot_ang) - cbw_tor*sin(rot_ang
                );
            cb_field(3,j,:) = cbw_tor*cos(rot_ang) + cbw_pol*sin(rot_ang
                );
        end
    end
    ins_depth(j) = mdsvalue(['\B_IMP_M_R' probe(j, :) 'R']);
end
```

B.3 Corrects the time base of internal probe signals connected to 612 and 2412 digitizers

This function is located at

bvictor\Matlab\filters\imp_time_shift.m

```
function [tout] = imp_time_shift(tin, shot, array, ...
    probe, dir)

% this function shifts the time base of the probe signals due to time
% base differences between digitizers

shift612 = 5e-6;
shift2412 = 2.5e-6;
tout = tin;
% this will be overwritten if necessary below

if shot < 117860
    tout = tin;

elseif shot >= 117860 && shot <= 118389
    if strcmp(array, 'M') == 1
        if strcmp(probe, '06') == 1
            if strcmp(dir, 'R') == 1
                tout = tin - shift2412;
            end
        end
    elseif strcmp(array, 'B') == 1
        if strcmp(probe, '02') == 1
            tout = tin - shift612;
        elseif strcmp(probe, '03') == 1
            tout = tin - shift612;
        elseif strcmp(probe, '04') == 1
            tout = tin - shift2412;
        elseif strcmp(probe, '05') == 1
            tout = tin - shift612;
        elseif strcmp(probe, '06') == 1
            tout = tin - shift612;
        end
    end

%     shifted probes:
%     2412:
%     bbot probe 4 all dir
%     bmid probe 6 rad
%     612:
%     bbot probes 2,3,5,6 all dir
```

```
elseif shot > 118389 && shot <= 121973
    if strcmp(array, 'M') == 1
        if strcmp(probe, '08') == 1
            if strcmp(dir, 'R') == 1
                tout = tin - shift2412;
            end
        elseif strcmp(probe, '10') == 1
            tout = tin - shift612;
        elseif strcmp(probe, '12') == 1
            tout = tin - shift612;
        elseif strcmp(probe, '14') == 1
            tout = tin - shift612;
        elseif strcmp(probe, '17') == 1
            tout = tin - shift612;
        end
    elseif strcmp(array, 'B') == 1
        if strcmp(probe, '08') == 1
            tout = tin - shift2412;
        end
    end

%     shifted probes:
%     2412:
%     bbot probe 8 all dir
%     bmid probe 8 rad
%     612:
%     bmid probes 10,12,14,17 all dir

elseif shot > 121973
    if strcmp(array, 'M') == 1
        if strcmp(probe, '06') == 1
            if strcmp(dir, 'P') == 1
                tout = tin - shift2412;
            elseif strcmp(dir, 'T') == 1
                tout = tin - shift2412;
            end
        elseif strcmp(probe, '15') == 1
            if strcmp(dir, 'P') == 1
                tout = tin - shift2412;
            elseif strcmp(dir, 'T') == 1
                tout = tin - shift2412;
            end
        end
        if strcmp(dir, 'R') == 1
            tout = tin - shift612;
        end
    end

%     shifted probes:
```

```
%       2412:
%       bmid probes 6,15 pol and tor
%       612:
%       bmid all rad

end
```

B.4 Takes the radial derivatives using the three stems of the internal probe

This function is located at

bvictor\Matlab\filters\imp_rad_deriv.m

```
function [dbrdi, dbpdi, dbtdi] = ...
    imp_rad_deriv(b, N, shot)

% this takes the derivative using data from the IMP
% the beginning and end probes use a first order deriv
% and the middle probes use a second order deriv

% b is the signal of interest
% N is the number of probes

if shot <= 118389
    % the radial distance between probes is 0.5 inches
    dr = 0.0127;
elseif shot > 118389
    % the radial distance between probes is 1 inch
    dr = 0.0254;
end

%-------------------------------------------------------------------------%
% b_rad derivative
dbrdi = zeros(N, length(b));

% 1st location
dbrdi(1, :) = (b(1, 2, :) - b(1, 1, :))/dr;

% 2nd order algorithm for 1st location
% dbrdi(1, :) = (-3*b(1,1,:) + 4*b(1,2,:) - b(1,3,:))/(2*dr);

% middle locations
for k = 1: N - 2
    kk = k + 1;
    dbrdi(kk, :) = (b(1, kk + 1, :) - b(1, k, :))/(2*dr);
end

% last location
dbrdi(N, :) = (b(1, N, :) - b(1, N - 1, :))/dr;

% 2nd order algorithm for last location
% dbrdi(N, :) = (b(1,N-2,:) - 4*b(1,N-1,:) + 3*b(1,N,:))/(2*dr);

%-------------------------------------------------------------------------%
```

```
% b_pol derivative
dbpdi = zeros(N, length(b));

% 1st location
dbpdi(1, :) = (b(2, 2, :) - b(2, 1, :))/dr;

% 2nd order algorithm for 1st location
% dbpdi(1, :) = (-3*b(2,1,:) + 4*b(2,2,:) - b(2,3,:))/(2*dr);

% middle locations
for k = 1: N - 2
    kk = k + 1;
    dbpdi(kk, :) = (b(2, kk + 1, :) - b(2, k, :))/(2*dr);
end

% last location
dbpdi(N, :) = (b(2, N, :) - b(2, N - 1, :))/dr;

% 2nd order algorithm for last location
% dbpdi(N, :) = (b(2,N-2,:) - 4*b(2,N-1,:) + 3*b(2,N,:))/(2*dr);

%-------------------------------------------------------------------------%
% b_tor derivative
dbtdi = zeros(N, length(b));

% 1st location
dbtdi(1, :) = (b(3, 2, :) - b(3, 1, :))/dr;

% 2nd order algorithm for 1st location
% dbtdi(1, :) = (-3*b(3,1,:) + 4*b(3,2,:) - b(3,3,:))/(2*dr);

% middle locations
for k = 1: N - 2
    kk = k + 1;
    dbtdi(kk, :) = (b(3, kk + 1, :) - b(3, k, :))/(2*dr);
end

% last location
dbtdi(N, :) = (b(3, N, :) - b(3, N - 1, :))/dr;

% 2nd order algorithm for last location
% dbtdi(N, :) = (b(3,N-2,:) - 4*b(3,N-1,:) + 3*b(3,N,:))/(2*dr);
```

B.5 Takes the poloidal derivatives using the three stems of the internal probe

This function is located at

bvictor\Matlab\filters\imp_pol_deriv.m

```
function [dbrdj, dbpdj, dbtdj] = ...
    imp_pol_deriv(top, mid, bot, array, order)

% this takes the poloidal derivative using data from the IMP
% using t, m, b specify the main stem of the calculation
% 1t is top - mid
% 1b is bot - mid
% 2 is the average of 1t and 1b

% b is the signal of interest
% N is the number of probes

% the tor and pol distance between the mid and either
% top or bot array is 0.875 inches
dr = 0.0222;

if array == 't'
    dbdj = (top - mid)/dr;

elseif array == 'm'
    if(strcmp(order, '1t'))
        dbdj = (top - mid)/dr;
    elseif(strcmp(order, '1b'))
        dbdj = (bot - mid)/dr;
    elseif(strcmp(order, '2'))
        dbdj = (top - 2*mid + bot)/(2*dr);
    end

elseif array == 'b'
    dbdj = (bot - mid)/dr;

end

dbrdj = squeeze(dbdj(1, :, :));
dbpdj = squeeze(dbdj(2, :, :));
dbtdj = squeeze(dbdj(3, :, :));
```

B.6 Takes the toroidal derivatives using the three stems of the internal probe

This function is located at

bvictor\Matlab\filters\imp_tor_deriv.m

```
function [dbrdk, dbpdk, dbtdk] = ...
    imp_tor_deriv(top, mid, bot, array, order)

% this takes the poloidal derivative using data from the IMP

% b is the signal of interest
% N is the number of probes

% the tor and pol distance between the mid and either
% top or bot array is 0.875 inches
dr = 0.0222;

if array == 't'
    if(strcmp(order, '1'))
        dbdk = (mid - top)/dr;
    elseif(strcmp(order, '2'))
        dbdk = (bot - top)/(2*dr);
    end

elseif array == 'm'
    if(strcmp(order, '1t'))
        dbdk = (mid - top)/dr;
    elseif(strcmp(order, '1b'))
        dbdk = (bot - mid)/dr;
    elseif(strcmp(order, '2'))
        dbdk = (bot - top)/(2*dr);
    end

elseif array == 'b'
    if(strcmp(order, '1'))
        dbdk = (bot - mid)/dr;
    elseif(strcmp(order, '2'))
        dbdk = (bot - top)/(2*dr);
    end

end

dbrdk = squeeze(dbdk(1, :, :));
dbpdk = squeeze(dbdk(2, :, :));
dbtdk = squeeze(dbdk(3, :, :));
```

B.7 Comparison of internal probe data to Taylor state

This analysis code is located at

bvictor\Matlab\dissertation\imp_taylor.m

```
%% this program compares the IMP data to Taylor

clear all;

addpath('S:\Matlab\filters');

%% global variables and inputs are here
% these constants scale the Taylor data
mu0 = 4*pi*1e-7;
kboltz = 1.38e-23;
Tscale = mu0/10.3;
Sph_scale = 1/0.201668947994763;
% the following scales the equilibrium field with (1)
% or without (0) the injector currents
inj_scale = 1;

f_order = 4; % order of all the filters
low_filt = 5000; % low pass frequency
high_filt = 100000; % high pass

% put this option in for probes, too
filterdata = 0; % 2 = bandpass, 1 = lowpass, 0 = no filter
% 3 = lowpass at half the Nyquist
% 4 = removes a frequency range from the data

% r is in the i direction
% p is in the j direction
% t is in the k direction
dir = ['R'; 'P'; 'T'];

shot = 122385; % input('What shot? ');
[a, status] = mdsopen('landau.hit::hitsi', shot);

% define variables
ts = -0.0001; % start time for new time base
ts2 = ts - 0.0002; % start time for cropping data in
te = 0.005; % end time for new time base
te2 = te + 0.0002; % end time for cropping data in
dtn = 0.4e-6; % dt for new time base (2.5 MHz)
t.base = ts: dtn: te; % new time base
color = ['-r'; '-g'; '-b'; '-c'; '-m'; '-k';
    ':r'; ':g'; ':b'; ':c'; ':m'; ':k'];
```

```
%-------------------------------------------------------------------------%
%% this brings in the data

% using the probe matrix
[b_probes, major_rad_m] = imp_data_in_construct('M', ...
    t.base, filterdata, f_order, low_filt, high_filt, shot, 'shift_time'
        , 'dafi_cf');

%-------------------------------------------------------------------------%
%% bringing in Taylor data

[t.ixinj, dt.ixinj, sig.ixinj] = gen_data_in('\i_inj_x');
[t.iyinj, dt.iyinj, sig.iyinj] = gen_data_in('\i_inj_y');
[t.itor, dt.itor, sig.itor] = gen_data_in('\i_tor_spaavg');

% the mid stem
% the spheromak field
s_mid = importdata('S:\Matlab\taylordata\chord.S_mid.dat', ' ', 1);
mid_x = s_mid.data(:,1); % x location
mid_y = s_mid.data(:,2); % y location
mid_z = s_mid.data(:,3); % z location
mid_r = -sqrt(2)/2*(mid_x + mid_y); % major radius
s_mid.rad = s_mid.data(:,4)*Tscale*Sph_scale;
s_mid.tor = s_mid.data(:,5)*Tscale*Sph_scale;
s_mid.pol = s_mid.data(:,6)*Tscale*Sph_scale;

% the x-inj field
x_mid = importdata('S:\Matlab\taylordata\chord.X_mid.dat', ' ', 1);
% the location data is the same as s_mid
x_mid.rad = x_mid.data(:,4)*Tscale;
x_mid.tor = x_mid.data(:,5)*Tscale;
x_mid.pol = x_mid.data(:,6)*Tscale;

% the y-inj field
y_mid = importdata('S:\Matlab\taylordata\chord.Y_mid.dat', ' ', 1);
% the location data is the same as s_mid
y_mid.rad = y_mid.data(:,4)*Tscale;
y_mid.tor = y_mid.data(:,5)*Tscale;
y_mid.pol = y_mid.data(:,6)*Tscale;

% ------------------------------------------------------------------ %
% interpolating all data onto the same time base
int.ixinj = interp1(t.ixinj, sig.ixinj, t.base);
int.iyinj = interp1(t.iyinj, sig.iyinj, t.base);
int.itor = interp1(t.itor, sig.itor, t.base);

% ------------------------------------------------------------------ %
% scaling the Taylor equilibrium fields
% based upon the respective currents
```

```
b_mid.rad = x_mid.rad*int.ixinj*inj_scale ...
    + y_mid.rad*int.iyinj*inj_scale ...
    + s_mid.rad*int.itor;

b_mid.pol = x_mid.pol*int.ixinj*inj_scale ...
    + y_mid.pol*int.iyinj*inj_scale ...
    + s_mid.pol*int.itor;

b_mid.tor = x_mid.tor*int.ixinj*inj_scale ...
    + y_mid.tor*int.iyinj*inj_scale ...
    + s_mid.tor*int.itor;


% more sign corrections
% b/c our sign conventions for positive poloidal fields are
% in the opposite direction
b_mid.pol = -b_mid.pol;

% find points closest to the probe points
for j = 1: length(major_rad_m)
    [aa, int.pm(j)] = min((mid_r - major_rad_m(j)).^2);
end
% indexes of Taylor:
% probe (numbered from inner to outer most)
b_mid.rad_pr = b_mid.rad(int.pm, :);
b_mid.pol_pr = b_mid.pol(int.pm, :);
b_mid.tor_pr = b_mid.tor(int.pm, :);

mdsclose;
%% plotting routines here

p_offset = .06*1e3;
prplots = [2, 5, 9, 13, 17];
% prplots = [13: 17];
% corresponds to probes 2, 5, 9, 13, 17

tps = .6;
tpe = 2.6;

%% looking at changing the injector phase here
%% this has no relation to the rest of the code, but I want to
%% keep it so I can look at the data in the future
% b_midy.rad = y_mid.rad*int.iyinj*inj_scale;
% b_midx.rad = x_mid.rad*int.ixinj*inj_scale;
% b_midx.rad_pr = b_midx.rad(int.pm, :);
% b_midy.rad_pr = b_midy.rad(int.pm, :);
% h101 = figure(1);
% clf;
% set(h101, 'Name', 'B_r')
```

```
% axes('Parent', h101,'YTick',[0 p_offset 2*p_offset 3*p_offset 4*
    p_offset], 'FontSize',14);
% box('on');
% hold('all');
% k = 0;
% for j = prplots
%     k = k + 1;
%     plot(t.base*1e3+.017, squeeze(b_midy.rad_pr(j,:))*1e3 + p_offset*(
    k-1), 'k', 'LineWidth', 2);
%     hold on;
%     plot(t.base*1e3, squeeze(b_midx.rad_pr(j,:))*1e3 + p_offset*(k-1),
     'r', 'LineWidth', 2);
% %     plot(t.base*1e3, squeeze(b_probes(1,j,:))*1e3 + p_offset*(k-1),
    'g', 'LineWidth', 2);
%     text(tpe - .2*(tpe-tps), p_offset*(k)-.5*p_offset, ...
%         {['R = ' num2str(major_rad_m(j),3)]}, 'Color', 'k', 'Fontsize
    ', 14);
% end
% xlim([tps tpe]);
% for j = 1: length(prplots)
%     line([0 tpe+1], [p_offset*(j-1) p_offset*(j-1)], 'Color', 'k', '
    LineStyle', ':');
% end
% % title(['Toroidal field from internal probe, shot ' int2str(shot)]);
% ylim([-.75*p_offset 5*p_offset]);
% text(tps + .01*(tpe-tps), 5*p_offset-.25*p_offset, num2str(shot), '
    FontSize', 12);
% ylabel('B [mT]', 'FontSize', 18);
% xlabel('t [ms]', 'FontSize', 18);

h101 = figure(101);
clf;
set(h101, 'Name', 'B_t')
axes('Parent', h101,'YTick',[0 p_offset 2*p_offset 3*p_offset 4*p_offset
    ], 'FontSize',14);
box('on');
hold('all');
k = 0;
for j = prplots
    k = k + 1;
    plot(t.base*1e3, squeeze(b_mid.tor_pr(j,:))*1e3 + p_offset*(k-1), 'r
        ', 'LineWidth', 2);
    hold on;
    plot(t.base*1e3, squeeze(b_probes(3,j,:))*1e3 + p_offset*(k-1), 'k',
         'LineWidth', 2);
    text(tpe - .2*(tpe-tps), p_offset*(k)-.5*p_offset, ...
        {['R = ' num2str(major_rad_m(j),3)]}, 'Color', 'k', 'Fontsize',
            14);
end
xlim([tps tpe]);
```

```
for j = 1:length(prplots)
    line([0 tpe+1], [p_offset*(j-1) p_offset*(j-1)], 'Color', 'k', '
        LineStyle', ':');
end
% title(['Toroidal field from internal probe, shot ' int2str(shot)]);
ylim([-.75*p_offset 5*p_offset]);
text(tps + .01*(tpe-tps), 5*p_offset-.25*p_offset, num2str(shot), '
    FontSize', 12);
ylabel('B [mT]', 'FontSize', 18);
xlabel('t [ms]', 'FontSize', 18);
saveas(h101, ['S:\Matlab\dissertation\figures\shot' num2str(shot) '
    taylor_tor' date], ...
    'png')

p_offset = .04*1e3;

h102 = figure(102);
clf;
set(h102, 'Name', 'B_p')
axes('Parent', h102,'YTick',[0 p_offset 2*p_offset 3*p_offset 4*p_offset
    ], 'FontSize',14);
box('on');
hold('all');
k = 0;
for j = prplots
    k = k + 1;
    plot(t.base*1e3, squeeze(b_mid.pol_pr(j,:))*1e3 + p_offset*(k-1), 'r
        ', 'LineWidth', 2);
    hold on;
    plot(t.base*1e3, squeeze(b_probes(2,j,:))*1e3 + p_offset*(k-1), 'k',
         'LineWidth', 2);
    text(tpe - .2*(tpe-tps), p_offset*(k)-.5*p_offset, ...
        {['R = ' num2str(major_rad_m(j),3)]}, 'Color', 'k', 'Fontsize',
            14);
end
xlim([tps tpe]);
for j = 1:length(prplots)
    line([0 tpe+1], [p_offset*(j-1) p_offset*(j-1)], 'Color', 'k', '
        LineStyle', ':');
end
% title(['Poloidal field from internal probe, shot ' int2str(shot)]);
ylim([-.75*p_offset 5*p_offset]);
text(tps + .01*(tpe-tps), 5*p_offset-.25*p_offset, num2str(shot), '
    FontSize', 12);
ylabel('B [mT]', 'FontSize', 18);
xlabel('t [ms]', 'FontSize', 18);
saveas(h102, ['S:\Matlab\dissertation\figures\shot' num2str(shot) '
    taylor_pol' date], ...
    'png')
```

```
p_offset = .04*1e3;

h103 = figure(103);
clf;
set(h103, 'Name', 'B_r')
axes('Parent', h103,'YTick',[0 p_offset 2*p_offset 3*p_offset 4*p_offset
    ], 'FontSize',14);
box('on');
hold('all');
k = 0;
for j = prplots
    k = k + 1;
    plot(t.base*1e3, squeeze(b_mid.rad_pr(j,:))*1e3 + p_offset*(k-1), 'r
        ', 'LineWidth', 2);
    hold on;
    plot(t.base*1e3, squeeze(b_probes(1,j,:))*1e3 + p_offset*(k-1), 'k',
         'LineWidth', 2);
    text(tpe - .2*(tpe-tps), p_offset*(k)-.5*p_offset, ...
        {['R = ' num2str(major_rad_m(j),3)]}, 'Color', 'k', 'Fontsize',
           14);
end
xlim([tps tpe]);
for j = 1: length(prplots)
    line([0 tpe+1], [p_offset*(j-1) p_offset*(j-1)], 'Color', 'k', '
       LineStyle', ':');
end
% title(['Radial field from internal probe, shot ' int2str(shot)]);
ylim([-p_offset 5*p_offset]);
text(tps + .01*(tpe-tps), 5*p_offset -.25*p_offset, num2str(shot), '
    FontSize', 12);
ylabel('B [mT]', 'FontSize', 18);
xlabel('t [ms]', 'FontSize', 18);
saveas(h103, ['S:\Matlab\dissertation\figures\shot' num2str(shot) '
    taylor_rad' date], ...
     'png')
```

B.8 Calculation of the current density and λ from the internal probe

This analysis code is located at

```
bvictor\Matlab\dissertation\imp_j_lambda.m
```

```
%% this program calculates j and lambda for probe data and
% synthesized Taylor data

clear all;

addpath('S:\Matlab\filters');

%% global variables and inputs are here
% these constants scale the Taylor data
mu0 = 4*pi*1e-7;
kboltz = 1.38e-23;
Tscale = mu0/10.3;
Sph_scale = 1/0.201668947994763;

f_order = 4; % order of all the filters
low_filt = 3000; % low pass frequency
high_filt = 27000; % high pass

% put this option in for probes, too
filterdata = 3; % 2 = bandpass, 1 = lowpass, 0 = no filter
% 3 = lowpass at half the Nyquist
% 4 = removes a frequency range from the data

% r is in the i direction
% p is in the j direction
% t is in the k direction
dir = ['R'; 'P'; 'T'];

% high current D 121860
% high current D neg. itor - nai
% low current D 121824
% No RF He 121826
% No RF He 121857, neg. itor
% IMP ID = 15.68 cm: 121962
% IMP ID = 8.06 cm:  121970
shot = 121963; % input('What shot? ');
[a, status] = mdsopen('landau.hit::hitsi', shot);

% define variables
ts = -0.0001; % start time for new time base
ts2 = ts - 0.0002; % start time for cropping data in
te = 0.005; % end time for new time base
```

```
te2 = te + 0.0002; % end time for cropping data in
dtn = 0.4e-6; % dt for new time base (2.5 MHz)
t_base = ts: dtn: te; % new time base
% color = ['-r'; '-g'; '-b'; '-c'; '-m'; '-k';
%      ':r'; ':g'; ':b'; ':c'; ':m'; ':k'];
color = ['-r'; '-b'; '-g'; '-c'; '-m'; '-k';
    ':r'; ':g'; ':b'; ':c'; ':m'; ':k'];

%-------------------------------------------------------------------%
%% this brings in the probe data

% using the smoothed probe data
[b_mid_sihi, mr] = imp_data_in_construct_sihi('M', ...
    t_base, 0, f_order, low_filt, high_filt, shot, 'shift_time', '
        dafi_cf');

[b_top_sihi, mr_top] = imp_data_in_construct_sihi('T', ...
    t_base, 0, f_order, low_filt, high_filt, shot, 'shift_time', '
        dafi_cf');

[b_bot_sihi, mr_bot] = imp_data_in_construct_sihi('B', ...
    t_base, 0, f_order, low_filt, high_filt, shot, 'shift_time', '
        dafi_cf');

% using the typical signal
[b_mid, mr2] = imp_data_in_construct('M', ...
    t_base, filterdata, f_order, low_filt, high_filt, shot, 'shift_time'
        , 'dafi_cf');

[b_top, mr_top2] = imp_data_in_construct('T', ...
    t_base, filterdata, f_order, low_filt, high_filt, shot, 'shift_time'
        , 'dafi_cf');

[b_bot, mr_bot2] = imp_data_in_construct('B', ...
    t_base, filterdata, f_order, low_filt, high_filt, shot, 'shift_time'
        , 'dafi_cf');

%-------------------------------------------------------------------%
%% bringing in other data

[t_itor, dt_itor, sig_itor] = gen_data_in('\i_tor_spaavg');

%-------------------------------------------------------------------%
%% this brings in the Taylor data

% the following scales the equilibrium field with (1)
% or without (0) the injector currents
inj_scale = 0;

[t.ixinj, dt.ixinj, sig.ixinj] = gen_data_in('\i_inj_x');
```

```
[t.iyinj, dt.iyinj, sig.iyinj] = gen_data_in('\i_inj_y');
[t.itor, dt.itor, sig.itor] = gen_data_in('sihi_smooth(\i_tor_spaavg)');

mdsclose;
%-------------------------%
% the mid stem
% the spheromak field
s_mid = importdata('S:\Matlab\taylordata\chord.S_mid.dat', ' ', 1);
mid_x = s_mid.data(:,1); % x location
mid_y = s_mid.data(:,2); % y location
mid_z = s_mid.data(:,3); % z location
mid_r = -sqrt(2)/2*(mid_x + mid_y); % major radius
s_mid.rad = s_mid.data(:,4)*Tscale*Sph_scale;
s_mid.tor = s_mid.data(:,5)*Tscale*Sph_scale;
s_mid.pol = s_mid.data(:,6)*Tscale*Sph_scale;

% the x-inj field
x_mid = importdata('S:\Matlab\taylordata\chord.X_mid.dat', ' ', 1);
% the location data is the same as s_mid
x_mid.rad = x_mid.data(:,4)*Tscale;
x_mid.tor = x_mid.data(:,5)*Tscale;
x_mid.pol = x_mid.data(:,6)*Tscale;

% the y-inj field
y_mid = importdata('S:\Matlab\taylordata\chord.Y_mid.dat', ' ', 1);
% the location data is the same as s_mid
y_mid.rad = y_mid.data(:,4)*Tscale;
y_mid.tor = y_mid.data(:,5)*Tscale;
y_mid.pol = y_mid.data(:,6)*Tscale;

%-------------------------%
% the bot stem
% the spheromak field
s_bot = importdata('S:\Matlab\taylordata\chord.S_bot.dat', ' ', 1);
bot_x = s_bot.data(:,1); % x location
bot_y = s_bot.data(:,2); % y location
bot_z = s_bot.data(:,3); % z location
bot_r = -sqrt(2)/2*(bot_x + bot_y); % major radius
s_bot.rad = s_bot.data(:,4)*Tscale*Sph_scale;
s_bot.tor = s_bot.data(:,5)*Tscale*Sph_scale;
s_bot.pol = s_bot.data(:,6)*Tscale*Sph_scale;

% the x-inj field
x_bot = importdata('S:\Matlab\taylordata\chord.X_bot.dat', ' ', 1);
% the location data is the same as s_bot
x_bot.rad = x_bot.data(:,4)*Tscale;
x_bot.tor = x_bot.data(:,5)*Tscale;
x_bot.pol = x_bot.data(:,6)*Tscale;

% the y-inj field
```

```
y_bot = importdata('S:\Matlab\taylordata\chord.Y_bot.dat', ' ', 1);
% the location data is the same as s_bot
y_bot.rad = y_bot.data(:,4)*Tscale;
y_bot.tor = y_bot.data(:,5)*Tscale;
y_bot.pol = y_bot.data(:,6)*Tscale;

%-------------------------%
% the top stem
% the spheromak field
s_top = importdata('S:\Matlab\taylordata\chord.S_top.dat', ' ', 1);
top_x = s_top.data(:,1); % x location
top_y = s_top.data(:,2); % y location
top_z = s_top.data(:,3); % z location
top_r = -sqrt(2)/2*(top_x + top_y); % major radius
s_top.rad = s_top.data(:,4)*Tscale*Sph_scale;
s_top.tor = s_top.data(:,5)*Tscale*Sph_scale;
s_top.pol = s_top.data(:,6)*Tscale*Sph_scale;

% the x-inj field
x_top = importdata('S:\Matlab\taylordata\chord.X_top.dat', ' ', 1);
% the location data is the same as s_top
x_top.rad = x_top.data(:,4)*Tscale;
x_top.tor = x_top.data(:,5)*Tscale;
x_top.pol = x_top.data(:,6)*Tscale;

% the y-inj field
y_top = importdata('S:\Matlab\taylordata\chord.Y_top.dat', ' ', 1);
% the location data is the same as s_top
y_top.rad = y_top.data(:,4)*Tscale;
y_top.tor = y_top.data(:,5)*Tscale;
y_top.pol = y_top.data(:,6)*Tscale;

%-------------------------%
% interpolating all data onto the same time base
int.ixinj = interp1(t.ixinj, sig.ixinj, t_base);
int.iyinj = interp1(t.iyinj, sig.iyinj, t_base);
int.itor = interp1(t.itor, sig.itor, t_base);


% ------------------------ %
% scaling the Taylor equilibrium fields
% based upon the respective currents

%-------------------------%
% the mid stem
b_mid_tay.rad = x_mid.rad*int.ixinj*inj_scale ...
    + y_mid.rad*int.iyinj*inj_scale ...
    + s_mid.rad*int.itor;
b_mid_tay.pol = x_mid.pol*int.ixinj*inj_scale ...
    + y_mid.pol*int.iyinj*inj_scale ...
```

```
    + s_mid.pol*int.itor;
b_mid_tay.tor = x_mid.tor*int.ixinj*inj_scale ...
    + y_mid.tor*int.iyinj*inj_scale ...
    + s_mid.tor*int.itor;

%-------------------------%
% the bot stem
b_bot_tay.rad = x_bot.rad*int.ixinj*inj_scale ...
    + y_bot.rad*int.iyinj*inj_scale ...
    + s_bot.rad*int.itor;

b_bot_tay.pol = x_bot.pol*int.ixinj*inj_scale ...
    + y_bot.pol*int.iyinj*inj_scale ...
    + s_bot.pol*int.itor;

b_bot_tay.tor = x_bot.tor*int.ixinj*inj_scale ...
    + y_bot.tor*int.iyinj*inj_scale ...
    + s_bot.tor*int.itor;

%-------------------------%
% the top stem
b_top_tay.rad = x_top.rad*int.ixinj*inj_scale ...
    + y_top.rad*int.iyinj*inj_scale ...
    + s_top.rad*int.itor;

b_top_tay.pol = x_top.pol*int.ixinj*inj_scale ...
    + y_top.pol*int.iyinj*inj_scale ...
    + s_top.pol*int.itor;

b_top_tay.tor = x_top.tor*int.ixinj*inj_scale ...
    + y_top.tor*int.iyinj*inj_scale ...
    + s_top.tor*int.itor;

%-------------------------%
% more sign corrections
% b/c our sign conventions for positive poloidal fields are
% in the opposite direction
b_mid_tay.pol = -b_mid_tay.pol;
b_bot_tay.pol = -b_bot_tay.pol;
b_top_tay.pol = -b_top_tay.pol;

%-------------------------%
% find points closest to the probe points
for j = 1: length(mr)
    [aa, int.pm(j)] = min((mid_r - mr(j)).^2);
    [aa, int.pb(j)] = min((bot_r - mr(j)).^2);
    [aa, int.pt(j)] = min((top_r - mr(j)).^2);
end

% creating similar structure as probe data
```

```
b_tay_mid = zeros(size(b_mid));
b_tay_bot = zeros(size(b_bot));
b_tay_top = zeros(size(b_top));

b_tay_mid(1,:,:) = b_mid_tay.rad(int.pm, :);
b_tay_mid(2,:,:) = b_mid_tay.pol(int.pm, :);
b_tay_mid(3,:,:) = b_mid_tay.tor(int.pm, :);

b_tay_bot(1,:,:) = b_bot_tay.rad(int.pm, :);
b_tay_bot(2,:,:) = b_bot_tay.pol(int.pm, :);
b_tay_bot(3,:,:) = b_bot_tay.tor(int.pm, :);

b_tay_top(1,:,:) = b_top_tay.rad(int.pm, :);
b_tay_top(2,:,:) = b_top_tay.pol(int.pm, :);
b_tay_top(3,:,:) = b_top_tay.tor(int.pm, :);

%-------------------------------------------------------------------------%
%% the magnitude of each array

% full data
b_mid_mag = sqrt(squeeze((b_mid(1,:,:).^2 + b_mid(2,:,:).^2 ...
    + b_mid(3,:,:).^2)));
b_top_mag = sqrt(squeeze((b_top(1,:,:).^2 + b_top(2,:,:).^2 ...
    + b_top(3,:,:).^2)));
b_bot_mag = sqrt(squeeze((b_bot(1,:,:).^2 + b_bot(2,:,:).^2 ...
    + b_bot(3,:,:).^2)));

% smoothed data
b_mid_mag_sihi = sqrt(squeeze((b_mid_sihi(1,:,:).^2 + b_mid_sihi(2,:,:)
    .^2 ...
    + b_mid_sihi(3,:,:).^2)));
b_top_mag_sihi = sqrt(squeeze((b_top_sihi(1,:,:).^2 + b_top_sihi(2,:,:)
    .^2 ...
    + b_top_sihi(3,:,:).^2)));
b_bot_mag_sihi = sqrt(squeeze((b_bot_sihi(1,:,:).^2 + b_bot_sihi(2,:,:)
    .^2 ...
    + b_bot_sihi(3,:,:).^2)));

% Taylor
b_tay_mid_mag = sqrt(squeeze((b_tay_mid(1,:,:).^2 + b_tay_mid(2,:,:).^2
    ...
    + b_tay_mid(3,:,:).^2)));
b_tay_top_mag = sqrt(squeeze((b_tay_top(1,:,:).^2 + b_tay_top(2,:,:).^2
    ...
    + b_tay_top(3,:,:).^2)));
b_tay_bot_mag = sqrt(squeeze((b_tay_bot(1,:,:).^2 + b_tay_bot(2,:,:).^2
    ...
    + b_tay_bot(3,:,:).^2)));

%-------------------------------------------------------------------------%
```

```
%% choosing the probe locations for the calculation

if shot <= 117860
    disp('This shot only has data with the main stem');
    break;

elseif shot > 117860 && shot <= 118389

    probe_m = [2 3 4 5 6];
    probe_t = [2 3 4 5 6];
    probe_b = [2 3 4 5 6];

    N_pm = length(probe_m);
    N_pt = length(probe_t);
    N_pb = length(probe_b);

elseif shot > 118389 && shot < 121973

    % the following are signals on 1612 digis
    probe_m = [2 4 6 8];
    probe_t = [2 4 6];
    probe_b = [2 4 6 8];

    N_pm = length(probe_m);
    N_pt = length(probe_t);
    N_pb = length(probe_b);

elseif shot > 121973
    disp('This shot only has data with the main stem');
    break;

end

% radii at locations of interest
mr_m = mr(probe_m);
mr_t = mr(probe_t);
mr_b = mr(probe_b);

%-------------------------------------------------------------------------%
%% finding j for probes using derivatives

% radial derivatives of main stem
[dbrdi, dbpdi, dbtdi] = imp_rad_deriv(b_mid(:, probe_m, :), N_pm, shot);
% smoothed
[dbrdi_sihi, dbpdi_sihi, dbtdi_sihi] = ...
    imp_rad_deriv(b_mid_sihi(:, probe_m, :), N_pm, shot);

% poloidal derivatives
[dbrdj, dbpdj, dbtdj] = imp_pol_deriv(b_top(:, probe_t, :), ...
    b_mid(:, probe_t, :), b_bot(:, probe_t, :), 'm', '2');
```

```
% smoothed
[dbrdj_sihi, dbpdj_sihi, dbtdj_sihi] = ...
    imp_pol_deriv(b_top_sihi(:, probe_t, :), ...
    b_mid_sihi(:, probe_t, :), b_bot_sihi(:, probe_t, :), 'm', '2');

% toroidal derivatives
[dbrdk, dbpdk, dbtdk] = imp_tor_deriv(b_top(:, probe_t, :), ...
    b_mid(:, probe_t, :), b_bot(:, probe_t, :), 'm', '2');
% smoothed
[dbrdk_sihi, dbpdk_sihi, dbtdk_sihi] = ...
    imp_tor_deriv(b_top_sihi(:, probe_t, :), ...
    b_mid_sihi(:, probe_t, :), b_bot_sihi(:, probe_t, :), 'm', '2');

% calculating curls
curlbr = dbtdj(1:N_pt,:) - dbpdk(1:N_pt,:);
curlbp = dbrdk(1:N_pt,:) - dbtdi(1:N_pt,:);
curlbt = dbpdi(1:N_pt,:) - dbrdj(1:N_pt,:);
% smoothed
curlbr_sihi = dbtdj_sihi(1:N_pt,:) - dbpdk_sihi(1:N_pt,:);
curlbp_sihi = dbrdk_sihi(1:N_pt,:) - dbtdi_sihi(1:N_pt,:);
curlbt_sihi = dbpdi_sihi(1:N_pt,:) - dbrdj_sihi(1:N_pt,:);

% and current densities
jrd = 1/mu0*(curlbr);
jpd = 1/mu0*(curlbp);
jtd = 1/mu0*(curlbt);
% smoothed
jrd_sihi = 1/mu0*(curlbr_sihi);
jpd_sihi = 1/mu0*(curlbp_sihi);
jtd_sihi = 1/mu0*(curlbt_sihi);

%-------------------------------------------------------------------------%
%% finding j for Taylor using derivatives

% radial derivatives of main stem
[dbrdi_tay, dbpdi_tay, dbtdi_tay] = imp_rad_deriv(b_tay_mid(:, probe_m,
    :), N_pm, shot);

% poloidal derivatives
[dbrdj_tay, dbpdj_tay, dbtdj_tay] = imp_pol_deriv(b_tay_top(:, probe_t,
    :), ...
    b_tay_mid(:, probe_t, :), b_tay_bot(:, probe_t, :), 'm', '2');

% toroidal derivatives
[dbrdk_tay, dbpdk_tay, dbtdk_tay] = imp_tor_deriv(b_tay_top(:, probe_t,
    :), ...
    b_tay_mid(:, probe_t, :), b_tay_bot(:, probe_t, :), 'm', '2');

% calculating curls
curlbr_tay = dbtdj_tay(1:N_pt,:) - dbpdk_tay(1:N_pt,:);
```

```
curlbp_tay = dbrdk_tay(1:N_pt,:) - dbtdi_tay(1:N_pt,:);
curlbt_tay = dbpdi_tay(1:N_pt,:) - dbrdj_tay(1:N_pt,:);

% and current densities
jrd_tay = 1/mu0*(curlbr_tay);
jpd_tay = 1/mu0*(curlbp_tay);
jtd_tay = 1/mu0*(curlbt_tay);

%-------------------------------------------------------------------------%
%% finding lambda

% Probes
% j dot b in each direction
jb_curl_r = jrd.*squeeze(b_mid(1, probe_t, :));
jb_curl_p = jpd.*squeeze(b_mid(2, probe_t, :));
jb_curl_t = jtd.*squeeze(b_mid(3, probe_t, :));
% smoothed
jb_curl_r_sihi = jrd_sihi.*squeeze(b_mid_sihi(1, probe_t, :));
jb_curl_p_sihi = jpd_sihi.*squeeze(b_mid_sihi(2, probe_t, :));
jb_curl_t_sihi = jtd_sihi.*squeeze(b_mid_sihi(3, probe_t, :));

% lambda = mu0 j dot b/b^2
lambda_imp = mu0*(jb_curl_r + jb_curl_p ...
    + jb_curl_t)./(b_mid_mag(probe_t, :).^2);
% smoothed
lambda_imp_sihi = mu0*(jb_curl_r_sihi + jb_curl_p_sihi ...
    + jb_curl_t_sihi)./(b_mid_mag_sihi(probe_t, :).^2);

% Taylor
% j dot b in each direction
jb_curl_r_tay = jrd_tay.*squeeze(b_tay_mid(1, probe_t, :));
jb_curl_p_tay = jpd_tay.*squeeze(b_tay_mid(2, probe_t, :));
jb_curl_t_tay = jtd_tay.*squeeze(b_tay_mid(3, probe_t, :));

% lambda = mu0 j dot b/b^2
lambda_tay = mu0*(jb_curl_r_tay + jb_curl_p_tay ...
    + jb_curl_t_tay)./(b_tay_mid_mag(probe_t, :).^2);

% checking lambda in each direction
lambda_tay_pol = mu0*jpd_tay./squeeze(b_tay_mid(2, probe_t, :));
lambda_tay_tor = mu0*jtd_tay./squeeze(b_tay_mid(3, probe_t, :));
lambda_tay_rad = mu0*jrd_tay./squeeze(b_tay_mid(1, probe_t, :));

%-------------------------------------------------------------------------%
%% plotting routines here

scrsz = get(0,'ScreenSize');
t_fit = 2065; % this draws a vertical line on the plots

h1 = figure(1);
```

```
set(h1, 'Units', 'pixels', 'Position', [1 scrsz(4)/10 960 720], 'Color',
    [1 1 1]);
set(h1, 'Name', 'itor and j')
hold('all');
clf;

axes1 = axes('Parent',h1,'YTick',[0 20 40],'XTickLabel','',...
    'XTick',[1 2],...
    'Position',[0.13 0.77 0.775 0.215],...
    'FontSize',18);
box('on');
grid('on');
hold('all');
xlim([0 2.5]);
ylim([-10 50]);
plot(t_itor*1e3, sig_itor*1e-3, 'k',...
    'Parent', axes1, 'LineWidth', 2);
% line([t_fit*1e-3 t_fit*1e-3], [-1000 1000], 'Color', 'b', 'LineWidth',
    2);
ylabel('I_{tor} [kA]','FontSize',18);
text(.1, 45, int2str(shot), 'FontSize', 16);

axes2 = axes('Parent',h1,'YTick',[0 200 400],'XTickLabel','',...
    'XTick',[1 2],...
    'Position',[0.13 0.55 0.775 0.215],... %x,y,width,height
    'FontSize',18);
box('on');
grid('on');
hold('all');
for j = 1
plot(t_base*1e3, jtd(j,:)*1e-3, 'k', 'Parent', axes2);
hold all;
plot(t_base*1e3, jtd_sihi(j,:)*1e-3, 'r', 'Parent', axes2, 'LineWidth',
   2);
text(.1, 450, ['R = ' num2str(mr_m(j),3)], ...
    'FontSize', 16);
end
% line([t_fit*1e-3 t_fit*1e-3], [-1000 1000], 'Color', 'b', 'LineWidth',
    2);
ylabel('j_{tor} [kA/m^{2}]','FontSize',18);
xlim([0 2.5]);
ylim([-100 500]);

axes3 = axes('Parent',h1,'YTick',[0 100 200],'XTickLabel','',...
    'XTick',[1 2],...
    'Position',[0.13 0.33 0.775 0.215],... %x,y,width,height
    'FontSize',18);
box('on');
grid('on');
hold('all');
```

```
for j = 1
plot(t_base*1e3, jpd(j,:)*1e-3, 'k', 'Parent', axes3);
hold all;
plot(t_base*1e3, jpd_sihi(j,:)*1e-3, 'r', 'Parent', axes3, 'LineWidth',
    2);
text(.1, 260, ['R = ' num2str(mr_m(j),3)], ...
    'FontSize', 16);
end
% line([t_fit*1e-3 t_fit*1e-3], [-1000 1000], 'Color', 'b', 'LineWidth',
    2);
ylabel('j_{pol} [kA/m^{2}]','FontSize',18);
xlim([0 2.5]);
ylim([-50 300]);

axes4 = axes('Parent',h1,'YTick',[-100 0 100],...
    'XTick',[1 2],...
    'Position',[0.13 0.11 0.775 0.215],... %x,y,width,height
    'FontSize',18);
box('on');
grid('on');
hold('all');
for j = 1
plot(t_base*1e3, jrd(j,:)*1e-3, 'k', 'Parent', axes4);
hold all;
plot(t_base*1e3, jrd_sihi(j,:)*1e-3, 'r', 'Parent', axes4, 'LineWidth',
    2);
text(.1, 160, ['R = ' num2str(mr_m(j),3)], ...
    'FontSize', 16);
end
% line([t_fit*1e-3 t_fit*1e-3], [-1000 1000], 'Color', 'b', 'LineWidth',
    2);
xlabel('Time [ms]', 'FontSize', 18);
ylabel('j_{rad} [kA/m^{2}]','FontSize',18);
xlim([0 2.5]);
ylim([-200 200]);

fig_save = getframe(h1);
[Xfig, mapfig] = frame2im(fig_save);
imwrite(Xfig, ['S:\Matlab\dissertation\figures\itor_j' num2str(shot) 't'
    num2str(t_fit) '.png'], ...
    'XResolution', 1000, 'YResolution', 1000);

fleg = {};
h1 = figure(2);
set(h1, 'Units', 'pixels', 'Position', [1 scrsz(4)/10 960 480], 'Color',
    [1 1 1]);
clf;
set(h1, 'Name', 'lambda')
axes('Parent', h1,'YTick',[0 10 20],'XTick',[1 1.5 2], 'FontSize',18);
box('on');
```

```
grid('on');
hold('all');
for j = 1: N_pt
plot(t_base*1e3, lambda_imp(j,:), color(j,:));
hold all;
fleg = [fleg; {['R = ' num2str(mr_m(j),3)]}];
end
for j = 1: N_pt
plot(t_base*1e3, lambda_imp_sihi(j,:), color(j,:), 'LineWidth', 5);
end
xlim([0.6 2.4]);
ylim([-2 20]);
ylabel('\lambda [m^{-1}]', 'FontSize', 18);
xlabel('t [ms]', 'FontSize', 18);
legend(fleg, 'Location', 'SouthWest');
text(2.05, -1, int2str(shot), 'Color', 'k', 'Fontsize', 16);

fig_save = getframe(h1);
[Xfig, mapfig] = frame2im(fig_save);
imwrite(Xfig, ['S:\Matlab\dissertation\figures\lambda' num2str(shot) 'n'
    date '.png']);

fleg = {};
x1p = 0.6;
x2p = 2.4;
h1 = figure(3);
set(h1, 'Units', 'pixels', 'Position', [1 scrsz(4)/10 960 480], 'Color',
    [1 1 1]);
clf;
set(h1, 'Name', 'lambda & itor')

axes1 = axes('Parent', h1,'YTick',[0 20 40],'XTick',[1 1.5 2], ...
    'XTickLabel', '', ...
    'Position',[0.13 0.55 0.775 0.43], ...
    'FontSize',18);
box('on');
grid('on');
hold('all');
xlim([x1p x2p]);
ylim([-10 50]);
plot(t_itor*1e3, sig_itor*1e-3, 'k',...
    'Parent', axes1, 'LineWidth', 2);
ylabel('I_{tor} [kA]','FontSize',18);
text(x1p+.05, 45, int2str(shot), 'FontSize', 16);

axes2 = axes('Parent',h1,'YTick',[0 10 20],...
    'XTick',[1 1.5 2],...
    'Position',[0.13 0.11 0.775 0.43],... %x,y,width,height
    'FontSize',18);
box('on');
```

```
grid('on');
hold('all');
for j = 1: N_pt
plot(t_base*1e3, lambda_imp(j,:), color(j,:), 'Parent', axes2);
hold all;
fleg = [fleg; {['R = ' num2str(mr_m(j),3)]}];
end
for j = 1: N_pt
plot(t_base*1e3, lambda_imp_sihi(j,:), color(j,:), 'LineWidth', 5, ...
    'Parent', axes2);
end
xlim([x1p x2p]);
ylim([-2 20]);
ylabel('\lambda [m^{-1}]', 'FontSize', 18);
xlabel('t [ms]', 'FontSize', 18);
legend(fleg, 'Location', 'SouthWest','Orientation', 'Horizontal');

fig_save = getframe(h1);
[Xfig, mapfig] = frame2im(fig_save);
imwrite(Xfig, ['S:\Matlab\dissertation\figures\lambda_itor' num2str(shot
    ) 'n' date '.png']);

fleg = {};
figure(11);
clf;
for j = 1: N_pt
plot(t_base, jrd(j,:), color(j,:));
hold all;
fleg = [fleg; {['R = ' num2str(mr_m(j),3)]}];
plot(t_base, jrd_tay(j,:), ['-' color(j,:)]);
fleg = [fleg; {['Tay, R = ' num2str(mr_m(j),3)]}];
end
title('radial j');
legend(fleg, 'Location', 'SouthEast');

fleg = {};
figure(12);
clf;
for j = 1: N_pt
plot(t_base, jpd(j,:), color(j,:));
hold all;
fleg = [fleg; {['R = ' num2str(mr_m(j),3)]}];
plot(t_base, jpd_tay(j,:), ['-' color(j,:)]);
fleg = [fleg; {['Tay, R = ' num2str(mr_m(j),3)]}];
end
title('pol j');
legend(fleg, 'Location', 'SouthEast');

fleg = {};
figure(13);
```

```
clf;
for j = 1: N_pt
plot(t_base, jtd(j,:), color(j,:));
hold all;
fleg = [fleg; {['R = ' num2str(mr_m(j),3)]}];
plot(t_base, jtd_tay(j,:), ['-' color(j,:)]);
fleg = [fleg; {['Tay, R = ' num2str(mr_m(j),3)]}];
end
title('tor j');
legend(fleg, 'Location', 'SouthEast');

fleg = {};
figure(21);
clf;
for j = 1: N_pt
plot(t_base, lambda_imp(j,:), color(j,:));
hold all;
fleg = [fleg; {['R = ' num2str(mr_m(j),3)]}];
plot(t_base, lambda_tay(j,:), ['-' color(j,:)]);
fleg = [fleg; {['Tay, R = ' num2str(mr_m(j),3)]}];
end
title('lambda');
ylim([0 30]);
legend(fleg, 'Location', 'SouthEast');

figure(22);
clf;
for j = 1: N_pt
plot(t_base, lambda_tay_pol(j,:), '-r');
hold all;
plot(t_base, lambda_tay_rad(j,:), 'b');
plot(t_base, lambda_tay_tor(j,:), ['-' color(j,:)]);
end

% why is the lambda calculation only reasonable in the toroidal
    direction?
% toroidal derivatives are wrong? YES!
% the Taylor data is offset in the poloidal and radial direction, BUT
% all three stems have data for the same toroidal location
% therefore this calc doesn't make since with Taylor data
% actually they are displaced in the toroidal direction
% the resolution is pretty poor though, ~ 1.5 cm, so my best guess now
% is that is the issue



% p_offset = .06*1e3;
% prplots = [2, 5, 9, 13, 17];
% % corresponds to probes 2, 5, 9, 13, 17
```

```
%
% tps = .6;
% tpe = 2.6;
%
% h101 = figure(101);
% clf;
% set(h101, 'Name', 'B_t')
% axes('Parent', h101,'YTick',[0 p_offset 2*p_offset 3*p_offset 4*
    p_offset], 'FontSize',14);
% box('on');
% hold('all');
% k = 0;
% for j = prplots
%     k = k + 1;
%     plot(t_base*1e3, squeeze(b_matrix(3,j,:))*1e3 + p_offset*(k-1), 'k
    ', 'LineWidth', 2);
%     hold on;
%     text(tpe - .2*(tpe-tps), p_offset*(k)-.5*p_offset, ...
%         {['R = ' num2str(major_rad_m(j),3)]}, 'Color', 'k', 'Fontsize
    ', 14);
% end
% xlim([tps tpe]);
% for j = 1: length(prplots)
%     line([0 tpe+1], [p_offset*(j-1) p_offset*(j-1)], 'Color', 'k', '
    LineStyle', ':');
% end
%% title(['Toroidal field from internal probe, shot ' int2str(shot)]);
% ylim([-.75*p_offset 5*p_offset]);
% text(tps + .01*(tpe-tps), 5*p_offset-.25*p_offset, num2str(shot), '
    FontSize', 12);
% ylabel('B [mT]', 'FontSize', 18);
% xlabel('t [ms]', 'FontSize', 18);
% saveas(h101, ['S:\Matlab\dissertation\figures\shot' num2str(shot) '
    typical_tor' date], ...
%     'png')
%
% p_offset = .04*1e3;
%
% h102 = figure(102);
% clf;
% set(h102, 'Name', 'B_p')
% axes('Parent', h102,'YTick',[0 p_offset 2*p_offset 3*p_offset 4*
    p_offset], 'FontSize',14);
% box('on');
% hold('all');
% k = 0;
% for j = prplots
%     k = k + 1;
%     plot(t_base*1e3, squeeze(b_matrix(2,j,:))*1e3 + p_offset*(k-1), 'k
    ', 'LineWidth', 2);
```

```
%     hold on;
%     text(tpe - .2*(tpe-tps), p_offset*(k)-.5*p_offset, ...
%         {['R = ' num2str(major_rad_m(j),3)]}, 'Color', 'k', 'Fontsize
    ', 14);
% end
% xlim([tps tpe]);
% for j = 1: length(prplots)
%     line([0 tpe+1], [p_offset*(j-1) p_offset*(j-1)], 'Color', 'k', '
    LineStyle', ':');
% end
%% title(['Poloidal field from internal probe, shot ' int2str(shot)]);
% ylim([-.75*p_offset 5*p_offset]);
% text(tps + .01*(tpe-tps), 5*p_offset-.25*p_offset, num2str(shot), '
    FontSize', 12);
% ylabel('B [mT]', 'FontSize', 18);
% xlabel('t [ms]', 'FontSize', 18);
% saveas(h102, ['S:\Matlab\dissertation\figures\shot' num2str(shot) '
    typical_pol' date], ...
%     'png')
%
% p_offset = .04*1e3;
%
% h103 = figure(103);
% clf;
% set(h103, 'Name', 'B_r')
% axes('Parent', h103,'YTick',[0 p_offset 2*p_offset 3*p_offset 4*
    p_offset], 'FontSize',14);
% box('on');
% hold('all');
% k = 0;
% for j = prplots
%     k = k + 1;
%     plot(t_base*1e3, squeeze(b_matrix(1,j,:))*1e3 + p_offset*(k-1), 'k
    ', 'LineWidth', 2);
%     hold on;
%     text(tpe - .2*(tpe-tps), p_offset*(k)-.5*p_offset, ...
%         {['R = ' num2str(major_rad_m(j),3)]}, 'Color', 'k', 'Fontsize
    ', 14);
% end
% xlim([tps tpe]);
% for j = 1: length(prplots)
%     line([0 tpe+1], [p_offset*(j-1) p_offset*(j-1)], 'Color', 'k', '
    LineStyle', ':');
% end
%% title(['Radial field from internal probe, shot ' int2str(shot)]);
% ylim([-p_offset 5*p_offset]);
% text(tps + .01*(tpe-tps), 5*p_offset-.25*p_offset, num2str(shot), '
    FontSize', 12);
% ylabel('B [mT]', 'FontSize', 18);
% xlabel('t [ms]', 'FontSize', 18);
```

```
% saveas(h103, ['S:\Matlab\dissertation\figures\shot' num2str(shot) '
    typical_rad' date], ...
%       'png')
```

B.9 Fast camera stereoscopic movies

This analysis code is located at

bvictor\Matlab\dissertation\stereoscopy_re_entrant12_21_11_sonymovie.m

```
% this program reads a *.mat file and makes a movie
% version 3 is for movies made on 7/11/11
clear all;

% good shots
% 124235, 124241, 124245 (12/21/11)

shot = 124241; %input('What shot? ');
[a, status] = mdsopen('landau.hit::hitsi', shot);

ph_cam = importdata(['shot' int2str(shot) '.mat']);
t_cam = importdata(['t' int2str(shot) '.mat']);

% movie start time
ts = .69;
% movie end time
te = .72;

[aa,Is] = min((t_cam-ts).^2); % start index
[aa,Ie] = min((t_cam-te).^2); % start index

% Is = 106;
% Ie = 107;

dph_cam = double(ph_cam);
clear ph_cam
dph_max = max(max(max(dph_cam)));
N_pixels = size(squeeze(dph_cam(1,:,:)));
inv_cam = dph_cam(:, end:-1:1, end:-1:1); % image inverted
clear dph_cam
inv_nor = inv_cam/dph_max;
clear inv_cam

figure(7);
clf;
pcolor(squeeze(inv_nor(Is,:,:)));
colormap('gray');

% remove dead fiber pixels
spot1x = 101: 103;
spot1y = 80: 82;
```

```
spot2x = 109: 111;
spot2y = 68: 70;

x_spots = {spot1x, spot2x};
y_spots = {spot1y, spot2y};

for j = Is: Ie
    for k = 1: length(x_spots)
        x_new = ones(length(x_spots{k}),1)*squeeze(inv_nor(j, y_spots{k
            }, x_spots{k}(1) - 1)) + ...
            squeeze(1:length(x_spots{k}))'/(length(x_spots{k}) + 1)* ...
            squeeze(inv_nor(j, y_spots{k}, x_spots{k}(end) + 1) -
                inv_nor(j, y_spots{k}, x_spots{k}(1) - 1));

        y_new = squeeze(inv_nor(j, y_spots{k}(1) - 1, x_spots{k}))*ones
            (1, length(y_spots{k})) + ...
            squeeze(inv_nor(j, y_spots{k}(end) + 1, x_spots{k}) -
                inv_nor(j, y_spots{k}(1) - 1, x_spots{k}))* ...
            squeeze(1: length(y_spots{k}))/(length(y_spots{k}) + 1);

        xy_new = 1/2*(x_new + y_new);
        inv_nor(j, y_spots{k}, x_spots{k}) = xy_new;
    end
end

figure(8);
clf;
pcolor(squeeze(inv_nor(Is,:,:)));
colormap('gray');

% for 12/21/11
left_pixels_y = 9:105;
left_pixels_x = 13:132;
right_pixels_y = 14:112;
right_pixels_x = 134:253;

left_im_dum = inv_nor(Is:Ie, left_pixels_y, left_pixels_x);
right_im_dum = inv_nor(Is:Ie, right_pixels_y, right_pixels_x);

X_pixels = 420;
Y_pixels = 420;

left_grid_x = linspace(1, length(left_pixels_x), X_pixels);
left_grid_y = linspace(1, length(left_pixels_y), Y_pixels);

right_grid_x = linspace(1, length(right_pixels_x), X_pixels);
right_grid_y = linspace(1, length(right_pixels_y), Y_pixels);

[xl, yl] = meshgrid(left_grid_x, left_grid_y);
[xr, yr] = meshgrid(right_grid_x, right_grid_y);
```

```
left_im = zeros(Ie-Is+1, X_pixels, Y_pixels);
right_im = zeros(Ie-Is+1, X_pixels, Y_pixels);
for j = 1: Ie - Is + 1
left_im(j,:,:) = interp2(squeeze(left_im_dum(j,:,:)), xl, yl);
right_im(j,:,:) = interp2(squeeze(right_im_dum(j,:,:)), xr, yr);
end

% figure(1);
% clf;
% imagesc(squeeze(left_im(1,end:-1:1,:)));
% title('left (red)');
% colormap('gray');
%
% figure(2);
% clf;
% imagesc(squeeze(right_im(1,end:-1:1,:)));
% title('right (cyan)');
% colormap('gray');

scrsz = get(0,'ScreenSize');
h1 = figure(3);
set(h1, 'Units', 'pixels', 'Position', [1 scrsz(4)/10 960 480]);
hold('all');
clf;
for j = 1: Ie - Is + 1
    axes('Parent', h1, 'position', [0 0 1 1]);
    clims = [0 1];
    imagesc([squeeze(left_im(j,end:-1:1,:)),squeeze(right_im(j,end
        :-1:1,:))], ...
         clims);
    colormap('gray');
    axis equal
    xlim([0 X_pixels*2]);
    ylim([0 Y_pixels]);
    pause(.1);
    camplot(j) = getframe(figure(3));
    clf;
end

filename = ['S:\Fast_Camera\Movies\d2_' num2str(shot)];
disp(['Writing File to: ' filename])
movie2avi(camplot, filename, 'fps', 10, ...
    'compression', 'None', 'quality', 100); %'compression','None');
```

B.10 Predicted currents from the IDCD equation

This analysis code is located at

bvictor\Matlab\dissertation\idcd_mult_shots.m

```
%% this program compares amperian plots

clear all;

addpath('S:\Matlab\filters');

%% global variables and inputs are here
% these constants scale the Taylor data
mu0 = 4*pi*1e-7;
kboltz = 1.38e-23;

f_order = 4; % order of all the filters
low_filt = 7000; % low pass frequency
high_filt = 30000; % high pass

shots = [121961, 122055, 121727];
% shots = [122131, 122055, 121797];

for j = 1: length(shots);

shot = shots(j);
[a, status] = mdsopen('landau.hit::hitsi', shot);

% define variables
ts = -0.0001; % start time for new time base
ts2 = ts - 0.0002; % start time for cropping data in
te = 0.005; % end time for new time base
te2 = te + 0.0002; % end time for cropping data in
dtn = 0.2e-6; % dt for new time base (5 MHz)
t.base = ts: dtn: te; % new time base
color = ['-r'; '-g'; '-b'; '-c'; '-m'; '-k';
    ':r'; ':g'; ':b'; ':c'; ':m'; ':k'];
color2 = ['r'; 'g'; 'c'; 'b'; 'm'; 'k'];

%-------------------------------------------------------------------------%
[t.iinjx, dt.iinjx, sig.iinjx(j,:)] = gen_data_in('\i_inj_x');
[t.iinjy, dt.iinjy, sig.iinjy(j,:)] = gen_data_in('\i_inj_y');
[t.qinj, dt.qinj, sig.qinj(j,:)] = ...
    gen_data_in('sihi_smooth(sigadd_quad(\i_inj_x,\i_inj_y))');
[t.itor, dt.itor, sig.itor(j,:)] = ...
    gen_data_in('\i_tor_spaavg');
[t.itorsp, dt.itorsp, sig.itorsp(j,:)] = ...
```

```
    gen_data_in('sihi_smooth(\i_tor_spaavg)');
[t.den, dt.den, sig.den(j,:)] = gen_data_in('sihi_smooth(\n_avg_s1)');
[t.rden, dt.rden, sig.rden(j,:)] = gen_data_in('\n_avg_s1');

[t.kdotinj, dt.kdotinj, sig.kdotinj(j,:)] = ...
    gen_data_in(['sigadd(sihi_smooth(\kdot_inj),'...
    '-sigmul(2*(.0075*sihi_smooth(sigadd_quad(\i_inj_x,\i_inj_y))),'...
    'sihi_smooth(sigadd_quad(\psi_inj_x,\psi_inj_y))))']);
% decreased by 20%
[t.kdotinjlow, dt.kdotinjlow, sig.kdotinjlow(j,:)] = ...
    gen_data_in(['sigadd(sihi_smooth(\kdot_inj),'...
    '-sigmul(2*(.8*.0075*sihi_smooth(sigadd_quad(\i_inj_x,\i_inj_y))),'
        ...
    'sihi_smooth(sigadd_quad(\psi_inj_x,\psi_inj_y))))']);
% increased by 20%
[t.kdotinjhigh, dt.kdotinjhigh, sig.kdotinjhigh(j,:)] = ...
    gen_data_in(['sigadd(sihi_smooth(\kdot_inj),'...
    '-sigmul(2*(1.2*.0075*sihi_smooth(sigadd_quad(\i_inj_x,\i_inj_y))),'
        ...
    'sihi_smooth(sigadd_quad(\psi_inj_x,\psi_inj_y))))']);

[t.k, dt.k, sig.k(j,:)] = ...
    gen_data_in(['sihi_smooth('...
    'sigadd('...
    'sigadd('...
    '3.517e-14*sigmul(\i_tor_spaavg,\i_tor_spaavg),'...
    '4.981e-14*sigmul(\i_inj_x,\i_inj_x)'...
    '),'...
    'sigadd('...
    '4.982e-14*sigmul(\i_inj_y,\i_inj_y),'...
    '3.954e-14*sigmul(\i_inj_x,\i_inj_y)'...
    ')'...
    ')'...
    ')']);

%-------------------------------------------------------------------------%
% calculating tau_lr from tau_k

diff_k = diff(sig.k(j,:));
deriv_k_dum = diff_k/dt.k;

deriv_k(j,:) = interp1(t.k(2:end), deriv_k_dum, t.base);
kdotinj_int(j,:) = interp1(t.kdotinj, sig.kdotinj(j,:), t.base);
kdotinjlow_int(j,:) = interp1(t.kdotinjlow, sig.kdotinjlow(j,:), t.base)
    ;
kdotinjhigh_int(j,:) = interp1(t.kdotinjhigh, sig.kdotinjhigh(j,:), t.
    base);
k_int(j,:) = interp1(t.k, sig.k(j,:), t.base);

tau_k(j,:) = k_int(j,:)./(kdotinj_int(j,:) - deriv_k(j,:));
```

```
tau_klow(j,:) = k_int(j,:)./(kdotinjlow_int(j,:) - deriv_k(j,:));
tau_khigh(j,:) = k_int(j,:)./(kdotinjhigh_int(j,:) - deriv_k(j,:));

tau_lr_k(j,:) = 2*tau_k(j,:);
tau_lr_klow(j,:) = 2*tau_klow(j,:);
tau_lr_khigh(j,:) = 2*tau_khigh(j,:);

itor(j,:) = interp1(t.itorsp, sig.itorsp(j,:), t.base);
iinj(j,:) = interp1(t.qinj, sig.qinj(j,:), t.base);
den(j,:) = interp1(t.den, sig.den(j,:), t.base);

c3 = 1.5e19; % chosen to fit data of shot 122385

% integral model
tint1(1) = .0011;
tint1(2) = .0011;
tint1(3) = .00145;
tint2 = .003;
t_int_b.(['shot' int2str(shot)]) = linspace(tint1(j), tint2, round((
    tint2-tint1(j))/dtn));
iinj_int.(['shot' int2str(shot)]) = interp1(t.qinj, sig.qinj(j,:),
    t_int_b.(['shot' int2str(shot)]));
den_int.(['shot' int2str(shot)]) = interp1(t.den, sig.den(j,:), t_int_b
    .(['shot' int2str(shot)]));

[aa, I_ic] = min((t.base - tint1(j)).^2);
itor_ic(j) = itor(j,I_ic); % itor = 22.8 kA at 1 ms
itor_m2.(['shot' int2str(shot)]) = zeros(1, length(t_int_b.(['shot'
    int2str(shot)]))) + itor_ic(j);
itor_m2low.(['shot' int2str(shot)]) = zeros(1, length(t_int_b.(['shot'
    int2str(shot)]))) + itor_ic(j);
itor_m2high.(['shot' int2str(shot)]) = zeros(1, length(t_int_b.(['shot'
    int2str(shot)]))) + itor_ic(j);

tau_lr_k_int.(['shot' int2str(shot)]) = interp1(t.base, tau_lr_k(j,:),
    t_int_b.(['shot' int2str(shot)]));
tau_lr_klow_int.(['shot' int2str(shot)]) = interp1(t.base, tau_lr_klow(j
    ,:), t_int_b.(['shot' int2str(shot)]));
tau_lr_khigh_int.(['shot' int2str(shot)]) = interp1(t.base, tau_lr_khigh
    (j,:), t_int_b.(['shot' int2str(shot)]));

for k = 1: length(t_int_b.(['shot' int2str(shot)]))-1
    itor_m2.(['shot' int2str(shot)])(k+1) = itor_m2.(['shot' int2str(
        shot)])(k)*(1 - ...
        dtn/tau_lr_k_int.(['shot' int2str(shot)])(k)) + ...
        c3*iinj_int.(['shot' int2str(shot)])(k)^2/den_int.(['shot'
            int2str(shot)])(k)*dtn;
    itor_m2low.(['shot' int2str(shot)])(k+1) = itor_m2low.(['shot'
        int2str(shot)])(k)*(1 - ...
        dtn/tau_lr_klow_int.(['shot' int2str(shot)])(k)) + ...
```

```
        c3*iinj_int.(['shot' int2str(shot)])(k)^2/den_int.(['shot'
            int2str(shot)])(k)*dtn;
    itor_m2high.(['shot' int2str(shot)])(k+1) = itor_m2high.(['shot'
        int2str(shot)])(k)*(1 - ...
        dtn/tau_lr_khigh_int.(['shot' int2str(shot)])(k)) + ...
        c3*iinj_int.(['shot' int2str(shot)])(k)^2/den_int.(['shot'
            int2str(shot)])(k)*dtn;
end


mdsclose;

end

scrsz = get(0,'ScreenSize');

h1 = figure(1);
clf;
set(h1, 'Units', 'pixels', 'Position', [1 scrsz(4)/10 720 360], 'Color',
    [1 1 1]);
axes1 = axes('Parent',h1,'YTick',[0 20 40],'YTickLabel',{'0','20','40'
    },...
    'XTick',[1 2],'XTickLabel',{'1','2'},...
    'FontSize',18);
box('on');
grid('on');
hold('all');
for j = 1: length(shots)
    for k = 1: length(t_int_b.(['shot' int2str(shots(j))]))
        line([t_int_b.(['shot' int2str(shots(j))])(k)*1e3 t_int_b.(['
            shot' int2str(shots(j))])(k)*1e3], ...
             [itor_m2low.(['shot' int2str(shots(j))])(k)*1e-3 itor_m2high
                 .(['shot' int2str(shots(j))])(k)*1e-3], 'Color', color2(j
                 ));
        hold on;
    end
    plot(t.itor*1e3,sig.itorsp(j,:)*1e-3,'k','LineWidth', 2,'Parent',
        axes1);
end
text(0.35, 48, ['Shot ' int2str(shots(1))], 'Color', color2(1), '
    Fontsize', 18);
text(0.35, 43, ['Shot ' int2str(shots(2))], 'Color', color2(2), '
    Fontsize', 18);
text(0.35, 38, ['Shot ' int2str(shots(3))], 'Color', color2(3), '
    Fontsize', 18);
ylabel('I_{tor} [kA]','FontSize',18);
xlabel('Time [ms]', 'FontSize', 18);
xlim([0.3 2.8]);
ylim([0 50]);
```

```
fig_save = getframe(h1);
[Xfig, mapfig] = frame2im(fig_save);
imwrite(Xfig, ['S:\Matlab\dissertation\figures\idcd_mult_shots' date '.
    png']);
```

Appendix C
MATLAB PLOTTING CODE

All of these codes are located on the HIT-SI Alfven drive under UserFiles

C.1 Internal magnetic probe

C.1.1 Processing of the internal magnetic probe signals

This code describes the result of each step of processing the internal probe signals.

bvictor\Matlab\dissertation\imp_processing.m

C.1.2 Time base correction for the internal magnetic probe signals

This code shows the effect of correcting the time base caused by using different types of digitizers to digitize the internal probe signals.

bvictor\Matlab\dissertation\imp_time_shift_plot.m

C.1.3 Amplitude correction for the internal magnetic probe signals

This code corrects for the variable internal resistance of the integrators and for the resistance of the cables from the internal probe junction box to the integrators.

bvictor\Matlab\dissertation\imp_dafi_cf_plot.m

C.1.4 Typical internal magnetic probe signals

This code plots typical internal magnetic probe signals.

bvictor\Matlab\dissertation\imp_typical.m

C.1.5 Comparison of the internal probe data to the Taylor equilibrium

This code compares five signals from each direction (radial, poloidal, toroidal) to the Taylor equilibrium.

bvictor\Matlab\dissertation\imp_taylor.m

C.1.6 Internal probe current density and λ calculations

This code plots current density and λ as calculated by the internal probe.

bvictor\Matlab\dissertation\imp_j_lambda.m

The following code compares the current density and λ calculated by the internal probe to those values calculated by the Grad-Shafranov equilibrium.

bvictor\Matlab\dissertation\imp_j_lambda_gs.m

C.2 Density

C.2.1 Density plots

This code makes a simple plot of the density from the interferometer.

bvictor\Matlab\dissertation\density_plots.m

This code adds the toroidal current to the plot of the density.

bvictor\Matlab\dissertation\chord_comparison.m

C.2.2 Comparison of density to line radiation

This code compares the density measured by the interferometer to line radiation from neighboring PMT signals.

bvictor\Matlab\dissertation\den_pmt.m

C.3 Plots of signals from various diagnostics

C.3.1 Shot parameters

This code is set up to do typical shot parameters such as injector voltage and current.

bvictor\Matlab\dissertation\shot_parameters.m

C.3.2 Typical VUV signals

This code plots the VUV signals and compares the ratio between the lines.

bvictor\Matlab\dissertation\vuv_data.m

C.3.3 Typical PMT signals

This code plots the signals from the PMT diagnostics.

bvictor\Matlab\dissertation\pmt_data.m

C.3.4 Toroidal current formation at low λ

This code plots the toroidal current, helicity injection rate and injector λ.

bvictor\Matlab\dissertation\lambda_itor.m

C.3.5 HISS data

This code makes plots the data from the HISS diagnostic.

bvictor\Matlab\dissertation\hiss.m

C.3.6 n = 1 mode amplitude vs. toroidal current

This code compares the n = 1 mode amplitude to the toroidal current for one shot.

bvictor\Matlab\dissertation\n1_itor.m

C.3.7 Multi-shot comparison between current amplification and n = 1 mode amplitude

This shot plots current amplification against n = 1 mode amplitude for several shots.

bvictor\Matlab\dissertation\itor_ratio_n1_compare.m

C.4 Grad-Shafranov equilibrium

All of the code used for the Grad-Shafranov solver is located in the following folder.

bvictor\Matlab\Hit_Fit

The most recent run code is

bvictor\Matlab\Hit_Fit\run_scripts\gs_bsv_surf_probes.m

The following code makes plots from the equilibrium output by the Grad-Shafranov solver.

bvictor\Matlab\ICC2011\gs_plots.m

C.5 IDCD model

C.5.1 Reconstruction of the local current at 45°

This code plots the reconstruction of the toroidal current at 45° based upon the injector currents and the separatrix current.

bvictor\Matlab\deuterium\d_pres_amp_recon_4plot.m

C.5.2 Calculation of the helicity decay time

This code plots the steps involved in calculating the helicity decay time.

bvictor\Matlab\dissertation\tau_k_calc.m

C.5.3 Comparison of the IDCD model to the measured toroidal current

This code compares the toroidal current predicted by the IDCD model to the measured toroidal current for one shot.

bvictor\Matlab\dissertation\idcd_1shot.m

C.5.4 Multi-shot comparison of the IDCD model to the measured toroidal current

This code compares the toroidal current predicted by the IDCD model to the measured toroidal current for multiple shots on the same plot.

bvictor\Matlab\dissertation\idcd_mult_shots.m

C.6 Gas flow rates

C.6.1 He and D gas flow rate comparison

This code compares the flow rates when D and He are used for the injected gas with variable throttle settings.

bvictor\Matlab\gas\throttle_profile_piezo_deuterium_he_x.m

C.6.2 D gas flow rates vs. puff pressure

These codes plot the gas flow rates at variable puff settings.

X-injector:

bvictor\Matlab\Gas\puff_profile_piezo_deuterium_x.m

Y-injector:

bvictor\Matlab\Gas\puff_profile_piezo_deuterium_y.m

C.6.3 D gas flow rates vs. throttle settings

These codes plot the gas flow rates at variable throttle settings.

X-injector:

bvictor\Matlab\Gas\throttle_profile_piezo_deuterium_x.m

Y-injector:

bvictor\Matlab\Gas\throttle_profile_piezo_deuterium_y.m

C.7 Writing data to the HIT-SI tree

This code makes the final toroidal and poloidal signals in the tree from the toroidal and poloidal windings.

bvictor\Matlab\Arboretum\signal_creation.m

This code writes the calibration data for the internal probe to the HIT-SI tree.

bvictor\Matlab\Arboretum\int_probe_cal_fact2.m

This code writes the rotation angle to the tree.

bvictor\Matlab\Arboretum\int_probe_rot_ang.m

Appendix D

CALIBRATION OF THE INTERNAL PROBE SIGNALS

To calibrate the internal magnetic probes a Wavetek function generator, Model 191, was connected to the Helmholtz coil (see Figs. 5.10 and 5.11) and the current through the Helmholtz coil and the measured probe voltage were measured with a Tektronics TDS3034B digital oscilloscope. The current through the Helmholtz coil was measured with a model 110 Pearson probe with 10 turns through the Pearson probe giving 1 V/A sensitivity. The Pearson probe was terminated into 1 MΩ. The magnetic field at the center of the Pearson probe can be calculated from the current through the coil. The probes were terminated to 50 Ω. The calibration of the coils was done at 50, 100, 150, 200, and 250 kHz. A protractor was mounted to the Helmholtz coil so that the orientation of the coil relative to the vertical could be measured. The Helmholtz coil was rotated to produce the largest magnitude signal and the angle was measured.

A picture of the calibration setup is shown in Fig. D.1. The tables in this appendix show the data for the calibration of the internal magnetic probe. The end result of the calibration is the effective area of each winding. Also important is the average angle, which is the rotation of a given spool with respect to the true toroidal and poloidal directions. A soft copy of these tables is located on the HIT-SI Alfven drive under

`UserFiles\bvictor\int_mag_probe\calibration.xls`

The calibration data from these tables is input into the signal directory of the HIT-SI tree so that the calibrated signals are calculated for each shot. See Appendix C.7 for the location of the code used to write the calibration data to the tree. The

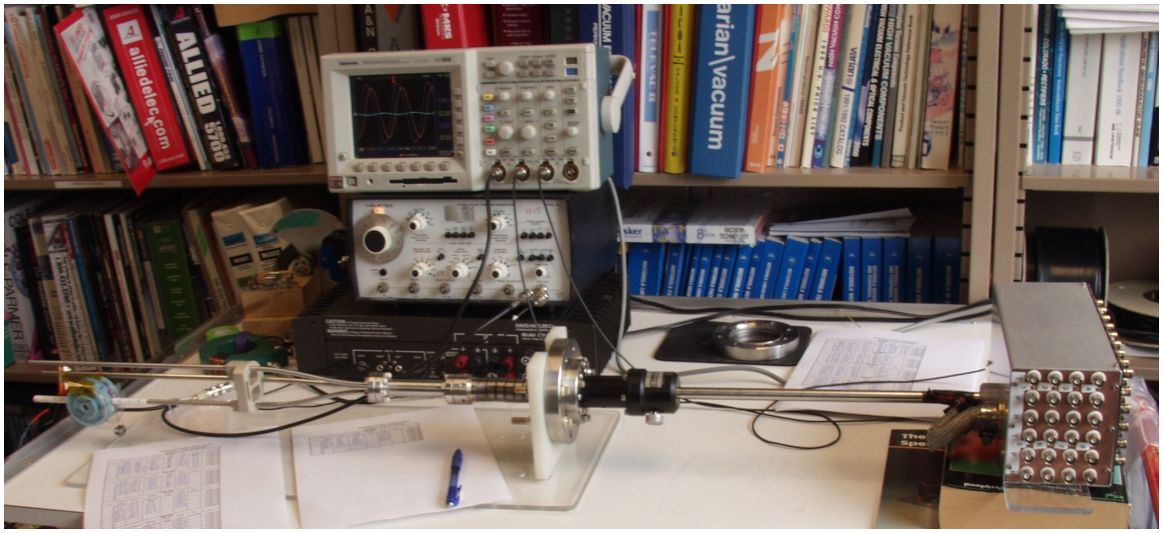

Figure D.1: The setup of the internal probe calibration. The Helmholtz coil is mounted on the bottom stem in position to produce poloidal field. The Helmholtz coil is driven by the function generator below the the oscilloscope. Three signals are measured by the oscilloscope: the current through the Helmholtz coil, the poloidal signal and the toroidal signal.

probe signals can be found in the HIT-SI tree at

HITSI.SIGNALS.INT_PROBES.MAG_TRIDENT

The naming convention for the internal probe signals in the tree is

\B_IMP_X_YZZ

where X is B, M, or T corresponding to the bottom, middle, and top stems; Y is R, P, or T corresponding to the radial, poloidal, and toroidal directions; and ZZ is the probe number with 01 the probe closest to the tip of the probe.

Internal Probe Calibration

17 Probe Array (Toroidal)

50 kHz										
Probe	Phase [deg]	Coil Amp. [mV]	Probe Amp. [mV]	Angle [deg]	Freq. [kHz]	Imp. [Ohms]	B, Helm [T]	Tor. Zero	Effec. Area (m^2)	average angle (deg.)
1								0		0.00
2	-96.1	280.3	26.7	181	49.9	5.5	3.44E-04	-1	2.47E-04	-1.00
3	-96.5	276.5	22.8	183	50.9	4.9	3.40E-04	-3	2.10E-04	-3.00
4	-96.7	278.0	28.3	183	50.3	4.8	3.41E-04	-3	2.62E-04	-3.00
5	-97.0	276.0	37.3	183	50.8	5.9	3.39E-04	-3	3.45E-04	-3.00
6	-96.9	276.0	32.4	183	50.8	5.8	3.39E-04	-3	2.99E-04	-3.00
7	-97.1	278.0	35.6	182	50.5	5.0	3.41E-04	-2	3.29E-04	-2.00
8	-97.2	280.0	38.7	182	50.0	5.2	3.44E-04	-2	3.58E-04	-2.00
9	-97.7	281.0	34.1	181	49.8	5.4	3.45E-04	-1	3.16E-04	-1.00
10	-96.8	280.0	37.2	182	50.0	5.0	3.44E-04	-3	3.44E-04	-2.50
11	-97.2	279.0	33.0	184	50.2	5.2	3.43E-04	-4	3.05E-04	-4.00
12	-97.3	279.0	35.2	185	50.1	5.7	3.43E-04	-3	3.26E-04	-4.00
13	-97.4	279.0	32.7	185	50.2	5.3	3.43E-04	-3	3.03E-04	-4.00
14	-97.0	280.0	29.0	184	50.0	5.5	3.44E-04	-5	2.68E-04	-4.50
15	-97.0	279.0	32.5	186	50.2	5.5	3.43E-04	-6	3.01E-04	-6.00
16	-97.1	279.0	33.2	184	50.3	5.3	3.43E-04	-5	3.07E-04	-4.50
17	-97.5	279.0	32.9	183	50.4	5.2	3.43E-04	-3	3.03E-04	-3.00

100 kHz										
Probe	Phase [deg]	Coil Amp. [mV]	Probe Amp. [mV]	Angle [deg]	Freq. [kHz]	Imp. [Ohms]	B, Helm [T]		Effec. Area (m^2)	
1							0.00E+00			
2	-103.5	157.0	30.2		99.7		1.93E-04		2.50E-04	
3	-103.4	156.0	25.5		100.5		1.92E-04		2.11E-04	
4	-103.6	156.0	31.8		100.7		1.92E-04		2.62E-04	
5	-103.8	156.0	41.9		100.4		1.92E-04		3.47E-04	
6	-104.0	156.0	36.7		100.3		1.92E-04		3.04E-04	
7	-104.0	156.8	39.9		99.8		1.93E-04		3.30E-04	
8	-104.1	157.0	43.5		100.0		1.93E-04		3.59E-04	
9	-104.1	156.1	38.5		100.4		1.92E-04		3.18E-04	
10	-104.1	156.0	41.9		100.4		1.92E-04		3.47E-04	
11	-104.1	156.0	37.1		100.4		1.92E-04		3.07E-04	
12	-104.0	156.4	39.7		100.3		1.92E-04		3.28E-04	
13	-103.9	157.2	36.7		99.6		1.93E-04		3.04E-04	
14	-103.8	156.4	32.7		100.1		1.92E-04		2.71E-04	
15	-103.5	157.3	36.6		100.1		1.93E-04		3.01E-04	
16	-103.9	156.8	37.3		99.9		1.93E-04		3.09E-04	
17	-104.0	155.6	37.1		100.7		1.91E-04		3.07E-04	

Internal Probe Calibration

17 Probe Array (Toroidal)

150 kHz										
Probe	Phase [deg]	Coil Amp. [mV]	Probe Amp. [mV]	Angle [deg]	Freq. [kHz]	Imp. [Ohms]	B, Helm [T]		Effec. Area (m^2)	
1							0.00E+00			
2	-110.8	106.5	30.2		150.2		1.31E-04		2.45E-04	
3	-110.3	106.6	25.6		149.9		1.31E-04		2.08E-04	
4	-110.4	106.7	32.0		150.0		1.31E-04		2.59E-04	
5	-111.1	106.4	42.2		149.7		1.31E-04		3.43E-04	
6	-111.1	106.2	36.6		150.5		1.30E-04		2.97E-04	
7	-111.0	105.6	40.0		150.0		1.30E-04		3.27E-04	
8	-111.3	106.0	43.8		149.9		1.30E-04		3.57E-04	
9	-110.8	106.1	38.5		149.7		1.30E-04		3.14E-04	
10	-110.9	105.2	42.0		150.3		1.29E-04		3.44E-04	
11	-111.2	105.6	37.3		149.8		1.30E-04		3.06E-04	
12	-111.3	104.8	39.9		150.7		1.29E-04		3.27E-04	
13	-111.0	105.2	36.8		150.4		1.29E-04		3.01E-04	
14	-111.0	106.0	32.8		149.7		1.30E-04		2.68E-04	
15	-111.3	104.8	36.7		150.4		1.29E-04		3.02E-04	
16	-111.1	105.8	37.3		150.3		1.30E-04		3.04E-04	
17	-111.0	105.2	37.0		150.2		1.29E-04		3.03E-04	

200 kHz										
Probe	Phase [deg]	Coil Amp. [mV]	Probe Amp. [mV]	Angle [deg]	Freq. [kHz]	Imp. [Ohms]	B, Helm [T]		Effec. Area (m^2)	
1							0.00E+00			
2	-117.0	76.0	29.5		201.0		9.33E-05		2.50E-04	
3	-116.0	78.3	25.4		199.6		9.62E-05		2.11E-04	
4	-116.0	78.5	31.7		199.4		9.64E-05		2.62E-04	
5	-117.7	78.1	41.6		199.6		9.59E-05		3.46E-04	
6	-117.1	78.0	36.2		200.1		9.58E-05		3.01E-04	
7	-117.3	77.2	39.4		199.8		9.48E-05		3.31E-04	
8	-117.3	77.2	43.2		199.4		9.48E-05		3.64E-04	
9	-117.2	77.2	38.0		199.5		9.48E-05		3.20E-04	
10	-117.3	77.2	41.6		199.5		9.48E-05		3.50E-04	
11	-117.0	77.6	36.8		199.3		9.53E-05		3.08E-04	
12	-117.5	77.2	39.4		200.0		9.48E-05		3.31E-04	
13	-117.4	76.8	36.3		199.7		9.43E-05		3.07E-04	
14	-117.0	76.8	32.4		199.8		9.43E-05		2.74E-04	
15	-116.7	77.8	36.2		200.0		9.56E-05		3.01E-04	
16	-117.0	77.8	36.9		199.5		9.56E-05		3.08E-04	
17	-117.4	77.2	36.6		200.1		9.48E-05		3.07E-04	

Internal Probe Calibration

17 Probe Array (Toroidal)

250 kHz										
Probe	Phase [deg]	Coil Amp. [mV]	Probe Amp. [mV]	Angle [deg]	Freq. [kHz]	Imp. [Ohms]	B, Helm [T]		Effec. Area (m^2)	
1							0.00E+00			
2	-122.0	58.0	29.0		250.1		7.12E-05		2.59E-04	
3	-122.7	59.0	24.8		249.4		7.25E-05		2.18E-04	
4	-122.3	58.0	30.7		251.7		7.12E-05		2.73E-04	
5	-123.7	58.5	40.2		252.3		7.18E-05		3.53E-04	
6	-123.5	59.0	35.4		250.7		7.25E-05		3.10E-04	
7	-123.2	58.8	38.6		249.3		7.22E-05		3.41E-04	
8	-124.1	58.6	42.2		249.6		7.20E-05		3.74E-04	
9	-123.5	59.0	37.0		248.7		7.25E-05		3.27E-04	
10	-123.6	58.8	40.4		250.6		7.22E-05		3.55E-04	
11	-123.8	58.4	36.0		251.3		7.17E-05		3.18E-04	
12	-123.8	58.5	38.2		251.1		7.18E-05		3.37E-04	
13	-123.7	58.4	35.6		250.6		7.17E-05		3.15E-04	
14	-123.6	58.4	31.6		250.5		7.17E-05		2.80E-04	
15	-123.6	58.6	35.5		250.0		7.20E-05		3.14E-04	
16	-123.7	58.4	35.9		250.2		7.17E-05		3.18E-04	
17	-123.2	58.8	35.8		250.4		7.22E-05		3.15E-04	

Internal Probe Calibration

9 Probe Array (Toroidal)

50 kHz										
Probe	Phase [deg]	Coil Amp. [mV]	Probe Amp. [mV]	Angle [deg]	Freq. [kHz]	Imp. [Ohms]	B, Helm [T]	Tor. Zero	Effec. Area (m^2)	average angle (deg.)
1	82.1	283.0	26.3	177	49.6	5.7	3.48E-04	1	2.43E-04	2.00
2	81.5	280.0	26.9	178	50.2	5.8	3.44E-04	1	2.48E-04	1.50
3	82.6	280.1	25.8	180	50.3	6.0	3.44E-04	1	2.37E-04	0.50
4	82.9	279.3	28.1	179	50.3	4.8	3.43E-04	0	2.59E-04	0.50
5	82.5	280.8	29.5	178	50.1	5.0	3.45E-04	0	2.72E-04	1.00
6	83.0	282.1	29.6	177	49.7	5.1	3.46E-04	2	2.74E-04	2.50
7	83.0	282.0	29.4	176	49.5	5.1	3.46E-04	1	2.73E-04	2.50
8	82.8	278.0	29.4	176	50.4	5.5	3.41E-04	0	2.72E-04	2.00
9	82.9	279.2	29.5	176	50.2	5.1	3.43E-04	2	2.73E-04	3.00
100 kHz										
Probe	Phase [deg]	Coil Amp. [mV]	Probe Amp. [mV]	Angle [deg]	Freq. [kHz]	Imp. [Ohms]	B, Helm [T]		Effec. Area (m^2)	
1	74.7	156.4	29.7		100.5		1.92E-04		2.45E-04	
2	73.7	158.0	30.1		99.8		1.94E-04		2.47E-04	
3	73.2	158.0	28.8		99.7		1.94E-04		2.37E-04	
4	73.2	158.9	31.3		99.9		1.95E-04		2.56E-04	
5	73.0	158.5	32.9		100.0		1.95E-04		2.69E-04	
6	73.2	158.0	33.1		99.9		1.94E-04		2.72E-04	
7	73.5	158.6	33.0		99.6		1.95E-04		2.71E-04	
8	72.8	156.0	32.9		100.3		1.92E-04		2.72E-04	
9	72.9	158.8	32.9		99.8		1.95E-04		2.69E-04	
150 kHz										
Probe	Phase [deg]	Coil Amp. [mV]	Probe Amp. [mV]	Angle [deg]	Freq. [kHz]	Imp. [Ohms]	B, Helm [T]		Effec. Area (m^2)	
1	68.6	106.0	29.5		150.1		1.30E-04		2.40E-04	
2	67.1	106.0	30.2		149.9		1.30E-04		2.46E-04	
3	65.7	106.4	28.5		149.3		1.31E-04		2.32E-04	
4	66.7	106.0	31.1		150.6		1.30E-04		2.52E-04	
5	65.2	106.0	32.8		149.6		1.30E-04		2.68E-04	
6	65.3	106.0	33.1		149.8		1.30E-04		2.70E-04	
7	65.4	105.0	32.8		150.0		1.29E-04		2.70E-04	
8	66.3	106.4	32.7		149.5		1.31E-04		2.66E-04	
9	66.4	106.3	32.7		150.0		1.31E-04		2.66E-04	

Internal Probe Calibration

9 Probe Array (Toroidal)

200 kHz										
Probe	Phase [deg]	Coil Amp. [mV]	Probe Amp. [mV]	Angle [deg]	Freq. [kHz]	Imp. [Ohms]	B, Helm [T]		Effec. Area (m^2)	
1	60.9	78.2	28.9		199.3		9.60E-05		2.40E-04	
2	58.9	77.0	29.4		200.6		9.46E-05		2.47E-04	
3	58.9	77.6	27.9		199.5		9.53E-05		2.34E-04	
4	59.4	77.0	30.4		199.7		9.46E-05		2.56E-04	
5	58.3	77.0	32.0		200.3		9.46E-05		2.69E-04	
6	58.8	77.0	32.1		199.6		9.46E-05		2.71E-04	
7	58.4	77.0	32.9		199.7		9.46E-05		2.77E-04	
8	58.7	78.1	31.8		198.8		9.59E-05		2.65E-04	
9	58.3	78.5	32.0		199.5		9.64E-05		2.65E-04	
250 kHz										
Probe	Phase [deg]	Coil Amp. [mV]	Probe Amp. [mV]	Angle [deg]	Freq. [kHz]	Imp. [Ohms]	B, Helm [T]		Effec. Area (m^2)	
1	55.1	58.6	28.1		250.0		7.20E-05		2.49E-04	
2	52.9	59.3	28.0		249.5		7.28E-05		2.45E-04	
3	52.6	58.8	26.8		250.2		7.22E-05		2.36E-04	
4	52.7	59.0	29.1		251.1		7.25E-05		2.55E-04	
5	52.0	59.6	30.7		246.6		7.32E-05		2.71E-04	
6	51.8	59.0	30.9		248.3		7.25E-05		2.73E-04	
7	53.7	62.4	31.0		238.4		7.66E-05		2.70E-04	
8	52.1	58.0	30.4		251.0		7.12E-05		2.71E-04	
9	52.8	58.0	30.5		250.9		7.12E-05		2.72E-04	

Internal Probe Calibration

7 Probe Array (Toroidal)

50 kHz										
Probe	Phase [deg]	Coil Amp. [mV]	Probe Amp. [mV]	Angle [deg]	Freq. [kHz]	Imp. [Ohms]	B, Helm [T]	Tor. Zero	Effec. Area (m^2)	average angle (deg.)
1	81.7	279.0	24.2	179	50.2	4.7	3.43E-04	0	2.24E-04	0.50
2	81.3	279.0	24.4	178	50.4	4.5	3.43E-04	1	2.25E-04	1.50
3	80.6	282.0	27.0	179	49.5	4.8	3.46E-04	3	2.51E-04	2.00
4	80.4	279.0	27.2	178	50.3	4.9	3.43E-04	2	2.51E-04	2.00
5	81.2	279.0	22.3	177	50.5	5.1	3.43E-04	0	2.05E-04	1.50
6	81.5	280.0	25.1	179	50.1	5.0	3.44E-04	1	2.32E-04	1.00
7	81.5	280.0	27.7	178	50.0	4.9	3.44E-04	0	2.56E-04	1.00
100 kHz										
Probe	Phase [deg]	Coil Amp. [mV]	Probe Amp. [mV]	Angle [deg]	Freq. [kHz]	Imp. [Ohms]	B, Helm [T]		Effec. Area (m^2)	
1	74.8	156.0	27.2		100.4		1.92E-04		2.25E-04	
2	74.1	156.0	27.3		100.2		1.92E-04		2.26E-04	
3	73.0	157.0	30.4		100.2		1.93E-04		2.50E-04	
4	73.6	155.6	30.4		100.5		1.91E-04		2.52E-04	
5	73.3	157.0	24.9		100.7		1.93E-04		2.04E-04	
6	74.1	157.2	28.0		99.5		1.93E-04		2.32E-04	
7	73.7	156.8	30.9		99.9		1.93E-04		2.56E-04	
150 kHz										
Probe	Phase [deg]	Coil Amp. [mV]	Probe Amp. [mV]	Angle [deg]	Freq. [kHz]	Imp. [Ohms]	B, Helm [T]		Effec. Area (m^2)	
1	68.4	105.6	27.0		150.1		1.30E-04		2.21E-04	
2	66.7	105.2	27.0		150.4		1.29E-04		2.21E-04	
3	67.0	105.2	30.0		150.3		1.29E-04		2.46E-04	
4	66.6	104.8	30.1		151.0		1.29E-04		2.46E-04	
5	66.9	105.6	24.6		149.8		1.30E-04		2.02E-04	
6	66.8	105.2	27.8		150.4		1.29E-04		2.28E-04	
7	66.6	105.6	30.5		150.2		1.30E-04		2.49E-04	
200 kHz										
Probe	Phase [deg]	Coil Amp. [mV]	Probe Amp. [mV]	Angle [deg]	Freq. [kHz]	Imp. [Ohms]	B, Helm [T]		Effec. Area (m^2)	
1	61.6	76.8	26.4		200.7		9.43E-05		2.22E-04	
2	59.1	77.2	26.4		200.1		9.48E-05		2.21E-04	
3	59.2	77.2	29.4		199.3		9.48E-05		2.48E-04	
4	59.0	77.2	29.4		200.2		9.48E-05		2.47E-04	
5	59.1	76.4	24.0		201.3		9.38E-05		2.02E-04	
6	59.8	77.6	27.0		199.5		9.53E-05		2.26E-04	
7	58.9	77.2	29.8		200.2		9.48E-05		2.50E-04	

Internal Probe Calibration

7 Probe Array (Toroidal)

250 kHz										
Probe	Phase [deg]	Coil Amp. [mV]	Probe Amp. [mV]	Angle [deg]	Freq. [kHz]	Imp. [Ohms]	B, Helm [T]		Effec. Area (m^2)	
1	55.8	58.0	25.8		251.3		7.12E-05		2.29E-04	
2	53.3	58.8	25.4		250.0		7.22E-05		2.24E-04	
3	53.3	58.0	28.2		251.9		7.12E-05		2.50E-04	
4	53.2	58.8	28.4		249.2		7.22E-05		2.51E-04	
5	53.3	58.8	23.2		250.8		7.22E-05		2.04E-04	
6	53.5	59.2	26.1		249.2		7.27E-05		2.29E-04	
7	52.3	57.6	28.7		254.4		7.07E-05		2.54E-04	

Internal Probe Calibration

17 Probe Array (Poloidal)

50 kHz

Probe	Phase [deg]	Coil Amp. [mV]	Probe Amp. [mV]	Angle [deg]	Freq. [kHz]	Imp. [Ohms]	B, Helm [T]	Pol. Zero	Effec. Area (m^2)	
1	84.1	279.0	23.6	90	50.4	6.2	3.43E-04		2.17E-04	
2	83.4	280.0	22.0	91	50.0	5.3	3.44E-04	-1	2.04E-04	
3	84.0	281.7	28.2	93	50.0	5.3	3.46E-04	-3	2.59E-04	
4	83.4	280.0	23.2	93	50.1	4.5	3.44E-04	-3	2.14E-04	
5	83.1	280.3	28.0	93	50.2	4.8	3.44E-04	-3	2.58E-04	
6	82.8	280.4	31.4	93	50.2	5.7	3.44E-04	-3	2.89E-04	
7	83.3	281.1	29.8	92	50.1	5.0	3.45E-04	-2	2.74E-04	
8	83.1	283.5	28.5	92	50.3	4.3	3.48E-04	-2	2.59E-04	
9	83.4	283.9	30.4	91	50.2	5.4	3.49E-04	-1	2.76E-04	
10	82.3	283.0	33.7	93	49.9	4.9	3.48E-04	-2	3.09E-04	
11	81.6	282.0	29.6	94	50.0	5.4	3.46E-04	-4	2.72E-04	
12	82.5	282.5	31.4	93	50.1	5.5	3.47E-04	-5	2.87E-04	
13	81.3	283.0	29.0	93	49.6	5.8	3.48E-04	-5	2.68E-04	
14	81.6	279.0	33.5	95	50.3	5.3	3.43E-04	-4	3.09E-04	
15	82.2	279.0	31.2	96	50.4	5.7	3.43E-04	-6	2.88E-04	
16	82.3	280.0	29.2	95	50.1	5.4	3.44E-04	-4	2.70E-04	
17	81.7	281.0	29.2	93	49.6	5.5	3.45E-04	-3	2.71E-04	

100 kHz

Probe	Phase [deg]	Coil Amp. [mV]	Probe Amp. [mV]	Angle [deg]	Freq. [kHz]	Imp. [Ohms]	B, Helm [T]		Effec. Area (m^2)	
1	76.7	157.0	26.7		100.6		1.93E-04		2.19E-04	
2	75.7	157.0	24.9		100.3		1.93E-04		2.05E-04	
3	75.3	156.0	31.8		100.5		1.92E-04		2.63E-04	
4	75.4	158.0	26.1		100.1		1.94E-04		2.14E-04	
5	75.7	158.0	31.5		100.3		1.94E-04		2.58E-04	
6	75.4	158.2	35.2		100.1		1.94E-04		2.88E-04	
7	75.7	157.0	33.5		100.7		1.93E-04		2.75E-04	
8	75.4	159.0	32.0		100.3		1.95E-04		2.60E-04	
9	74.7	159.5	34.1		99.9		1.96E-04		2.77E-04	
10	75.3	157.2	37.9		100.6		1.93E-04		3.11E-04	
11	75.2	157.6	33.2		100.2		1.94E-04		2.72E-04	
12	75.4	157.6	35.3		99.9		1.94E-04		2.91E-04	
13	75.2	156.0	32.7		100.7		1.92E-04		2.70E-04	
14	75.5	156.8	37.5		100.0		1.93E-04		3.10E-04	
15	75.3	156.0	35.0		100.8		1.92E-04		2.88E-04	
16	75.3	156.8	32.8		100.1		1.93E-04		2.71E-04	
17	75.2	157.6	32.8		99.5		1.94E-04		2.71E-04	

Internal Probe Calibration

17 Probe Array (Poloidal)

150 kHz										
Probe	Phase [deg]	Coil Amp. [mV]	Probe Amp. [mV]	Angle [deg]	Freq. [kHz]	Imp. [Ohms]	B, Helm [T]		Effec. Area (m^2)	
1	70.8	105.6	26.5		150.1		1.30E-04		2.17E-04	
2	69.8	106.0	24.9		150.0		1.30E-04		2.03E-04	
3	69.2	106.2	31.8		150.1		1.30E-04		2.59E-04	
4	69.7	106.0	26.0		150.4		1.30E-04		2.11E-04	
5	68.9	105.6	31.3		150.3		1.30E-04		2.56E-04	
6	68.5	105.6	35.3		150.7		1.30E-04		2.87E-04	
7	68.9	106.4	33.7		150.5		1.31E-04		2.73E-04	
8	69.0	106.4	31.9		150.1		1.31E-04		2.59E-04	
9	69.1	106.4	34.1		150.5		1.31E-04		2.76E-04	
10	69.0	106.4	37.8		150.1		1.31E-04		3.07E-04	
11	69.2	106.8	33.2		149.8		1.31E-04		2.69E-04	
12	68.5	105.6	35.3		150.6		1.30E-04		2.88E-04	
13	69.0	105.6	32.7		150.5		1.30E-04		2.67E-04	
14	69.4	105.6	37.4		150.4		1.30E-04		3.05E-04	
15	69.0	106.0	35.0		149.8		1.30E-04		2.86E-04	
16	69.4	105.2	32.8		150.5		1.29E-04		2.68E-04	
17	69.3	105.2	32.9		150.7		1.29E-04		2.69E-04	
200 kHz										
	Phase [deg]	Coil Amp. [mV]	Probe Amp. [mV]	Angle [deg]	Freq. [kHz]	Imp. [Ohms]	B, Helm [T]		Effec. Area (m^2)	
1	64.4	77.8	26.3		200.0		9.56E-05		2.19E-04	
2	62.6	77.2	24.6		200.3		9.48E-05		2.06E-04	
3	62.3	77.2	31.3		200.8		9.48E-05		2.62E-04	
4	62.7	77.8	25.7		200.6		9.56E-05		2.13E-04	
5	62.6	77.6	30.9		200.2		9.53E-05		2.58E-04	
6	61.9	77.6	35.0		200.3		9.53E-05		2.92E-04	
7	62.2	78.0	33.2		199.6		9.58E-05		2.76E-04	
8	62.7	78.0	31.3		199.8		9.58E-05		2.60E-04	
9	61.9	77.6	33.5		200.8		9.53E-05		2.79E-04	
10	61.9	77.6	37.2		200.8		9.53E-05		3.09E-04	
11	61.9	77.6	32.6		199.7		9.53E-05		2.73E-04	
12	61.9	77.6	34.7		199.6		9.53E-05		2.90E-04	
13	61.9	77.2	32.2		201.0		9.48E-05		2.69E-04	
14	61.8	78.2	36.9		199.0		9.60E-05		3.07E-04	
15	61.8	77.2	34.4		200.6		9.48E-05		2.88E-04	
16	62.2	77.6	32.3		199.8		9.53E-05		2.70E-04	
17	62.0	77.6	32.3		199.2		9.53E-05		2.71E-04	

Internal Probe Calibration

17 Probe Array (Poloidal)

250 kHz										
Probe	Phase [deg]	Coil Amp. [mV]	Probe Amp. [mV]	Angle [deg]	Freq. [kHz]	Imp. [Ohms]	B, Helm [T]		Effec. Area (m^2)	
1	58.6	58.4	25.8		250.4		7.17E-05		2.29E-04	
2	57.7	59.2	23.7		249.3		7.27E-05		2.08E-04	
3	57.2	58.8	30.5		250.6		7.22E-05		2.68E-04	
4	57.2	58.7	25.1		251.3		7.21E-05		2.20E-04	
5	56.7	59.2	30.2		249.2		7.27E-05		2.65E-04	
6	55.8	59.2	33.9		248.9		7.27E-05		2.98E-04	
7	56.3	59.6	32.3		250.0		7.32E-05		2.81E-04	
8	56.4	59.2	30.7		251.0		7.27E-05		2.68E-04	
9	56.5	59.6	32.7		249.9		7.32E-05		2.85E-04	
10	56.3	59.2	36.3		250.6		7.27E-05		3.17E-04	
11	56.6	59.2	31.8		249.8		7.27E-05		2.79E-04	
12	56.6	59.2	33.9		248.9		7.27E-05		2.98E-04	
13	56.0	58.5	31.3		251.3		7.18E-05		2.76E-04	
14	56.6	58.6	35.9		249.9		7.20E-05		3.18E-04	
15	55.8	58.7	33.5		250.7		7.21E-05		2.95E-04	
16	56.6	58.8	31.5		249.7		7.22E-05		2.78E-04	
17	56.2	58.4	31.5		251.3		7.17E-05		2.78E-04	

Internal Probe Calibration

9 Probe Array (Poloidal)

50 kHz										
Probe	Phase [deg]	Coil Amp. [mV]	Probe Amp. [mV]	Angle [deg]	Freq. [kHz]	Imp. [Ohms]	B, Helm [T]	Pol. Zero	Effec. Area (m^2)	
1	83.3	282.5	23.7	89	50.0	6.1	3.47E-04	3	2.17E-04	
2	82.5	280.0	26.1	89	50.1	5.7	3.44E-04	2	2.41E-04	
3	82.4	280.0	27.1	89	50.1	5.7	3.44E-04	0	2.50E-04	
4	82.3	280.3	19.6	90	50.3	5.2	3.44E-04	1	1.80E-04	
5	82.2	280.3	33.5	90	50.2	5.2	3.44E-04	2	3.09E-04	
6	82.1	280.4	33.5	88	50.2	5.3	3.44E-04	3	3.08E-04	
7	82.9	281.3	33.4	89	49.9	5.3	3.45E-04	4	3.08E-04	
8	82.2	280.2	33.1	90	50.3	5.6	3.44E-04	4	3.04E-04	
9	82.4	280.0	33.3	88	50.1	5.1	3.44E-04	4	3.08E-04	
100 kHz										
Probe	Phase [deg]	Coil Amp. [mV]	Probe Amp. [mV]	Angle [deg]	Freq. [kHz]	Imp. [Ohms]	B, Helm [T]		Effec. Area (m^2)	
1	74.9	158.2	26.6		100.3		1.94E-04		2.17E-04	
2	73.3	159.2	29.2		99.5		1.96E-04		2.39E-04	
3	73.6	158.1	30.4		100.3		1.94E-04		2.48E-04	
4	73.1	157.4	22.0		100.5		1.93E-04		1.80E-04	
5	72.7	157.3	37.4		100.6		1.93E-04		3.06E-04	
6	73.4	158.4	37.4		100.1		1.95E-04		3.06E-04	
7	72.8	157.3	37.4		100.5		1.93E-04		3.07E-04	
8	73.3	157.0	37.0		100.4		1.93E-04		3.04E-04	
9	72.9	158.0	37.3		100.0		1.94E-04		3.06E-04	
150 kHz										
Probe	Phase [deg]	Coil Amp. [mV]	Probe Amp. [mV]	Angle [deg]	Freq. [kHz]	Imp. [Ohms]	B, Helm [T]		Effec. Area (m^2)	
1	67.7	106.5	26.4		150.1		1.31E-04		2.14E-04	
2	66.0	106.3	29.0		150.4		1.31E-04		2.35E-04	
3	66.2	106.5	30.2		149.6		1.31E-04		2.46E-04	
4	66.7	106.4	21.8		149.9		1.31E-04		1.77E-04	
5	65.8	106.3	37.2		150.0		1.31E-04		3.02E-04	
6	65.9	106.5	37.4		149.8		1.31E-04		3.04E-04	
7	65.9	106.2	37.2		150.3		1.30E-04		3.02E-04	
8	66.2	106.0	36.9		149.6		1.30E-04		3.02E-04	
9	65.5	105.2	37.1		150.6		1.29E-04		3.03E-04	

Internal Probe Calibration

9 Probe Array (Poloidal)

200 kHz										
Probe	Phase [deg]	Coil Amp. [mV]	Probe Amp. [mV]	Angle [deg]	Freq. [kHz]	Imp. [Ohms]	B, Helm [T]		Effec. Area (m^2)	
1	61.3	78.2	26.0		199.1		9.60E-05		2.16E-04	
2	58.3	77.0	28.3		201.2		9.46E-05		2.37E-04	
3	58.8	78.5	29.3		199.7		9.64E-05		2.42E-04	
4	58.4	77.4	21.4		200.5		9.51E-05		1.79E-04	
5	58.9	78.3	36.2		199.0		9.62E-05		3.01E-04	
6	57.6	77.0	36.2		201.6		9.46E-05		3.02E-04	
7	57.5	77.2	36.2		201.3		9.48E-05		3.02E-04	
8	58.2	77.6	35.8		199.5		9.53E-05		3.00E-04	
9	58.3	77.2	36.1		200.6		9.48E-05		3.02E-04	
250 kHz										
Probe	Phase [deg]	Coil Amp. [mV]	Probe Amp. [mV]	Angle [deg]	Freq. [kHz]	Imp. [Ohms]	B, Helm [T]		Effec. Area (m^2)	
1	55.1	58.0	25.0		250.6		7.12E-05		2.23E-04	
2	52.7	58.0	27.0		250.6		7.12E-05		2.41E-04	
3	52.5	58.0	28.1		250.6		7.12E-05		2.51E-04	
4	52.7	58.0	20.4		251.8		7.12E-05		1.81E-04	
5	52.7	59.1	34.6		250.5		7.26E-05		3.03E-04	
6	53.0	59.3	34.7		250.1		7.28E-05		3.03E-04	
7	51.6	58.2	34.6		251.5		7.15E-05		3.06E-04	
8	51.5	58.0	34.1		252.3		7.12E-05		3.02E-04	
9	52.2	59.3	34.6		249.2		7.28E-05		3.03E-04	

Internal Probe Calibration

7 Probe Array (Poloidal)

50 kHz

Probe	Phase [deg]	Coil Amp. [mV]	Probe Amp. [mV]	Angle [deg]	Freq. [kHz]	Imp. [Ohms]	B, Helm [T]	Pol. Zero	Effec. Area (m^2)	
1	82.6	281.4	27.3	90	49.9	4.9	3.46E-04	1	2.52E-04	
2	82.0	281.4	27.4	89	49.9	4.7	3.46E-04	2	2.53E-04	
3	81.9	281.4	24.1	87	49.9	4.8	3.46E-04	1	2.22E-04	
4	82.2	281.2	24.0	88	49.9	4.7	3.45E-04	2	2.22E-04	
5	82.1	281.4	27.4	90	49.9	4.9	3.46E-04	3	2.53E-04	
6	82.1	281.1	27.4	89	49.9	4.8	3.45E-04	1	2.53E-04	
7	82.0	281.2	24.1	90	49.9	4.9	3.45E-04	2	2.23E-04	

100 kHz

Probe	Phase [deg]	Coil Amp. [mV]	Probe Amp. [mV]	Angle [deg]	Freq. [kHz]	Imp. [Ohms]	B, Helm [T]		Effec. Area (m^2)	
1	75.2	158.3	30.7		100.2		1.94E-04		2.51E-04	
2	74.1	159.2	30.7		99.0		1.96E-04		2.52E-04	
3	73.7	158.3	26.9		100.1		1.94E-04		2.20E-04	
4	73.8	158.8	27.0		100.0		1.95E-04		2.20E-04	
5	73.4	156.0	30.8		101.1		1.92E-04		2.53E-04	
6	73.4	156.5	30.8		101.1		1.92E-04		2.52E-04	
7	73.4	157.4	26.9		100.4		1.93E-04		2.21E-04	

150 kHz

Probe	Phase [deg]	Coil Amp. [mV]	Probe Amp. [mV]	Angle [deg]	Freq. [kHz]	Imp. [Ohms]	B, Helm [T]		Effec. Area (m^2)	
1	68.2	105.2	30.6		151.0		1.29E-04		2.50E-04	
2	66.7	107.0	30.5		150.0		1.31E-04		2.46E-04	
3	66.7	106.0	26.7		149.4		1.30E-04		2.18E-04	
4	66.7	106.5	26.6		150.0		1.31E-04		2.16E-04	
5	66.5	106.3	30.4		150.1		1.31E-04		2.47E-04	
6	67.0	106.0	30.4		149.3		1.30E-04		2.49E-04	
7	67.1	106.0	26.6		149.9		1.30E-04		2.17E-04	

200 kHz

Probe	Phase [deg]	Coil Amp. [mV]	Probe Amp. [mV]	Angle [deg]	Freq. [kHz]	Imp. [Ohms]	B, Helm [T]		Effec. Area (m^2)	
1	61.6	78.2	30.1		199.7		9.60E-05		2.50E-04	
2	59.0	76.0	29.7		200.6		9.33E-05		2.52E-04	
3	58.1	77.1	26.0		200.5		9.47E-05		2.18E-04	
4	59.1	78.5	26.0		200.0		9.64E-05		2.15E-04	
5	59.1	78.7	29.7		199.8		9.67E-05		2.45E-04	
6	58.7	77.2	29.6		200.6		9.48E-05		2.48E-04	
7	58.9	77.0	25.9		199.5		9.46E-05		2.18E-04	

Internal Probe Calibration

7 Probe Array (Poloidal)

250 kHz										
Probe	Phase [deg]	Coil Amp. [mV]	Probe Amp. [mV]	Angle [deg]	Freq. [kHz]	Imp. [Ohms]	B, Helm [T]		Effec. Area (m^2)	
1	56.2	58.0	29.2		250.6		7.12E-05		2.60E-04	
2	53.4	58.5	28.5		251.9		7.18E-05		2.51E-04	
3	54.3	59.1	25.0		250.0		7.26E-05		2.19E-04	
4	52.0	58.5	24.9		251.3		7.18E-05		2.19E-04	
5	52.6	58.0	28.5		251.7		7.12E-05		2.53E-04	
6	52.5	58.3	28.5		253.2		7.16E-05		2.50E-04	
7	53.6	59.0	24.9		250.5		7.25E-05		2.18E-04	

Internal Probe Calibration

17 Probe Array (Radial)

50 kHz									
Probe	Phase [deg]	Coil Amp. [mV]	Probe Amp. [mV]	Angle [deg]	Freq. [kHz]	Imp. [Ohms]	B, Helm [T]		Effec. Area (m^2)
1	82.6	279.0	36.1		50.2	7.1	3.43E-04		3.34E-04
2	82.2	280.7	38.0		50.2	6.1	3.45E-04		3.49E-04
3	82.2	279.0	36.3		50.2	6.7	3.43E-04		3.36E-04
4	82.3	280.0	36.9		50.0	6.1	3.44E-04		3.42E-04
5	82.4	282.4	33.3		49.6	5.2	3.47E-04		3.08E-04
6	82.6	279.0	33.6		50.1	4.8	3.43E-04		3.11E-04
7	82.3	280.0	33.8		49.9	4.6	3.44E-04		3.13E-04
8	82.5	279.1	33.4		50.2	4.9	3.43E-04		3.09E-04
9	82.4	279.0	35.5		50.1	5.7	3.43E-04		3.29E-04
10	82.4	277.1	38.0		50.7	5.2	3.40E-04		3.51E-04
11	82.6	279.1	33.6		50.2	4.8	3.43E-04		3.11E-04
12	82.4	282.1	34.6		49.4	5.8	3.46E-04		3.22E-04
13	82.3	280.4	34.6		49.8	5.3	3.44E-04		3.21E-04
14	82.7	279.0	34.9		49.9	5.8	3.43E-04		3.25E-04
15	82.6	281.3	33.7		49.8	4.5	3.45E-04		3.12E-04
16	82.4	281.6	34.8		49.7	5.8	3.46E-04		3.22E-04
17	82.2	278.2	34.4		50.3	5.9	3.42E-04		3.19E-04
100 kHz									
Probe	Phase [deg]	Coil Amp. [mV]	Probe Amp. [mV]	Angle [deg]	Freq. [kHz]	Imp. [Ohms]	B, Helm [T]		Effec. Area (m^2)
1	74.5	158.2	40.5		99.5		1.94E-04		3.33E-04
2	73.8	159.2	42.3		99.3		1.96E-04		3.47E-04
3	73.5	158.0	40.6		99.4		1.94E-04		3.35E-04
4	73.8	157.0	41.2		100.5		1.93E-04		3.38E-04
5	74.2	157.2	37.4		100.6		1.93E-04		3.06E-04
6	74.3	157.8	37.6		100.3		1.94E-04		3.08E-04
7	74.3	157.7	38.0		100.3		1.94E-04		3.11E-04
8	74.3	157.0	37.5		99.8		1.93E-04		3.10E-04
9	74.0	156.0	39.7		100.7		1.92E-04		3.27E-04
10	73.4	155.0	42.5		101.4		1.90E-04		3.50E-04
11	74.6	159.1	37.6		99.0		1.95E-04		3.09E-04
12	74.6	158.3	38.8		99.1		1.94E-04		3.21E-04
13	74.2	157.0	38.8		99.6		1.93E-04		3.22E-04
14	74.1	157.5	39.2		100.4		1.93E-04		3.21E-04
15	74.4	159.4	37.9		99.0		1.96E-04		3.11E-04
16	74.0	157.0	39.1		99.7		1.93E-04		3.24E-04
17	74.2	157.9	38.6		100.1		1.94E-04		3.16E-04

Internal Probe Calibration

17 Probe Array (Radial)

150 kHz									
Probe	Phase [deg]	Coil Amp. [mV]	Probe Amp. [mV]	Angle [deg]	Freq. [kHz]	Imp. [Ohms]	B, Helm [T]		Effec. Area (m^2)
1	66.6	106.4	40.7		149.1		1.31E-04		3.32E-04
2	66.6	105.0	42.5		150.1		1.29E-04		3.49E-04
3	66.8	105.0	40.9		149.5		1.29E-04		3.38E-04
4	66.7	105.0	41.3		150.3		1.29E-04		3.39E-04
5	67.2	105.0	37.5		149.7		1.29E-04		3.09E-04
6	67.2	105.0	37.5		150.1		1.29E-04		3.08E-04
7	67.4	105.0	37.9		150.2		1.29E-04		3.11E-04
8	66.4	105.5	37.6		150.4		1.30E-04		3.07E-04
9	67.0	105.0	39.8		149.5		1.29E-04		3.29E-04
10	66.9	105.0	42.5		150.0		1.29E-04		3.50E-04
11	66.7	106.3	37.5		149.5		1.31E-04		3.06E-04
12	66.9	105.0	39.0		149.3		1.29E-04		3.22E-04
13	67.0	105.0	38.8		150.1		1.29E-04		3.19E-04
14	66.9	105.0	39.2		149.7		1.29E-04		3.23E-04
15	67.4	105.0	37.8		150.2		1.29E-04		3.11E-04
16	66.8	105.5	39.2		150.9		1.30E-04		3.19E-04
17	67.1	105.0	38.6		149.7		1.29E-04		3.18E-04
200 kHz									
	Phase [deg]	Coil Amp. [mV]	Probe Amp. [mV]	Angle [deg]	Freq. [kHz]	Imp. [Ohms]	B, Helm [T]		Effec. Area (m^2)
1	59.1	77.7	39.9		200.6		9.54E-05		3.32E-04
2	58.4	77.5	41.7		200.8		9.52E-05		3.47E-04
3	58.8	77.0	40.1		199.0		9.46E-05		3.39E-04
4	59.3	77.5	40.6		200.1		9.52E-05		3.39E-04
5	59.9	77.0	36.8		199.8		9.46E-05		3.10E-04
6	59.7	77.3	37.0		201.3		9.49E-05		3.08E-04
7	59.9	77.0	37.2		200.0		9.46E-05		3.13E-04
8	60.2	77.5	36.8		199.6		9.52E-05		3.08E-04
9	59.3	77.0	39.0		198.8		9.46E-05		3.30E-04
10	58.8	77.0	41.7		199.6		9.46E-05		3.52E-04
11	60.6	78.3	36.9		198.6		9.62E-05		3.07E-04
12	59.4	77.6	38.2		200.6		9.53E-05		3.18E-04
13	59.1	77.9	38.1		200.2		9.57E-05		3.17E-04
14	59.3	77.7	38.4		200.2		9.54E-05		3.20E-04
15	59.9	77.0	37.1		200.4		9.46E-05		3.12E-04
16	59.6	77.0	38.4		199.6		9.46E-05		3.24E-04
17	59.7	77.4	37.9		200.1		9.51E-05		3.17E-04

Internal Probe Calibration

17 Probe Array (Radial)

250 kHz									
Probe	Phase [deg]	Coil Amp. [mV]	Probe Amp. [mV]	Angle [deg]	Freq. [kHz]	Imp. [Ohms]	B, Helm [T]		Effec. Area (m^2)
1	53.9	58.2	38.5		251.3		7.15E-05		3.41E-04
2	52.1	57.0	39.9		251.6		7.00E-05		3.61E-04
3	52.2	59.0	38.5		248.6		7.25E-05		3.40E-04
4	51.9	57.0	38.9		253.0		7.00E-05		3.50E-04
5	53.0	57.0	35.4		252.5		7.00E-05		3.19E-04
6	53.8	58.1	35.6		251.3		7.14E-05		3.16E-04
7	53.9	59.0	36.0		247.9		7.25E-05		3.19E-04
8	53.3	60.0	35.6		249.2		7.37E-05		3.09E-04
9	52.8	59.0	37.6		248.1		7.25E-05		3.33E-04
10	53.4	58.0	40.1		252.0		7.12E-05		3.56E-04
11	54.0	59.0	35.8		248.0		7.25E-05		3.17E-04
12	53.6	58.1	36.8		250.6		7.14E-05		3.28E-04
13	53.3	59.6	36.9		249.9		7.32E-05		3.21E-04
14	53.1	59.6	37.2		249.7		7.32E-05		3.24E-04
15	52.8	57.5	35.8		254.6		7.06E-05		3.17E-04
16	53.6	58.0	37.0		251.3		7.12E-05		3.29E-04
17	53.9	58.1	36.6		251.0		7.14E-05		3.25E-04

Internal Probe Calibration

9 Probe Array (Radial)

50 kHz									
Probe	Phase [deg]	Coil Amp. [mV]	Probe Amp. [mV]	Angle [deg]	Freq. [kHz]	Imp. [Ohms]	B, Helm [T]		Effec. Area (m^2)
1	81.8	279.0	35.2		50.1	6.1	3.43E-04		3.26E-04
2	81.4	279.0	36.1		50.2	6.1	3.43E-04		3.34E-04
3	81.2	279.1	35.6		50.2	6.2	3.43E-04		3.29E-04
4	81.3	279.2	36.8		50.1	5.3	3.43E-04		3.41E-04
5	81.2	277.0	34.3		50.6	5.6	3.40E-04		3.17E-04
6	81.4	279.1	35.0		50.2	5.0	3.43E-04		3.24E-04
7	81.4	279.0	34.3		50.1	5.7	3.43E-04		3.18E-04
8	81.3	279.8	34.1		50.2	5.3	3.44E-04		3.15E-04
9	81.3	279.0	36.1		50.1	5.1	3.43E-04		3.35E-04
100 kHz									
Probe	Phase [deg]	Coil Amp. [mV]	Probe Amp. [mV]	Angle [deg]	Freq. [kHz]	Imp. [Ohms]	B, Helm [T]		Effec. Area (m^2)
1	72.5	157.0	39.3		99.7		1.93E-04		3.25E-04
2	71.6	157.9	40.2		100.2		1.94E-04		3.29E-04
3	71.5	157.8	39.6		100.2		1.94E-04		3.25E-04
4	71.6	157.2	40.9		100.4		1.93E-04		3.36E-04
5	71.9	157.5	38.1		100.0		1.93E-04		3.13E-04
6	71.5	155.0	38.9		100.8		1.90E-04		3.23E-04
7	71.9	157.3	38.2		100.5		1.93E-04		3.13E-04
8	71.7	157.0	37.9		100.0		1.93E-04		3.13E-04
9	71.6	157.5	40.3		100.3		1.93E-04		3.31E-04
150 kHz									
Probe	Phase [deg]	Coil Amp. [mV]	Probe Amp. [mV]	Angle [deg]	Freq. [kHz]	Imp. [Ohms]	B, Helm [T]		Effec. Area (m^2)
1	64.5	105.0	39.1		150.2		1.29E-04		3.21E-04
2	63.6	105.0	39.9		150.6		1.29E-04		3.27E-04
3	63.4	105.5	39.4		150.5		1.30E-04		3.22E-04
4	63.3	105.0	40.6		149.9		1.29E-04		3.34E-04
5	63.8	105.0	37.9		149.6		1.29E-04		3.13E-04
6	63.8	105.0	38.6		149.8		1.29E-04		3.18E-04
7	63.8	105.0	38.0		150.3		1.29E-04		3.12E-04
8	63.5	105.0	37.6		150.3		1.29E-04		3.09E-04
9	63.1	105.3	39.9		150.4		1.29E-04		3.26E-04

Internal Probe Calibration

9 Probe Array (Radial)

200 kHz									
Probe	Phase [deg]	Coil Amp. [mV]	Probe Amp. [mV]	Angle [deg]	Freq. [kHz]	Imp. [Ohms]	B, Helm [T]		Effec. Area (m^2)
1	56.1	77.0	38.1		200.0		9.46E-05		3.21E-04
2	55.4	77.0	38.8		199.5		9.46E-05		3.27E-04
3	55.0	77.6	38.1		200.6		9.53E-05		3.17E-04
4	55.3	77.0	39.3		199.0		9.46E-05		3.32E-04
5	55.2	77.4	36.6		200.3		9.51E-05		3.06E-04
6	54.9	77.3	37.3		201.0		9.49E-05		3.11E-04
7	55.5	77.0	36.7		200.5		9.46E-05		3.08E-04
8	55.7	77.0	36.5		199.6		9.46E-05		3.08E-04
9	55.0	77.0	38.7		199.3		9.46E-05		3.27E-04
250 kHz									
Probe	Phase [deg]	Coil Amp. [mV]	Probe Amp. [mV]	Angle [deg]	Freq. [kHz]	Imp. [Ohms]	B, Helm [T]		Effec. Area (m^2)
1	49.6	57.0	36.4		251.8		7.00E-05		3.29E-04
2	48.9	58.0	37.0		249.6		7.12E-05		3.31E-04
3	48.3	59.3	36.3		250.3		7.28E-05		3.17E-04
4	48.2	59.1	37.4		250.6		7.26E-05		3.27E-04
5	48.7	59.1	34.9		250.9		7.26E-05		3.05E-04
6	49.9	58.3	35.6		250.6		7.16E-05		3.16E-04
7	49.5	58.0	35.0		250.0		7.12E-05		3.13E-04
8	48.1	59.1	34.8		249.4		7.26E-05		3.06E-04
9	49.7	58.5	36.9		250.1		7.18E-05		3.27E-04

Internal Probe Calibration

7 Probe Array (Radial)

50 kHz									
Probe	Phase [deg]	Coil Amp. [mV]	Probe Amp. [mV]	Angle [deg]	Freq. [kHz]	Imp. [Ohms]	B, Helm [T]		Effec. Area (m^2)
1	81.4	278.0	36.9		50.3	5.2	3.41E-04		3.42E-04
2	81.2	279.0	38.0		50.1	5.1	3.43E-04		3.52E-04
3	81.2	279.2	39.0		50.3	4.5	3.43E-04		3.60E-04
4	81.2	281.1	35.3		49.8	5.2	3.45E-04		3.27E-04
5	81.0	277.0	35.9		50.6	6.7	3.40E-04		3.32E-04
6	81.0	279.2	37.1		50.4	5.4	3.43E-04		3.42E-04
7	81.2	281.4	36.5		49.8	5.2	3.46E-04		3.38E-04
100 kHz									
Probe	Phase [deg]	Coil Amp. [mV]	Probe Amp. [mV]	Angle [deg]	Freq. [kHz]	Imp. [Ohms]	B, Helm [T]		Effec. Area (m^2)
1	72.6	157.0	41.1		99.7		1.93E-04		3.40E-04
2	71.5	157.5	42.1		100.5		1.93E-04		3.45E-04
3	71.8	157.4	43.3		100.0		1.93E-04		3.56E-04
4	71.6	158.4	39.5		99.8		1.95E-04		3.24E-04
5	71.6	157.0	39.8		100.2		1.93E-04		3.28E-04
6	71.7	157.1	41.2		100.2		1.93E-04		3.39E-04
7	71.9	157.4	40.7		100.1		1.93E-04		3.35E-04
150 kHz									
Probe	Phase [deg]	Coil Amp. [mV]	Probe Amp. [mV]	Angle [deg]	Freq. [kHz]	Imp. [Ohms]	B, Helm [T]		Effec. Area (m^2)
1	64.0	105.4	41.1		150.4		1.29E-04		3.36E-04
2	63.4	105.0	41.9		150.1		1.29E-04		3.45E-04
3	63.0	105.4	43.0		150.3		1.29E-04		3.52E-04
4	64.0	106.0	39.3		149.8		1.30E-04		3.21E-04
5	62.6	105.0	39.5		150.6		1.29E-04		3.24E-04
6	63.0	105.5	40.9		150.4		1.30E-04		3.34E-04
7	63.1	105.4	40.4		150.4		1.29E-04		3.30E-04
200 kHz									
Probe	Phase [deg]	Coil Amp. [mV]	Probe Amp. [mV]	Angle [deg]	Freq. [kHz]	Imp. [Ohms]	B, Helm [T]		Effec. Area (m^2)
1	57.1	77.4	39.9		199.6		9.51E-05		3.35E-04
2	55.3	77.1	40.5		200.3		9.47E-05		3.40E-04
3	55.2	77.2	41.7		200.5		9.48E-05		3.49E-04
4	55.9	77.3	37.9		199.8		9.49E-05		3.18E-04
5	54.6	76.0	38.2		200.4		9.33E-05		3.25E-04
6	55.3	77.0	39.5		200.0		9.46E-05		3.32E-04
7	55.9	77.3	39.1		199.6		9.49E-05		3.28E-04

Internal Probe Calibration

7 Probe Array (Radial)

250 kHz									
Probe	Phase [deg]	Coil Amp. [mV]	Probe Amp. [mV]	Angle [deg]	Freq. [kHz]	Imp. [Ohms]	B, Helm [T]		Effec. Area (m^2)
1	50.1	58.0	38.1		250.4		7.12E-05		3.40E-04
2	47.8	59.2	38.7		248.8		7.27E-05		3.40E-04
3	47.8	58.0	39.7		250.7		7.12E-05		3.54E-04
4	48.8	58.0	36.2		249.4		7.12E-05		3.24E-04
5	48.2	58.0	36.4		250.5		7.12E-05		3.25E-04
6	48.3	58.0	37.7		250.7		7.12E-05		3.36E-04
7	48.5	58.0	37.3		250.3		7.12E-05		3.33E-04

Appendix E

BANDPASS FILTERS FOR LIGHT DIAGNOSTICS

HIT-SI has several bandpass filters that can be used to isolate line radiation for plasma diagnostics.

E.1 25 mm diameter bandpass filters

These filters are typically used with the PMTs. There is an additional 25 mm diameter bandpass filter for H_α radiation at 656.3 nm.

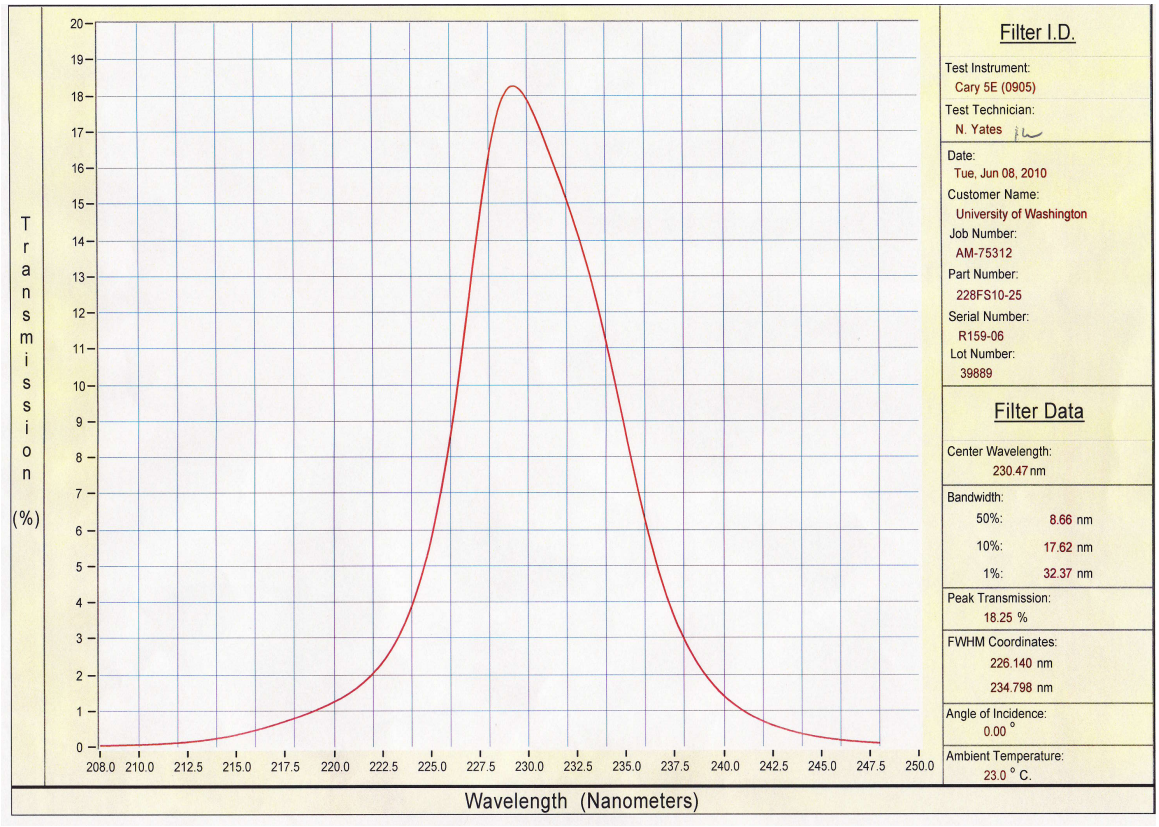

Figure E.1: Transmission curve of the bandpass filter for the C III line at 229.7 nm.

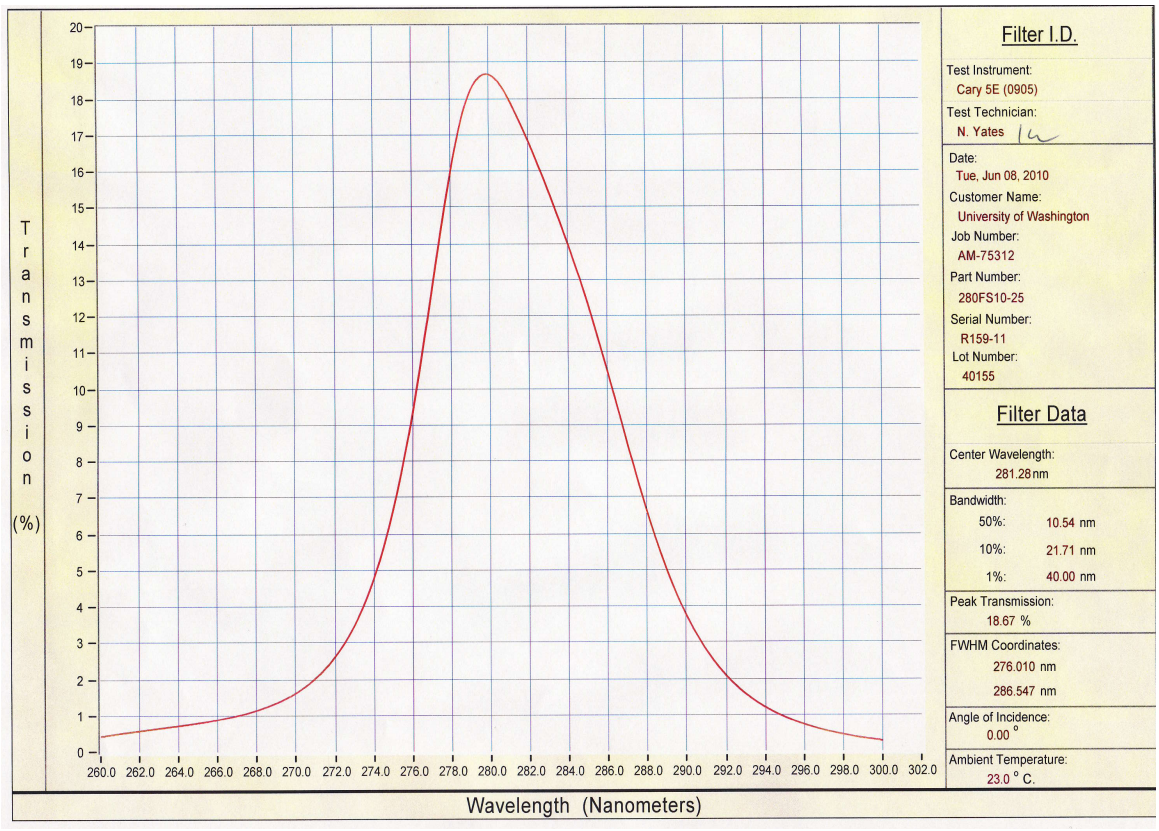

Figure E.2: Transmission curve of the bandpass filter for the C II line at 283.7 nm.

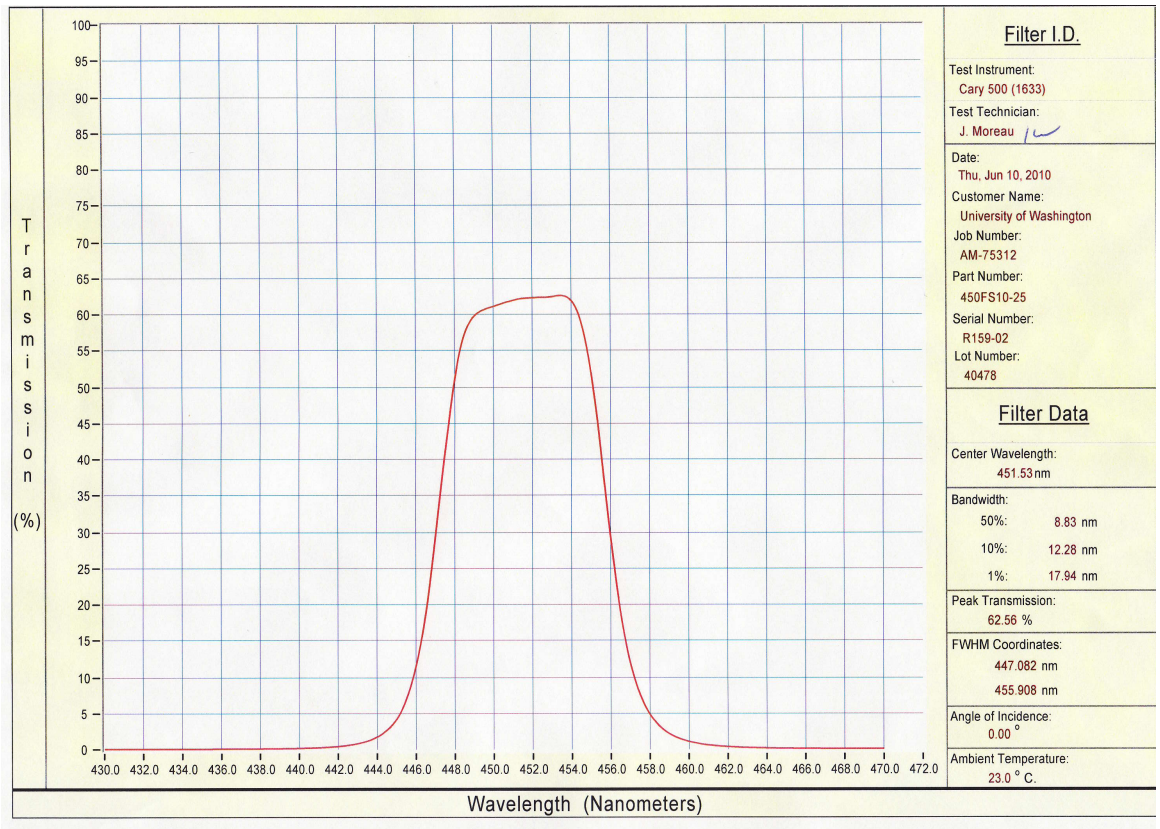

Figure E.3: Transmission curve of the bandpass filter for the He I line at 447.1 nm.

E.2 50 mm diameter bandpass filters

These filters are typically used with the high-speed camera.

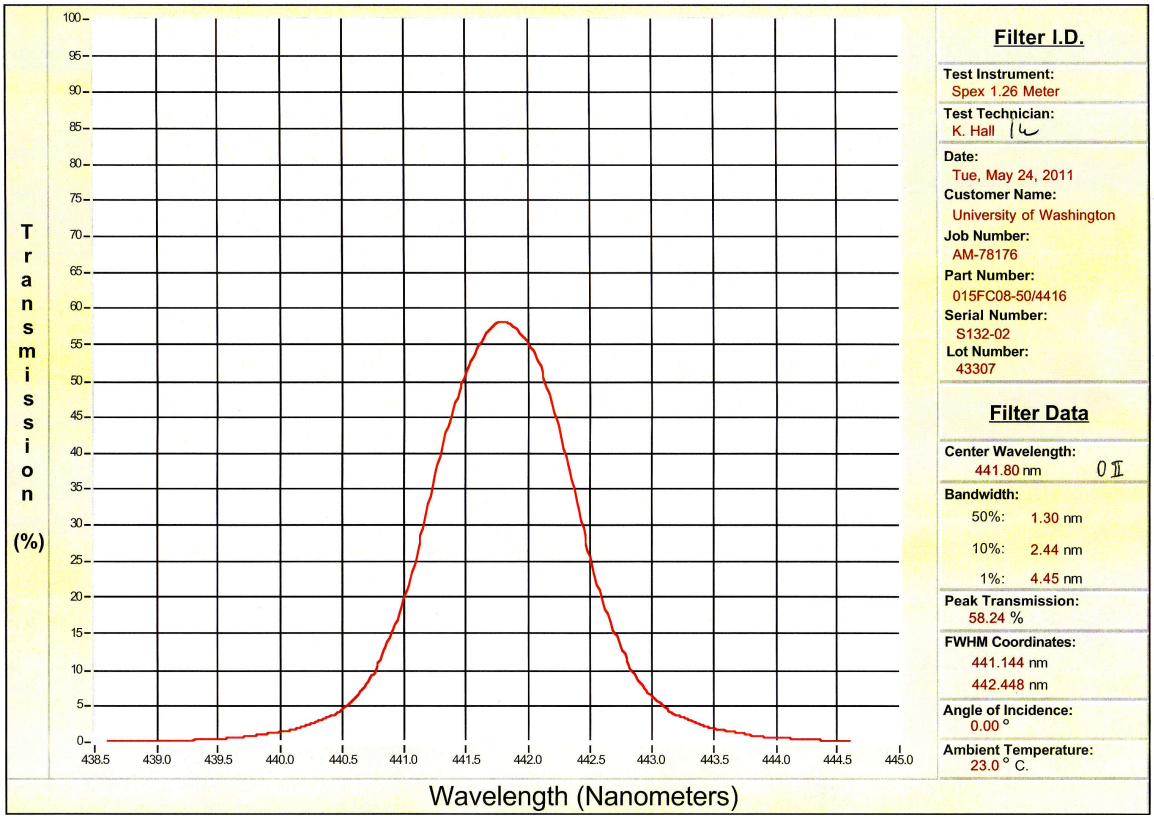

Figure E.4: Transmission curve of the bandpass filter for the O II line at 441.6 nm.

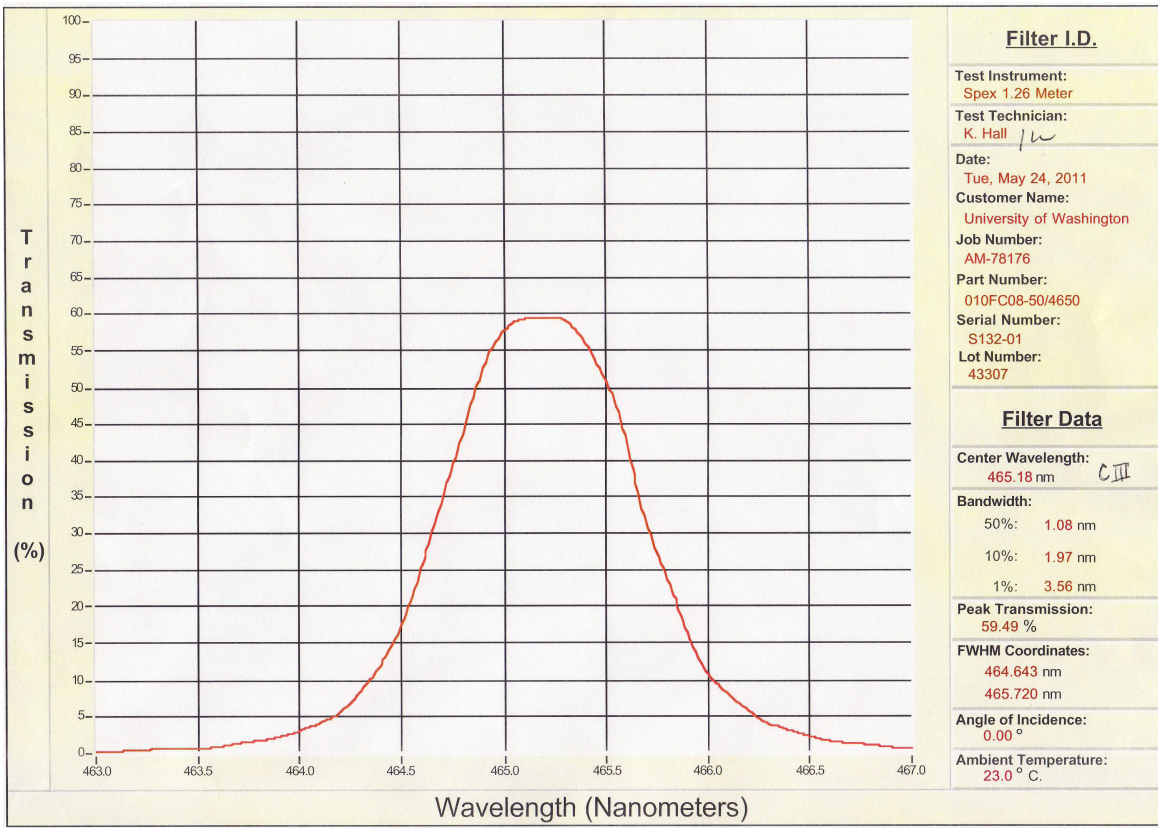

Figure E.5: Transmission curve of the bandpass filter for the C III line at 465.0 nm.

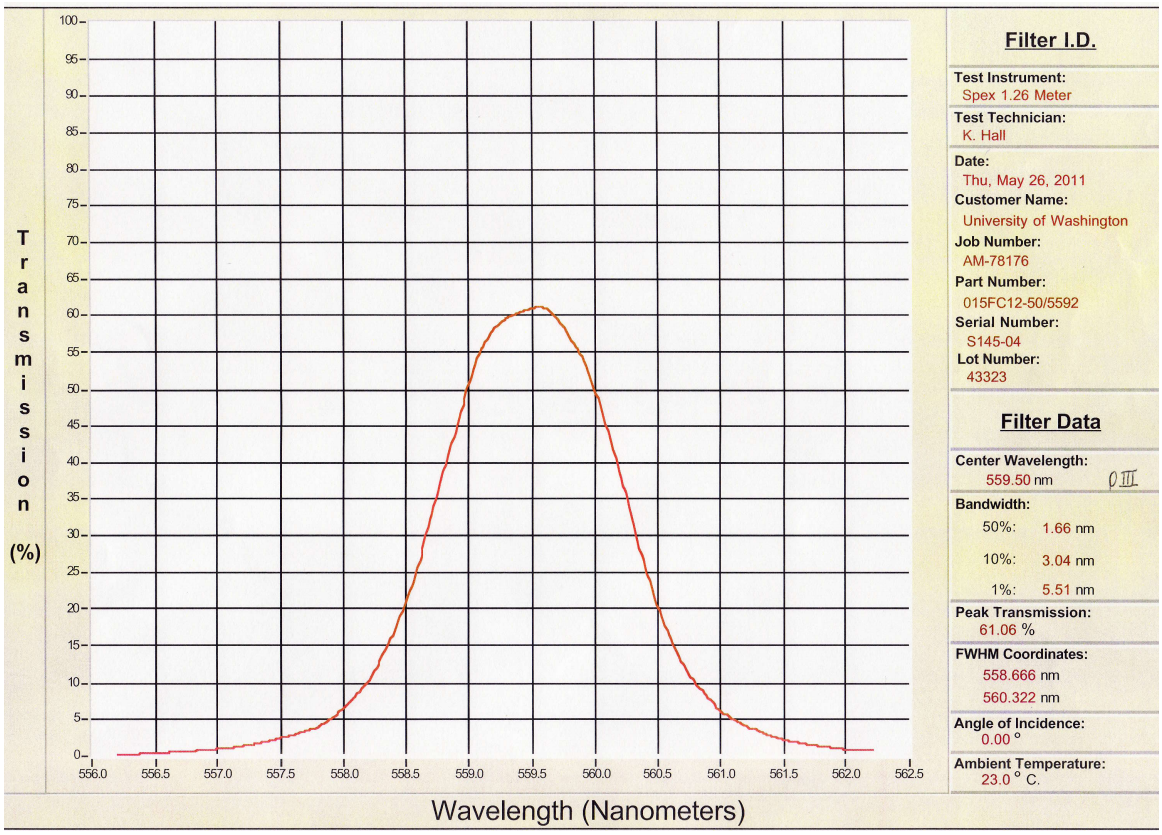

Figure E.6: Transmission curve of the bandpass filter for the O III line at 559.2 nm.

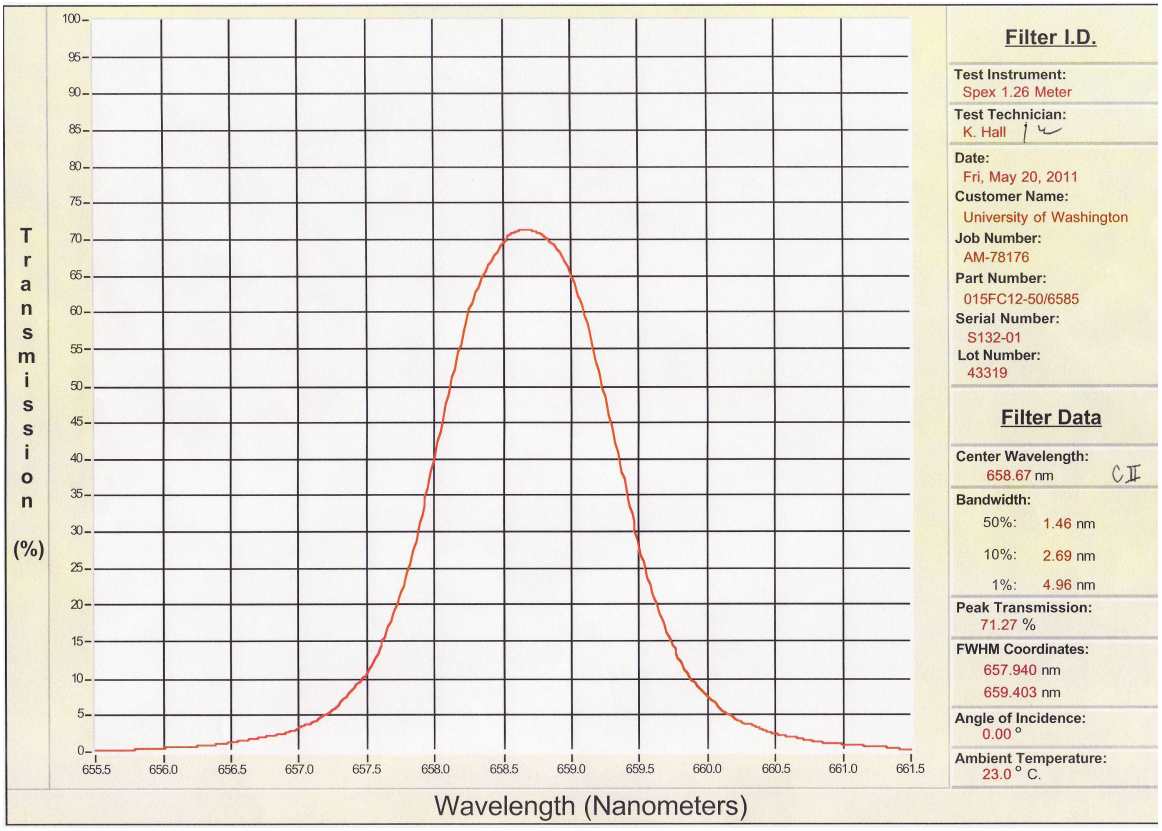

Figure E.7: Transmission curve of the bandpass filter for the C II line at 658.5 nm.

Appendix F

VUV DIAL SETTINGS

VUV Upper

Radiation Line	λ (Å)	Dial Setting (Å)	NIST Relative Intensity
H Lyman$_\alpha$	1215.7	1215.7	1000/500
D Lyman$_\alpha$	1215.3	1215.3	
C II	1335.7	1335.7	300
C III	1175.7	1175.7	500
C IV	1548.2	1548.0	1000
C V	2270.9	2273.0	40
O V	1371.3	1371.5	640
O V	629.7		1000
O VI	1031.9	1031.5	
O VII	1623.6	1624.0	

VUV Lower

Radiation Line	λ (Å)	Dial Setting (Å)	NIST Relative Intensity
H Lyman$_\alpha$	1215.7	1217.7	1000/500
D Lyman$_\alpha$	1215.3	1217.3	
C II	1335.7	1337.7	300
C III	1175.7	1177.7	500
C IV	1548.2	1550.0	1000
C V	2270.9	2273.0	40
O V	1371.3	1373.5	640
O V	629.7		1000
O VI	1031.9	1033.5	
O VII	1623.6	1626.0	